Measuring spin fluorescence with a microwave photon detector

Emanuele Albertinale

université PARIS-SACLAY

Measuring spin fluorescence with a microwave photon detector

Mesure de la fluorescence de spin avec un compteur de photons à micro-ondes

Thèse de doctorat de l'université Paris-Saclay

École doctorale n°564, physique de l'Ile-de-France (PIF)
Spécialité de doctorat: physique
Unité de recherche : Université Paris-Saclay, CEA, CNRS, SPEC, 91191, Gif-sur-Yvette, France
Référent : Faculté des sciences d'Orsay

Thèse présentée et soutenue à Paris-Saclay, le 16/07/2021, par

Emanuele ALBERTINALE

Composition du Jury

Jean-François ROCH Professeur, ENS Paris-Saclay	Président
Yasunobu NAKAMURA Professeur, RCAST Tokyo	Rapporteur & Examinateur
Gunnar JESCHKE Professeur, ETH Zurich	Rapporteur & Examinateur
Audrey BIENFAIT Chargée de recherche, CNRS Lyon	Examinatrice
Yuimaru KUBO Directeur de recherche, OIST	Examinateur
Anaïs DREAU Chargée de recherche, CNRS Montpellier	Examinatrice

Direction de la thèse

Patrice BERTET Directeur de recherche, CEA Saclay	Directeur de thèse
Emmanuel FLURIN Ingénieur-chercheur, CEA Saclay	Co-Encadrant & Examinateur

Thèse de doctorat
NNT : 2021UPASP059

This project has received funding from the European Union's Horizon 2020 research and innovation programme under the Marie Skłodowska-Curie grant agreement No 765267.

A Gio e Vero

Acknowledgements

When I look back at the last four years I can't but feel grateful for the richness that they are to me. And this is largely due to the people that guided and accompanied me day by day.

My first thanks are for Patrice and Emmanuel. For the relentless care they had in teaching me how to do research and develop intuition. Thanks Patrice for having taught me the importance of being rigorous, for your scientific advices, and the kindness with which you guided me across all the projects. Thanks Manu for all the work together, for the passion you communicate, your profound physical insight that goes straight to the point and your sparkling cordiality.

Also, this adventure would have been much harder without the help of many people. An immense thanks to Denis, who taught me everything I know about fabrication. His rigorous method and the care for the details are among the most valuable teachings I received. Thanks to Vishal, who fabricated and characterized the spin device, and whose technical help, scientific insight and friendship were vital in many occasions. Thanks to Leo, who built the first version of the setup and is now carrying on the experiment, his helpfulness and resilience are more than valuable. Thanks to Dan, who was always ready to help with codes and with questions about the future. Thanks to Pief, Sebastian and Pascal for the technical support and their friendliness. This work would not have been possible without the collaborators that contributed to its realization. Thanks to Thomas Schenkel who provided the bismuth sample, Thanks to Audrey for scientific discussions, for her support and encouragement. Thanks to the ENS collaborators and friends: Raph, Zaki, Samuel, Ulysse and Marius, who developed the first version of the photon counter and whose help was fruitful in many occasions. Finally, thanks to Andrea, Eugenio, Simone, Mattia and all the friends and members of the Marie-Curie QuSCo project, the framework in which this work was realized.

A huge thanks goes to Bartolo and Fernanda, fellows, office mates and friends, who shared with me great part of this adventure. I still smile recalling the joyful atmosphere you created. Thanks to all the new and old fellows, for their friendliness and help: thanks Eric, for your deep physical questions and your friendliness. Thanks Marianne, for your moral support in tough times and the help on the setup. Thanks Boris for your kindness and support in the lab. Thanks Nicolas, for your quiet sympathy, your practical sense and all the "lunch" callings. Thanks Anil, for the scientific discussions and the help on the measurements. Thanks Milos for your joyful attitude and technical support. Thanks to Yutian, Zhiren, Cyril, Maria, and Louis, because discussing with you and having you around felt like family. Thanks to all the Quantros for the friendly environment and the rich scientific discussions. A huge thanks to Daniel Esteve, whose scientific support and encouragement during these years were critical along the path.

Finally thanks to my family and to all the friends, they helped me making huge and small steps in this adventure.

Contents

Resumé

La résonance magnétique est une branche de la science qui vise à détecter les spins via leur absorption et leur émission de rayonnement électromagnétique. On peut distinguer deux domaines : la résonance magnétique nucléaire (RMN) qui vise à détecter les spins des noyaux, et la résonance de spin électronique (ESR) qui concerne la détection du spin des électrons non appariés. Cette thèse porte sur le développement d'une nouvelle méthodologie pour la spectroscopie ESR.

La spectroscopie ESR a de multiples applications [1]. En chimie, elle permet la détection et l'identification des radicaux libres et l'étude de la structure moléculaire et des réactions chimiques ; en biologie, elle fournit des informations structurelles sur les molécules à l'aide d'étiquettes de spin ; en archéologie, elle fournit une méthode de datation basée sur les dommages causés par les rayonnements ; en traitement quantique de l'information, elle permet d'aborder les qubits de spin à longue durée de vie.

La méthode dominante pour effectuer des mesures de spectroscopie ESR consiste à coupler de manière résonante les spins à un résonateur micro-ondes à une fréquence ω_0 et à les piloter avec des séquences d'impulsions micro-ondes, comme l'écho de Hahn. Elles conduisent à l'accumulation d'une aimantation transversale oscillante transitoire, qui provoque l'émission d'une impulsion micro-onde cohérente en phase, appelée écho de spin, dans la ligne de détection. Le signal d'écho est ensuite amplifié, et ses quadratures X, Y sont détectées par démodulation homodyne. La spectroscopie ESR commerciale souffre d'une faible sensibilité due au faible couplage entre les spins et le champ électromagnétique. Cela implique que de grands ensembles de spins sont nécessaires pour générer un signal suffisamment fort pour surmonter le bruit expérimental.

Une amélioration de la sensibilité a été démontrée avec l'utilisation de circuits supraconducteurs. L'utilisation d'un résonateur supraconducteur micrométrique à proximité de l'ensemble de spins permet de concentrer le champ micro-ondes dans un petit volume (jusqu'au femtolitre), ce qui augmente le couplage spin-photon. Ce couplage accru, combiné aux faibles pertes du résonateur supraconducteur, permet d'atteindre le régime dit de Purcell, dans lequel le taux de relaxation radiative du spin est augmenté de plusieurs ordres de grandeur [2]. Cela permet des temps de répétition rapides pour les expériences et donc un moyennage rapide. Enfin, à basse température, l'ensemble des spins a une polarisation d'équilibre plus importante, et l'utilisation d'amplificateurs paramétriques Josephson limités en quantum permet d'amplifier le signal de spin émis avec un minimum de bruit ajouté. [3]. Avec cette méthode, une sensibilité de $12\,\mathrm{spins}/\sqrt{\mathrm{Hz}}$ a été démontrée [4]. Un gain supplémentaire en sensibilité serait cependant souhaitable, afin d'atteindre la détection de spin unique.

Le but de cette thèse est d'introduire et de donner une preuve de principe d'une nouvelle méthode de détection de spin, avec un potentiel accru pour la

détection de petits nombres de spins. Contrairement à la détection par écho de Hahn, cette nouvelle méthode consiste à détecter le signal de fluorescence micro-onde incohérent émis par les spins se relaxant vers leur état fondamental après une impulsion d'excitation. Nous exploitons le taux de relaxation radiative amélioré par Purcell pour stimuler l'émission d'un signal de fluorescence micro-onde à partir d'un petit ($\sim 10^3$) ensemble de spins électroniques appartenant à des donneurs de bismuth dans du silicium. La sortie du résonateur est connectée à l'entrée d'un détecteur de photons micro-ondes unique accordable en fréquence (SMPD) récemment développé, basé sur un mélange à quatre ondes avec un qubit supraconducteur. Nous comparons cette nouvelle technique à la détection par écho de Hahn et discutons du potentiel de la détection par fluorescence pour de petits nombres de spins.

La première partie du manuscrit fournit les outils conceptuels nécessaires à la compréhension de l'expérience. Dans le chapitre 2, nous décrivons la description quantique des modes électromagnétiques, et des circuits quantiques élémentaires tels que le résonateur LC. Dans le chapitre 3, nous décrivons la dynamique des spins couplés à un résonateur, en mettant l'accent sur le champ émis par les spins pendant une séquence d'écho de spin et lors de la relaxation radiative.

La deuxième partie du manuscrit décrit la conception et la mise en œuvre des deux dispositifs utilisés dans l'expérience. Le chapitre 4 se concentre sur le dispositif de résonateur de spin, avec la caractérisation de l'écho de spin détecté en quadrature des spins donneurs de bismuth utilisés dans l'expérience. Le chapitre 5 décrit le principe, la conception et la caractérisation du SMPD.

La dernière partie du manuscrit présente les résultats expérimentaux démontrant la détection de spin avec le SMPD, à la fois en fluorescence et en écho de spin.

0.1 Détection de la fluorescence du spin

Le principe de l'expérience est illustré dans la figure 0.1(a), nous considérons N spins couplés avec une constante de couplage g_0 à un résonateur LC supraconducteur de fréquence ω_0 et de taux de décroissance d'énergie totale $\kappa = \kappa_{\text{int}} + \kappa_{\text{ext}}$. Un champ magnétique statique B_0 est appliqué à l'ensemble de spins afin d'accorder leur fréquence de Larmor en résonance avec le résonateur $\omega_{\text{s}} = \omega_0$. Nous considérons que les spins sont dans le régime de Purcell. La sortie du résonateur est reliée par des câbles micro-ondes à un détecteur de photons micro-ondes unique (SMPD), et les deux systèmes sont refroidis à des températures de l'ordre du milliKelvin. Une source de micro-ondes permet d'envoyer des impulsions pour exciter l'ensemble de spin.

L'ensemble de spin est décrit par les opérateurs de spin total $\hat{S}_i = \sum_n \hat{S}_i^{(n)}$, avec $i \in \{x, y, z\}$. Nous considérons l'ensemble initialement dans son état fondamental $\langle \hat{S}_z \rangle = -N/2$. Au temps $t = 0$, nous appliquons une impulsion π à l'ensemble (voir Fig.0.1(b,c,d)), inversant sa polarisation. En raison de l'effet Purcell, l'ensemble se relaxe spontanément avec un temps caractéristique T_{P} en émettant un signal photonique $\langle \hat{a}^\dagger \hat{a} \rangle(t)$ dans la cavité. La fuite du signal, $\kappa_{\text{ext}} \langle \hat{a}^\dagger \hat{a} \rangle(t)$, est acheminé vers un détecteur de photons micro-ondes unique. La détection se fait sans bruit intrinsèque, car la mesure est effectuée sur la base propre de l'énergie, où les fluctuations du vide sont nulles. Les seules sources de bruit résident dans les imperfections du détecteur et dans la température des lignes micro-ondes.

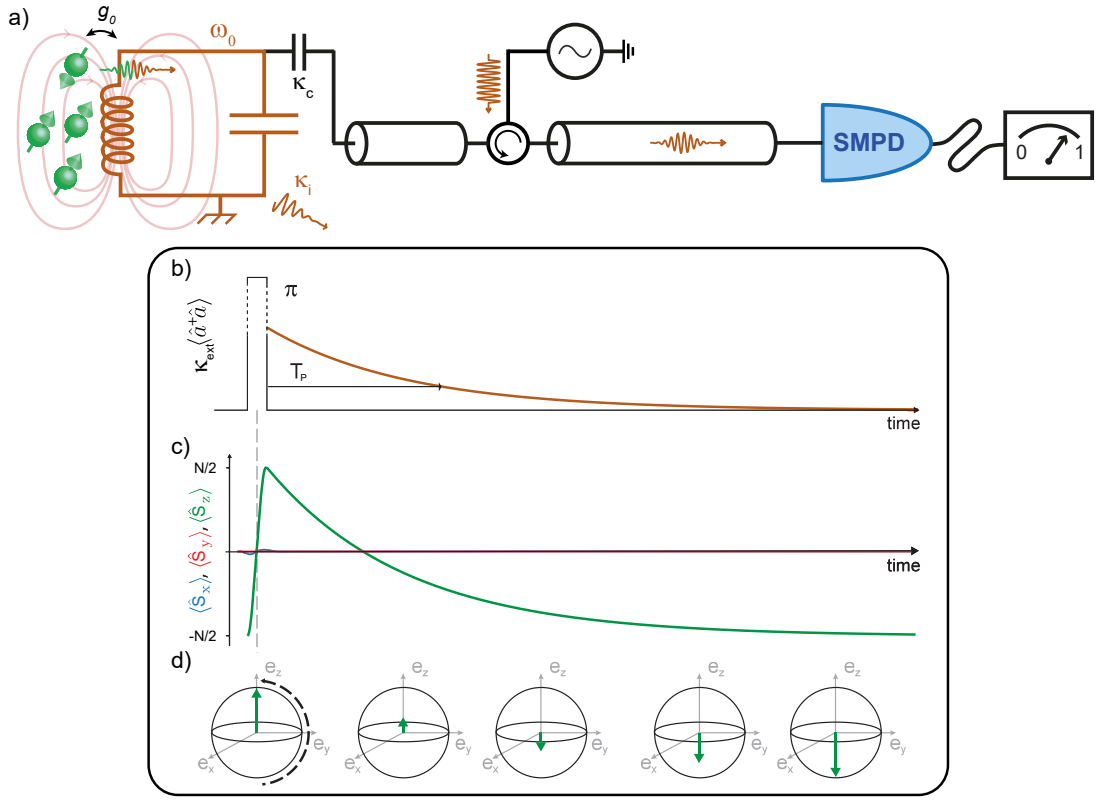

Figure 0.1: **Principe de la détection de la fluorescence de spin.** (a) Illustration du montage pour la détection photonique de la fluorescence de spin. Un ensemble de spins est couplé magnétiquement avec une constante de couplage g_0 à un résonateur LC résonnant, qui est lui-même couplé à une ligne externe avec un taux de décroissance énergétique κ_{ext}. Nous supposons un régime dans lequel le couplage avec le résonateur augmente le taux de relaxation radiative de l'ensemble de spins, en raison de l'effet Purcell. La ligne externe est utilisée pour acheminer les impulsions micro-ondes vers le résonateur et la fuite du signal est acheminée vers un détecteur de photons micro-ondes unique. (b) Une impulsion π est appliquée à l'ensemble de spins, inversant ainsi la polarisation longitudinale moyenne $\langle\hat{\sigma}_z\rangle$ de chaque spin (voir (c)). L'ensemble de spins se relaxe ensuite spontanément pour revenir à son état d'équilibre par émission de photons en un temps caractéristique T_{P}, dû à l'effet Purcell. (d) Esquisse de l'évolution du vecteur de Bloch de spin pendant la relaxation spontanée.

Afin de décrire et d'interpréter l'expérience, nous avons besoin d'outils pour modéliser l'interaction entre les différents systèmes. C'est pourquoi nous introduisons des concepts de base dans la partie de la thèse consacrée au contexte. Nous commençons le chapitre 2 par la description quantique des modes électromagnétiques, puis nous introduisons le concept de résonateur LC quantique, utile à la fois pour le module de spin et le détecteur de photons. Dans la section 2.4, nous présentons la jonction Josephson, l'élément non linéaire au cœur du détecteur de photons uniques. Après un aperçu de l'amplificateur linéaire, nous terminons le chapitre par la section 2.6, en établissant une comparaison entre la détection en quadrature et la détection de photons dans les cas monomode et multimode pour différents états du champ. Nous montrons ici que lorsqu'un petit nombre de photons est émis sur un grand nombre de modes, la détection de photons présente un meilleur rapport signal/bruit que la détection en quadrature.

Afin de décrire l'ensemble de spins et la dynamique résultant du couplage à un résonateur, nous commençons le chapitre 3 par un modèle pour un seul spin couplé à un résonateur LC. Nous généralisons ensuite le modèle à un seul spin à un ensemble de N spins dans le régime où les effets collectifs sont négligeables (faible coopérativité, ou de manière équivalente, pas d'amortissement par rayonnement). Nous calculons enfin le champ moyen et le nombre moyen de photons émis par un ensemble de spins dans trois types d'expériences : fluorescence, désintégration par induction libre et écho de Hahn.

0.2 Spectroscopie ESR des donneurs de bismuth dans le silicium

Pour notre démonstration expérimentale de la détection de spin par fluorescence, nous utilisons des spins donneurs de bismuth dans le silicium comme système modèle. Dans la première partie du chapitre 4 nous décrivons leurs propriétés, et justifions leur traitement comme un ensemble de spin effectif $1/2$.

Nous décrivons ensuite la conception du résonateur de spin. Comme l'illustre la figure 0.2, le dispositif consiste en un substrat de $^{28}\mathrm{Si}$ silicium enrichi dans lequel des donneurs de bismuth ont été implantés sur une profondeur de $\sim 100\,\mathrm{nm}$. Un résonateur LC supraconducteur de fréquence ω_0 est implanté dans l'aluminium sur la surface de la puce. Un champ magnétique statique externe B_0 est appliqué parallèlement au fil inducteur. Le champ externe permet d'accorder la fréquence de transition de spin ω_s en résonance avec ω_0 (voir Fig.0.2(c)).

Afin de caractériser l'ensemble de spin, nous effectuons une spectroscopie ESR pulsée en utilisant l'écho de spin détecté en quadrature. L'amplitude $A_\mathrm{e}(B_0)$ du signal de l'écho de Hahn montre que la première transition de bismuth se produit à un champ de $16.7\,\mathrm{mT}$ (Fig.0.2(d)). Nous mesurons ensuite le temps de relaxation de l'ensemble à l'aide d'une séquence de récupération par inversion, et trouvons un temps de relaxation du spin $T_\mathrm{P} = 300 \pm 10\,\mathrm{ms}$ (Fig.0.2(e)).

0.3 Compteur de photons micro-ondes unique

Le chapitre 5 présente le principe de fonctionnement, la conception, et la caractérisation du dispositif SMPD opérationnel, qui sont résumés dans la Fig 0.3.

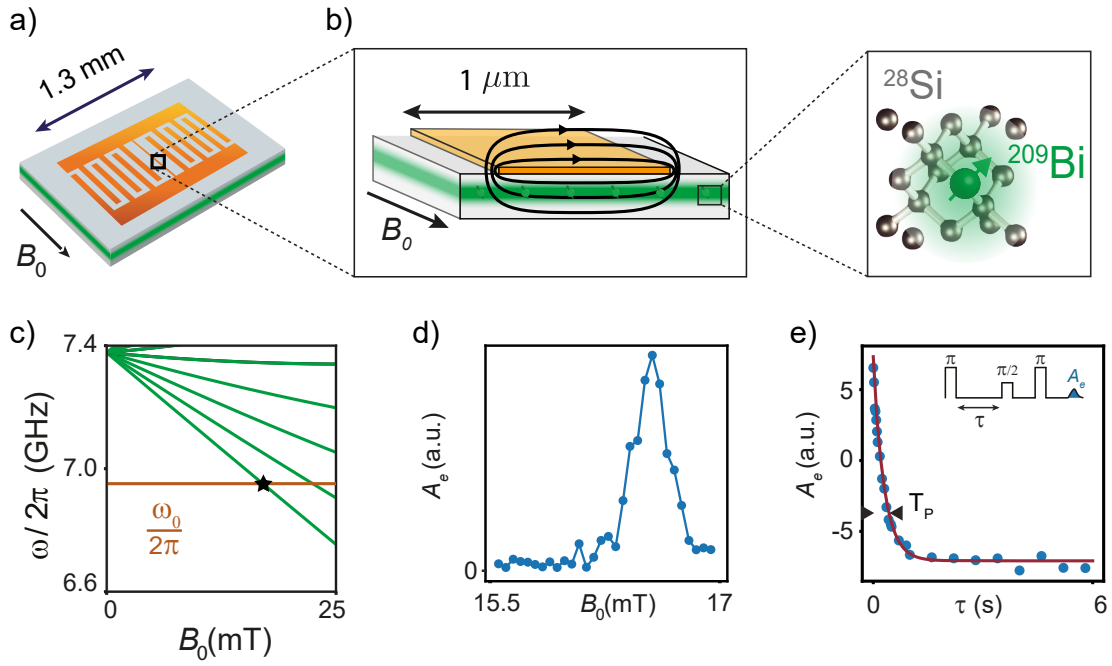

Figure 0.2: **RSE des donneurs de bismuth dans le silicium.** (a,b) Une puce de silicium intrinsèque est implantée avec des donneurs de bismuth sur une profondeur de $\sim 100\,\mathrm{nm}$. Sur la surface, un résonateur LC en aluminium est modelé à l'aide de techniques lithographiques. Un courant alternatif passant par le fil inducteur du résonateur LC produit un champ magnétique oscillant à la fréquence ω_0, qui se couple au moment magnétique du spin. Un champ magnétique externe, dans le plan, B_0 est appliqué afin d'accorder la fréquence de Larmor du spin en résonance avec ω_0 (c). (d) Amplitude mesurée de l'écho de Hahn A_e en fonction du champ B_0 utilisé pour accorder la fréquence du spin. (e) Amplitude mesurée de l'écho de Hahn A_e après un temps de retard τ d'une impulsion π sur l'ensemble de spins. Un ajustement exponentiel (ligne rouge pleine) permet d'extraire un temps de relaxation de Purcell $T_\mathrm{P} = 300 \pm 10\,\mathrm{ms}$.

Le principe du SMPD est l'excitation déterministe d'un qubit supraconducteur lorsqu'un photon entre dans le détecteur. Le processus au cœur du SMPD est le mélange à quatre ondes, illustré dans la figure 0.3(a) : la non-linéarité de la jonction Josephson convertit l'excitation du photon entrant à la fréquence ω_b, collecté dans un résonateur tampon, avec un photon provenant d'une pompe auxiliaire à ω_p, en une excitation du qubit à ω_q plus un photon à une fréquence différente ω_w qui est libéré dans un résonateur de déchets suramorcé. Le mélange à quatre ondes nécessite la satisfaction d'une condition de conservation de l'énergie : $\omega_b + \omega_p = \omega_q + \omega_w$. Le qubit peut être réinitialisé à son état fondamental par le processus inverse, qui est activé par l'émission de micro-ondes à ω_w sur le résonateur de déchets. Nous fournissons un modèle pour le fonctionnement du SMPD, qui permet de calculer l'efficacité et la largeur de bande. Le modèle montre qu'il existe une amplitude de pompe optimale pour laquelle l'efficacité du mélange à quatre ondes atteint 1.

Dans la section 5.4, nous présentons la conception de la puce SMPD, composée de deux résonateurs à guide d'ondes coplanaire agissant comme tampon et déchet, couplés à un qubit transmon. Le résonateur tampon est rendu accordable en fréquence par l'insertion d'un SQUID dans l'inductance. Les paramètres

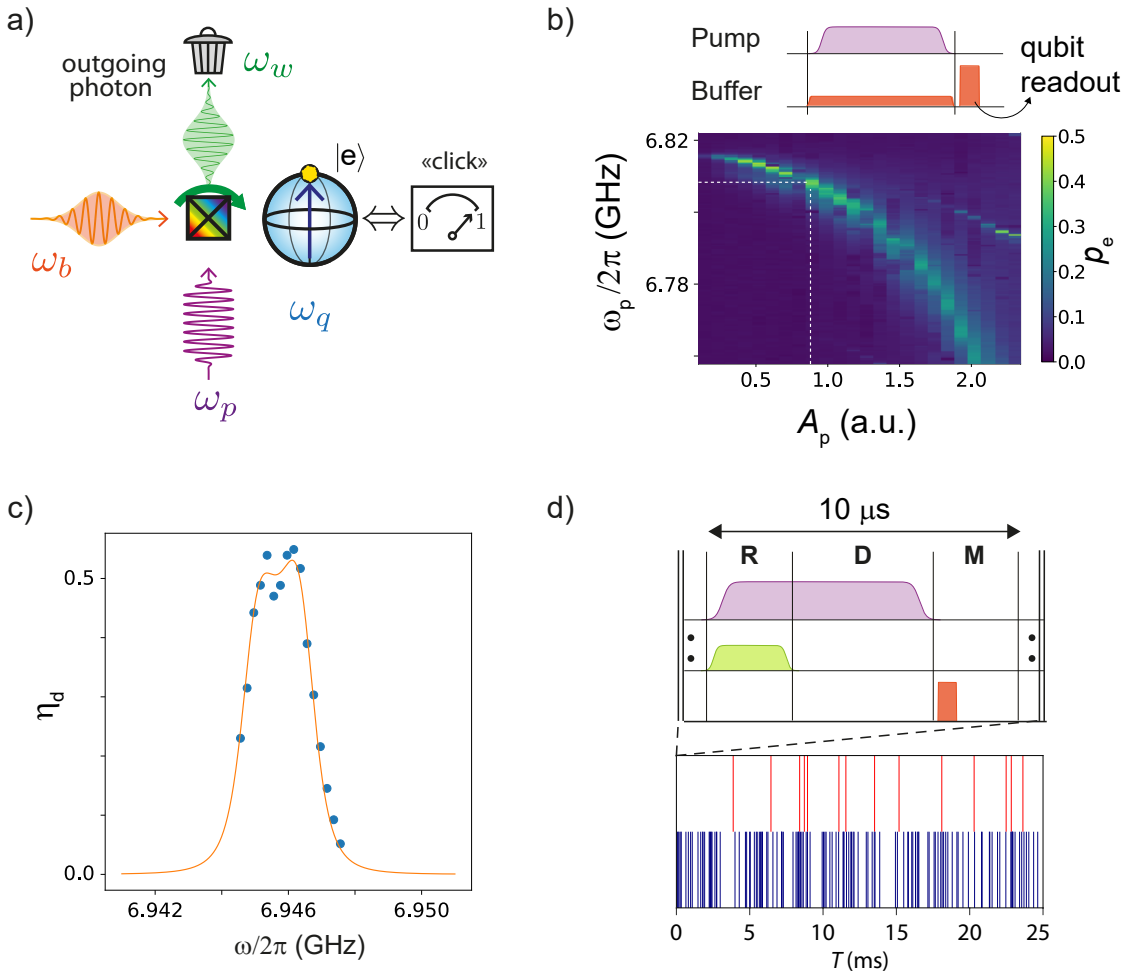

Figure 0.3: **SMPD.** (a) Principe du processus de mélange à quatre ondes au cœur du SMPD. La non-linéarité d'un qubit supraconducteur (carré noir barré) permet le mélange en fréquence d'un photon entrant à la fréquence ω_b et d'un signal de pompe à la fréquence ω_p, favorisant l'excitation du qubit à la fréquence ω_q et la libération d'un photon dans un mode résiduel suramorcé à la fréquence ω_w. L'activation du processus est soumise à la condition d'adaptation de fréquence $\omega_\mathrm{p} = \omega_\mathrm{q} + \omega_\mathrm{w} - \omega_\mathrm{b}$. (b) Accord de ω_p à la condition de résonance. (En haut) Un état cohérent faible à la fréquence ω_b est envoyé au SMPD tandis qu'un son de pompe de fréquence ω_p et d'amplitude A_p est émis sur le qubit avant la lecture du qubit. (En bas) Probabilité d'état excité du qubit p_e en fonction de ω_p et A_p. Les lignes blanches indiquent les paramètres de fonctionnement choisis. (c) Efficacité de détection SMPD mesurée (points bleus) et calculée (ligne orange) en fonction de la fréquence du photon incidente ω. Une efficacité maximale de $0,53 \pm 1$ est atteinte sur une largeur de bande $\Delta_\mathrm{det} = 2\pi \times 2.1\,\mathrm{MHz}$. (d) Fonctionnement cyclique du SMPD. Une séquence de détection de $11,7\,\mu\mathrm{s}$ de long (en haut), composée d'une réinitialisation du détecteur, d'une détection de photons et d'une mesure de qubit, est jouée de manière cyclique afin de recueillir des informations en continu sur les photons qui frappent le détecteur. Lorsqu'aucun signal n'est envoyé au SMDP, un taux de comptage sombre $\nu_\mathrm{dc} = 1.53\,\mathrm{comptes/ms}$ est enregistré (en bas, lignes rouges), lorsqu'un son cohérent est envoyé (en bas, lignes bleues), le taux augmente proportionnellement au nombre moyen de photons jusqu'à ce qu'une saturation se produise (non représenté).

du circuit sont conçus à l'aide de simulations micro-ondes par éléments finis, complétées par une bibliothèque Python pour calculer les couplages non linéaires. La fabrication du circuit est réalisée sur une puce de silicium intrinsèque où une couche d'aluminium de $60\,\mathrm{nm}$ d'épaisseur est modelée à l'aide de la lithographie par faisceau d'électrons et de la gravure humide, la recette complète est décrite dans la section 5.4.

Dans la section 5.5, nous présentons la configuration utilisée pour caractériser le SMPD à des températures de l'ordre du milliKelvin. Dans la section 5.6 nous mesurons les fréquences et les taux de décroissance d'énergie des éléments du SMPD, du résonateur tampon, du résonateur résiduel et du qubit. Nous caractérisons ensuite le processus de mélange à quatre ondes en mode continu en envoyant un son de pompe de fréquence ω_p et d'amplitude A_p sur le qubit, tout en alimentant le résonateur tampon en photons. L'activation du processus, en fonction de ω_p et de A_p, est révélée par une augmentation de la probabilité d'excitation du qubit p_e, comme le montre la fig.0.3(b). Dans la section 5.6, nous mesurons un pic d'efficacité de détection $\eta_\mathrm{d} = 0,53$ et une largeur de bande de détection $\Delta_\mathrm{det} = 2\pi \times 2.1\,\mathrm{MHz}$ (voir fig.0.3(c)).

Le fonctionnement cyclique du SMPD est illustré à la Fig.0.3(d). Il se compose de 3 étapes : une étape de réinitialisation où le qubit est placé dans son état de base, une étape de détection où un photon est converti en une excitation du qubit par le processus de mélange à quatre ondes, une étape de lecture du qubit conduisant à la réponse "click/no-click". Le SMPD est caractérisé par une efficacité de détection η_d, définie comme la probabilité moyenne de détecter un clic dans une fenêtre de détection T_d lorsqu'un photon est incident. D'autre part, le taux de comptage sombre du détecteur ν_dc donne le nombre de comptages par unité de temps enregistré lorsqu'aucun signal n'est envoyé au SMPD.

Figure 1.3(d) montre le détecteur de photons en fonctionnement lorsqu'aucun signal n'est envoyé à l'entrée. De rares événements de clics sont enregistrés, avec un "taux de comptage sombre" $\nu_\mathrm{dc} = 1.53\,\mathrm{comptes/ms}$. Lorsqu'un faible son cohérent est émis, comme décrit dans la section 5.6, un flux de photons est détecté, comme illustré dans 0.3(d). Le cycle de détection est répété $\sim 2.5 \times 10^3\,\mathrm{times}$ sur $25\,\mathrm{ms}$, à chaque cycle l'état du qubit apporte la réponse binaire "click/no-click".

0.4 Mesure de la fluorescence des spins avec un détecteur de photons micro-ondes

Dans le chapitre 6 nous décrivons les principaux résultats obtenus dans cette thèse. La section 6.1 présente l'état de l'art sur la détection de la fluorescence de spin, avec les expériences de *Sleator et al.* [5] et *McCoy and Ernst* [6], montrant la détection de la fluorescence de spin par des mesures de bruit de puissance.

La section 6.2 décrit notre expérience, où nous connectons avec des câbles micro-ondes la sortie du dispositif de spin à l'entrée du SMPD, comme le montre la Fig. 0.1. Les spins sont accordés en résonance avec le résonateur couplé $\omega_\mathrm{s} = \omega_0$ et le résonateur tampon du SMPD est accordé en résonance avec le dispositif de spin $\omega_\mathrm{b} = \omega_0$.

La mesure de la fluorescence est présentée dans la section 6.2. Nous appliquons une impulsion π à l'ensemble de spin et détectons le signal photonique en faisant fonctionner le SMPD de manière cyclique sur $\sim 1\,\mathrm{s}$. Figure 0.4(a) mon-

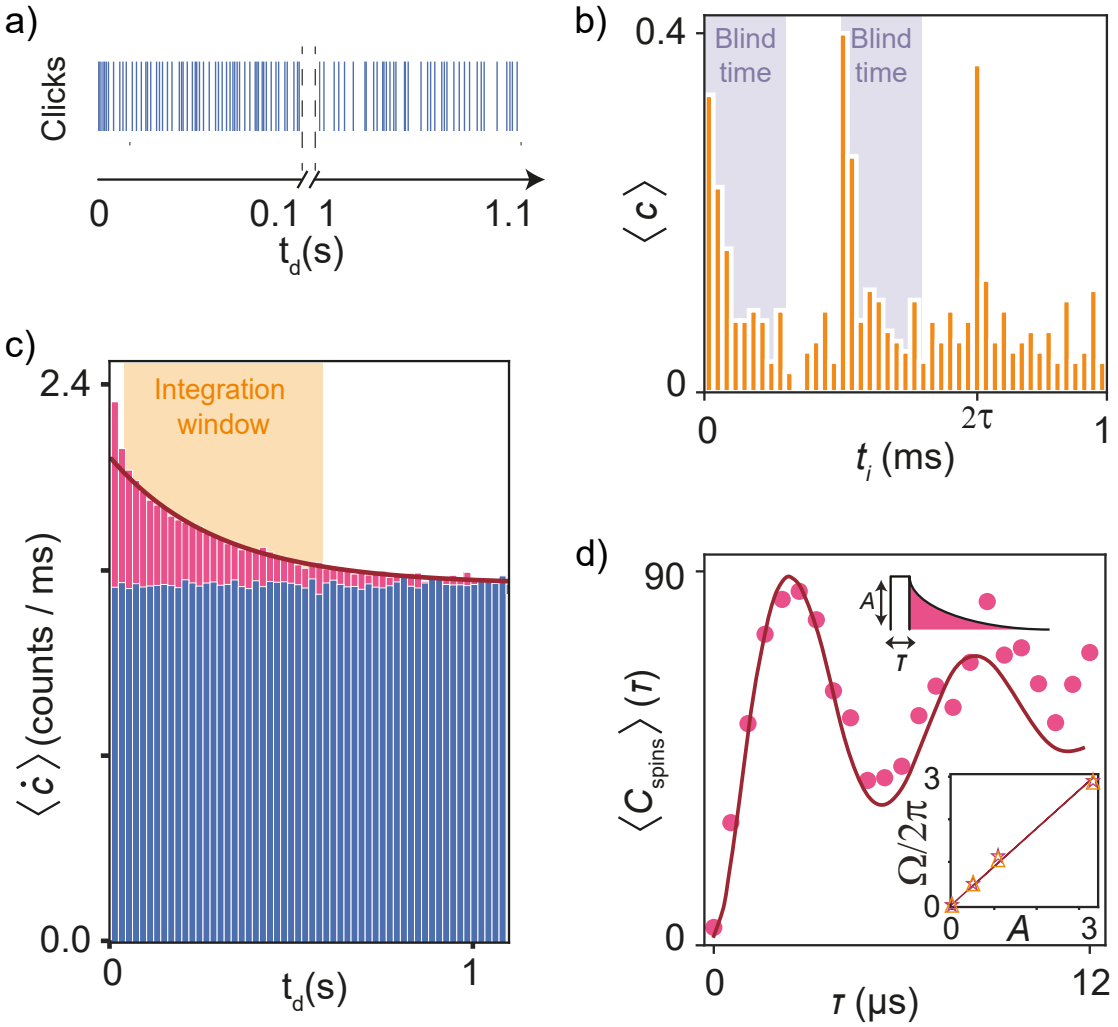

Figure 0.4: **SMPD detection.** (a) Trace de clics SMPD au début ($0\,sto0.1\,\mathrm{s}$) et à la fin ($1\,sto1.1\,\mathrm{s}$) du temps t_d après une impulsion π appliquée sur l'ensemble de spins. Plus de clics sont enregistrés aux premiers temps. (c) Histogramme du taux de comptage SMPD $\langle \dot{c} \rangle$ mesuré sur des intervalles de temps de $19\,\mathrm{ms}$, en fonction du temps t_d après une impulsion π (rose) ou sans impulsion (bleu) sur l'ensemble de spins. Lorsque l'impulsion est appliquée, un signal de photons est enregistré, décroissant exponentiellement avec un temps caractéristique $\sim 309 \pm 10\,\mathrm{ms}$, compatible avec le temps de relaxation de Purcell du spin T_P. (b) Nombre moyen de comptages $\langle c \rangle$ enregistrés dans chaque $23\mu s$ de temps pendant une séquence d'écho de Hahn. Une augmentation de $\langle c \rangle$ est observée en correspondance des impulsions de Hahn et au temps d'écho 2τ. (d) Nombre intégré moyen de comptages $\langle C_\mathrm{spins} \rangle$ dans une fenêtre temporelle de $500\mathrm{ms}$ de long (voir (c)) après une impulsion de longueur T et d'amplitude fixe A appliquée à l'ensemble de spins. Les oscillations dans C_spins révèlent des nutations de Rabi de l'ensemble de spins, avec une fréquence Ω, qui dépend linéairement de A (encadré).

tre la trace de photocomptage obtenue, où nous observons plus de clics aux premiers temps qu'aux temps ultérieurs. En répétant l'expérience 500 fois et en traçant le taux de comptage mesuré pour chaque tranche de temps de $20\,\mathrm{ms}$ (voir Fig.0.4(c)), nous observons un taux de comptage décroissant exponentiellement vers la ligne de base du comptage sombre sur une échelle de temps $300\,\mathrm{ms}$, compatible avec le taux de décroissance radiative de Purcell de l'ensemble de spins (voir Fig.0.2). L'efficacité globale est de $\eta = 0.01$, limitée par les pertes du résonateur $\kappa_{\mathrm{ext}}/\kappa = 0.22$. Nous obtenons un SNR de ~ 5 sur une seule mesure, montrant une amélioration de cinq fois par rapport au SNR obtenu en détection par écho quadrature sur le même échantillon. Dans la section 6.3, nous montrons la détection de photons de l'écho de Hahn (voir Fig.0.4(b)), avec un rapport signal/bruit similaire à celui de la détection en quadrature. Enfin, dans la section 6.5, nous utilisons le détecteur de photons pour mesurer les oscillations de Rabi (voir Fig.1.4(d)) et réalisons la spectroscopie de l'ensemble de spins, à la fois avec des techniques de fluorescence et d'écho. Nous concluons ce chapitre par une estimation du nombre de spins et quelques remarques concernant le potentiel de cette nouvelle méthode de détection des spins.

Chapter 1

Introduction

Magnetic resonance is a branch of science that aims to detect spins via their absorption and emission of electromagnetic radiation. Two areas can be distinguished: nuclear magnetic resonance (NMR) which aims at detecting the spins of nuclei, and electron spin resonance (ESR) that concerns the detection of the spin of unpaired electrons. This thesis focuses on the development of a new methodology for ESR spectroscopy.

ESR spectroscopy has multiple applications [1]. In chemistry, it allows the detection and identification of free radicals and the study of molecular structure and chemical reactions; in biology it yields structural information on molecules using spin labels; in archaeology it provides a dating method based on radiation damage; in quantum information processing it provides a way to address long-lived spin qubits.

The dominant method for performing ESR spectroscopy measurements is to couple resonantly the spins to a microwave resonator at a frequency ω_0 and drive them with sequences of microwave pulses, such as the Hahn echo. They lead to the build-up of a transient oscillating transverse magnetization, which causes the emission of a phase-coherent microwave pulse called a spin-echo in the detection line. The echo signal is then amplified, and its quadratures X, Y detected by homodyne demodulation. Commercial ESR spectroscopy suffers from poor sensitivity due to the weak coupling between spins and the electromagnetic field. This implies that large spin ensembles are required to generate a signal strong enough to overcome experimental noise.

An improvement in sensitivity has been demonstrated with the use of superconducting circuits. Using a micrometric superconducting resonator in close vicinity to the spin ensemble allows to focus the microwave field in a small volume (down to the femtoliter), thus increasing the spin-photon coupling. This increased coupling, combined with the low losses of the superconducting resonator, allows to reach the so-called Purcell regime, in which the spin radiative relaxation rate is increased by several orders of magnitude [2]. This allows fast repetition times for the experiments and thus fast averaging. Finally, at low temperatures the spin ensemble has larger equilibrium polarization, and the use of quantum-limited Josephson Parametric amplifiers allows for the amplification of the emitted spin signal with minimum added noise [3]. With this method, a sensitivity of $12\,\mathrm{spins}/\sqrt{\mathrm{Hz}}$ has been demonstrated [4]. A further gain in sensitivity would be however desirable, in order to reach single spin detection.

The aim of this thesis is to introduce and give a proof-of-principle of a new method for spin sensing, with increased potential for the detection of small num-

bers of spins. In contrast to Hahn echo detection, this novel method comprises the detection of the incoherent microwave fluorescence signal emitted by spins relaxing to their ground state after an excitation pulse. We exploit the Purcell-enhanced radiative relaxation rate to stimulate the emission of a microwave fluorescence signal from a small ($\sim 10^3$) ensemble of electron spins belonging to bismuth donors in silicon. The output of the resonator is connected to the input of a newly-developed frequency-tunable single microwave photon detector (SMPD) based on four-wave mixing with a superconducting qubit. We compare this new technique to Hahn-echo detection and discuss the potential of fluorescence detection for small numbers of spins. The main results of this thesis are also reported in Ref. [7].

The first part of the manuscript provides the necessary conceptual tools to understand the experiment. In Chapter 2, we outline the quantum description of electromagnetic modes, and of elementary quantum circuits such as the LC resonator. In Chapter 3 we describe the dynamics of spins coupled to a resonator, with an emphasis on the field emitted by the spins both during a spin-echo sequence, and upon radiative relaxation.

The second part of the manuscript describes the design and implementation of the two devices used in the experiment. Chapter 4 focuses on the spin resonator device, with quadrature-detected spin-echo characterization of the bismuth donor spins used in the experiment. Chapter 5 describes the SMPD principle, design and characterization.

The last part of the manuscript presents the experimental results demonstrating spin detection with the SMPD, both in fluorescence and in spin-echo detection.

1.1 Spin fluorescence detection

The principle of the experiment is illustrated in figure 1.1(a), we consider N spins coupled with coupling constant g_0 to a superconducting LC resonator of frequency ω_0 and total energy decay rate $\kappa = \kappa_{\text{int}} + \kappa_{\text{ext}}$. A static magnetic field B_0 is applied to the spin ensemble in order to tune their Larmor frequency in resonance with the resonator $\omega_{\text{s}} = \omega_0$. We consider the spins to be in the Purcell regime. The output of the resonator is connected with microwave cables to a single microwave photon detector (SMPD), and both systems are cooled down to milliKelvin temperatures. A microwave source allows to send pulses to excite the spin ensemble.

The spin ensemble is described by the total spin operators $\hat{S}_i = \sum_n \hat{S}_i^{(n)}$, with $i \in \{x, y, z\}$. We consider the ensemble initially in its ground state $\langle \hat{S}_z \rangle = -N/2$. At time $t = 0$ we apply a π-pulse to the ensemble (see Fig.1.1(b,c,d)), inverting its polarization. Due to the Purcell effect, the ensemble spontaneously relaxes with characteristic time T_{P} by emitting a photon signal $\langle \hat{a}^\dagger \hat{a} \rangle(t)$ into the cavity. The signal leaking, $\kappa_{\text{ext}} \langle \hat{a}^\dagger \hat{a} \rangle(t)$, is routed towards a single microwave photon detector. The detection happens without intrinsic noise, because the measurement is performed on the energy eigenbasis, where vacuum fluctuations are zero. The only noise sources are in the imperfections of the detector and in the temperature of microwave lines.

In order to describe and interpret the experiment we need tools to model the interplay between different systems. For this reason in the background part of

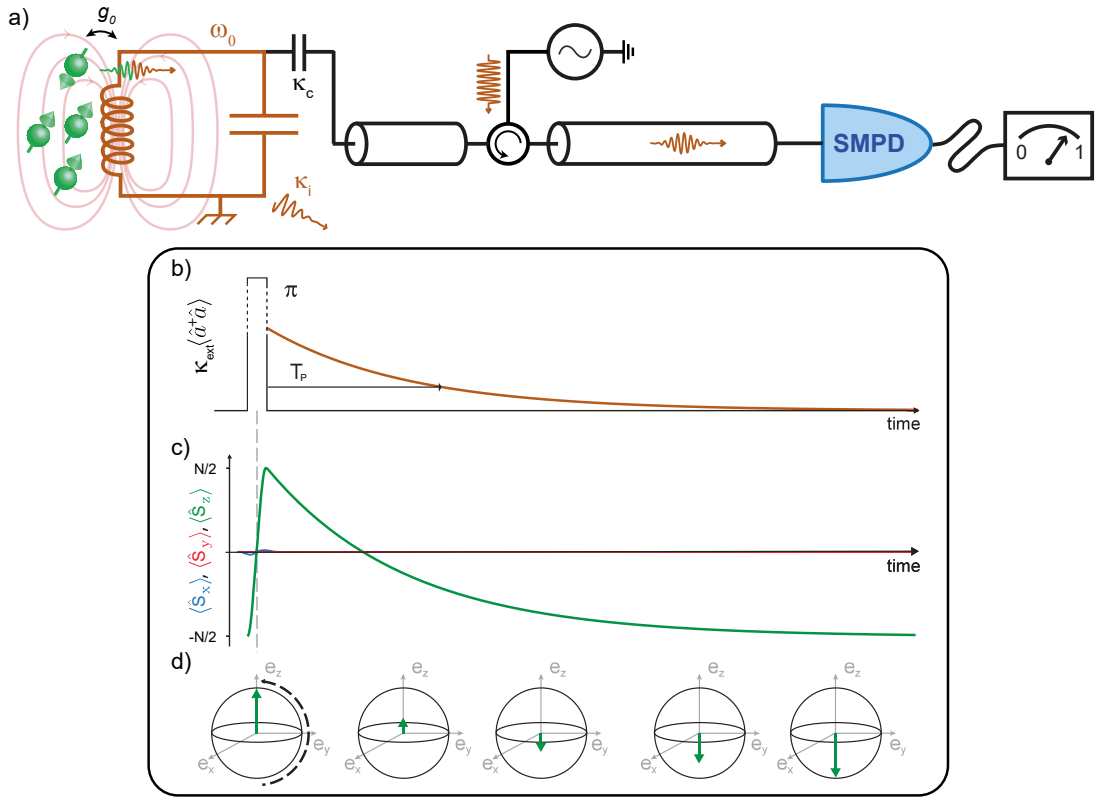

Figure 1.1: **Principle of spin fluorescence detection.** (a) Illustration of the setup for the photon detection of spin fluorescence. An ensemble of spins is magnetically coupled with coupling constant g_0 to a resonant LC resonator, which is itself coupled to an external line with energy decay rate κ_{ext}. We assume a regime in which the coupling with the resonator enhances the radiative relaxation rate of the spin ensemble, due to the Purcell effect. The external line is used to convey microwave pulses to the resonator and the signal leaking is routed towards a single microwave photon detector. (b) A π-pulse is applied to the spin ensemble, thus flipping the average longitudinal polarization $\langle\hat{\sigma}_z\rangle$ of each spin (see (c)). The spin ensemble then spontaneously relaxes back to its equilibrium state by photon emission in a characteristic time T_{P}, due to the Purcell effect. (d) Sketch of the spin Bloch vector evolution during spontaneous relaxation.

the thesis we introduce basic concepts. We begin chapter 2 with the quantum description of electromagnetic modes, we then introduce the concept of quantum LC resonator, useful both for the spin module and the photon detector. In section 2.4 we introduce the Josephson junction, the non-linear element at the heart of the single photon detector. After an overview of linear amplifier, we finish the chapter with section 2.6, drawing a comparison between quadrature detection and photon detection in the single-mode and multi-mode cases for different states of the field. Here, we show that when a small number of photons is emitted on a large number of modes photon detection has larger SNR than quadrature detection.

In order to describe the spin ensemble and the dynamics arising due to the coupling to a resonator we start chapter 3 with a model for a single spin coupled to an LC resonator. We then generalize the single-spin model to an ensemble of N spins in the regime where collective effects are negligible (low cooperativity,

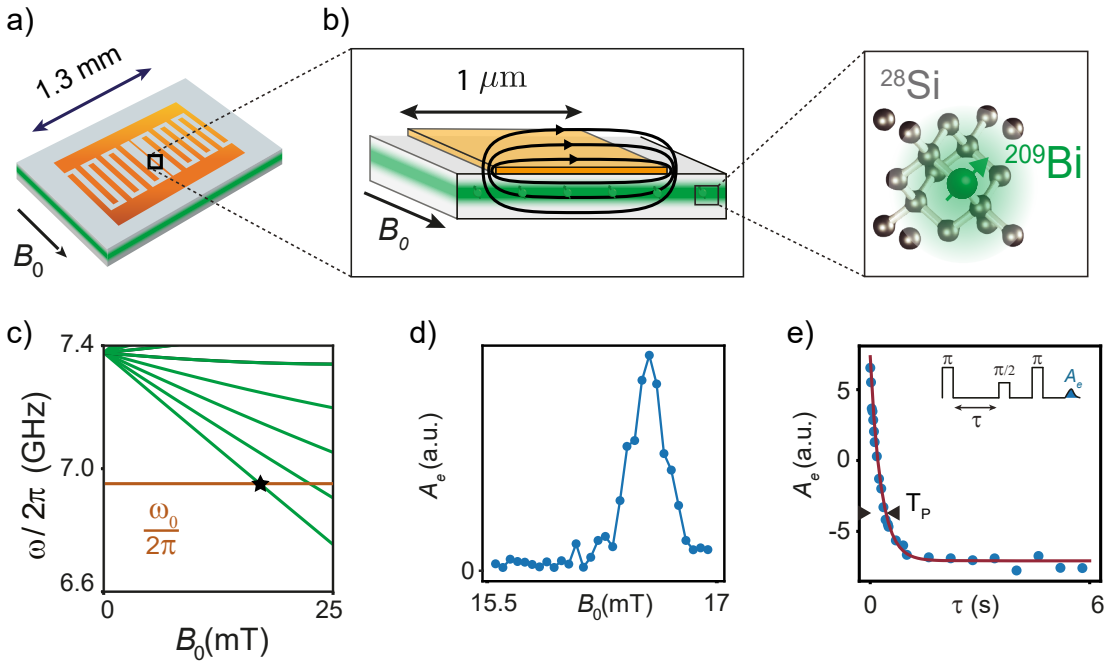

Figure 1.2: **ESR spectroscopy of bismuth donors in silicon.** (a,b) An intrinsic-silicon chip is implanted with bismuth donors over a depth of $\sim 100\,\mathrm{nm}$. On top of the surface an aluminium LC resonator is patterned using lithographic techniques, ac current passing through the inductor wire of the LC resonator produces an oscillating magnetic field at frequency ω_0, which couples to the spin magnetic moment. An external, in-plane, magnetic field B_0 is applied in order to tune the spin Larmor frequency in resonance with ω_0 (c). (d) Measured Hahn echo amplitude A_e as a function of the field B_0 used to tune the spin frequency. (e) Measured Hahn echo amplitude A_e after a delay time τ from a π-pulse on the spin ensemble. An exponential fit (solid red line) allows to extract a Purcell relaxation time $T_\mathrm{P} = 300 \pm 10\,\mathrm{ms}$.

or equivalently no radiation damping). We finally compute the average field and average photon number emitted by a spin ensemble in three types of experiments: fluorescence, free-induction decay and Hahn-echo.

1.2 ESR spectroscopy of bismuth donors in silicon

For our experimental demonstration of spin detection by fluorescence, we use bismuth donor spins in silicon as a model system. In the first part of chapter 4 we describe their properties, and justify their treatment as an ensemble of effective spin $1/2$.

We then describe the design of the spin resonator. As illustrated in figure 1.2, the device consists in a substrate of ^{28}Si-enriched silicon in which bismuth donors have been implanted over a depth of $\sim 100\,\mathrm{nm}$. A superconducting lumped LC resonator of frequency ω_0 is patterned in aluminium on top of the chip surface. An external static magnetic field B_0 is applied parallel to the inductor wire. The external field allows to tune the spin transition frequency ω_s into resonance with ω_0 (see Fig.1.2(c)).

In order to characterize the spin ensemble, we perform pulsed ESR spec-

troscopy using quadrature-detected spin-echo. The amplitude $A_{\mathrm{e}}(B_0)$ of the Hahn echo signal shows the first bismuth transition occurring at a field of $16.7\,\mathrm{mT}$ (Fig.1.2(d)). We then measure the relaxation time of the ensemble with an inversion recovery sequence, finding a spin relaxation time $T_{\mathrm{P}} = 300 \pm 10\,\mathrm{ms}$ (Fig.1.2(e)).

1.3 Single microwave photon counter

Chapter 5 presents the working principle, design, and characterization of the operational SMPD device, which are summarized in Fig 1.3.

The SMPD principle is the deterministic excitation of a superconducting qubit when a photon enters the detector. The process at the heart of the SMPD is four wave mixing, illustrated in figure 1.3(a): the non-linearity of the Josephson junction converts the incoming photon excitation at frequency ω_b, collected in a buffer resonator, together with a photon from an auxiliary pump tone at ω_p, into a qubit excitation at ω_q plus a photon at a different frequency ω_w which is released into an overdamped waste resonator. Four-wave mixing requires an energy-conserving condition to be satisfied: $\omega_b + \omega_p = \omega_q + \omega_w$. The qubit can be reset to its ground state by the reverse process, which is activated by shining microwave at ω_{w} on the waste resonator. We provide a model for SMPD operation, which allows to calculate efficiency and bandwidth. The model shows that there is an optimal pump amplitude for which the four-wave-mixing efficiency reaches 1.

In section 5.4 we report the design of the SMPD chip, consisting of two coplanar-waveguide resonators acting as buffer and waste, coupled to a transmon qubit. The buffer resonator is made frequency-tunable by inserting a SQUID in the inductance. The circuit parameters are designed using microwave finite-element simulations, complemented by a Python library package to compute the non-linear couplings. Fabrication of the circuit is realized on an instrinsic silicon chip where a $60\,\mathrm{nm}$-thick aluminium layer is patterned using electron-beam lithography and wet etching, the full recipe is described in section 5.4.

In section 5.5 we present the setup used to characterize the SMPD at milliKelvin temperatures. In section 5.6 we measure the frequencies and energy decay rates of the SMPD elements, buffer resonator, waste resonator and qubit. We then characterize the four-wave mixing process in continuous mode by shining a pump tone of frequency ω_{p} and amplitude A_{p} on the qubit, while populating the buffer resonator with photons. The activation of the process, as a function of ω_{p} and A_{p}, is revealed by an increased qubit excited probability p_{e}, as shown in fig.1.3(b). In section 5.6, we measure a peak detection efficiency $\eta_{\mathrm{d}} = 0.53$ and a detector bandwidth $\Delta_{\mathrm{det}} = 2\pi \times 2.1\,\mathrm{MHz}$ (see Fig.1.3(c)).

Cyclic operation of the SMPD is shown in Fig. 1.3(d). It consists in 3 steps: a reset step where the qubit is set to its ground state, a detection step where a photon is converted into a qubit excitation through the four-wave mixing process, a qubit readout step leading the response "click/no-click". The SMPD is characterized by a detection efficiency η_{d}, defined as the average probability of detecting a click in a detection window T_{d} when a photon is impinging. On the other hand, the detector dark count rate ν_{dc} gives the number of counts per unit time recorded when no signal is sent to the SMPD.

Figure 1.3(d) shows the photon detector in operation when no signal is shined on the input. Rare click events are recorded, with a "dark count rate" $\nu_{\mathrm{dc}} = 1.53\,\mathrm{counts/ms}$. When a weak coherent tone is shined, as described in section

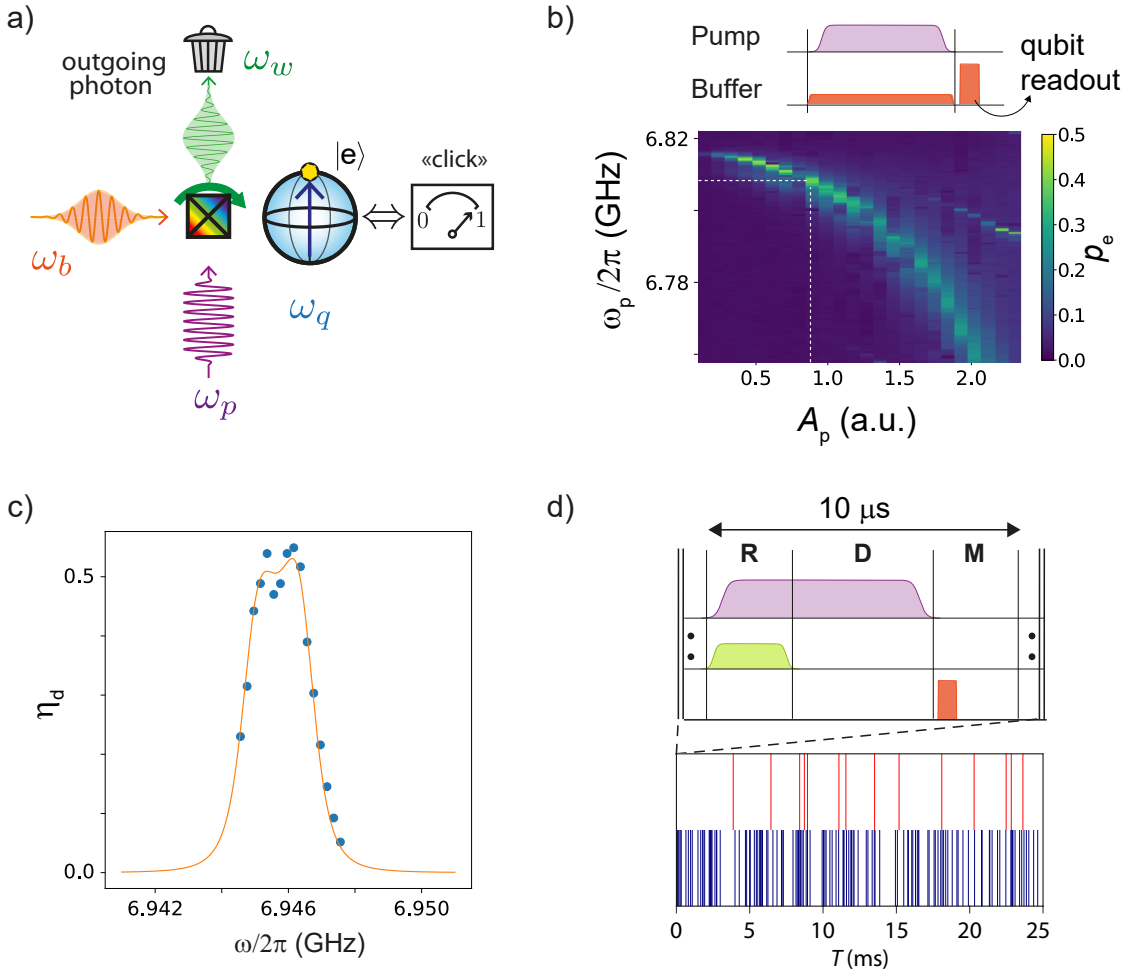

Figure 1.3: **SMPD.** (a) Principle of the four-wave mixing process at the heart of the SMPD. The non-linearity of a superconducting qubit (black crossed square) allows frequency mixing of an incoming photon at frequency ω_b and a pump tone at frequency ω_p, promoting the excitation of the qubit at frequency ω_q and the releasing of a photon in an overdamped waste mode at frequency ω_w. The activation of the process is submitted to the frequency matching condition $\omega_\mathrm{p} = \omega_\mathrm{q} + \omega_\mathrm{w} - \omega_\mathrm{b}$. (b) Tuning ω_p to the resonance condition. (Top) A weak coherent state at frequency ω_b is sent to the SMPD while a pump tone of frequency ω_p and amplitude A_p is shined on the qubit prior to qubit readout. (Bottom) Qubit excited state probability p_e as a function of ω_p and A_p. White lines indicate the chosen operation parameters. (c) Measured (blue dots) and computed (orange line) SMPD detection efficiency as a function of the impinging photon frequency ω. A peak efficiency of 0.53 ± 1 is reached over a bandwidth $\Delta_\mathrm{det} = 2\pi \times 2.1\,\mathrm{MHz}$. (d) Cyclic operation of the SMPD. A $11.7\,\mu$s-long detection sequence (top), consisting of detector reset, photon detection and qubit measurement, is played cyclically in order to gather information continuously on the photons impinging on the detector. When no signal is sent to the SMDP a dark count rate $\nu_\mathrm{dc} = 1.53\,\mathrm{counts/ms}$ is recorded (bottom, red lines), when a coherent tone is sent (bottom, blue lines) the rate increases proportionally to the average photon number until saturation occurs (not shown).

5.6, a stream of photons are detected, as seen in 1.3(d). The detection cycle is repeated $\sim 2.5 \times 10^3$ times over $25\,\mathrm{ms}$, on each cycle the qubit state brings the binary response "click/no-click".

1.4 Measuring spins fluorescence with a microwave photon detector

In chapter 6 we describe the main results obtained in this thesis. Section 6.1 introduces the state of the art about spin fluorescence detection, with the experiments of *Sleator et al.* [5] and *McCoy and Ernst* [6], showing detection of spin fluorescence through power noise measurements.

Section 6.2 describes our experiment, where we connect with microwave cables the output of the spin device to the input of the SMPD, as shown in Fig.1.1. The spins are tuned into resonance with the coupled resonator $\omega_\mathrm{s} = \omega_0$ and the buffer resonator of the SMPD is tuned into resonance with the spin device $\omega_\mathrm{b} = \omega_0$.

Fluorescence measurement is presented in section 6.2. We apply a π-pulse to the spin ensemble and detect the photon signal by operating the SMPD cyclically over $\sim 1\,\mathrm{s}$. Figure 1.4(a) shows the obtained photo-counting trace, were we observe more clicks at earlier times than at later times. Repeating the experiment 500 times and plotting the measured count rate for each $20\,\mathrm{ms}$-time bin (see Fig.1.4(c)) we observe a count rate exponentially decaying towards the dark count baseline within a timescale $\sim 300\,\mathrm{ms}$, compatible with the Purcell radiative decay rate of the spin ensemble (see Fig.1.2). The overall efficiency is $\eta = 0.01$, limited by resonator losses $\kappa_\mathrm{ext}/\kappa = 0.22$. We obtain a SNR of ~ 5 over a single measurement, showing a five-fold improvement with respect to the SNR obtained in echo quadrature detection on the same sample. In section 6.3 we show photon detection of the Hahn-echo (see Fig.1.4(b)), with a similar SNR as in quadrature detection. Finally, in section 6.5 we use the photon detector to measure Rabi oscillations (see Fig.1.4(d)) and perform spectroscopy of the spin ensemble, both with fluorescence and echo techniques. We conclude the chapter with an estimation of the number of spins and some remarks concerning the potential of this new spin detection method.

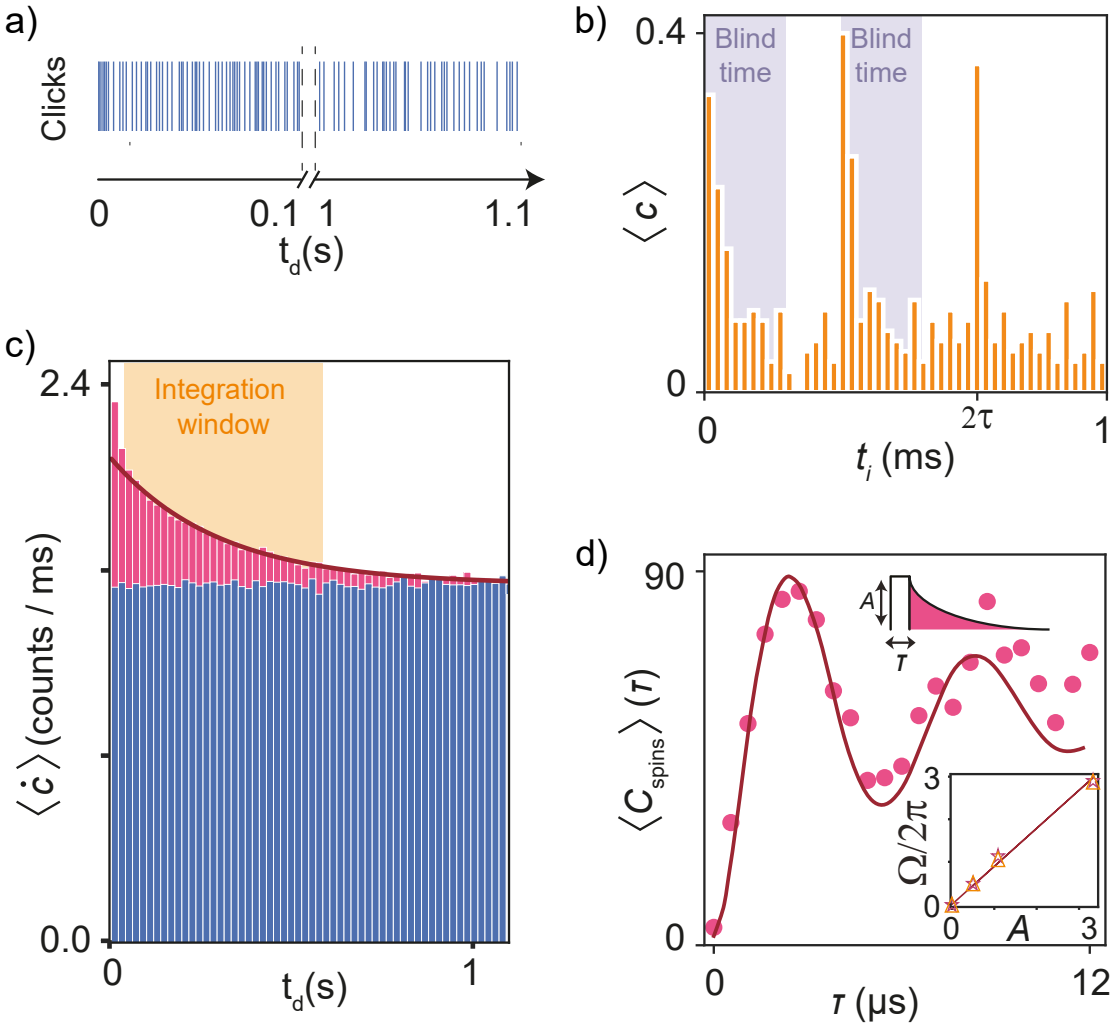

Figure 1.4: **SMPD detection.** (a) SMPD click trace at early ($0\,sto 0.1\,\mathrm{s}$) and late ($1\,sto 1.1\,\mathrm{s}$) time t_d after a π-pulse applied on the spin ensemble. More clicks are recorded at early times. (c) Histogram of the SMPD count rate $\langle \dot{c} \rangle$ measured on $19\,\mathrm{ms}$-long time bins, as a function of the time t_d after a π-pulse (pink) or no-pulse (blue) on the spin ensemble. When the pulse is applied a photon signal is recorded, exponentially decaying with characteristic time $\sim 309 \pm 10\,\mathrm{ms}$, compatible with the spin Purcell relaxation time T_P. (b) Average number of counts $\langle c \rangle$ recorded in each $23\mu s$-long time bin during a Hahn echo sequence. Increased $\langle c \rangle$ is observed in correspondence of the Hahn pulses and at the echo time 2τ. (d) Average integrated number of counts $\langle C_\mathrm{spins} \rangle$ in a $500\,\mathrm{ms}$-long time window (see (c)) after a pulse of length T and fixed amplitude A applied to the spin ensemble. Oscillations in C_spins reveal Rabi nutations of the spin ensemble, with a frequency Ω, which is linearly dependent on A (inset).

Part I

Background

Chapter 2

Quantum circuits

In this chapter we will provide the background on superconducting quantum circuits that is necessary to understand the experiments described in this thesis.

In section 2.1 we present the quantum description of some relevant states of the electromagnetic field, all appearing at various stages through the manuscript. Sections 2.2 and 2.3 introduce the theory of quantum LC resonators and lossless transmission lines. In section 2.4 we introduce the Josephson junction and basic circuits such as the SQUID. In section 2.5 we discuss quantum-limited amplification and its implementation at microwave frequencies with so-called Josephson Parametric Amplifiers. In section 2.6 we compare the detection of electromagnetic field states using quadrature (i.e. linear) or energy (i.e. quadratic) detectors, showing the achievable SNR and the performances of each method in different cases.

2.1 Quantum description of an electromagnetic mode

For full quantization of the electromagnetic field the reader can refer to Ref. [8], here we just give results used through this thesis.

The Hamiltonian for a single electromagnetic mode of frequency ω can be written in terms of the operator $\hat{a}$, which acts on a quantum state by removing a quantum of energy $\hbar\omega$, as:

$$\hat{H} = \hbar\omega\hat{a}^\dagger\hat{a} \tag{2.1}$$

where we neglected the constant zero-point energy, not playing any role in the equations of motion. The relevant field observables that we will measure to characterise a particular state of the field are the number of photons $\hat{n} = \hat{a}^\dagger\hat{a}$, and the dimensionless field quadratures $\hat{X}$ and $\hat{Y}$, defined as:

$$\hat{X} = \frac{\hat{a}^\dagger + \hat{a}}{2}, \qquad \hat{Y} = \frac{\hat{a}^\dagger - \hat{a}}{2i}, \tag{2.2}$$

which satisfy the commutation relation $[\hat{X}, \hat{Y}] = i/2$, and whose standard deviations $\Delta X = \sqrt{\langle \Delta\hat{X}^2 \rangle}$ and $\Delta Y = \sqrt{\langle \Delta\hat{Y}^2 \rangle}$ are bounded by the Heisenberg uncertainty relation:

$$\Delta X \Delta Y \geq \frac{1}{4}. \tag{2.3}$$

In the following we will briefly go through some states of the electromagnetic field that will appear in this thesis: vacuum, Fock, coherent and thermal states.

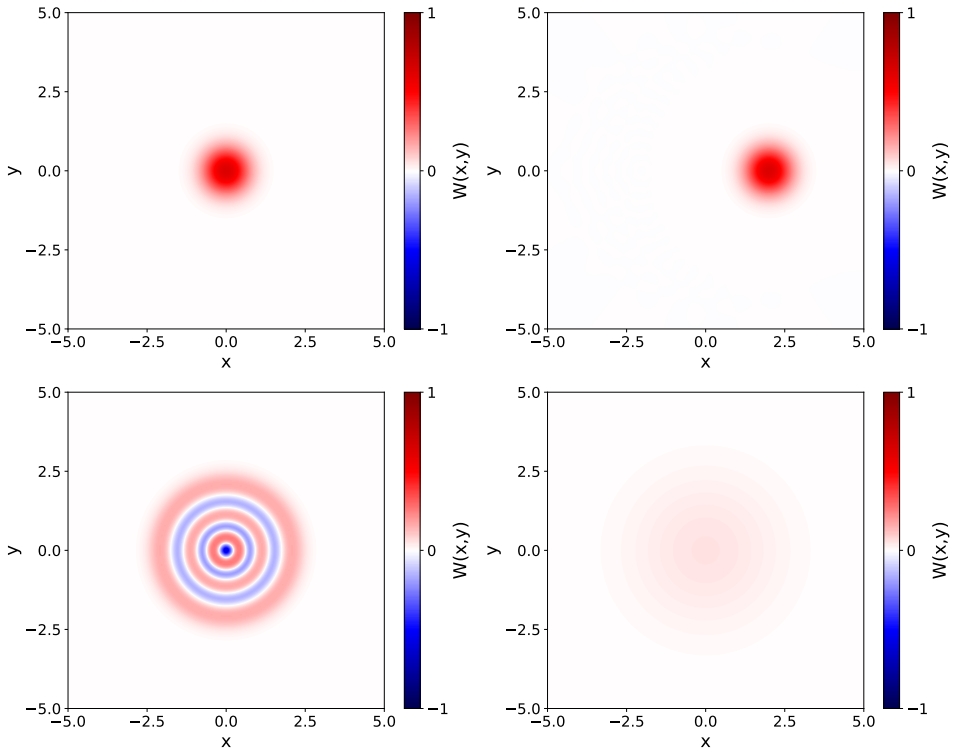

Figure 2.1: **Wigner quasiprobability distributions.** From left to right, top to down the Wigner distributions of: (a) Vacuum state, (b) Coherent state with $\alpha = 2$, (c) Fock state $n = 5$, (d) thermal state $\bar{n} = 5$. The axes indicate the values of the quadratures of the field.

Note on graphical representation of quantum states

One can represent graphically a quantum state in multiple ways, here we will adopt Wigner's method and represent a generic quantum state $|\psi\rangle$ by means of its Wigner quasi-probability distribution in phase space $W(x, y)$. This approach has the advantageous property that the marginal distributions $p(x) = \int W(x, y)dy$ and $p(y) \int W(x, y)dx$ provide directly the probability density of the outcome of each quadrature measurement.

Fock states

Fock states $|n\rangle$ are eigenstates of the Hamiltonian 2.1, n being the number of excitations (photons) populating the mode of interest. For instance, a single photon is described by the Fock state $|n = 1\rangle$. The expectation values of field quadratures on a Fock state are

$$\langle \hat{X} \rangle = \langle \hat{Y} \rangle = 0 \tag{2.4}$$

and their standard deviations are

$$\Delta X = \Delta Y = \frac{1}{2}\sqrt{2n + 1}. \tag{2.5}$$

Mean value and standard deviation of the photon number operator are:

$$\langle \hat{n} \rangle = n \tag{2.6}$$
$$\Delta \hat{n} = 0. \tag{2.7}$$

The Wigner distribution of a Fock state is [9]:

$$W(x,y) = \frac{2}{\pi}(-1)^n L_n(4\,|x+iy|^2)e^{-2|x+iy|^2} \tag{2.8}$$

where L_n are Laguerre polynomials. Fig.2.1a and c shows the Wigners for the vacuum state $n = 0$ and the Fock state $n = 5$, respectively.

Coherent states

The electromagnetic classical signals used as drives for spins and cavity, as well as the echo signal emitted by a spin ensemble in a typical electron spin resonance (ESR) experiment can be described as coherent states $|\alpha\rangle$, that are eigenstates of the annihilation operator $\hat{a}$. A coherent state of amplitude α can be written as

$$|\alpha\rangle = e^{-\frac{|\alpha|^2}{2}} \sum_{n=0}^{\infty} \frac{\alpha^n}{\sqrt{n!}} |n\rangle \,. \tag{2.9}$$

From this equation we see that $|\alpha = 0\rangle$ coincides with $|n = 0\rangle$. Another property of coherent states is that they verify $|\alpha\rangle = D(\alpha)\,|0\rangle$, where $D(\alpha)$ is the displacement operator. As a consequence the Wigner function of a coherent state is a Gaussian of standard deviation $\sigma = 1/2$ centred around (x_0, y_0) with $\alpha = x_0 + iy_0$, as shown in Fig. 2.1b for $\alpha = 2$.

As seen from Eq.2.9, the photon number distribution $p(n) = |\langle\alpha|\,|n\rangle|^2$ is Poissonian, with mean value and standard deviation:

$$\langle \hat{n} \rangle = |\alpha|^2 \tag{2.10}$$
$$\Delta n = |\alpha| \,, \tag{2.11}$$

while the field quadratures $\hat{X}$ and $\hat{Y}$ show the same standard deviation of the vacuum:

$$\Delta X = \Delta Y = \frac{1}{2}. \tag{2.12}$$

Thermal states

A thermal state describes an electromagnetic mode at thermal equilibrium with a bath at temperature T. In the Fock states basis, it is represented by a statistical mixture with probability given by the Boltzmann distribution. The density matrix of a thermal state is:

$$\hat{\rho} = \frac{1}{n_{\text{th}}+1} \sum_{n=0}^{\infty} \left(\frac{n_{\text{th}}}{n_{\text{th}}+1}\right)^n |n\rangle\langle n| \tag{2.13}$$

with average number of thermal photons:

$$\langle \hat{n} \rangle \equiv n_{\text{th}} = \frac{1}{e^{\frac{\hbar\omega}{k_{\text{B}}T}} - 1}, \tag{2.14}$$

and standard deviation:

$$\Delta n = \sqrt{n_{\mathrm{th}}\left(n_{\mathrm{th}}+1\right)} \tag{2.15}$$

The expectation value and standard deviation of quadratures are:

$$\langle \hat{X} \rangle = \langle \hat{Y} \rangle = 0 \tag{2.16}$$

$$\Delta X = \Delta Y = \sqrt{n_{\mathrm{th}} + \frac{1}{2}} \tag{2.17}$$

Being a statistical mixture of different Fock states, a thermal state doesn't have a well defined phase, as seen by the Wigner representation in Fig. 2.1. We will use thermal states to model the fluorescence emitted by an ensemble of emitters.

2.2 Cavities and propagating modes

In this section, I will introduce the quantum description of LC resonators (or cavities), and transmission lines that support propagating microwave fields.

Quantum LC resonator

One way to implement the single-mode field Hamiltonian Eq. 2.1 is through a LC resonator, consisting of a parallel capacitor and inductor, supporting a single mode of the electromagnetic field at frequency $\omega_0 = 1/\sqrt{LC}$. The reader can find a pedagogical description of the quantization of the LC resonator Hamiltonian in appendix B.2, here we present the known results useful for this work. This type of resonator is called "lumped-element" because the capacitor and inductance dimensions may be arbitrarily smaller than the wavelength.

The LC resonator Hamiltonian reads:

$$\hat{H} = \hbar\omega_0 \hat{a}^\dagger \hat{a}. \tag{2.18}$$

The oscillating mode sustains across the inductor an oscillating current $\hat{I}$, whose expression in term of the field-mode quantum annihilation operator $\hat{a}$ is:

$$\hat{I} = I_{\mathrm{zpf}}\left(\hat{a} + \hat{a}^\dagger\right), \tag{2.19}$$

where $I_{\mathrm{zpf}} = \sqrt{\hbar\omega_0^2/2Z_0}$ are the fluctuations of the current in the field vacuum state, with $Z_0 = \sqrt{L/C}$ is the resonator characteristic impedance. Such current produces an oscillating magnetic field in the space surrounding the inductance, this field can be expressed as:

$$\hat{\mathbf{B}}(\mathbf{r}) = \mathbf{B}_{\mathrm{zpf}}(\mathbf{r})\left(\hat{a} + \hat{a}^\dagger\right), \tag{2.20}$$

where the magnitude of $\mathbf{B}_{\mathrm{zpf}}$ is proportional to the current zero point fluctuations I_{zpf}. In this work, we will use LC resonators to couple to the spins.

Coplanar waveguide resonators

A second way to implement an electromagnetic mode at microwave frequency is through a distributed resonator in a coplanar waveguide (CPW) geometry. As reported in Fig. 2.3a, the CPW geometry consists of a central conducting track

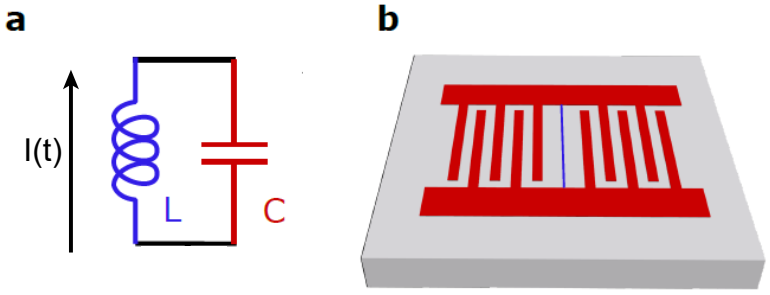

Figure 2.2: **LC resonator.** (a) Lumped-elements model of an LC resonator, current passing through the inductance L generated a spatially-dependent magnetic field $\hat{\mathbf{B}}(\mathbf{r})$. (b) Realistic illustration of an LC resonator design, here the role of the inductance (blue) is played by a wire shunting the two capacitor plates (red).

on top of a dielectric substrate and surrounded by two grounded conductors, ideally infinite planes. A segment of a coplanar waveguide can be modeled as a chain of infinitesimal lumped elements LC circuits with series capacitance and inductance per unit length respectively $\mathcal{C}$ and $\mathcal{L}$, as illustrated in Fig. 2.3b.

A CPW distributed resonator is obtained from a coplanar waveguide of length L by imposing current and voltage boundary conditions at the two extrema, by means of a characteristic-impedance mismatch (Fig. 2.3c). Standing waves at fundamental frequency ω_0 and upper harmonics, both determined by the nature of the boundary conditions, are supported in such a distributed resonator. A CPW resonator is "1-dimensional" in the sense that its transverse dimensions can be arbitrarily small compared to the wavelength but its length is a multiple of order 1.

In this work, we will make use of "open-circuit" boundary conditions, imposing a current node and thus voltage anti-node. If c is the speed of light propagating along the waveguide, the modes supported have frequencies $\omega_{\mathrm{n}} = nc/L$ with $\mathrm{n} = 1, 2, ...$

Lumped vs distributed resonators

In this work, we use both lumped-element and CPW resonators.

Lumped-element resonators may have small size, and moreover the current is constant throughout the inductance. They are therefore well-suited for coupling to spins and will be used in the spin resonator device.

On the other hand, the resonance frequency of CPW resonators can be easily controlled because it is governed by its length. For this property, it will be used for designing the SMPD device.

Lossless transmission line

In our experiments, the quantum devices are measured and inter-connected by lossless transmission lines, implemented by coaxial cables; they also need to be treated quantum-mechanically. For a complete treatment the reader can refer to ref. [10].

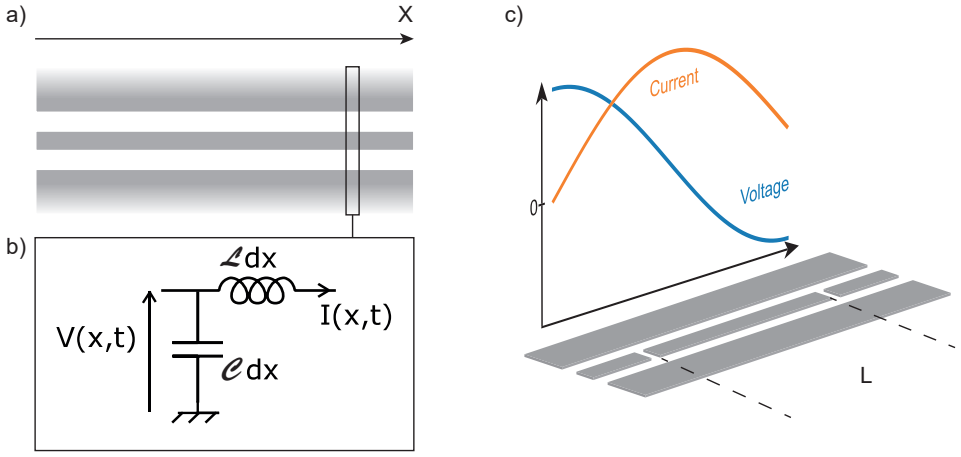

Figure 2.3: **Coplanar waveguide geometry.** (a) Typical coplanar waveguide geometry consisting of a central conducting line surrounded by two grounded planes. Each infinitesimal section dx of waveguide can be modeled as the lumped element circuit (b), characterized by capacitance and inductance per unit length $\mathcal{C}$ and $\mathcal{L}$. (c) Example of a coplanar waveguide resonator. Boundary conditions given by the interruption of the waveguide allows resonant modes to be supported in the isolated section. Current and voltage profiles of the fundamental mode are showed.

A classical transmission line can be modeled as a chain of infinitesimal lumped element LC circuits, described by a series inductance $\mathcal{L}$ and a parallel capacitance $\mathcal{C}$ per unit length, as already introduced above in the particular case of a CPW transmission line (Fig. 2.3). The electromagnetic modes, obtained as solution of the wave equation associated to the circuit, consist of a left-propagating and a right-propagating wave, whose sum gives the voltage at time t across the infinitesimal capacitance $\mathcal{C}\,dx$ at located between x and $x + dx$:

$$V(x,t) = V^{\rightarrow}(x,t) + V^{\leftarrow}(x,t) \tag{2.21}$$

$$V^{\leftrightharpoons}(x,t) = V_0^{\leftrightharpoons}\cos(\omega t \pm x\omega/c + \phi_0^{\leftrightharpoons}) \tag{2.22}$$

with the phase velocity $c = 1/\sqrt{\mathcal{L}\mathcal{C}}$ and the initial phases $\phi_0^{\leftrightharpoons}$. The current flowing in the infinitesimal inductance $\mathcal{L}\,dx$ is related to $V^{\leftrightharpoons}$ via the characteristic impedance $Z_c = \sqrt{\mathcal{L}/\mathcal{C}}$

$$I(x,t) = \frac{V^{\rightarrow}(x,t) - V^{\leftarrow}(x,t)}{Z_c} \tag{2.23}$$

where the sign accounts for opposite flowing direction in the case of left or right propagating wave. In the case of an infinite transmission line the left- and right-propagating waves are independent, on the contrary if a load of impedance Z_l is present (at $x = 0$ for convenience) the two waves should respect current-voltage relation at the load boundary:

$$Z_l = \frac{V(0,t)}{I(0,t)} = \frac{V^{\rightarrow}(t) + V^{\leftarrow}(t)}{V^{\rightarrow}(t) - V^{\leftarrow}(t)} Z_c \tag{2.24}$$

which allows to relate the left- and right-propagating wave amplitudes to the impedance mismatch

$$\frac{V^{\leftarrow}(t)}{V^{\rightarrow}(t)} = \frac{Z_c - Z_l}{Z_c + Z_l} =: R \tag{2.25}$$

where R is the reflection coefficient.

Quantum description

We will now turn to the quantum description of a lossless transmission line. The reader can find a full review in [11].
For each direction of propagation in a transmission line (left and right), and for each monochromatic mode of the electromagnetic field (identified by its frequency ω) one can associate a pair of operators $\hat{a}^{\leftrightharpoons}(\omega)$ and $\hat{a}^{\leftrightharpoons\dagger}(\omega)$ which respectively annihilate and create a photon in that mode and propagation direction. These operators satisfy the commutation relation $[\hat{a}^{\leftrightharpoons}(\omega), \hat{a}^{\leftrightharpoons\dagger}(\omega')] = 2\pi\delta(\omega - \omega')$, which implies orthogonality of different modes. Since we are here generally interested in narrow-band signals of central frequency ω_0, it is convenient to work in the time-domain in a frame rotating at ω_0. Neglecting contributions from frequencies far from ω_0, the rotating wave approximation leads to the following expression for the propagating field operator at $x = 0$:

$$\hat{V}^{\leftrightharpoons}(t) = \sqrt{\frac{\hbar\omega_0 Z_c}{4\pi}}\left(\hat{a}^{\leftrightharpoons}(t) + \hat{a}^{\leftrightharpoons\dagger}(t)\right) \tag{2.26}$$

where $\hat{a}^{\leftrightharpoons}(t)$ is the Fourier transform of $\hat{a}^{\leftrightharpoons}(\omega)$ satisfying $[\hat{a}^{\leftrightharpoons}(t), \hat{a}^{\leftrightharpoons\dagger}(t'),] = 2\pi\delta(t-t')$ (performing a Markov approximation). $\hat{a}^{\leftrightharpoons}(t)$ are operators describing the field amplitude flux associated to a propagating mode, thus the power carried by the quasi-monochromatic wave of frequency ω_0 is described by the quantum observable

$$\hat{P}^{\leftrightharpoons}(t) = \hbar\omega_0 \hat{a}^{\leftrightharpoons\dagger}(t)\hat{a}^{\leftrightharpoons}(t). \tag{2.27}$$

Note that $\hat{a}^{\leftrightharpoons}(t)$ describes a mode of infinite bandwidth, in realistic experiments this is almost never the case and a typical electromagnetic signal have finite temporal and spectral extensions. For this reason we introduce the orthonormal envelopes $u_i(t)$ of the propagating mode of bandwidth $\Delta\omega$ and duration $\Delta\tau = 2\pi/\Delta\omega$ satisfying:

$$\int u_i(t)u_j^*(t)dt = \delta_{i,j} \tag{2.28}$$

The index i labels the discrete wavelet basis tiling the time-frequency plane. We define a new operator describing the annihilation of the mode:

$$\hat{a}_i^{\leftrightharpoons} = \int \hat{a}^{\leftrightharpoons}(t)u_i(t)dt. \tag{2.29}$$

Note that the commutation relation becomes now the well known $[\hat{a}_i^{\leftrightharpoons}, \hat{a}_i^{\leftrightharpoons\dagger}] = 1$ and the description becomes analogous to that of section 2.1.

2.3 Cavity coupled to a transmission line

In our experiments, microwave resonators are used to interface quantum systems (spins, or superconducting qubits), and are inter-connected by propagating microwave fields that carry the signal of interest. A complete quantum description

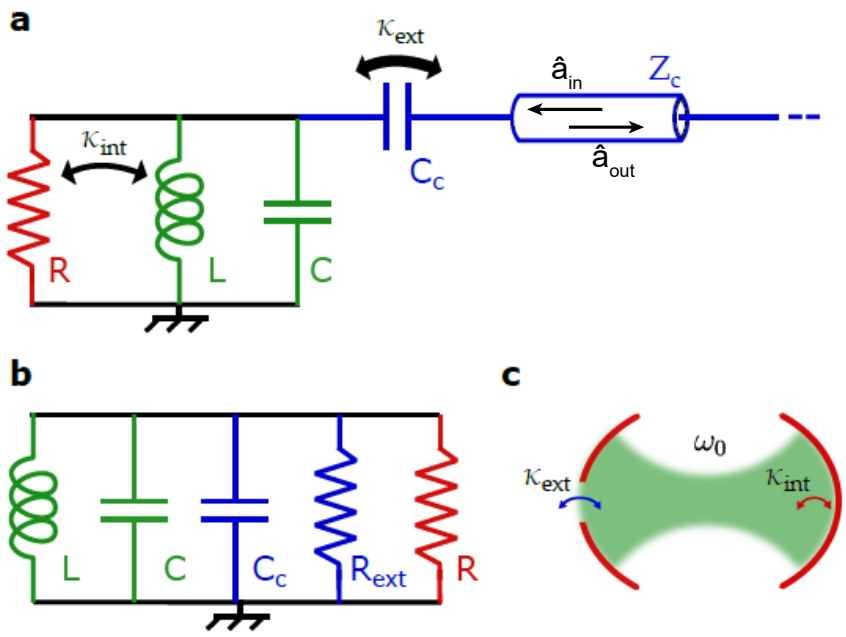

Figure 2.4: **Resonator coupled to transmission line.** (a) Representation of a resonator coupled to a transmission line. Input and output fields are associated to the quantum operators $\hat{a}_{\rm in}$ and $\hat{a}_{\rm out}$. The energy stored in the mode of the LC resonator is dissipated into the internal resistance at rate $\kappa_{\rm int}$ and leaks out into the capacitively coupled transmission line with rate $\kappa_{\rm ext}$. (b) Norton equivalent circuit. (c) Quantum optics equivalent representation.

of both the intra-resonator field and its coupling to propagating fields is therefore needed. This is provided by the input-output theory, which can be found in detail in Ref.[12] and which is briefly outlined in this section.

Equivalent circuit and cavity damping rates

The coupling of a LC resonator to a transmission line results in the appearance of losses. We thus consider a LC resonator, with internal losses modeled by a resistor R, and coupled to a $Z_0 = 50\,\Omega$hms transmission line through a coupling capacitance $C_{\rm c}$ (see Fig.2.4a) The bare frequency and impedance of a parallel RLC circuit are given by:

$$\omega_0 = \frac{1}{\sqrt{LC}} \tag{2.30}$$

$$\frac{1}{Z_0(\omega)} = \frac{1}{R} + iC\omega + \frac{1}{i\omega L}, \tag{2.31}$$

but as a result of the presence of the coupling capacitance $C_{\rm c}$ and of the impedance $Z_{\rm c}$ of the transmission line, these bare values get renormalized. In the low coupling limit $Z_c C_c \omega_0 \ll 1$ and for frequencies close to resonance $\omega \sim \omega_0$ an equivalent approximate RLC circuit can be built using the renormalized capacitance and resistance

$$C' \approx C + C_{\rm c} \tag{2.32}$$

$$\frac{1}{R'} \approx \frac{1}{R} + \frac{1}{R_{\rm ext}}, \quad \text{with} \quad R_{\rm ext} \approx \frac{1}{Z_{\rm c} C_{\rm c}^2 \omega_0^2}. \tag{2.33}$$

The damping of the resonator is determined by its loaded quality factor $Q^{-1} = R'^{-1}\sqrt{L/C'}$ which can be decomposed as the sum of two contributions, describing internal and external losses:

$$Q_{\rm int}^{-1} = R^{-1}\sqrt{\frac{L}{C'}} \tag{2.34}$$

$$Q_{\rm ext}^{-1} = R_{\rm ext}^{-1}\sqrt{\frac{L}{C'}} \tag{2.35}$$

$Q_{\rm int}$ is often referred as unloaded quality factor. From the above relations one can obtain the two energy dissipation rates $\kappa_{\rm int} = \omega_0/Q_{\rm int}$ and $\kappa_{\rm ext} = \omega_0/Q_{\rm ext}$.

Input-output theory for a driven damped cavity

With these definitions, we can now give the main results of the input-output theory which provides the link between the intra-cavity field operator $\hat{a}(t)$ (in the Heisenberg picture) and the input and output fields (see Fig.2.4).

In addition of the input and output operators $\hat{a}_{\rm in}$ and $\hat{a}_{\rm out}$ defined starting from Eqs.2.26, we also need to introduce operators $\hat{a}_{\rm in,int}$ and $\hat{a}_{\rm out,int}$ for the fields dissipated in the resonator internal losses, by treating internal losses as fictitious transmission lines. The evolution of $\hat{a}(t)$ in the Heisenberg picture is given by the following master equation:

$$\partial_t \hat{a}(t) = \frac{1}{i\hbar}[\hat{a}, \hat{H}] - \frac{\kappa}{2}\hat{a}(t) + \sqrt{\kappa_{\rm int}}\hat{a}_{\rm in,int}(t) + \sqrt{\kappa_{\rm ext}}\hat{a}_{\rm in}(t) \tag{2.36}$$

where $\kappa = \kappa_{\rm int} + \kappa_{\rm ext}$ is the total cavity damping rate. The right term consists of three main contributions: the Heisenberg evolution of $\hat{a}$ under the Hamiltonian $\hat{H}$ (which may include for instance terms describing the coupling to spins), the field damping at rate κ, and finally the coupling to the input field $\hat{a}_{\rm in}$.
At the interface between the cavity and the transmission line the sum of left- and right-propagating fields must equal the field radiated by the cavity, thus the following continuity equation holds:

$$\hat{a}_{\rm in}(t) + \hat{a}_{\rm out}(t) = \sqrt{\kappa_{\rm i}}\hat{a}. \tag{2.37}$$

Cavity under coherent driving

The classical fields we send to the cavity in our experiments are described by the coherent states $|\alpha\rangle$ introduced in Sec.2.1. Under this classical drive, the cavity input mode is in the eigenstate $|\alpha_{\rm in}\rangle$ of the propagating operator $\hat{a}_{\rm in}$, carrying the power $P_{\rm in} = \hbar\omega\,|\alpha_{\rm in}|^2$ Eq.2.27. The expectation value of the intra-cavity field $\langle\hat{a}\rangle(t) = \alpha(t)$ is then obtained from Eq. 2.36:

$$\partial_t \alpha(t) = -i\omega_0\alpha(t) - \frac{1}{2}(\kappa_{\rm ext} + \kappa_{\rm int})\alpha(t) + \sqrt{k_{\rm ext}}\alpha_{\rm in}(t). \tag{2.38}$$

We now perform a Fourier transform to find that the $\alpha(\omega)$ Fourier component of the field satisfies:

$$\alpha(\omega) = \frac{2\sqrt{\kappa_{\rm ext}}}{\kappa_{\rm int} + \kappa_{\rm ext} - 2i(\omega - \omega_0)}\alpha_{\rm in}(\omega). \tag{2.39}$$

The amplitude of the coherent intra-cavity field determines the photon population, relevant for the functioning of the photon detector, and the transverse

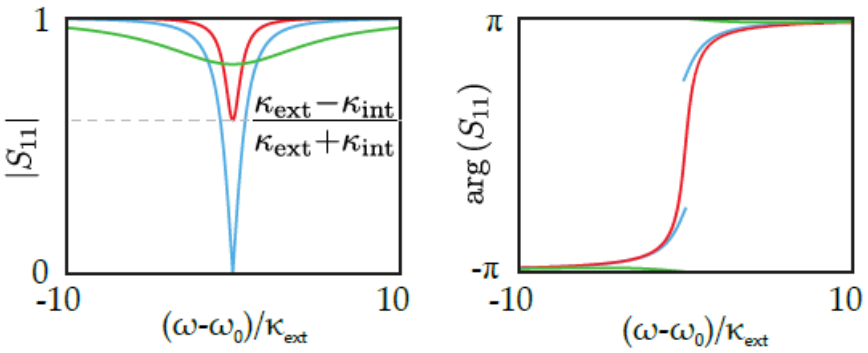

Figure 2.5: **Scattering matrix measurements.** Reflection coefficient $S_{11}(\omega)$ module (left panel) and phase (right panel) calculated in the case $\kappa_{\text{int}} = 10\kappa_{\text{ext}}$ (green), $\kappa_{\text{int}} = \kappa_{\text{ext}}$ (blue), and $\kappa_{\text{int}} = 0.25\kappa_{\text{ext}}$ (red).

magnetic field generated by the inductance L, relevant for driving the spin ensemble through coherent oscillations.
At resonance $\omega = \omega_0$, driving a cavity with a power P_{in} will generate in the steady-state a mean photon number $\bar{n} = |\alpha|^2$ given by:

$$\bar{n} = \frac{4\kappa_{\text{ext}}|\alpha_{\text{in}}|}{\hbar\omega_0(\kappa_{\text{ext}} + \kappa_{\text{int}})^2}, \tag{2.40}$$

leading to an oscillating current and magnetic fields:

$$\langle I\rangle(t) = 2I_{\text{zpf}}\sqrt{\bar{n}}\cos(\omega_0 t) \tag{2.41}$$

$$\langle B\rangle(t) = 2B_{\text{zpf}}\sqrt{\bar{n}}\cos(\omega_0 t). \tag{2.42}$$

Scattering matrix measurements

The behavior of an n-port linear device connected to n transmission lines is fully described by the $n \times n$ scattering matrix $\hat{S}$, whose elements are the reflection and transmission coefficients $\hat{S}_{\text{i,j}}$ of the propagating fields:

$$\hat{S}_{\text{i,j}} = \frac{\hat{a}_{\text{out,i}}}{\hat{a}_{\text{in,j}}} \quad \text{measured when} \quad \hat{a}_{\text{in,k}} = 0,\ \forall k \neq j \tag{2.43}$$

The scattering coefficients $\hat{S}_{\text{i,j}}$ are usually measured using classical coherent input drives, through a Vector Network Analyzer (VNA). In this case, the propagating field operators can be replaced by the coherent amplitudes $\alpha_{\text{in,i}}$ and $\alpha_{\text{out,i}}$, the same holds for the coherent intra-cavity field $\alpha(\omega)$. We can now exploit the continuity equation 2.37 and the expression of the intra-cavity field 2.39 to give an explicit expression for the S_{11} scattering coefficient in the case of a cavity coupled to a transmission line:

$$S_{11}(\omega) = \frac{\sqrt{\kappa_{\text{ext}}}\alpha(\omega) - \alpha_{\text{in}}}{\alpha_{\text{in}}} = \frac{\kappa_{\text{ext}} - \kappa_{\text{int}} + 2i(\omega - \omega_0)}{\kappa_{\text{ext}} + \kappa_{\text{int}} - 2i(\omega - \omega_0)}. \tag{2.44}$$

The relative strength of the external and internal damping rates defines three different regimes, as illustrated in Fig.2.5:

- **Under-coupling** ($\kappa_{\text{int}} \gg \kappa_{\text{ext}}$): most of the signal impinging on the cavity is reflected back, only a small absorption dip and phase shift are observed.

- **Critical coupling** ($\kappa_{\text{int}} \approx \kappa_{\text{ext}}$): all the impinging power is absorbed by the cavity, which behaves as an impedance-matched load. The phase of $S_{11}(\omega)$ changes sign when ω crosses ω_0, by consequence a phase change is observed in the reflected signal.

- **Over-coupling** ($\kappa_{\text{int}} \ll \kappa_{\text{ext}}$): the signal is partly absorbed by the cavity and partly reflected and the phase of the reflected signal rotates by 2π across the resonance.

The above analysis took into account the reflection S_{11} parameter for a cavity under coherent drive. This is relevant for most of the analysis needed in this work, as both spin resonator and the single microwave photon detector are probed in reflection.

Internal loss sources

In this subsection we will discuss the mechanisms leading to internal losses in superconducting microwave resonators, contributing to the internal cavity damping rate κ_{int}. The three main sources of microwave losses discussed here are (i) dielectric losses, (ii) vortices and (iii) quasiparticles. For a more detailed description of these loss mechanisms the reader can refer to [13] for dielectric losses, [14] for vortices and [15] for quasiparticles .

Dielectric losses

The microscopic origin of most dielectric losses in superconducting circuits is still unknown, but many clues point towards the presence of unwanted two-levels systems (TLS) in the dielectrics surrounding the circuit, which absorb part of the microwave field energy. Potential sources of dielectric loss are (i) the oxides formed at the metal-air interfaces by the atmosphere exposure during the fabrication process, (ii) oxides and unterminated dangling bonds at the substrate-air interface of the chip and (iii) defects in the bulk of the material or at the interface between the substrate and the metal [13]. These TLS couple electrically to the field, absorbing part of the energy and causing losses. TLS contributions manifest at low temperature and low electromagnetic powers, when at thermal equilibrium the defects are mostly in their ground state. Increasing the temperature or the injected power saturates the TLS transitions, thus inhibiting further energy absorption. Losses by TLS absorption therefore lead to a power and temperature dependent internal quality factor, a clear experimental signature that we will encounter in our measurements.

Mitigation of dielectric losses is realized mostly through improvement of the fabrication process, with a particular care on the cleanliness of all interfaces and on the removal of amorphous oxides. Moreover use of substrate trenching and specific aspect ratios for transmission lines dimension allows to reduce further the fraction of electric field interacting with lossy surfaces [16].

Magnetic vortices

When subjected to a magnetic field, superconductors expel this field by generating a screening current - this is the Meissner effect. In Type-2 superconductors, the field can nevertheless penetrate the superconductor in the form of "magnetic

vortices". In such a vortex, the magnetic field penetrates along a narrow metallic region that becomes non-superconducting (the normal core), around which screening currents flow in the superconducting part. A magnetic vortex carries a quantum of magnetic flux Φ_0.

All thin-film superconductors can be penetrated by magnetic vortices (in that sense, they all behave as type-2 superconductors) when they are placed in an externally generated magnetic field. In a thin-film microwave resonator, vortices can cause microwave losses through the following mechanism. Oscillating currents act on the vortex via the Lorentz force; and the displacement of these vortices is dissipative and therefore leads to internal microwave losses.

In our experiment, the spin resonator is subject to a moderately large magnetic field, which causes the penetration of vortices, and the appearance of additional losses at high magnetic field.

Quasiparticles

Quasiparticles are above-gap excitations of the superconducting condensate and can be qualitatively understood as normal electrons. Their presence in the superconducting thin-film leads to dissipation at non-zero frequency. Indeed, due to the inductive surface impedance of the superconductor, a finite fraction of ac currents is always carried by the quasi-particles and is therefore dissipated by Joule effect.

It is thus essential to minimize quasiparticles in superconducting quantum circuits : resonators and qubits. At mK temperatures, the thermal equilibrium population of quasiparticles should be vanishingly small. However, it is well-known [17] that a non-equilibrium population of quasiparticles is systematically observed. Recent work identified at least two sources of out-of-equilibrium quasiparticles : absorption of high-energy photons (above-gap) by the superconducting film, and high-energy phonons generated in the substrate by cosmic rays or gamma photons. Superconducting quantum cricuits therefore need to be carefully shielded against high-energy photons, in particular in the 100 GHz to infrared frequency range. This is achieved by inserting infra-red absorbers in all measurement lines, and in carefully designing the sample holder and its shielding.

2.4 The Josephson junction

In this section we introduce the concept of Josephson junction, one of the building blocks of circuit quantum electrodynamics experiments, as it provides the non-linearity required to build artificial two-level systems or couple different microwave modes. We present here a brief analysis of the physics of the Josephson junction, for a complete approach see for example ref. [18].

A Josephson junction consists of two pieces of superconductors separated by a thin ($\sim 2\,$nm) barrier of insulating material. When the barrier is thin enough to allow tunneling of electrons between the two sides, one can derive the so called Josephson relations that link the electric current I through the barrier with the superconducting phase difference φ between the two sides and this latter with

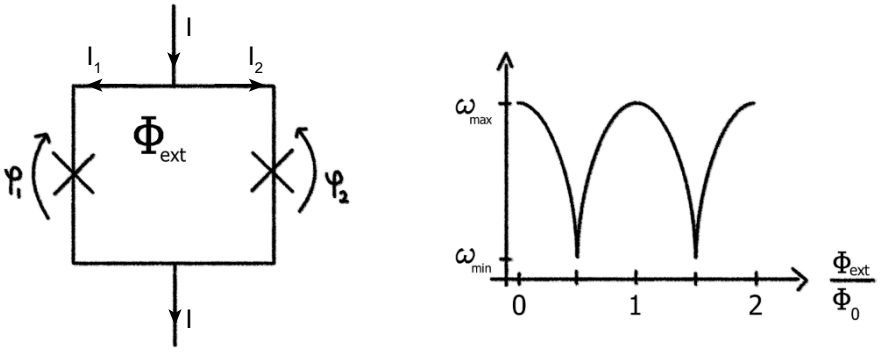

Figure 2.6: **SQUID.** Schematic of a SQUID (left) constituted by a loop interrupted by two Josephson junctions, described by superconducting phase differences φ_1 and φ_2. External flux Φ_{ext} threading the loop allows to tune the effective inductance of the SQUID. Embedding a SQUID in a resonator allows frequency tunability (right panel).

the voltage drop V across the junction:

$$I = I_{\text{c}} \sin \varphi \tag{2.45}$$

$$\frac{\partial \varphi}{\partial t} = \frac{2e}{\hbar} V \tag{2.46}$$

where I_{c} is known as critical current and e is the electron charge. From these equations, by using the flux-phase relation $\Phi = (\hbar/2e)\varphi = \phi_0 \varphi$ one can verify that the inductance associated to the junction has a non-linear behavior:

$$L(\varphi) = \frac{\partial \Phi / \partial t}{\partial I / \partial t} = \frac{\phi_0}{I_{\text{c}}} \frac{1}{\cos(\varphi)}. \tag{2.47}$$

The inductive energy associated with the Josephson junction is

$$\mathcal{U}_{\text{J}}(t) = \int_{-\infty}^{t} V I dt' = \phi_0 \int_{-\infty}^{t} I d\varphi = -E_{\text{J}} \cos \varphi(t) \tag{2.48}$$

where $E_{\text{J}} = \phi_0 I_{\text{c}}$ is called Josephson energy and we have made use of eqs. 2.45 and 2.46.

Superconducting Quantum Interference Device

One of the prominent superconducting circuits is the superconducting quantum interference device (SQUID). This device behaves as a tunable inductor and can thus be embedded in superconducting resonators to make them tunable. In this thesis it is employed for the design of the buffer resonator of the tunable single microwave photon detector, and it is also used in the functioning of the Josephson parametric amplifier.

A SQUID is a superconducting loop interrupted by one (RF SQUID) or two (DC SQUID) Josephson junctions, here we present the basic working principle of the symmetric DC SQUID [19], the one used in this work. The current-phase relation describing the device is:

$$I = 2 I_{\text{c}} \cos \left(\phi \frac{\Phi_{\text{ext}}}{\Phi_0} \right) \sin \left(\frac{\varphi_1 + \varphi_2}{2} \right) \tag{2.49}$$

where I_c is the critical current of the two junctions, Φ_{ext} is the external flux bias through the SQUID loop and φ_1, φ_2 are the superconducting phase differences across the two junctions. One directly sees that Eq. 2.49 corresponds to the single-junction current-phase relation Eq. 2.45 with an effective critical current that depends on the external flux applied. The tunable inductance associated with the device is:

$$L_{\text{squid}} = \frac{1}{2E_J \cos \pi \frac{\Phi_{ext}}{\Phi_0}}. \tag{2.50}$$

Tunable LC resonator

Since a SQUID effectively behaves as a variable inductor, it can be embedded in an LC resonator to make its frequency tunable. One can deduce the tunability range by considering the logarithmic derivative of the frequency $\omega = 1/\sqrt{LC}$:

$$\log \omega = -\frac{1}{2} \log L + \text{const} \tag{2.51}$$

$$\frac{\delta\omega}{\omega} = -\frac{1}{2}\frac{\delta L}{L} = -\frac{1}{2} p \frac{\delta L}{L_{\text{squid}}}, \tag{2.52}$$

so that the frequency range depends on the inductance tunability via the participation ratio $p = L_{\text{squid}}/L$ of the SQUID inductance L_{squid} to the total circuit inductance L. In the most general case in which the junctions constituting the SQUID are not equal, the inductance variation δL is obtained as (see Eq. B.37):

$$\delta L = \frac{2L_1^2 L_2}{L_1^2 - L_2^2} \tag{2.53}$$

where L_1 and L_2 are the inductances associated with the two junctions, and the SQUID inductance can be taken approximately to be $L_{\text{squid}} \approx (L_{\min} + L_{\max})/2 = L_2^2 L_1/(L_1^2 - L_2^2)$. We can thus write:

$$\frac{\delta\omega}{\omega} = -p\frac{L_1}{L_2}. \tag{2.54}$$

This formula is used in the design of tunable resonator to calibrate the ratio of SQUID inductances, the participation ratio p is usually obtained via electromagnetic finite-element simulation, calculating the fraction of the field present in the SQUID junctions.

Flux noise

The major drawback of embedding a SQUID in a resonator comes from the presence of magnetic flux noise in the system. This noise can have multiple sources but the main contribution is supposed to come from vortices and fluctuations of the external magnetic field Φ_{ext} used to bias the SQUID at its working point. This noise induces fluctuations in the resonance frequency of the tunable LC resonator.

Consider an LC resonator subjected to noise on its resonance frequency $\omega(t) = \omega_0 + \delta\omega(t)$, the $S_{11}(\omega)$ parameter introduced in Eq. 2.44 has now to be convolved with some kernel $f(\omega)$ corresponding to the noise Fourier transform:

$$\breve{S}_{11}(\omega) = \int_{-\infty}^{+\infty} d\omega' f(\omega - \omega') S_{11}(\omega'), \tag{2.55}$$

if we assume Gaussian noise centred at the resonator frequency ω_0 with variance σ^2 we can write:

$$\breve{S}_{11}(\omega) = \frac{1}{\sigma\sqrt{2\pi}} \int_{-\infty}^{+\infty} d\omega' \frac{\kappa_{\text{ext}} - \kappa_{\text{int}} + 2i(\omega' - \omega_0)}{\kappa_{\text{ext}} + \kappa_{\text{int}} - 2i(\omega' - \omega_0)} e^{-\frac{(\omega-\omega'-\omega_0)^2}{2\sigma^2}} \tag{2.56}$$

This expression will be used to model the presence of flux noise in the case tunable resonators.

2.5 Noise and amplification

In the experiments reported in this thesis, we will detect two types of signals, either spin-echoes, or qubit readout pulses (to operate the SMPD). Both signals originate from quantum devices and have ultra-low amplitudes, on the order of $1\,\text{fW} - 1\,\text{pW}$, and corresponding to a few microwave photons.

It is therefore essential to have a low noise amplification chain. The best commercially available low-noise amplifiers are High-Electron-Mobility Transistors with a noise temperature of a few Kelvin when cooled at 4K, corresponding to $\sim$ 10-20 noise photons at 4-8 GHz. They are not sufficient for our experiments, which require the best possible amplifiers allowed by quantum mechanics. This can be obtained through the use of superconducting amplifiers cooled at 10 mK, called Josephson Parametric Amplifiers (JPAs). In this section, we give a brief account of the theory of quantum-limited amplification, and of the operating principle of the JPA used in this thesis.

Amplification at the quantum limit

A microwave amplifier of gain G is a two port device (see Fig.2.7). The input and output signals of frequency ω and of narrow bandwidth $\Delta\omega$ are conveniently described by the right propagating spatio-temporal modes $\hat{a}_{\text{in}}$ and $\hat{a}_{\text{out}}$ introduced in Eq.2.29.

The amplified signal is measured at the end of the output transmission line by homodyne demodulation, yielding the quadratures I and Q. The I and Q quadratures obtained by the homodyne demodulation are proportional to the $\hat{X}$ and $\hat{Y}$ operators, with arbitrary rotation in the XY plane tuned via the local oscillator phase. The average signal in one quadrature is then proportional to $\langle\hat{X}\rangle$ and the variance to $\langle\Delta\hat{X}^2\rangle$.

If we naively applied the classical relations between input and output quadratures of a linear amplifier to the quantum case, we would define $\hat{X}_{\text{out}} = \sqrt{G}\hat{X}_{\text{in}}$ and $\hat{Y}_{\text{out}} = \sqrt{G}\hat{Y}_{\text{in}}$. This definition however does not satisfy the commutation relation for the operators $\hat{a}_{\text{out}}$ and $\hat{a}_{\text{in}}$, besides the trivial case $G = 1$:

$$[\hat{a}_{\text{out}}, \hat{a}^\dagger_{\text{out}}] = \sqrt{G}[\hat{a}_{\text{in}}, \hat{a}^\dagger_{\text{in}}] = \sqrt{G} \neq 1. \tag{2.57}$$

The appropriate quantum theory of amplification was expressed by Caves [20], and we will give a brief account of it in the following.

Phase-preserving amplifier

Phase-preserving amplifiers have identical gain on both quadratures $G_{\text{X}} = G_{\text{Y}} = G$. To satisfy the commutation relation for the amplified operators $[\hat{a}_{\text{out}}, \hat{a}^\dagger_{\text{out}}] = 1$

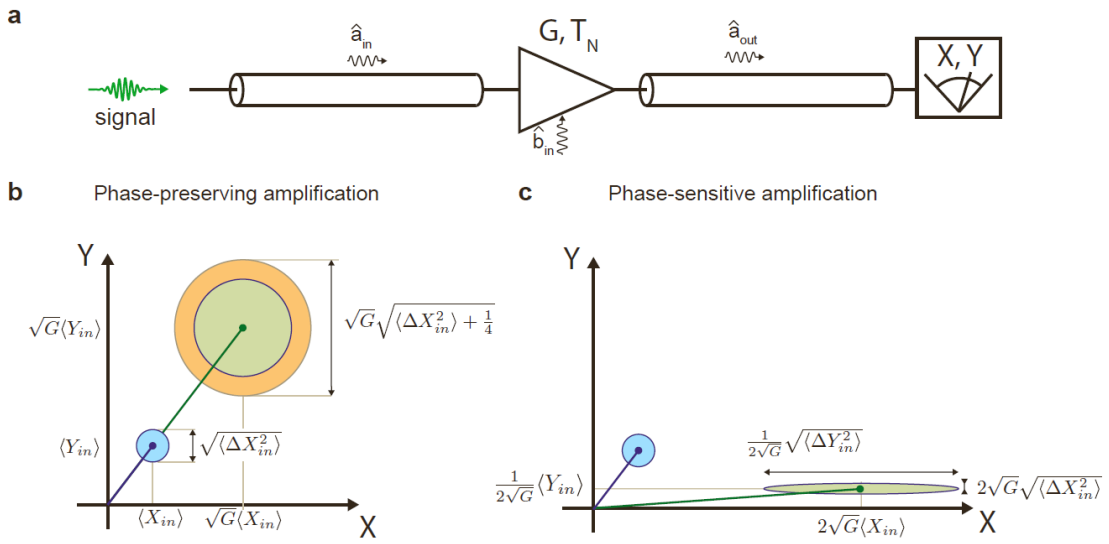

Figure 2.7: **Linear amplifiers.** (a) A linear amplifier of gain G and noise temperature T_{N} is used to detect a narrow-band signal. (b)-(c) Phase-preserving and phase-sensitive amplification in phase-plane representation in the limit of high gain. The disks indicate the contour of the Wigner function. A phase preserving amplifier degrades the SNR, with the added noise represented in red. In phase-sensitive amplification, one quadrature is amplified at the expense of the other, but one can evade the noise added by the Heisenberg uncertainty principle.

one needs to introduce a mode $\hat{b}_{\mathrm{in}}$ internal to the amplifier, that commutes with $\hat{a}_{\mathrm{in}}$:

$$\hat{a}_{\mathrm{out}} = \sqrt{G}\hat{a}_{\mathrm{in}} + \sqrt{1-G}\hat{b}_{\mathrm{in}}^{\dagger} \tag{2.58}$$

satisfying $[\hat{b}_{\mathrm{in}}, \hat{b}_{\mathrm{in}}^{\dagger}] = 1$ and $[\hat{b}_{\mathrm{in}}, \hat{a}_{\mathrm{in}}^{\dagger}] = 0$. By imposing $\langle \hat{b}_{\mathrm{in}} \rangle = 0$, one finds:

$$\langle \hat{X}_{\mathrm{out}} \rangle = \sqrt{G}\langle \hat{X}_{\mathrm{in}} \rangle \tag{2.59}$$

$$\langle \hat{Y}_{\mathrm{out}} \rangle = \sqrt{G}\langle \hat{Y}_{\mathrm{in}} \rangle \tag{2.60}$$

which are the expected relations for the amplified signal.

Quantum limits on amplification

For a phase-preserving amplifier, one can derive from the input-output equations (Eq. 2.58) that the outcoming noise referred to the input in the absence of a signal is:

$$\frac{\langle \Delta\hat{X}_{\mathrm{out}}^2 \rangle + \langle \Delta\hat{Y}_{\mathrm{out}}^2 \rangle}{G} = \langle \Delta\hat{X}_{\mathrm{in}}^2 \rangle + \langle \Delta\hat{Y}_{\mathrm{in}}^2 \rangle + \left(1 - \frac{1}{G}\right)\left(\langle \Delta\hat{X}_{\mathrm{b}}^2 \rangle + \langle \Delta\hat{Y}_{\mathrm{b}}^2 \rangle\right) \tag{2.61}$$

where $\hat{X}_{\mathrm{b}}^2$ are the internal mode fluctuations. The output noise is thus the sum of two contributions: the input noise and the noise added by the amplifier due to internal mode fluctuations. We define the noise detected on a single quadrature as:

$$n = \frac{\langle \Delta\hat{X}_{\mathrm{out}}^2 \rangle}{G} = \langle \Delta\hat{X}_{\mathrm{in}}^2 \rangle + \langle \Delta\hat{X}_{\mathrm{b}}^2 \rangle \tag{2.62}$$

For an incoming field in a thermal equilibrium state, the input noise $\langle \Delta \hat{X}_{\rm in}^2 \rangle$ is given by Eq. 2.14. For sufficiently low temperatures $k_{\rm B}T \ll \hbar\omega$ the vacuum state is reached and the fluctuations saturate the Heisenberg uncertainty relation $\langle \Delta \hat{X}_{\rm in}^2 \rangle = 1/4$, while in general:

$$\langle \Delta \hat{X}_{\rm in}^2 \rangle \geq 1/4 \tag{2.63}$$

The noise added by the amplifier is also bounded by the Heisenberg relation $\langle \Delta \hat{X}_{\rm b}^2 \rangle \geq 1/4$ in the case of phase-preserving amplification.

Phase-sensitive amplifier

A phase-sensitive device amplifies one quadrature at the expense of the other. We consider here only amplifiers for which $G_{\rm s} = G_{\rm X} = 1/G_{\rm Y}$, so that the condition $\sqrt{G_{\rm X} G_{\rm Y}} = 1$ is satisfied. In that case, the input and output quadratures are linked by the relation:

$$\hat{X}_{\rm out} = \sqrt{G_s}\hat{X}_{\rm in} \tag{2.64}$$

$$\hat{Y}_{\rm out} = \frac{1}{\sqrt{G_s}}\hat{Y}_{\rm in}. \tag{2.65}$$

Interestingly, the phase-sensitive amplifier is just a particular case of the phase-preserving amplifier. Writing $\hat{a}_{\rm out} = \sqrt{G_{\rm s}}\hat{X}_{\rm in} + i\frac{1}{\sqrt{G_{\rm s}}}\hat{Y}_{\rm in}$ yields Eq. 2.58 by choosing $\hat{b}_{\rm in} = \hat{a}_{\rm in}$ and $\sqrt{G_{\rm s}} = \sqrt{G} - \sqrt{G-1}$. At large gains, one can identify $\sqrt{G_{\rm s}} = 2\sqrt{G}$.

Quantum limits on amplification

A phase-sensitive amplifier can escape on one quadrature the quantum-limit of amplification:

$$\langle \Delta \hat{X}_{\rm b}^2 \rangle \geq 0 \tag{2.66}$$

The price to pay for this noiseless amplification is that we access only one quadrature of the field. This does not necessarily constitute an issue if the output signal phase is deterministic and constant, as is the case for spin echoes and qubit readout pulses. Upon quantum-limited amplification with a noiseless phase-preserving amplifier, the only remaining noise is therefore the quantum fluctuations of the input field $\langle \Delta \hat{X}_{\rm in}^2 \rangle = 1/4$.

Josephson Parametric Amplifier

In the last decade, various designs for an amplifier operating at the quantum limit have been developed [21, 22, 23, 24, 25, 26, 27, 28]. These designs are based on Josephson junctions embedded in superconducting resonators following pioneering work by Yurke et al. [29]. These elements enable parametric amplification of a signal at frequency $\omega_{\rm s} \approx \omega_0$ by transfer of energy from a pump at frequency $\omega_{\rm p}$ to the signal and to a complementary idler of frequency $\omega_{\rm I}$. In the device used in this thesis, we exploit the tunability of a SQUID array (see Sec. 2.4) to modulate the resonator frequency at $\omega_p \approx 2\omega_0$ and create a three-wave mixing process with $\omega_{\rm p} = \omega_{\rm s} + \omega_{\rm I}$ [25, 26, 27, 28]. Due to the use of dissipationless elements these amplifiers can add the minimum amount of noise allowed quantum mechanically

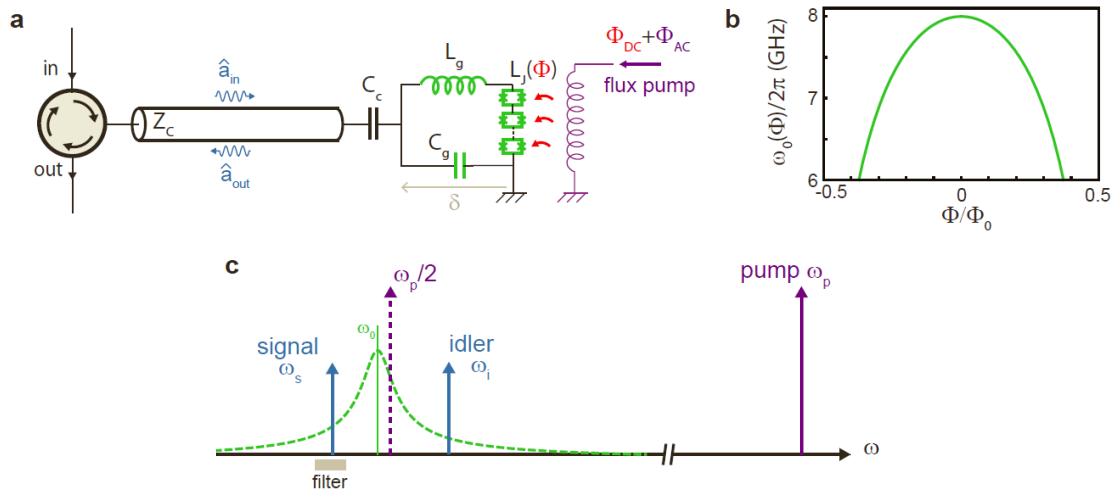

Figure 2.8: **Josephson parametric amplifier.** (a) The JPA comprises a geometrical inductance and capacitance in parallel with an array of SQUIDs, it is probed in reflexion via a transmission line capacitively coupled. (b) Modulation of the frequency of the resonator as a function of the SQUIDs DC flux bias. (c) Phase-preserving amplification operation of the JPA: a pump applied at $\omega_p \approx 2\omega_0$ amplifies the signal and generates an idler signal. The idler signal can be removed by filtering.

when operated in phase-preserving mode ($\omega_s \neq \omega_I$) and no noise in the amplified quadrature for phase-sensitive amplification ($\omega_s = \omega_I$). In this paragraph, we only intend to give an overview of the device operating principle. We refer the reader to [28, 30, 31] for more details and rigorous demonstrations.

The tunability of the SQUID inductance is exploited to provide parametric amplification. Consider a resonator with the geometry shown in Fig. 2.8a: a capacitance C_g in parallel with an inductance L_g and an array of N symmetric SQUID loops, probed via a transmission line of characteristic impedance Z_c coupled by a capacitance C_c to the resonator. As illustrated in Fig. 2.8a, the resonator is probed in reflexion: a circulator is needed to route the input signal to the resonator, and the output signal towards the output line.

The tunability of ω_0 with respect to Φ is obtained by placing a flux line nearby the SQUIDs array (see Figure 2.8a). For a resonator of bare frequency $\omega_0(0) = 8\,\text{GHz}$ and characteristic impedance $Z_0 = 100\,\Omega$, the frequency tunability ranges over several hundreds of MHz, as shown in Fig. 2.8b.

According to Landau [32], modulating the resonator frequency at a frequency close to $2\omega_0$, gives rise to the phenomenon of parametric amplification. The amplifier thus consists in a tunable resonator $\omega_0(\Phi_{DC})$, a pump signal sent through the flux-line at frequency $\omega_p \approx 2\omega_0$, and an input port through which a signal at a frequency $\omega \approx \omega_0$ is sent, with the reflected signal being amplified.The JPA

being composed of dissipation-less elements and based on the simple parametric amplification process, it reaches the quantum limit of amplifier-added noise discussed earlier. More precisely, it can be used in either of the two modes of operation:

- **Phase-preserving amplification:** non degenerate pumping ($\omega_\mathrm{p} \neq 2\omega_\mathrm{s}$)
  In this operation mode both the signal frequency ω_s and the idler one ω_I gets amplified (see Figure 2.8c). The power gain G achieved on the signal increases by increasing the pump amplitude, until it exceeds the damping occurring via the transmission line, thus entering in an auto-oscillating regime. Below this threshold the system behaves as a phase-preserving amplifier, adding a noise corresponding to half a photon to each quadrature. In practice a narrow band filter is then used to get rid of the idler contribution.

  In this work, phase preserving amplification is use to perform homodyne detection.

- **Phase-sensitive amplification:** degenerate pumping ($\omega_\mathrm{p} = 2\omega_\mathrm{s}$)
  In this case interferences between the idler mode and the input signal leads to a phase sensitive amplification depending on the relative phase between the signal and the pump $\Delta\phi$:

$$G(\Delta\phi) = \left(G_\mathrm{s} - \frac{1}{G_\mathrm{s}}\right)\cos^2\Delta\phi + \frac{1}{G_\mathrm{s}} \tag{2.67}$$

  As discussed earlier, this degenerate amplifier does not add noise to the incoming signal and amplifies noiselessly one of its quadratures.

  In this work, phase sensitive amplification with a JPA is employed to readout the state of the Transmon qubit as a part of the microwave photo-detection process. This operation mode is justified by the high readout fidelity required to reach the best performances during photon detection.

2.6 Quadrature and photon detection

In this thesis, we will use a single-microwave-photon detector to detect spin signals, which are more usually detected with linear amplification followed by demodulation (ie, quadrature detection). In this section, we compare the SNRs of quadrature and photon detection for various input field statistics.

Model

Our model is sketched in Fig. 2.9. We consider a source, emitting a field in a state:

$$\hat{\rho} = \sum_{n,m} \rho_{nm} \left|n\right\rangle \left\langle m\right| \tag{2.68}$$

where $|n\rangle$ is the Fock basis. The fields is routed in a transmission line towards a detector.

The transmission line may have losses, reducing the field energy by a factor η_c, the collection efficiency. Another non-ideality is the possible presence in the line of a background microwave field, at a non-zero temperature. This is always the case in the experiments, first because they are performed at non-zero temperature, resulting in an equilibrium thermal field, but also because of thermal radiation propagating through the input (or output) lines and being insufficiently

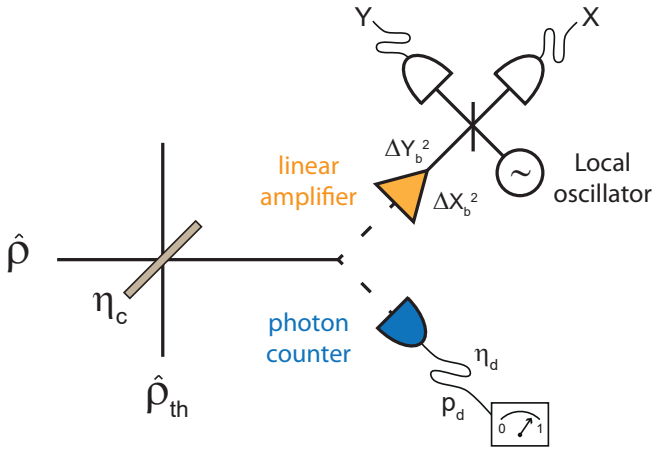

Figure 2.9: **Detector imperfections.** Schematic model for quadrature and photon detector non-idealities. A quantum beam-splitter model accounts for the finite collection efficiency $\eta_{\rm c}$ and thermal dark counts $\hat{\rho}_{\rm th}$. In addition to these non-idealities, quadrature detection has noise contribution $\Delta X_{\rm b}^2$, $\Delta Y_{\rm b}^2$ from the quantum-limited linear amplifier. On the other hand, photon counting has additional contributions $\eta_{\rm d}$, $p_{\rm d}$ to efficiency and dark count due to detector imperfections.

attenuated or filtered. This results in a background field with approximately thermal statistics, but with an effective temperature which may be much higher than the cryostat physical temperature. The physical quantity that describes best this temperature is the average number of photons per mode, which we call $p_{\rm th}$.

We model both the losses and the thermal population by the introduction of a beam-splitter in-between the source and the detector, with transmission $\eta_{\rm c}$. The source is on one input port, and the other input port is connected to a fictitious thermal field, with an average photon number $p_{\rm th}/(1-\eta_{\rm c})$.

When we apply the beam splitter model to a state $\hat{\rho}$, it is transformed in a non trivial way. The explicit expression for the transformed state traced over the non-measured port of the beam-splitter, in the case of a coherent state, and a Fock state $|1\rangle$ in the limit $\eta_{\rm c} p_{\rm th} \ll 1$ are:

$$|\alpha\rangle\langle\alpha| \otimes \hat{\rho}_{\rm th} \rightarrow (1-p_{\rm th})\,|\alpha\sqrt{\eta_{\rm c}}\rangle\langle\alpha\sqrt{\eta_{\rm c}}| + p_{\rm th}\,|1,\alpha\sqrt{\eta_{\rm c}}\rangle\langle 1,\alpha\sqrt{\eta_{\rm c}}| \tag{2.69}$$

$$|1\rangle\langle 1| \otimes \hat{\rho}_{\rm th} \rightarrow (1-\eta_{\rm c})(1-p_{\rm th})\,|0\rangle\langle 0| + (p_{\rm th}+\eta_{\rm c})\,|1\rangle\langle 1| \tag{2.70}$$

where $|1,\alpha\sqrt{\eta_{\rm c}}\rangle = D(\alpha\sqrt{\eta_{\rm c}})\hat{a}^\dagger|0\rangle$ is a displaced number state. These expressions will be used in the following to calculate average values of observables.

We consider two detection modalities: quadrature detection, and photon counting.

Quadrature detection

Quadrature detection measures projectively the operator:

$$\hat{X}_{j,\theta} = \frac{1}{2}\left(\hat{a}_j e^{-i\theta} + \hat{a}_j^\dagger e^{i\theta}\right) \tag{2.71}$$

where $\hat{a}_j$ and $\hat{a}_j^\dagger$ are the single-mode annihilation and creation operators and where θ a phase identifying the quadrature that is measured. This is the case of

homodyne detection, in which mixing of the signal with a local oscillator allows to extract the quadratures I and Q of the field, proportional to the $\hat{X}$ and $\hat{Y}$ operators introduced in section 2.1.

In order to model a real detector we will adopt the above mentioned beam splitter model. In addition to this non-ideality we recall that a phase-preserving (pp) linear amplifier adds to the input quadrature the equivalent noise of half photon, while a phase-sensitive (ps) amplifier can escape this limit at the expense of arbitrarily large noise on the orthogonal quadrature. If we restrict to a single mode, disregard the orthogonal quadrature and take $\hat{X}_{j,\theta} = \hat{X}$ the expressions for standard deviations in these two regimes are:

$$\frac{\Delta X_{\text{out,pp}}}{\sqrt{G}} = \sqrt{\langle \Delta X_{\text{in}}^2 \rangle + \frac{1}{4}} \tag{2.72}$$

$$\frac{\Delta X_{\text{out,ps}}}{\sqrt{G}} = \Delta X_{\text{in}}. \tag{2.73}$$

Photon detection

In this thesis, we use a single-photon detector. This detector measures the field in the energy eigenbasis. Nevertheless, it does not exactly detect the photon number operator $a^\dagger a$, because it saturates for incoming photon numbers larger than 1. Therefore, the correct description is that it measures the operator:

$$\hat{P}_\perp = 1 - |0\rangle \langle 0| . \tag{2.74}$$

The click probability therefore yields the probability that the field contains one photon or more.

A real photon detector can be modeled with the beam-splitter model reported above, with an additional non-ideality coming from the imperfections of the detector. All such non-idealities factor into two main effects: inefficiency and dark counts. The detector can miss a signal photon (finite efficiency), or instead click when no photon is present (dark count).

The two distinct processes that can lower the detection efficiency are:

- as seen in the beam splitter model, the signal may be absorbed or reflected during the propagation from the source to the detector, this occurs with a probability $1 - \eta_{\text{c}}$.
- moreover an incoming photon at the detector may not be detected because of the detector imperfections; this occurs with a probability $1 - \eta_{\text{d}}$. η_{d} is called the detector efficiency.

The total detector efficiency is $\eta = \eta_{\text{c}}\eta_{\text{d}}$. Dark counts are also due to two types of processes:

- Unwanted photons may arrive on the detector, due to radiation either at thermal equilibrium or (more likely) leaking from the higher temperature stages of the cryostat, and leading to a click. This happens with a probability p_{th}, defined in the beam splitter model.
- Moreover, even in absence of physical photons, imperfect detector operation may lead to a click, with a probability p_{d}.

State	p_0
Vacuum	$1 - p_{\rm th}$
Fock $\|n\rangle$	$(1-\eta_{\rm c})^n - p_{\rm th}\left[(1-\eta_{\rm c})^n - n\eta_{\rm c}(1-\eta_{\rm c})^{n-1}\right]$
Coherent $\|\alpha\rangle$	$\left[1 - p_{\rm th}\left(1-\eta_{\rm c}\left\|\alpha\right\|^2\right)\right] e^{-\eta_{\rm c}\left\|\alpha\right\|^2}$

Table 2.1: Detector click probability

The total dark count probability per detector cycle is then $p_{\rm dc} = p_{\rm th} + p_{\rm d}$. All imperfections occurring during photon counting can be taken into account through a straightforward calculation reported in appendix A. If we consider a field state described by the density matrix $\hat{\rho}$, the total probability of measuring a click when the state impinges on the detector is:

$$p_{\rm click} = p_{\rm d} p_0 + \eta_{\rm d}(1 - p_0) \tag{2.75}$$

where:

$$p_0 = (1 - p_{\rm th}) \sum_{n=0}^{\infty} \rho_{nn}(1-\eta_{\rm c})^n + p_{\rm th} \sum_{n=0}^{\infty} n\rho_{nn}\eta_{\rm c}(1-\eta_{\rm c})^{n-1}. \tag{2.76}$$

2.7 Signal-to-noise ratios in single-mode detection

The aim of this section is to compare the performances of quadrature detection and photon detection for some states of the electromagnetic field in a known mode. In order to compare the two measurements we will make use of the SNRs, defined for a generic operator $\hat{O}$ as the ratio between the average signal above the average vacuum signal $\langle \hat{O} \rangle_{|0\rangle} = \langle 0 | \hat{O} | 0 \rangle$, and its standard deviation:

$$\mathrm{SNR} = \frac{\langle \hat{O} \rangle - \langle \hat{O} \rangle_{|0\rangle}}{\sqrt{\langle \Delta \hat{O}^2 \rangle}}. \tag{2.77}$$

We remark that, in the case of a photon counter, $\hat{O} = \hat{P}_\perp$ is a projection operator (i.e. $\hat{P}_\perp^2 = \hat{P}_\perp$) so that the variance is easily obtained from the mean value as:

$$\langle \Delta \hat{P}_\perp^2 \rangle = \langle \hat{P}_\perp \rangle - \langle \hat{P}_\perp \rangle^2 = p_{\rm click}(1 - p_{\rm click}) \tag{2.78}$$

which – as expected – is the variance of a binomial distribution, and the photon counting SNR is:

$$\mathrm{SNR}_{\rm pc} = \frac{p_{\rm click} - p_{\rm click}^{|0\rangle}}{\sqrt{p_{\rm click}\left(1 - p_{\rm click}\right)}}. \tag{2.79}$$

For quadrature detection we take $\hat{O} = \hat{X}_{\rm out}$, the quadrature operator after the amplifier, in the following we will omit the subscript to keep the notation light.

To compare SNRs for quadrature and photon detection we will often take the limits $p_{\rm d} \ll 1$, $p_{\rm d} \ll \eta_{\rm d}$, $p_{\rm th} \ll 1$, $p_{\rm th} \ll \eta_{\rm c}$, which are relevant for our experiments. We will now consider various states, and compute the signal and noise for quadrature and photon-counting detection, taking into account detector imperfections.

Coherent state

Consider the case where the source emits a coherent state $\hat{\rho} = |\alpha\rangle\langle\alpha|$.

Quadrature We calculate the expectation value of a quadrature measurement using Eq. 2.69:

$$\frac{\langle \hat{X} \rangle}{\sqrt{G}} = \mathrm{Re}[\alpha]\sqrt{\eta_{\rm c}}. \tag{2.80}$$

The variance is:

$$\frac{\langle \Delta \hat{X}^2 \rangle}{G} = \frac{1}{4} + \frac{p_{\rm th}}{2} + \langle \Delta \hat{X}^2 \rangle_{\rm amp} \tag{2.81}$$

If the phase of the coherent state is known, as in our experiments we can take α to be real. In the limit where $\langle \Delta \hat{X}^2 \rangle_{\rm amp} = 0$ (phase-sensitive amplification) and $p_{\rm th} \ll 1$, we get

$$\mathrm{SNR}_{\rm qd} = 2\alpha\sqrt{\eta_{\rm c}}. \tag{2.82}$$

Photon counting For abritrary α, the SMPD signal is a complicated expression because of saturation. The relevant limit is $\alpha \ll 1$, in which case:

$$p_{\rm click} = \eta_{\rm d}\left(\eta_{\rm c}|\alpha|^2 + p_{\rm th}(1-\eta_{\rm c}|\alpha|^2)^2\right) + p_{\rm d}\left(1 - \eta_{\rm c}|\alpha|^2 - p_{\rm th}(1-\eta_{\rm c}|\alpha|^2)^2\right) \tag{2.83}$$

and in the limit $p_{\rm th} \ll 1$, $p_{\rm d} \ll 1$:

$$\mathrm{SNR}_{\rm pc} = \alpha\sqrt{\eta_{\rm c}\eta_{\rm d}} \tag{2.84}$$

Note that, in this limit, the only source of photo-counting noise is the shot-noise due to the probabilistic nature of vacuum/no-vacuum measurement on a coherent state. The ratio of SNRs is:

$$\frac{\mathrm{SNR}_{\rm pc}}{\mathrm{SNR}_{\rm qd}} = \frac{\sqrt{\eta_{\rm d}}}{2} \tag{2.85}$$

This implies that detecting a single-mode coherent state with a photon counter is less sensitive of at least a factor 2 compared to quadrature detection. Both detection modalities are limited by the same physical phenomenon: shot-noise.

One-photon Fock state

Consider a single-mode Fock state $\hat{\rho} = |1\rangle\langle 1|$.

Quadrature Measuring $\hat{X}$ in quadrature detection has no interest since $\langle 1|\hat{X}|1\rangle = 0$. Instead, one can measure $\hat{X}^2$.

$$\frac{\langle \hat{X}^2 \rangle - \langle \hat{X}^2 \rangle_{|0\rangle}}{G} = \eta_{\rm c}\frac{1+p_{\rm th}}{2}. \tag{2.86}$$

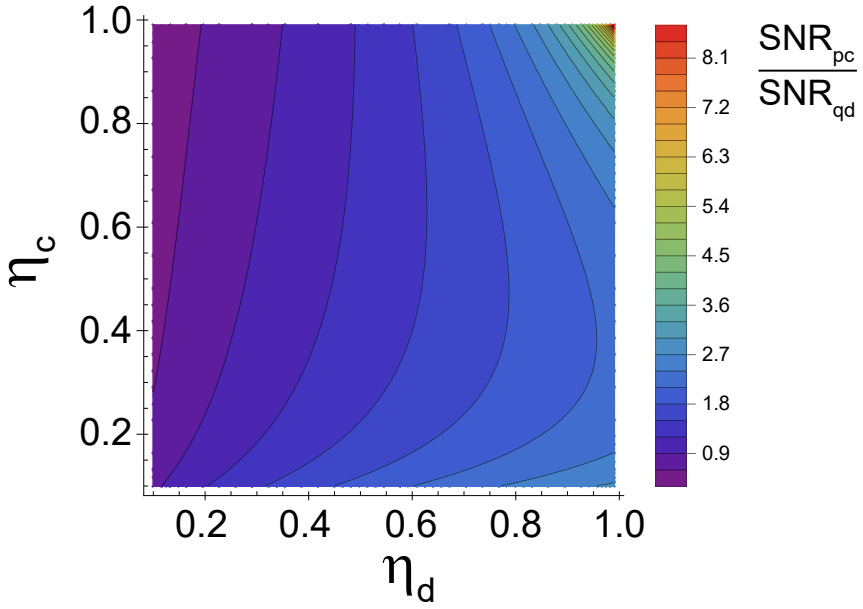

Figure 2.10: **SNR ratio for Fock state** $|1\rangle$**.** Computed ratio of SNRs in the case of photon and quadrature detection of a single photon Fock state, as a function of collection and detection efficiencies η_c and η_d.

The variance of $\hat{X}^2$ (assuming noiseless phase-sensitive amplification) is

$$\frac{\langle \hat{X}^4 \rangle - \langle \hat{X}^2 \rangle^2}{G^2} = \frac{1}{8} + \frac{\eta_c}{2} - \frac{\eta_c^2}{4}, \tag{2.87}$$

so that the SNR in the limit $p_{th} \ll 1$ is:

$$\mathrm{SNR}_{qd} = \frac{2\eta_c}{\sqrt{2 + 8\eta_c - 4\eta_c^2}}. \tag{2.88}$$

Photon counting For a single-photon counter one has:

$$p_{click} = \eta_d(\eta_c + p_{th}(1 - \eta_c)) + p_d(1 - \eta_c - p_{th}(1 - \eta_c)) \tag{2.89}$$

and the associated SNR in the limit $p_{th} \ll 1$, $p_d \ll 1$ is:

$$\mathrm{SNR}_{pc} = \frac{\eta_d \eta_c}{\sqrt{\eta_d \eta_c (1 - \eta_d \eta_c)}} \tag{2.90}$$

The above expression increases without bound in the limit of perfect detection $\eta_c \eta_d \to 1$. This means that for sufficiently high efficiencies, photon counting is more adapted at detecting Fock states with respect to quadrature detection. This is because the Fock state is an eigenstate of the measured operator. The ratio of the SNR in quadrature and photon-counting is plotted in Fig.2.10. We see that photon counting is more efficient than quadrature detection over a large range of parameters.

2.8 Signal-to-noise ratios in multi-mode detection

We have since now examined signals emitted and detected in a known mode of the electromagnetic field. In this section we consider the detection of a microwave

signal that can be emitted on one of many modes. This case is relevant for this thesis because it describes the detection of fluorescence signal emitted on many temporal modes by a spin ensemble coupled to a microwave cavity.

Consider a state $|\psi\rangle$ of the field, emitted in a stochastic way in an unknown mode out of M electromagnetic modes, the associated density matrix is:

$$\hat{\rho}_{\text{in}} = \frac{1}{M}\sum_{m=1}^{M} |0..\psi_m..0\rangle\langle 0..\psi_m..0| \tag{2.91}$$

$$= \frac{1}{M}\sum_{m=1}^{M} |\psi\rangle\langle\psi|_m \bigotimes_{m'\neq m} |0\rangle\langle 0|_{m'} \tag{2.92}$$

where the index m labels the modes. We use a beam splitter interaction to model thermal noise injected on each mode. For modes in the vacuum, the state after the beam splitter traced on the ancillary degree of freedom is a thermal state $\hat{\rho}_{\text{th}}$ with average number of photons $p_{\text{th}} \ll 1$. For the general state $|\psi\rangle\langle\psi|_m$ the evolution is not trivial, we define $\hat{\rho}_\psi$ as:

$$\hat{\rho}_\psi := \text{Tr}_{\text{th}}\left[B^\dagger |\psi\rangle\langle\psi|_m \otimes \hat{\rho}_{\text{th,in}} B\right]$$

where B denotes the beam-splitter evolution, $\hat{\rho}_{\text{th,in}}$ is the thermal state before the beam splitter and Tr_{th} the partial trace on the thermal state subspace. We write the full density matrix after the beam-splitter and traced on the ancillary mode as:

$$\hat{\rho} = \frac{1}{M}\sum_{m=1}^{M}\bigotimes_{m'=1}^{M}\hat{\rho}_{m'}. \tag{2.93}$$

where:

$$\hat{\rho}_{m'} = \begin{cases}\hat{\rho}_\psi & \text{if } m' = m\\ \hat{\rho}_{\text{th}} & \text{if } m' \neq m\end{cases} \tag{2.94}$$

Since the mode hosting the state $|\psi\rangle$ is not known in advance, in order to measure any single-mode operator $\hat{O}_m$ one needs to sum on all modes:

$$\hat{O} = \sum_{m=1}^{M}\hat{O}_m \otimes \mathbb{1}^{\otimes M-1}. \tag{2.95}$$

The average value is thus the sum of average values:

$$\langle\hat{O}\rangle_\psi = \frac{1}{M}\sum_{k=1}^{M}\sum_{m=1}^{M}\text{Tr}[\hat{\rho}_m\hat{O}_m\bigotimes_{k'\neq m}^{M}\hat{\rho}_{k'}\otimes\mathbb{1}] = (M-1)\langle\hat{O}_m\rangle_{\text{th}} + \langle\hat{O}_m\rangle_\psi. \tag{2.96}$$

where $\langle\hat{O}_m\rangle_{\text{th}} = \text{Tr}[\hat{\rho}_{\text{th}}\hat{O}_m]$ and $\langle\hat{O}_m\rangle_\psi = \text{Tr}[\hat{\rho}_\psi\hat{O}_m]$ We observe that this value contains contributions from all modes, which become relevant when $\text{Tr}[\hat{\rho}_{\text{th},m}\hat{O}_m] \neq 0$. In the following we take $M \gg 1$, so $M - 1 \simeq M$.

Multi-mode quadrature detection

In quadrature detection the measured multi-mode operator is:

$$\hat{X} = \sum_{m=1}^{M}\hat{X}_m \otimes \mathbb{1}^{\otimes M-1} \tag{2.97}$$

its average value, in the sense of Eq.2.96, is always equal to the single-mode case, because thermally populated modes have $\langle \hat{X}_m \rangle_{\rm th} = 0$:

$$\langle \hat{X} \rangle_\psi = \langle \hat{X}_m \rangle_\psi. \tag{2.98}$$

In contrast, each mode contributes to the noise:

$$\langle \hat{X}^2 \rangle_\psi = M \left(\frac{p_{\rm th}}{2} + \frac{1}{4} \right) + \langle \hat{X}_m^2 \rangle_\psi, \tag{2.99}$$

the SNR is:

$$\mathrm{SNR}_{\rm qd} = \frac{\langle \hat{X}_m \rangle_\psi}{\sqrt{M \left(\frac{p_{\rm th}}{2} + \frac{1}{4} \right) + \langle \hat{X}_m^2 \rangle_\psi}} \to \frac{2\langle \hat{X}_m \rangle_\psi}{\sqrt{M}} \tag{2.100}$$

where we took the limit of low thermal occupation $p_{\rm th} \ll 1$ and $M \gg \langle \hat{X}_m^2 \rangle_\psi$ due to the large number of modes. This expression shows that the SNR is lower than in the single-mode case, due to the contribution of all the modes to the signal noise. This added noise cannot be eliminated, being due to vacuum zero point fluctuations.

In cases in which $\langle \hat{X} \rangle_\psi = 0$, one can measure the operator:

$$\hat{X}^2 = \sum_{m=1}^{M} \hat{X}_m^2 \otimes \mathbb{1}^{\otimes M-1} \tag{2.101}$$

and the signal above noise is:

$$\langle \hat{X}^2 \rangle_\psi - \langle \hat{X}^2 \rangle_{\rm th} = \langle \hat{X}_m^2 \rangle_\psi - \left(\frac{p_{\rm th}}{2} + \frac{1}{4} \right) \tag{2.102}$$

which is equal to the single-mode case. Again, the noise has contribution from all modes:

$$\langle \hat{X}_m^4 \rangle_\psi - \langle \hat{X}_m^2 \rangle_\psi^2 + \frac{M}{8} \left(2p_{\rm th} + 1 \right)^2, \tag{2.103}$$

In the limit $p_{\rm th} \ll 1$ and $M \gg \langle \hat{X}_m^4 \rangle_\psi - \langle \hat{X}_m^2 \rangle_\psi^2$, we can write for the SNR:

$$\mathrm{SNR}_{\rm qd} = \frac{\langle \hat{X}_m^2 \rangle_\psi - 1/4}{\sqrt{M/8}}. \tag{2.104}$$

Again, even in the limit of vanishingly low thermal noise, the SNR is reduced by a factor $\sqrt{M/8}$ compared to the single mode case, because of the vacuum noise contribution of all the modes.

Multi-mode photon detection

In the case of photon detection the measured operator is:

$$\hat{P}_\perp = \sum_{m=1}^{M} \hat{P}_{\perp m} \otimes \mathbb{1}^{\otimes M-1}. \tag{2.105}$$

The signal is given by:

$$\langle \hat{P}_\perp \rangle_\psi - \langle \hat{P}_\perp \rangle_{\rm th} = \langle \hat{P}_{\perp m} \rangle_\psi - p_{\rm th} \tag{2.106}$$

which is equal to the single-mode case. For the noise we have:

$$\langle \Delta P_\perp^2 \rangle = M(1-p_{\rm th})p_{\rm th} + \langle \Delta P_{\perp m}^2 \rangle_\psi \tag{2.107}$$

The variance is the single mode variance, with in addition terms arising from the finite thermal population $p_{\rm th}$ of the modes. The term $(1-p_{\rm th})p_{\rm th}$ is the variance of the dark counts of each mode, typical of a binomial process. In the limit $p_{\rm th} \ll 1$, the SNR is:

$$\mathrm{SNR}_{\rm pc} = \frac{\langle \hat{P}_{\perp m} \rangle_\psi - p_{\rm th}}{\sqrt{M p_{\rm th} + \langle \Delta P_{\perp m}^2 \rangle_\psi}}. \tag{2.108}$$

Importantly, we note that the noise added by the M modes vanishes in the limit of zero temperature ($p_{\rm th} = 0$). In this limit, there is no difference between multi-mode and single-mode photon detection.

Using Eqs. 2.108 and 2.104, the ratio of SNRs for quadrature and photon detection in the multimode case, in the limit $p_{\rm th} \ll 1$ and large number of modes is approximately equal to:

$$\frac{\mathrm{SNR}_{\rm pc}}{\mathrm{SNR}_{\rm qd}} \simeq \frac{\langle \hat{P}_{\perp m} \rangle_\psi}{\langle \hat{X}_m^2 \rangle_\psi} \times \begin{cases} 1/\sqrt{p_{\rm th}}, & \text{if } M p_{\rm th} \gg \langle \Delta P_{\perp m}^2 \rangle_\psi \\ \sqrt{M}, & \text{if } M p_{\rm th} \ll \langle \Delta P_{\perp m}^2 \rangle_\psi \end{cases} \tag{2.109}$$

In both cases, photon detection is more sensitive than quadrature detection in the limit $M \gg 1$ and $p_{th} \ll 1$.

Finally, note that in the case in which the modes are spatio-temporal modes impinging sequentially during a time T, we can rewrite $\mathrm{SNR}_{\rm pc}$ defining a dark count rate $\nu_{\rm dc} := p_{\rm th} M/T$:

$$\mathrm{SNR}_{\rm pc} = \frac{\langle \hat{P}_{\perp m} \rangle_\psi - p_{\rm th}}{\sqrt{\nu_{\rm dc} T + \langle \Delta P_{\perp m}^2 \rangle_\psi}}. \tag{2.110}$$

The important conclusion of this chapter is therefore that photon counting is much more sensitive for detecting weak incoherent signals (i.e., small photon numbers) emitted randomly over many modes. This is particularly true in optics. For instance, the fluorescence of an individual NV consists of $\sim 10^5$ photons emitted over a bandwidth $\Delta\omega/2\pi \sim 10$ THz during 1 s. This corresponds to $M = 10^{13}$ modes. Even assuming quadrature detection would be possible over such a large bandwidth (which is obviously not the case), we see from Eq. 2.104 that the 10^5 photons signal would be completely blurred by vacuum noise. Photon counters, on the other hand, have dark count rates in the $\mathrm{kCount/s}$ in a $10\,\mathrm{THz}$ bandwidth, which corresponds to an effective $p_{\rm th} \sim 10^{-10}$. Low dark-count photon counters in the optical domain are therefore a key resource for the detection of individual quantum emitters, which emit weak incoherent photons. We thus anticipate that the counterpart at microwave frequency will open the way to many novel experiments.

Photon detection of a multi-mode Fock state

The fluorescence signal emitted by an ensemble of spin relaxing spontaneously is described by a multimode Fock state, containing $N \ll M$ photons, each one on a different mode. The SNR formula in the case of photon detection will turn to be useful in chapter 6:

$$\mathrm{SNR}_{\rm pc} = \frac{N\eta}{\sqrt{\nu_{\rm dc} T + N\eta(1-\eta)}}. \tag{2.111}$$

As one expects, the signal is given by the number of photons multiplied by the total efficiency $\eta_{\rm c}\eta_{\rm d}$. The noise has one contribution from dark counts $\nu_{\rm dc}T$ and one contribution from the partition noise due to finite detection efficiency.

Chapter 3

Spins coupled to a resonator

In this chapter we present the dynamics of one and many spins coupled to a cavity, and the effects arising from this interaction.

3.1 Single spin in an external magnetic field

We consider a spin-$\frac{1}{2}$ described by the dimensionless vector operator:

$$\hat{\mathbf{S}} = \frac{1}{2}(\hat{\sigma}_x, \hat{\sigma}_y, \hat{\sigma}_z), \tag{3.1}$$

$$[\hat{\sigma}_i, \hat{\sigma}_j] = 2i\epsilon_{ijk}\hat{\sigma}_k, \tag{3.2}$$

where $\hat{\sigma}_i$ are the Pauli matrices. The associated magnetic dipole is:

$$\hat{\boldsymbol{\mu}} = -\gamma_e \hbar \hat{\mathbf{S}}, \tag{3.3}$$

where the gyromagnetic ratio is $\gamma_e = 28\,\mathrm{GHz/T}$. A classical external magnetic field $\mathbf{B}_0$ is applied in order to lift the energy degeneracy of spin states with different orientations. The spin-field interaction is described by the Hamiltonian:

$$\hat{H}_s = -\hat{\boldsymbol{\mu}} \cdot \mathbf{B}_0 = \frac{\hbar\omega_s}{2}\hat{\sigma}_z, \tag{3.4}$$

with $\omega_s = \gamma_e B_0$ and where we assumed without loss of generality that the magnetic field is directed along $\hat{\boldsymbol{e}}_z$. The presence of $\mathbf{B}_0$ introduces a quantization axis in the system, such that the energy degeneracy of the states with $\hat{S}_z$ eigenvalues $m_z = \pm 1$ is lifted. We denote the ground and excited state of the spin system as $|g\rangle$ and $|e\rangle$, eigenvectors of $\hat{\sigma}_z$. On this basis, the Pauli operators can be explicitly written as

$$\hat{\sigma}_x = \begin{pmatrix} 0 & 1 \\ 1 & 0 \end{pmatrix}, \qquad \hat{\sigma}_y = \begin{pmatrix} 0 & -i \\ i & 0 \end{pmatrix}, \qquad \hat{\sigma}_z = \begin{pmatrix} 1 & 0 \\ 0 & -1 \end{pmatrix}. \tag{3.5}$$

3.2 Single spin coupled to a harmonic resonator

Consider now an LC resonator placed in the vicinity of the spin, such that the current flowing in the inductor generates a quantum magnetic field $\hat{\mathbf{B}}_1(t)$ at the spin position. The total Hamiltonian describing the system is:

$$\hat{H} = \hat{H}_\mathrm{r} + \hat{H}_\mathrm{s} + \hat{H}_\mathrm{int} = \hbar\omega_0 \left(\hat{a}^\dagger \hat{a} + \frac{1}{2}\right) + \frac{\hbar\omega_\mathrm{s}}{2}\hat{\sigma}_z + \hat{H}_\mathrm{int}, \tag{3.6}$$

with the interaction Hamiltonian:

$$\hat{H}_{\rm int} = -\hat{\boldsymbol{\mu}} \cdot \hat{\mathbf{B}}_1 = \hbar\gamma_e \hat{\boldsymbol{S}} \cdot \boldsymbol{B}_{\rm zpf}(\hat{a} + \hat{a}^\dagger). \tag{3.7}$$

This Hamiltonian can be expressed on the basis of the spin eigenstates $|g\rangle, |e\rangle$ as:

$$\hat{H}_{\rm int} = \hbar(\hat{a} + \hat{a}^\dagger)\left(g_0\hat{\sigma}_+ + g_0^*\hat{\sigma}_- + \alpha_g |g\rangle\langle g| + \alpha_e |e\rangle\langle e|\right), \tag{3.8}$$

where:

$$g_0 = \gamma_e \langle e| \hat{\boldsymbol{S}} \cdot \boldsymbol{B}_{\rm zpf} |g\rangle,$$
$$\alpha_j = \gamma_e \langle j| \hat{\boldsymbol{S}} \cdot \boldsymbol{B}_{\rm zpf} |j\rangle.$$

The diagonal elements α_j represent Note that in the following we assume a real transition matrix element $g_0 = g_0^*$, allowed by an appropriate redefinition of $|e\rangle$ and $|g\rangle$.

In order to perform the rotating wave approximation, we move to interaction picture with respect to $\hat{H}_0 = \hat{H}_{\rm r} + \hat{H}_{\rm s}$, such that $\hat{H}_{\rm int}$ takes the form:

$$\begin{aligned}\hat{\tilde{H}}_{\rm int}(t) &= e^{\frac{i\hat{H}_0 t}{\hbar}} \hat{H}_{\rm int} e^{-\frac{i\hat{H}_0 t}{\hbar}} = \\ &= \hbar g_0 \left(\hat{a}\hat{\sigma}_+ e^{i(\omega_s-\omega_0)t} + \hat{a}\hat{\sigma}_- e^{-i(\omega_s+\omega_0)t} + \hat{a}^\dagger\hat{\sigma}_+ e^{i(\omega_s+\omega_0)t} + \hat{a}^\dagger\hat{\sigma}_- e^{-i(\omega_s-\omega_0)t}\right) \\ &\quad + \hbar(\hat{a}e^{-i\omega_0 t} + \hat{a}^\dagger e^{i\omega_0 t})\mathrm{Diag}(\alpha_{\rm e}, \alpha_{\rm g}),\end{aligned} \tag{3.9}$$

where $\mathrm{Diag}(\alpha_{\rm e}, \alpha_{\rm g})$ is a diagonal matrix with $\alpha_{\rm e}$ and $\alpha_{\rm g}$ on the diagonal. One can now apply the rotating wave approximation that consists in discarding the fast rotating terms $\pm(\omega_s + \omega_0)$ and keeping the slow rotating ones $\pm(\omega_s - \omega_0)$. Reverting back to the Schrodinger picture, leads to the full Jaynes-Cummings Hamiltonian:

$$\hat{H} = \hbar\omega_0\left(\hat{a}^\dagger\hat{a} + \frac{1}{2}\right) + \frac{\hbar\omega_{\rm s}}{2}\hat{\sigma}_z + \hbar g_0\left(\hat{a}\hat{\sigma}_+ + \hat{a}^\dagger\hat{\sigma}_-\right), \tag{3.10}$$

which describes the interaction between the spin and the resonator in terms of the exchange of a quantum of excitation.

Open system

In order to model the environment surrounding the spin (lattice phonons, nearby spins) and the resonator (loss channels, external drive), we add the following elements to the description of the system:

- **Drive:** in a usual experiment a coherent tone of amplitude β and frequency $\omega_{\rm d}$ is used to the drive the resonator. With this additional term, the Hamiltonian of Eq. 3.10 becomes:

$$\hat{H} = \hbar\omega_0\hat{a}^\dagger\hat{a} + \frac{\hbar}{2}\omega_{\rm s}\hat{\sigma}_z + \hbar g_0\left(\hat{a}\hat{\sigma}_+ + \hat{a}^\dagger\hat{\sigma}_-\right) + i\hbar\sqrt{\kappa_{\rm ext}}\left(\beta\hat{a}^\dagger e^{-i\omega_{\rm d}t} + \beta^*\hat{a}e^{i\omega_{\rm d}t}\right). \tag{3.11}$$

- **Spin relaxation:** resonant coupling of the spin with a lattice-phonon bath containing on average $n_{\rm ph}$ phonons, causes energy exchange between the two at rate $\Gamma_{\rm phon}$. The net effect is the relaxation of the longitudinal component of the spin magnetization vector $\langle\hat{\sigma}_z\rangle$ towards thermal equilibrium. This process is taken into account through the Lindblad operators:

$$\hat{L}_{\text{phon-}} = \sqrt{\Gamma_{\rm phon}(1 + n_{\rm ph})}\hat{\sigma}_-, \tag{3.12}$$

$$\hat{L}_{\text{phon+}} = \sqrt{\Gamma_{\rm phon} n_{\rm ph}}\hat{\sigma}_+. \tag{3.13}$$

- **Homogeneous broadening:** fluctuations of the magnetic environment of the spin over typical evolution timescales are at the origin of a decoherence effect called homogeneous broadening. Fluctuating magnetic fields cause a dynamical variation of the resonance frequency of the spin, leading it to dephase with a rate $\Gamma_2 = 1/T_2$, affecting the decay of transverse components $\langle\hat{\sigma}_{x,y}\rangle$ of the magnetization vector. In our system this effect is due to fluctuating nearby electronic or nuclear spins, and is described through the Lindblad operator:

$$\hat{L}_2 = \sqrt{\frac{\Gamma_2}{2}}\hat{\sigma}_z. \tag{3.14}$$

- **Resonator dissipation:** the resonator exchanges energy with uncontrolled internal degrees of freedom at rate κ_{int} and with an external transmission line at rate κ_{ext}. This process is described through the Lindblad operators:

$$\hat{L}_{\text{phot-}} = \sqrt{\kappa(1+n_{\text{th}})}\hat{a}, \tag{3.15}$$

$$\hat{L}_{\text{phot+}} = \sqrt{\kappa n_{\text{th}}}\hat{a}^\dagger, \tag{3.16}$$

  where n_{th} is the mean number of excitation of the coupled photon bath.

Master equation

In presence of loss channels describing the coupling with the environment, the reduced dynamics of the system is determined by a master equation in the Lindblad form, namely:

$$\dot{\hat{\rho}} = \hat{\mathcal{L}}(\hat{\rho}) = \frac{1}{i\hbar}[\hat{H},\hat{\rho}] + \sum_i \mathcal{D}_{\hat{L}_i}(\hat{\rho}) \tag{3.17}$$

where the Lindblad super-operators $\mathcal{D}_{\hat{L}_i}$ have explicit action on the density matrix given by:

$$\mathcal{D}_{\hat{L}_i}(\hat{\rho}) = \hat{L}_i\hat{\rho}\hat{L}_i^\dagger - \frac{1}{2}\left\{\hat{L}_i^\dagger\hat{L}_i,\hat{\rho}\right\} \tag{3.18}$$

and the $\hat{L}_i$ operators are the ones listed above.

Adiabatic elimination and Purcell effect

In this section, we perform adiabatic elimination of the resonator degrees of freedom, in order to obtain a master equation for the reduced spin density matrix. Adiabatic elimination will also turn to be useful for the treatment of the single microwave photon detector, a step-by-step derivation is reported in appendix C.

If $\kappa \gg g_0, \Gamma_{\text{phon}}, \Gamma_2$, the degrees of freedom of the resonator evolve on a much shorter timescale than that of spin-resonator interaction and spin-environment interaction. One can thus consider the state of the intra-resonator field to have reached its stationary value over these slow timescales. If no drive is applied the intra-resonator field is exponentially damped towards the vacuum, thus, any field emitted by the spin is dissipated before any back-interaction can occur. This evolution, induced by the coupling of the spin with the resonator, effectively increases the spin radiative relaxation rate producing an effect known as Purcell effect.

Formally, adiabatic elimination is achieved by expanding the system density matrix $\hat{\rho}$ in terms of the low-photons intra-resonator field states $\{\delta^{m+n} |m\rangle \langle n|\}_{m+n\leq 2}$, with $\delta \sim g_0/\kappa$. Solving the equations of motion for $\hat{\rho}_{mn}$, plugging them back in the expression of $\hat{\rho}$, and finally tracing over the field degrees of freedom leads to the dynamics of the reduced spin system. The master equation obtained after adiabatic elimination reads:

$$\dot{\hat{\rho}}_{\rm s} = \frac{1}{i\hbar}[\hat{H}_{\rm s}, \hat{\rho}_{\rm s}] + \mathcal{D}_{\hat{P}}(\hat{\rho}_{\rm s}) + \sum_i \mathcal{D}_{\hat{L}_i}(\hat{\rho}_{\rm s}), \tag{3.19}$$

where $\hat{H}_{\rm s} = \langle 0| \hat{H} |0\rangle$ is the reduced Hamiltonian, and:

$$\hat{P} = \sqrt{\Gamma_{\rm p}(\Delta)}\hat{\sigma}_-, \tag{3.20}$$

$$\Gamma_{\rm p}(\Delta) = \frac{\kappa g_0^2}{\left(\frac{\kappa}{2}\right)^2 + \Delta^2}. \tag{3.21}$$

where $\Delta = \omega_{\rm s} - \omega_0$. The new Lindbladian term $\mathcal{D}_{\hat{P}}$, is the result of the adiabatic elimination process, it describes the radiative relaxation of the spin through the resonator at rate $\Gamma_{\rm p}$. This enhanced relaxation phenomenon, the Purcell effect, allows for a regime in which radiative relaxation is dominant over non radiative relaxation $\Gamma_{\rm p} \gg \Gamma_{\rm phon}$. In our experiments this regime is attained, we will thus neglect non-radiative spin relaxation channels in the following.

Bloch equations in the drive frame at zero temperature

The evolution of the spin Bloch vector in the displaced frame rotating at the drive frequency, when taking into account the coupled decoherence and dissipation channels, is directly computed using the master equation in the adiabatic approximation Eq. 3.19:

$$\begin{aligned}\frac{d}{dt}\begin{pmatrix}\langle\sigma_x\rangle\\ \langle\sigma_y\rangle\\ \langle\sigma_z\rangle\end{pmatrix} &= \begin{pmatrix}0 & \Delta_{\rm s} & -2ig_0\mathfrak{Im}[\alpha]\\ -\Delta_{\rm s} & 0 & -2ig_0\mathfrak{Re}[\alpha]\\ 2ig_0\mathfrak{Im}[\alpha] & 2ig_0\mathfrak{Re}[\alpha] & 0\end{pmatrix}\begin{pmatrix}\langle\sigma_x\rangle\\ \langle\sigma_y\rangle\\ \langle\sigma_z\rangle\end{pmatrix}\\ &\quad - \frac{1}{2}\begin{pmatrix}\Gamma_{\rm phon}+\Gamma_{\rm p}+2\Gamma_2\\ \Gamma_{\rm phon}+\Gamma_{\rm p}+2\Gamma_2\\ 2\Gamma_{\rm phon}+2\Gamma_{\rm p}\end{pmatrix}\begin{pmatrix}\langle\sigma_x\rangle\\ \langle\sigma_y\rangle\\ \langle\sigma_z\rangle+1\end{pmatrix},\end{aligned} \tag{3.22}$$

where $\Delta_{\rm s} = \omega_{\rm s} - \omega_{\rm d}$. Assuming for simplicity $\alpha = \alpha^*$, the first term describes the rotation of the magnetization vector around the axis $(-2g_0\alpha)\hat{e}_x + \Delta_{\rm s}\hat{e}_z$ at the Rabi frequency:

$$\Omega_{\rm R} = \sqrt{\Delta_{\rm s}^2 + (2g_0\alpha)^2} \tag{3.23}$$

The second term describes the decay of the magnetization components due to coupling with external channels.

Single spin fluorescence signal

Because of the Purcell effect, spin relaxation gives rise to the emission of a flux of photons in the detection line, the fluorescence signal. This can be seen as

follows. Consider the evolution of the spin-cavity system from time t_0 to time t_1. The number of photons emitted in the line is given by:

$$F = \kappa_{\text{ext}} \int_{t_0}^{t_1} \langle \hat{a}^\dagger \hat{a} \rangle dt. \tag{3.24}$$

But, from the master equation 3.17 one finds the following relations:

$$\frac{d}{dt}\langle \frac{\hat{\sigma}_z}{2} \rangle = \frac{1}{2i\hbar}\text{Tr}[\hat{\rho}[\hat{\sigma}_z, \hat{H}]] = -ig_0\langle \hat{a}\hat{\sigma}_+ - \hat{a}^\dagger\hat{\sigma}-\rangle \tag{3.25}$$

$$\frac{d}{dt}\langle \hat{a}^\dagger\hat{a}\rangle = ig_0\langle \hat{a}\hat{\sigma}_+ - \hat{a}^\dagger\hat{\sigma}_-\rangle - \kappa\langle \hat{a}^\dagger\hat{a}\rangle = -\frac{d}{dt}\langle \frac{\hat{\sigma}_z}{2}\rangle - \kappa\langle \hat{a}^\dagger\hat{a}\rangle \tag{3.26}$$

where we assumed no drive, neglected the slow non-radiative spin relaxation channel ($\Gamma_{\text{phon}} \ll \Gamma_{\text{p}}$), and used the commutation relations $[\hat{\sigma}_z, \hat{\sigma}_\pm] = \pm 2\hat{\sigma}_\pm$. Thus, we get that:

$$F = \frac{\kappa_{\text{ext}}}{\kappa}\left[\frac{1}{2}\langle \hat{\sigma}_z\rangle(t_0) - \langle \hat{\sigma}_z\rangle(t_1) - \langle \hat{a}^\dagger\hat{a}\rangle(t_1) - \langle \hat{a}^\dagger\hat{a}\rangle(t_0)\right]. \tag{3.27}$$

This relation expresses the conservation of energy, the photons leaking from the cavity must equal the variation of $\langle \hat{\sigma}_z \rangle$ over the time interval minus the number of photons left in the cavity, up to a multiplicative term $\kappa_{\text{ext}}/\kappa$ due to cavity losses.

Since moreover in the weak coupling limit $\Gamma_{\text{p}} \ll \kappa$, the intra-resonator photon number is small at all times, such that $\langle \hat{a}^\dagger\hat{a}\rangle(t_0) \sim \langle \hat{a}^\dagger\hat{a}\rangle(t_1) \sim 0$. We then get a direct link between the change in longitudinal polarization and the number of fluorescence photons emitted. This allows to rewrite Eq. 3.27 neglecting the second term on the right hand side:

$$F = \kappa_{\text{ext}} \int_{t_0}^{t_1} \langle \hat{a}^\dagger\hat{a}\rangle dt = \frac{\kappa_{\text{ext}}}{\kappa}\frac{\langle \hat{\sigma}_z\rangle(t_0) - \langle \hat{\sigma}_z\rangle(t_1)}{2} \tag{3.28}$$

This result shows that the fluorescence signal is directly proportional to the variation of $\langle \hat{\sigma}_z \rangle$ through the ratio $\kappa_{\text{ext}}/\kappa$, the latter accounting for the part of emitted photons that gets lost in internal losses.

3.3 Spin ensemble coupled to a harmonic oscillator

We have since now considered a single spin coupled to a LC resonator in the weak coupling limit, here we extend this analysis to an ensemble of N spins.

It is well known that when N identical spins are coupled symmetrically to an electromagnetic mode, collective effects appear in the dynamics [33, 34, 35]; for instance, spontaneous relaxation may occur by super-fluorescence, a process in which the spin ensemble emits spontaneously and collectively a strong pulse of radiation (pulsed maser regime). In our case however, the spins are not identical; they have slightly different Larmor frequency because of variations in their local environment (due to strain in the crystal, distribution of nuclear or electron spins, ...). This inhomogeneous broadening is characterized by the FWHM linewidth Γ_2^* of the spin ensemble. For sufficiently large Γ_2^*, the spins are no longer identical; collective relaxation effects are washed out, and spins behave and relax as independent emitters. The criterion for this weak coupling regime is that the so-called cooperativity parameter is:

$$C \equiv \frac{2g_0^2 N}{\kappa\Gamma_2^*} = N\frac{\Gamma_{\text{P}}}{2\Gamma_2^*} \ll 1. \tag{3.29}$$

This is the regime in which all the experiments of this thesis are conducted. In this regime, the dynamics of each individual spin is independent of the dynamics of the other spins, and in particular this also applies to the relaxation. Thus, the results derived in the single-spin case apply by replacing single-spin variables with collective variables:

$$\hat{S}_i \to \hat{S}_i = \sum_n \hat{S}_i^{(n)} \tag{3.30}$$

where $i = x, y, z$. Note that $-N/2 < \langle \hat{S}_i \rangle < N/2$. The output fields can be computed making use of $\langle \hat{S}_i \rangle$.

Field observables in the N spin case

In the single-spin case the adiabatic approximation allows to obtain a direct relation between the average value of the photon number and cavity field and the components $\langle \hat{\sigma}_i \rangle$ of the magnetization vector. Such relations are derived in the appendix, Eqs. C.27 and C.28, in the single-spin case, and keep holding in the case of a N-spin ensemble where decoherence and damping effect are present, as detailed above. In the drive frame one has:

$$\langle \hat{a}^\dagger \hat{a} \rangle(t) = \sum_n \frac{\Gamma_p(\Delta_n)}{\kappa} \frac{\langle 1 + \hat{\sigma}_z^{(n)} \rangle(t)}{2} \tag{3.31}$$

$$\langle \hat{a} \rangle(t) = \sum_n \frac{-ig_0}{\frac{\kappa}{2} + i\Delta_n} \frac{\langle \hat{\sigma}_x^{(n)} - i\hat{\sigma}_y^{(n)} \rangle(t)}{2} e^{-i\Delta_n t} \tag{3.32}$$

where the variable Δ_n denotes the inhomogeneous frequency shift of each spin with respect to the average spin Larmor frequency ω_s.

Note that, while in the N-spins case the number of photons is an additive observable, the evolution of the field amplitude depends on the ensemble frequency inhomogeneity. Thus, unless a particular pulse sequence is employed to get rid of this inhomogeneous broadening, the transversal magnetization quickly decays to zero due to ensemble-average effects:

$$\langle \hat{a} \rangle \approx 0. \tag{3.33}$$

In the following, we will see how a Hahn echo sequence suppresses the inhomogeneous broadening, allowing to recover a non-zero field amplitude.

In the next sections, we derive the electromagnetic signal emitted by a spin ensemble after three different excitation pulses. First, the case of a π-pulse, which causes the emission of a spin fluorescence signal. Second, the case of a $\pi/2$-pulse, which stimulates the emission of a free-induction-decay (FID) signal, exponentially damped due to inhomogeneous broadening. Third, a Hahn echo sequence, which counteracts the effect of inhomogeneous broadening and stimulates the emission of a coherent echo from the spin ensemble.

Model for analytical derivation

Analytical results for computing the signal emitted by a spin ensemble can only be obtained under some approximations that do not necessarily reflect the experimental situation. Nevertheless, these results are interesting because they allow to estimate the dependence of emitted signals from relevant parameters. Exact results can be obtained through numerical simulations.

In the following calculations, we consider an ensemble of N spins in a static magnetic field $\mathbf{B_0}$, we consider each spin to have a Larmor frequency $\omega_s+\Delta$, where the detuning Δ, due to inhomogeneous broadening, has a Lorentzian distribution $f(\Delta)$ of HWHM Γ_2^*:

$$f(\Delta) = \frac{1}{\pi}\frac{\Gamma_2^*}{\Gamma_2^{*2}+\Delta^2}. \tag{3.34}$$

We consider that the spin-resonator system is in the low cooperativity regime $C \ll 1$, and is in the Purcell regime. Moreover, we consider an identical spin-resonator coupling g_0 for all spins. Finally, we assume that the resonator linewidth is larger than the spin inhomogeneous linewidth, $\kappa \gg \Gamma_2^*$. In that limit, ideal control pulses can be applied to the spins (ie, with an identical Rabi angle, and quasi-instantaneous).

Under these approximations all the spins relax with the same Purcell rate $\Gamma_\mathrm{p} = 4g_0^2/\kappa$. In the continuum limit, by replacing the sum over spins with an integral over detunings, Eq.3.31 and 3.32 become:

$$\langle\hat{a}^\dagger\hat{a}\rangle(t) = \frac{\Gamma_p}{\kappa}\left(\frac{N}{2} + \langle\hat{S}_z\rangle(t)\right) \tag{3.35}$$

$$\langle\hat{a}\rangle(t) = \frac{-4ig_0}{\kappa}\langle\hat{S}_-\rangle(0)\int f(\Delta)e^{-i\Delta t}d\Delta \tag{3.36}$$

where $\langle\hat{S}_-\rangle = \langle\hat{S}_x - i\hat{S}_y\rangle/2$.

In the following, the starting condition is the spin ensemble in its ground state, with a polarization $p = 2\langle\hat{S}_\mathrm{z}\rangle/N = -1$, and $\langle\hat{S}_\mathrm{x}\rangle = \langle\hat{S}_\mathrm{y}\rangle = 0$.

Fluorescence

Consider a π-pulse applied to the spin ensemble at $t = 0$. The resulting state (all spins excited) verifies $\langle\hat{S}_\mathrm{z}\rangle(0) = N/2$. From Eq. 3.22, the evolution of $\langle\hat{S}_\mathrm{z}\rangle$ is an exponential decay with rate Γ_P:

$$\langle\hat{S}_\mathrm{z}\rangle(t) = -\frac{N}{2} + Ne^{-\Gamma_\mathrm{P}t}, \tag{3.37}$$

while at any time $\langle\hat{S}_\mathrm{x}\rangle(t) = \langle\hat{S}_\mathrm{y}\rangle(t) = 0$. The signal emitted by the spins is obtained from Eqs.3.31 and 3.32:

$$\langle\hat{a}^\dagger\hat{a}\rangle(t) = \frac{\Gamma_\mathrm{P}}{\kappa}\left(\frac{N}{2} + \langle\hat{S}_z\rangle(t)\right) = \frac{\Gamma_\mathrm{P}N}{\kappa}e^{-\Gamma_\mathrm{P}t} \tag{3.38}$$

$$\langle\hat{a}\rangle(t) = 0 \tag{3.39}$$

The spin ensemble relaxes to the equilibrium state by emitting a stream of photons exponentially decaying at rate Γ_p, the fluorescence signal. A fraction κ_ext of photons leaks from the cavity and can be detected, while the rest is lost into internal cavity losses. These photons are incoherent, as can be seen from the fact that $\langle a\rangle(t) = 0$.

We now estimate the SNR for photon detection of the fluorescence signal, taking into account the imperfect detector, following the discussion in Chapter 2. The number of counts detected are integrated over a time window t_w (with $t_\mathrm{w} \sim T_1$ to maximize the photon counting signal). The number of clicks expected is equal to ηN with $\eta = \eta_\mathrm{c}\eta_\mathrm{d}\eta_\mathrm{int}$, where $\eta_\mathrm{int} = 1 - \mathrm{e}^{-\Gamma_\mathrm{P}t_\mathrm{w}}$ a factor of order unity caused by the finite integration window. Therefore, Eq. 2.111 leads to:

$$\mathrm{SNR}_\mathrm{pc} = \frac{\eta N}{\sqrt{\nu_\mathrm{dc}t_\mathrm{w} + \eta(1-\eta)N}}. \tag{3.40}$$

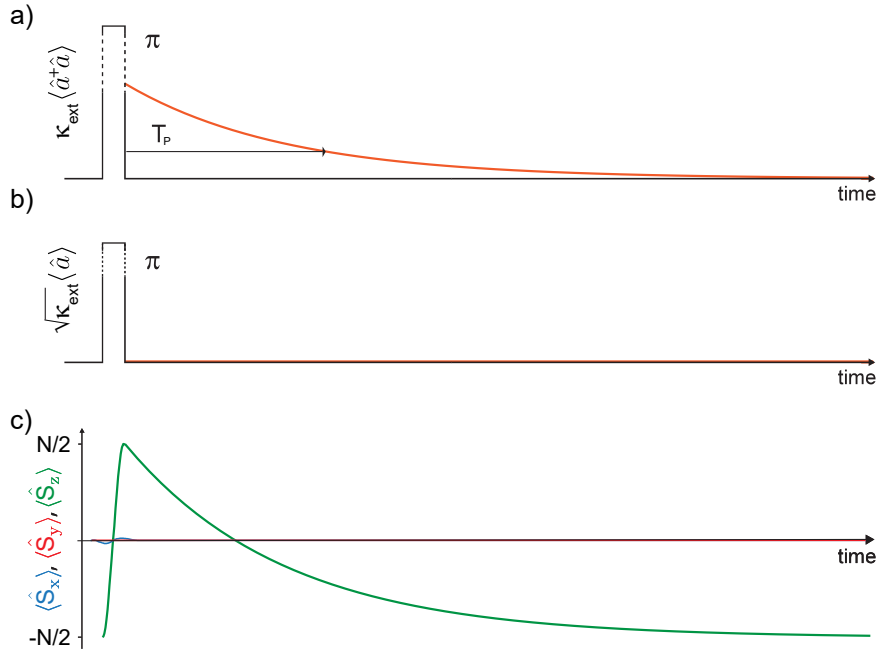

Figure 3.1: **Spin fluorescence emission.** Evolution of average field and spin observables after a π-pulse on the spin ensemble. (a) A flux of photons leaks from the resonator and decays over a characteristic time equal to the spin Purcell relaxation time T_{P}. This is the spin fluorescence signal. (b) The average field amplitude at the output of the resonator is zero. (c) The total spin component $\hat{S}_z$ is flipped and relaxes back to the ground state with characteristic decay time T_{P}.

It is interesting to note that this SNR can in principle become arbitrarily large for an ideal SMPD for which $\nu_{\mathrm{dc}} \sim 0$ and $\eta \sim 1$, even for N approaching 1. This reflects the fact that in the Purcell regime, N spins once excited will emit N photons over a timescale of a few T_1, and that an ideal SMPD will detect them all noiselessly. SMPD detection of spin fluorescence in the Purcell regime thus appears as a particularly promising method for detecting small numbers of spins, which motivates the experimental effort undertaken in this thesis.

Free induction decay

Consider now the evolution of the spin ensemble after a $\pi/2$-pulse along the x direction, as showed in Fig. 3.2. The average total spin values at $t = 0$, after the pulse, are $\langle\hat{S}_x\rangle = 0$, $\langle\hat{S}_y\rangle = N/2$ and $\langle\hat{S}_z\rangle = 0$. We have:

$$\langle\hat{S}_{\mathrm{z}}\rangle(t) = -\frac{N}{2} + \left(\langle\hat{S}_{\mathrm{z}}\rangle(0) + \frac{N}{2}\right) e^{-\Gamma_{\mathrm{P}} t}, \tag{3.41}$$

$$\langle\hat{S}_-\rangle(t) = \langle\hat{S}_-\rangle(0) e^{-\Gamma_2^* t}. \tag{3.42}$$

The transverse spin component $\langle\hat{S}_-\rangle$ is exponentially damped at rate Γ_2^* due to the inhomogeneous distribution of spin frequencies, while the longitudinal spin component is damped at rate $\Gamma_{\mathrm{P}} \gg \Gamma_2^*$ due to Purcell relaxation.

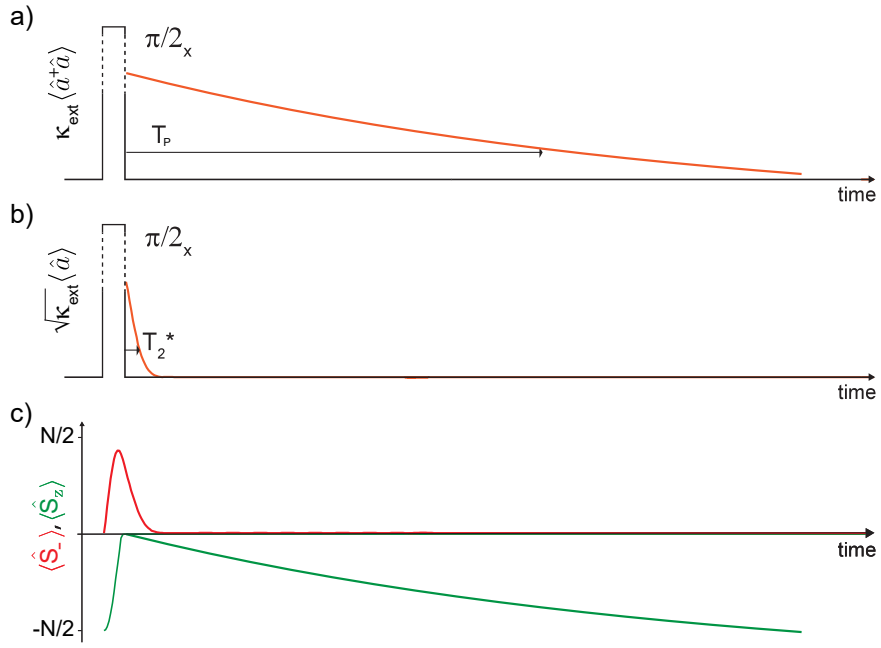

Figure 3.2: **Free induction decay.** Evolution of average field and spin observables after a $\pi/2$-pulse on the spin ensemble. (a) A flux of fluorescence photons leaks from the resonator and vanishes with characteristic T_{P}. (b) A non-zero average field amplitude is emitted at the output of the resonator, constituting the FID signal emitted by the spin precessing vector precessing in the equatorial plane. This signal decays over a timescale $T_2^* \ll T_{\mathrm{P}}$. (c) Evolution of the average $\hat{S}_z$ and $\hat{S}_-$ spin components.

The microwave field generated in the resonator by the spin dynamics is:

$$\langle \hat{a}^\dagger \hat{a} \rangle(t) = \frac{\Gamma_{\mathrm{p}} N}{2\kappa} e^{-\Gamma_{\mathrm{P}} t} \tag{3.43}$$

$$\langle \hat{a} \rangle(t) = -\frac{g_0 N}{2\kappa} e^{-\Gamma_2^* t} \tag{3.44}$$

The term $\langle \hat{a}^\dagger \hat{a} \rangle$ describes the fluorescence due to Purcell relaxation, occurring on a timescale $T_{\mathrm{P}} = \Gamma_{\mathrm{P}}^{-1}$, as seen above. The field $\langle \hat{a} \rangle$ describes an oscillating signal decaying exponentially with time $T_2^* = \Gamma_2^{*-1} \ll T_{\mathrm{p}}$, the so-called free-induction decay.

Hahn echo

Finally, we show how the exponential suppression of the FID signal can be counteracted with the Hahn echo pulse sequence [36]; showed in Fig.3.3.

A $\pi/2$ pulse is applied to the spins along the x axis, such that a state with $\langle \hat{S}_{\mathrm{y}} \rangle = N/2$ is prepared, which then decays in T_2^* by FID. After a delay $\tau \gg T_2^*$, a π pulse is applied along the y axis, reversing the spin evolution: as a result, after another waiting time τ, the transverse total spin component recovers to its initial value, generating a signal in the detection circuit known as "spin-echo". This echo signal decays as a function of 2τ, with time constant T_2 due to spin decoherence associated to homogeneous broadening.

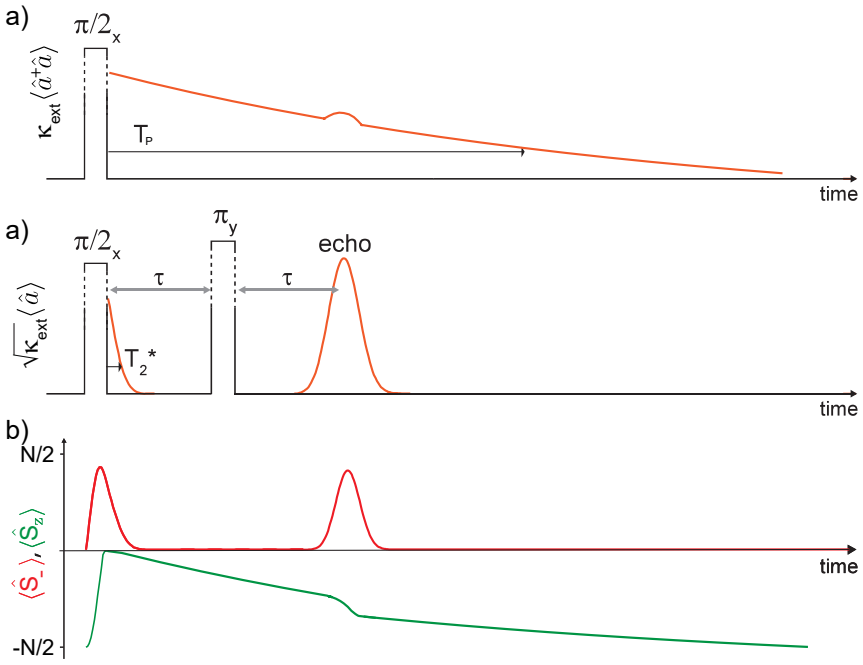

Figure 3.3: **Hahn echo.** Evolution of average field and spin observables after a Hahn-echo sequence on the spin ensemble. (a) A flux of fluorescence photons leaks from the resonator and vanishes with characteristic T_{P}. On top of the fluorescence a weaker photon signal is emitted in correspondence of the spin echo. (b) The first $\pi/2$ pulse stimulates the emission of a FID signal, appearing as a non-zero field amplitude decaying over T_2^*. Application of a π-pulse after a time τ allows to refocus the spin ensemble, producing a coherent echo signal at time 2τ. (c) Evolution of the average $\hat{S}_z$ and $\hat{S}_-$ spin components. At echo time 2τ refocusing of the average transversal spin component $\hat{S}_-$ is at the origin of the echo signal. Moreover, photons are emitted causing a drop in the average longitudinal spin component $\hat{S}_z$.

Taking the origin of times when the echo emission happens, the first $\pi/2$ pulse about the x-axis at $t = -2\tau$, takes each spin to the state $\langle \hat{S}_-^{(j)}(-2\tau)\rangle = -i/4$, and after the refocusing π-pulse, the free evolution will bring the spin back in phase at $t = 0$:

$$\langle \hat{S}_-^{(j)}\rangle(t) = -\frac{i}{4} e^{-i\Delta_j t}. \tag{3.45}$$

In the continuous limit, integrating on detunings leads to:

$$\langle \hat{S}_-\rangle(t) = -\frac{iN}{4} e^{-\Gamma_2^*|t|}, \tag{3.46}$$

such that the intra-resonator field is:

$$\langle \hat{a}\rangle(t) = -\frac{g_0 N}{\kappa} e^{-\Gamma_2^*|t|}. \tag{3.47}$$

The field leaving the resonator is $\langle \hat{a}_{\mathrm{out}}\rangle(t) = \sqrt{\kappa_{\mathrm{ext}}}\langle \hat{a}\rangle(t)$, and assuming that $\langle \hat{a}(t)\rangle$ is real-valued in our calculations the mean signal is carried by the quadrature $\hat{X}_{\mathrm{out}} = (\hat{a}_{\mathrm{out}} + \hat{a}_{\mathrm{out}}^\dagger)/2$.

We now define single modes of the propagating field using a real-valued normalized mode function $u(t)$:

$$\hat{a}_{\text{out}} = \int \hat{a}_{\text{out}}(t)u(t)dt \tag{3.48}$$

$$\hat{X}_{\text{out}} = \int \hat{X}_{\text{out}}(t)u(t)dt. \tag{3.49}$$

The optimal choice for $u(t)$ is the one that maximizes the weighted signal, in an experiment it may be the measured shape of the emitted pulse averaged over many experimental runs. Since we are interested in analytical estimates, we choose:

$$u(t) = \frac{\langle \hat{X}_{\text{out}} \rangle(t)}{\langle \hat{X}_{\text{out}} \rangle}. \tag{3.50}$$

The correct normalization $\int |u(t)|^2 dt = 1$ is satisfied if:

$$\langle \hat{X}_{\text{out}} \rangle^2 = \int \langle \hat{X}_{\text{out}} \rangle(t)^2 dt = \kappa_{\text{ext}} \frac{g_0^2 N^2}{\kappa^2 \Gamma_2^*} \tag{3.51}$$

which leads to an integrated echo signal:

$$\langle \hat{X}_{\text{out}} \rangle = N \sqrt{\frac{\kappa_{\text{ext}}}{\kappa} \frac{\Gamma_{\text{P}}}{2\Gamma_2^*}}. \tag{3.52}$$

The Hahn echo is with good approximation a single-mode coherent state of amplitude $\text{Re}[\alpha] = \langle \hat{X}_{\text{out}} \rangle$ (assumed real since the known phase reference is set by the exciting pulse). The SNRs for quadrature and photon detection are thus readily calculated from Eqs. 2.82 and 2.84, with a collection efficiency $\eta_{\text{c}} = \kappa_{\text{ext}}/\kappa$:

$$\text{SNR}_{\text{qd}} = 2N \sqrt{\eta_{\text{c}} \frac{\Gamma_{\text{P}}}{2\Gamma_2^*}}, \tag{3.53}$$

$$\text{SNR}_{\text{pc}} = N \sqrt{\eta_{\text{d}} \eta_{\text{c}} \frac{\Gamma_{\text{P}}}{2\Gamma_2^*}}. \tag{3.54}$$

In contrast with the fluorescence detection (see previous paragraph), the SNR of echo detection is always lower than $2N\sqrt{\Gamma_P/2\Gamma_2^*}$ for an ideal quadrature detection, and $N\sqrt{\Gamma_P/2\Gamma_2^*}$ for an ideal photon counter. This is due to vacuum fluctuations, or equivalently shot noise.

Fluorescence detection versus Hahn-echo detection of a spin ensemble

A number of interesting aspects are worth underlining at this point, in the comparison between fluorescence and Hahn echo signals.

First, we note that the echo intensity (i.e., mean photon number $\langle \hat{X}_{\text{out}} \rangle^2$) scales like N^2 (see Eq.3.51), in contrast with the number of photons emitted by fluorescence (Eq.3.38), which scales like N. This reflects the fact that the spin-echo results from the constructive interference of the fields radiated by all spins when their dipole comes back in phase at the echo time, and is therefore in essence a super-radiant process in the sense of Dicke [33]. In contrast, fluorescence is emitted by each spin independently from the others, and is therefore incoherent.

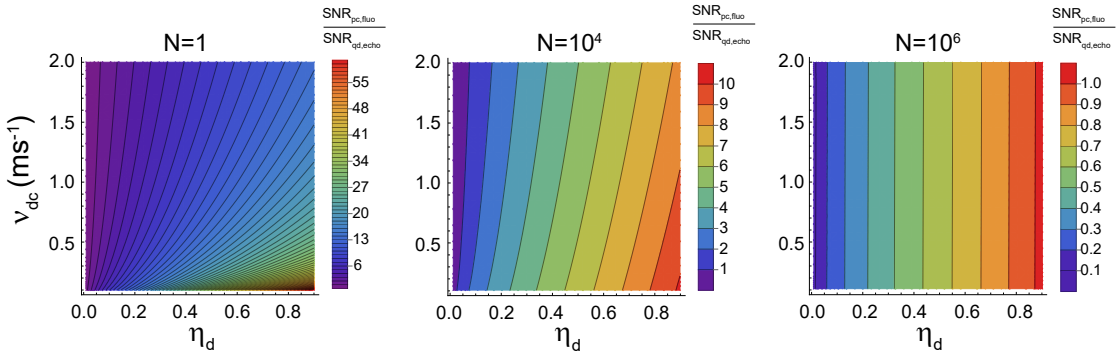

Figure 3.4: **Fluorescence versus echo detection.** Ratio of SNRs in the case of fluorescence photo-detection and echo quadrature detection, for different numbers N of spins, and realistic experimental parameters. The sensitivity favours fluorescence photo-detection at low number of spins $N \leq 10^5$ while at large $N > 10^5$ echo quadrature detection has better performances.

Another aspect noteworthy is that spin echoes contain much less photons than fluorescence. This is expected, since N excited spins can produce at most N photons; in that sense the integrated fluorescence signal contains as much signal as possible from a spin ensemble. It is not immediately visible that the echo intensity $\langle X_{\text{out}} \rangle^2 = N^2 \eta_c \Gamma_P / (2\Gamma_2^*)$ is much lower than N. It is indeed the case, because of the low cooperativity condition Eq. 3.29 which states that $N\Gamma_P/(2\Gamma_2^*) \ll 1$. In the vocabulary of magnetic resonance, this condition is also equivalent to negligible radiation damping.

Finally, we wish to compare the SNRs for quadrature detection of a Hahn-echo and photon detection of the fluorescence signal. Because of the different scaling of the number of photons emitted in an echo and in fluorescence, one can expect that in the limit of large N, echo detection gives a better SNR than fluorescence; however, in the limit of low spin numbers, fluorescence may, for certain parameters, become more advantageous. This intuition is confirmed by the figure 3.4, which shows $SNR_{\text{pc,fluo}}/SNR_{\text{qd,echo}}$ as a function of η_{d} and ν_{dc} for different N, using our experimental values of $\kappa = 4.23 \times 10^6\,\text{s}^{-1}, \Gamma_P = 3.33\,\text{s}^{-1}, \Gamma_2^* \simeq \kappa$ (see experimental chapters below). We see that for large $N \sim 10^5$ quadrature echo detection is more sensitive, while at low number of spins $N < 10^3$ photon counting of fluorescence signal becomes more adapted for spin detection for a large range of parameters η_{d} and ν_{dc}.

3.4 Simulating spin dynamics

In this work we will often make use of numerical simulations to reproduce and validate the measurements performed on the spin ensemble. For this, we employ a simulation code, which, starting from the master equation 3.19, computes the spin ensemble dynamics and extract the components of the magnetisation vector. The software allows to initialise the density matrix of the system based on the spin relaxation times, and the experimental repetition time. It also includes the back-action of the spin-generated field on the spin dynamics, i.e., radiation damping. Finally, the software can take into account inhomogeneity in the spin-photon coupling g_0 by simulating multiple experiments with different coupling values

and convoluting the obtained result with the computed $\rho(g_0)$ distribution.

Part II

Experiment

Chapter 4

Spin device

The experiment at the heart of this thesis consists in the measurement of the fluorescence signal of an ensemble of electron spins by means of a microwave photon counter.

The first part of this chapter is devoted to the description of the spin device. In section 4.1 we give a short introduction to bismuth donors in silicon, presenting the elements useful to understand the results of this work, and the characteristics of the chip employed in the experiment. In section 4.2 we describe the design of the superconducting LC resonator used to couple the spin to the field, show relevant simulations of the field profile and coupling constant and detail the fabrication process.

In the second part, section 4.3, we characterize the spin ensemble. We measure the spin relaxation time $T_1 \simeq T_P$, estimate the average spin-photon coupling $\bar{g_0}$ and its standard deviation σ_{g_0} and finally estimate the spectral density of spins ρ_{spin}. The latter will be used in chapter 6 to infer the total efficiency of the photodetection process.

4.1 Bismuth donor spins in silicon

Physical description

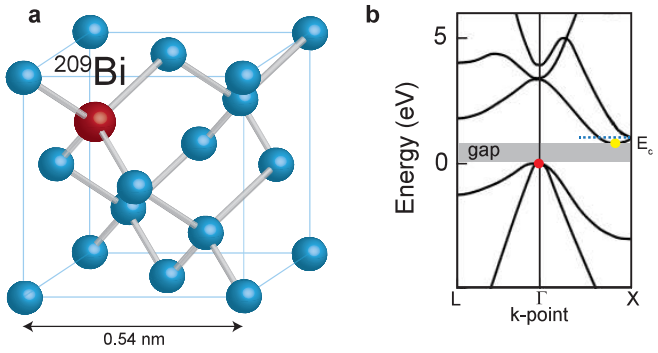

Figure 4.1: **Bismuth donor in silicon.** (a) A single bismuth substitutional impurity in silicon diamond lattice. (b) Silicon energy band diagram; valence band maximum and conduction band minimum highlighted in red and yellow, respectively.

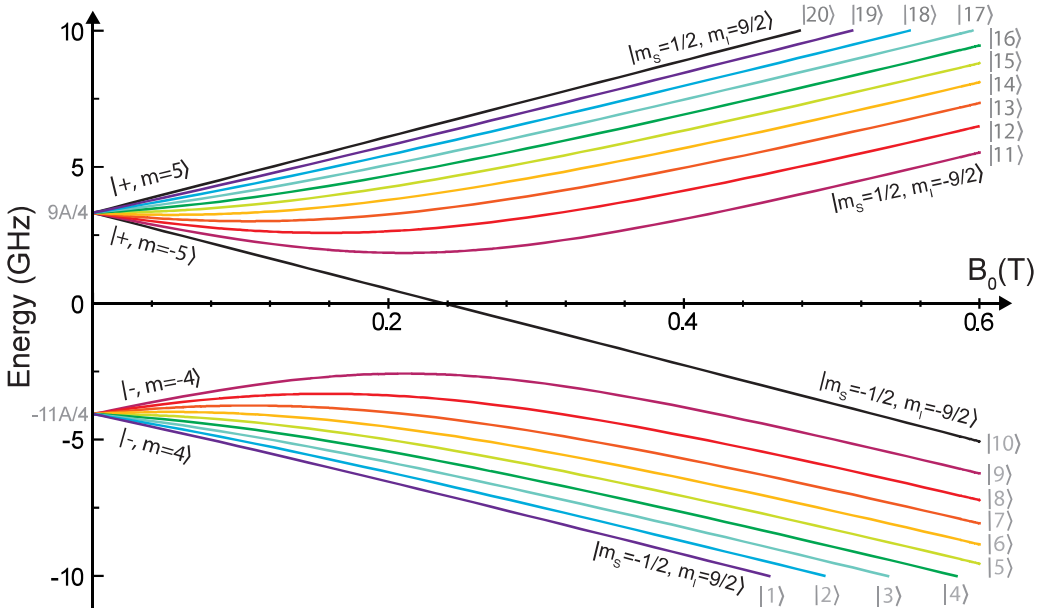

Figure 4.2: **Bismuth energy spectrum.** Energy-levels computed from the diagonalisation of the Si:Bi Hamiltonian as a function of B_0 (Eq.4.2). The coupled energy-levels $E_m^{\pm}$ are color-coded from purple to red, the uncoupled energy-levels are in black. Figure adapted from [37, 38]

Silicon is an element of the IV-group crystallizing in a diamond structure, where each silicon atom is at the center of a tetrahedron whose vertices are occupied by its four first neighbours to which is covalently bound (see Fig.4.1(a)). The band structure represented in Fig.4.1(b), shows an indirect band-gap of energy $E_g = 1.1\,\text{eV}$ at 300 K.

A donor is a group-V impurity substituting a silicon atom in the lattice. Four of its valence electrons form covalent bonds with the four neighbouring silicon atoms, keeping almost unaltered the local geometry (see Fig.4.1). The fifth electron is either bound to the donor nucleus Coulombic potential ('neutral donor') or ionized to the conduction band. In this thesis, we work with bismuth donors. Their ionization energy is E_D =71 meV. Given the concentration of bismuth donors in our sample $\approx 10^{16}\,\text{cm}^{-3}$ and an ionization energy of 71 meV, bismuth donors are found in their neutral state for temperatures up to 40 K. In our experiment, which is performed at T <20 mK, all donors are expected to be in their neutral state.

Spin Hamiltonian and energy levels

In this thesis, we are interested in the electron spin degree of freedom $S = 1/2$ of the neutral bismuth donor. In this section we provide a brief qualitative description of their Hamiltonian and energy states; much more details can be found in [38] for instance.

This electron spin is coupled by the contact hyperfine interaction with a strength $A/2\pi = 1.4754\,\text{GHz}$ to the nuclear spin $I = 9/2$ of the bismuth atom. In presence of a static magnetic field $\boldsymbol{B}_0 = B_0\boldsymbol{e}_z$ applied along z, the spin Hamiltonian reads [39]:

$$\hat{H}/\hbar = \boldsymbol{B}_0 \cdot \left(\gamma_{\mathrm{e}} \hat{\boldsymbol{S}} \otimes \mathbb{1} - \gamma_{\mathrm{n}} \mathbb{1} \otimes \hat{\boldsymbol{I}}\right) + A \hat{\boldsymbol{S}} \cdot \hat{\boldsymbol{I}} = \tag{4.1}$$

$$A \hat{S}_z \hat{I}_z + \frac{A}{2}(\hat{S}_+ \hat{I}_- + \hat{S}_- \hat{I}_+) + \omega_{\mathrm{s}}(\hat{S}_z - \delta \hat{I}_z), \tag{4.2}$$

where $\gamma_{\mathrm{e}}/2\pi = 27.997\,\mathrm{GHz/T}$ and $\gamma_{\mathrm{n}}/2\pi = 6.962\,\mathrm{MHz/T}$ are the electronic and nuclear gyromagnetic ratios, respectively, and we defined $\omega_{\mathrm{s}} = B_0\gamma_e$ and $\delta = \gamma_n/\gamma_e = 10^{-3}$. The first term describes the Zeeman effect and the second the hyperfine coupling. Due to this hyperfine term, the energy eigenstates are hybridized electro-nuclear states where the hybridization degree depends on the relative magnitude of the Zeeman and hyperfine terms. The computed spectrum is shown in Fig. 4.2.

Because the operator $S_z + I_z$ commutes with the Hamiltonian, its eigenvalue m (which varies between -5 and $+5$) is a good quantum number that can be used to label the states. At $B = 0$, the eigenstates are grouped in two degenerate multiplets of respectively 9 and 11 states, corresponding to the total spin eigenvalue $F \in \{4, 5\}$, and separated by $5A = 2\pi \times 7.377\,\mathrm{GHz}$. States from the ground (excited) multiplet are labeled as $-$ $(+)$. In the experiments performed in this thesis we will address the spin transition $|-,-4\rangle \rightarrow |+,-5\rangle$. The associated transition-matrix element can be computed :

$$\langle +,-5 \left| \hat{S}_x \right| -,-4\rangle = 0.47. \tag{4.3}$$

In the experiment we will treat this transition as an effective spin $1/2$, a good approximation since other transitions are not within the resonator bandwidth.

Sensitivity to strain

Bismuth donor spins are sensitive to mechanical strain in the substrate. Indeed, strain affects the donor orbital wavefunction, which in turn impacts the value of the hyperfine coupling constant A. This effect was quantified in recent work [40] by direct measurement of the bismuth donor ESR spectrum under the application of strain; a sensitivity $\partial A/\partial\epsilon = 28\,\mathrm{GHz/strain}$ was measured, where ϵ is the hydrostatic strain.

Coherence properties

We now give a brief qualitative account of bismuth donor spin decoherence at millikelvin temperatures.

Non-radiative relaxation The only measurement of bismuth non-radiative energy relaxation at temperatures compared to the ones of our experiment has been reported by Bienfait et al. [2]. In their work they measure $\Gamma_1^{-1} = 1500\,\mathrm{s}$ at $20\,\mathrm{mK}$ using a superconducting resonator similar to the one of our experiments. In our experiment, performed in similar conditions, we take the same estimation of the spin non-radiative relaxation rate $\Gamma_{\mathrm{non-rad}} = 1/1500\,s^{-1}$. As we will see, the Purcell relaxation time is orders of magnitude shorter, and is therefore the only relevant spin relaxation mechanism in our experimental conditions.

Coherence time In Chapter 2, spin decoherence was modelled by a rate Γ_2, in the framework of the Bloch equations, which predict an exponential damping of the transverse spin operator. This description is only phenomenological, and does not apply well to the dominant decoherence mechanisms for spins in solids, which is spectral diffusion caused by changes in the spin magnetic environment. In natural silicon, the dominant spectral diffusion mechanism is due to ^{29}Si nuclear spins, which are present at a 4.7% abundance, and it limits the spin coherence time T_2 to $\sim 600 - 800\mu$s [39]. In our experiment, we use a silicon substrate that has been isotopically enriched in the nuclear-spin-free ^{28}Si isotope, so that nuclear-spin spectral diffusion is suppressed. In such samples, the electron spin coherence time can be very long, up to 1 s [41]. However, in our device, the spins are close to the silicon/silicon oxide interface, where dangling bonds cause additional decoherence [42] with a typical $T_2 \sim 2 - 8$ ms.

Bismuth-implanted sample

The chip measured in this work consists in a silicon substrate implanted with bismuth atoms (Fig. 4.3a). The implantation depth is about 100 nm with a peak density of $\sim 8 \times 10^{16}$ cm^{-3}, as shown in fig. 4.3b. An external in-plane magnetic field B_0 is applied to lift the degeneracy of the spin states, as explained above. Figure 4.3c shows the computed transition frequency of several EPR-allowed transitions as a function of B_0, at low magnetic fields. The $|+,-5\rangle \leftrightarrow |-,-4\rangle$ transition crosses the spin resonator frequency $\omega_0/2\pi = 6.95$ GHz (see below) around $B_0 = 17$ mT.

4.2 Superconducting lumped LC resonator

In this section we present the superconducting LC resonator that inductively couples to the bismuth electron spins.

Design

Reaching the Purcell regime requires a sufficiently high spin-photon coupling constant g_0, and a low energy loss rate κ.

The resonator design is based on the previous work of Bienfait et al. [2].

Geometry

The resonator design is shown in Fig. 4.4a. It is a millimeter-sized lumped LC resonator formed by an interdigitated capacitor, shunted with a $1\,\mu$m-wide, $450\,\mu$m-long inductive wire, patterned on top of the silicon sample by evaporation of a 50 nm-thick aluminum film. The resonator interacts with implanted bismuth donors through the ac magnetic field B_1 generated in the inductor, as shown in Figs. 4.3d-e.

Coupling to the measurement line

The total resonator damping rate $\kappa = \kappa_{\text{int}} + \kappa_{\text{ext}}$ has contribution from unwanted internal losses (κ_{int}) and losses due to the coupling to the measurement line (κ_{ext}).

In order to suppress radiation losses, the sample is enclosed in a leak-tight copper box (Fig. 4.4b), whose modes lay well above the LC resonator frequency.

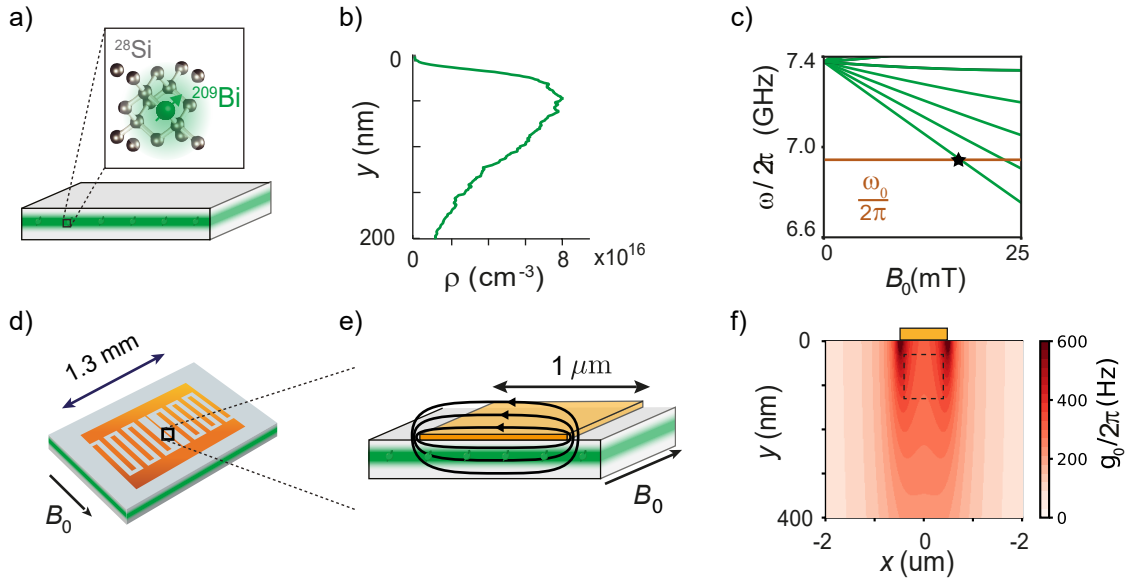

Figure 4.3: **Spin chip.** (a) Bismuth donors are implanted below the surface of an silicon chip isotopically-enriched in ^{28}Si. The implantation profile (b) is spread over the first few hundred nanometers, with a peak density of $\approx 8 \times 10^{16}\,\mathrm{cm}^{-3}$. (c) Transition frequencies between bismuth spin levels as a function of the applied external magnetic field B_0, used to tune a spin ensemble transition in resonance with a microwave resonator patterned on the chip surface (d). (e) Illustration of the magnetic field generated by microwave radiation oscillating in the resonator, the field is perpendicular to B_0 and used to drive and detect the spin magnetic moment. (f) Simulation of the spin-resonator coupling constant g_0 for a $1\,\mu$m-wide wire at position $x = 0$ (shown schematically as an orange rectangle), as a function of the spin location with respect to the sample surface $y = 0$. The dashed rectangle shows the approximate location of the spins measured throughout this thesis.

The choice of copper with respect to less lossy superconducting boxes is due to the necessity of applying external magnetic fields to tune the spin into resonance with the LC resonator. The coupling rate to the measurement line κ_{ext} is set by the value of the coupling capacitance to the external lines. This capacitance is set by an antenna that is entering the box through a drilled hole (see Fig. 4.4b). The antenna is soldered to the inner conductor of a SMA connector screwed in the cavity wall. The insertion-depth of the SMA in the box wall determines the length of the antenna inside the box, and therefore κ_{ext}.

Resonant frequency

The resonator frequency is designed to be $\omega_0/2\pi = 7.0\,\mathrm{GHz}$, not far from the Si:Bi zero-field splitting of about $7.4\,\mathrm{GHz}$, and within the tunability range of the microwave photon detector.

Electromagnetic simulations

The resonator frequency $\omega_0/2\pi \simeq 7\,\mathrm{GHz}$ and coupling to the measurement line $\kappa_{\mathrm{ext}} \simeq 1 \times 10^6\,\mathrm{s}^{-1}$ via the copper box and the antenna are designed using 3D elec-

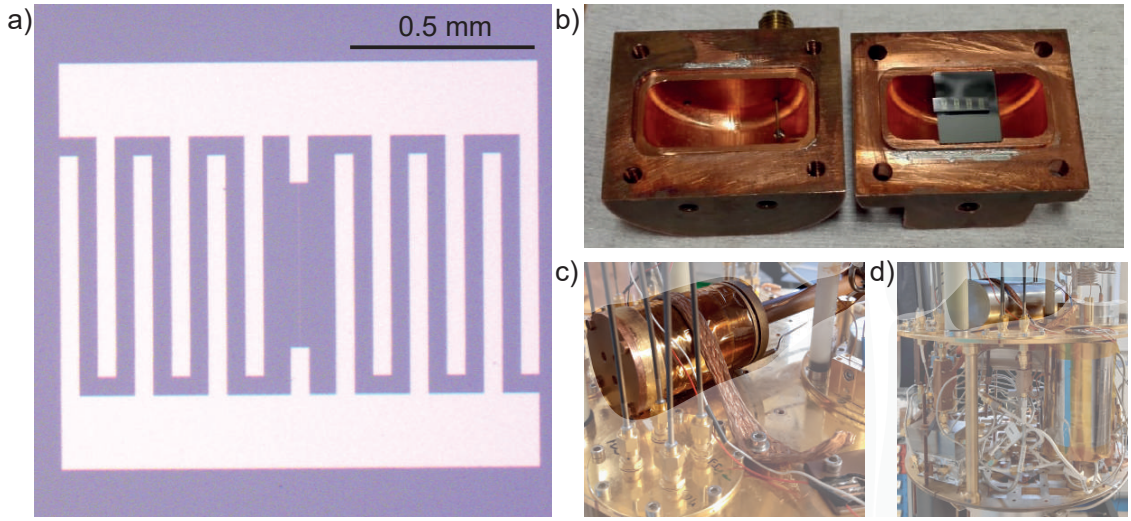

Figure 4.4: **Spin box.** (a) Optical image of the aluminum resonator patterned on the surface of the silicon chip, the $1\,\mu m$-long inductor wire shunting the two capacitor is barely visible in the center of the resonator. (b) Copper box containing the patterned spin chip. Coupled to the external line used to inject field and collect signal is done via a tunable antenna protruding into the cavity (left image). (c) The copper cavity hosting the chip is inserted in a cylindrical coil used to generate the in-plane magnetic field B_0, everything is then inserted in a cryoperm shield (d) in order to minimize magnetic interferences from external sources.

tromagnetic simulations realized with CST microwave studio and ANSYS HFSS (see Fig. 4.5).

Always using the simulations, the resonator impedance $Z_0 = 45\Omega$ is obtained by computing the current flowing in the circuit for fixed eigenmode energy. The vacuum fluctuations of the current flowing in the wire are then computed using this value (see paragraph 2.2). Using COMSOL simulations, we can then compute the spatial profile of $|\mathrm{B}_{\mathrm{zpf}}|$, the vacuum fluctuations of B_1 generated by this current around the wire. And using Eq. 3.8, the spatial profile of the spin-resonator coupling constant g_0 is finally obtained (see Fig. 4.3f). Below the wire, $g_0/2\pi \simeq 300\,\mathrm{Hz}$ is predicted.

Fabrication

The whole circuit is fabricated out of a $50\,\mathrm{nm}$-thick aluminum film, evaporated on the implanted silicon substrate through a PMMA resist mask patterned using electron beam lithography. A subsequent lift-off step allows to remove the metal in excess. A scaning electron microscopy image of the resonator is showed in Fig. 4.4a, the fabrication steps are:

1. Substrate cleaning: acetone/isopropanol/water + ultrasonic bath
2. Resist spinning:
   a) dehydratation bake (7'/156°C)
   b) MAA(8.5) spinning (5s@4000rpm/60s@6000rpm/2s@8000rpm)
   c) bake (3'/156°C)

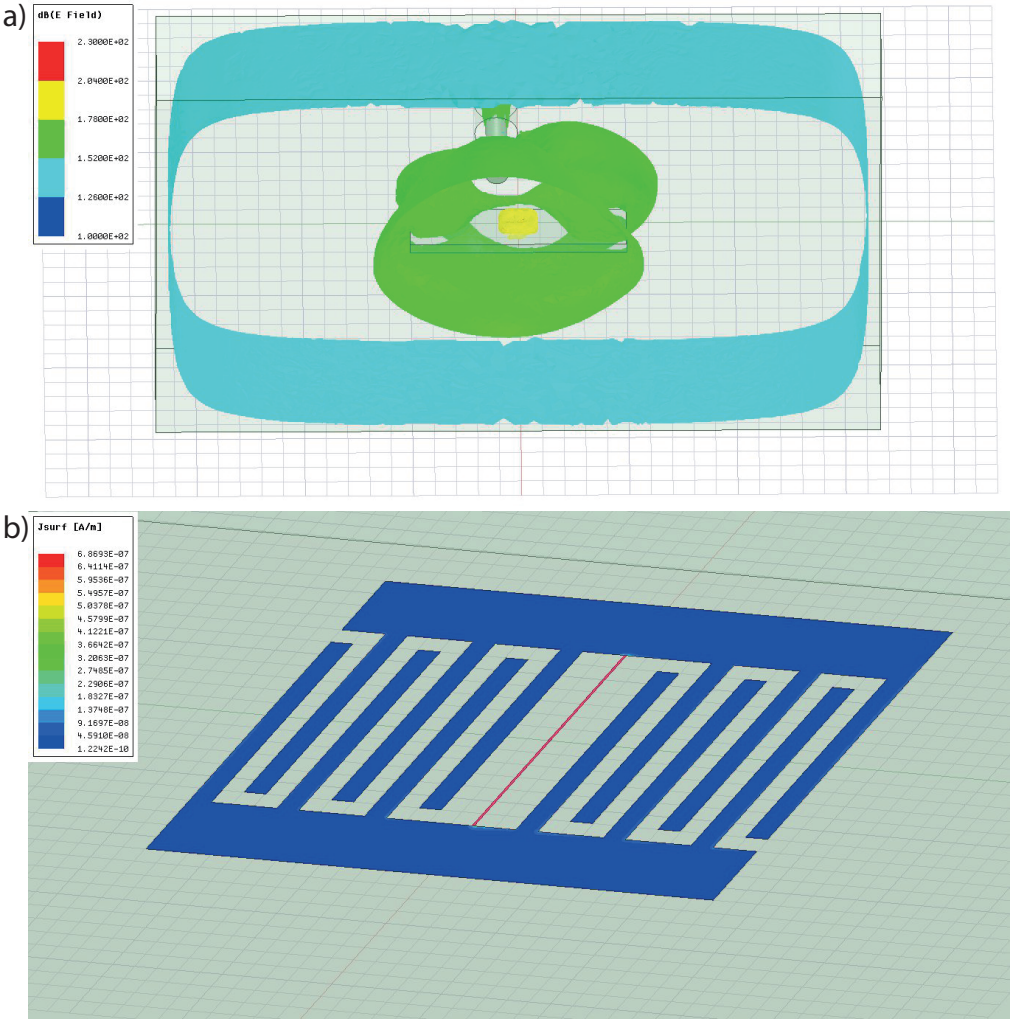

Figure 4.5: **Spin chip simulations.** (a) HFSS electromagnetic simulation of the electric field associated to the mode of the aluminum resonator, the outermost boundary denotes the copper box holding the sample chip (in the middle where the field is more intense). (b) Electromagnetic simulation of the absolute value of the surface current across the resonator, when the resonant mode is excited with 1 Joule of energy.

d) PMMA A3 spinning (5s@4000rpm/60s@5000rpm/2s@8000rpm)

e) bake (15'/175°C)

3. Electron-beam lithography (Raith):

a) Voltage: 10 kV

b) Options: meander mode

c) Pads and fingers: aperture(60 μm)/dose(160 μC cm^{-2})/wfield(500 μm)

d) Wire: aperture(10 μm)/dose(140 μC cm^{-2})/wfield(500 μm)

e) : develop MIBK:IPA 1:3 for 55 s. Rince in IPA for 10 s.

f) Oxygen plasma cleaning: power(80W)/pressure(0.2 mbar)/30 s

4. Aluminum evaporation

a) Aluminum: 50 nm @ 1nm/s

b) Lift-off: ultrasonication(15 s)/acetone(2 h)/acetone(50°C/1 h + 70°C/10').

4.3 ESR spectroscopy of bismuth donors in silicon

In what follows we present the results of ESR spectroscopy based on Hahn-echo detection for the bismuth-implanted chip introduced in the previous sections.

Sample mounting

The bismuth-implanted silicon chip on which surface the superconducting LC resonator has been patterned, is inserted in a 3D copper cavity (Fig. 4.4b). This cavity is then positioned inside a superconducting coil (Fig. 4.4c) that will be used to generate the static magnetic field $\mathbf{B}_0$, parallel to the superconducting inductor wire, in order to tune the spin resonant frequency. The coil is inserted in a 1-mm-thick cryoperm magnetic shield (Fig. 4.4d) to minimize stray magnetic field which may introduce vortices in the film during cool down. The whole packet is then mounted at the 20 mK stage of a dilution refrigerator.

Experimental setup

In this thesis, both ESR spectroscopy and photon-counting are performed on the same sample within the same experimental run. For this reason both measurement setups are connected to the sample. However, only one device at a time is used for the measurement, while the other is properly turned off, or detuned, not to disturb the measurement. Each measurement setup will be introduced at the time it is employed, unused devices are reported in transparency on figures and assumed to perfectly reflect any signal at frequencies employed. Here we present the necessary to perform homodyne detection of ESR signals.

The measurement setup consists of a room temperature part, used to generate control pulses and collect output signals, and a low temperature part, comprising sample, filters and low noise amplification stages. In the following paragraphs we will present the details of both setup.

Room-temperature setup

The room-temperature setup is illustrated on the top part of Fig. 4.6, it includes two microwave sources Keysight (yellow and purple) and a 4-channel arbitrary waveform generator (AWG 5014 from Tektronix). All microwave pulses needed to perform measurement sequences on the spins are generated by mixing signals from yellow microwave source with 2 AWG outputs, used to drive the I and Q ports of an I/Q mixer. The same source serves as local oscillator for homodyne signal demodulation, to extract the quadratures of the electromagnetic field from the output signal.

The JPA needs dc flux biasing to adjust the JPA frequency, this is provided by an on-chip antenna close to the JPA SQUID array, fed by a constant voltage source (red) biasing a resistor at room-temperature (input line 1 in Fig. 4.6). The JPA also requires flux-pumping to achieve gain, in the homodyne-detection configuration the pump tone is generated by the purple microwave source, and the JPA is operated in non-degenerate mode.

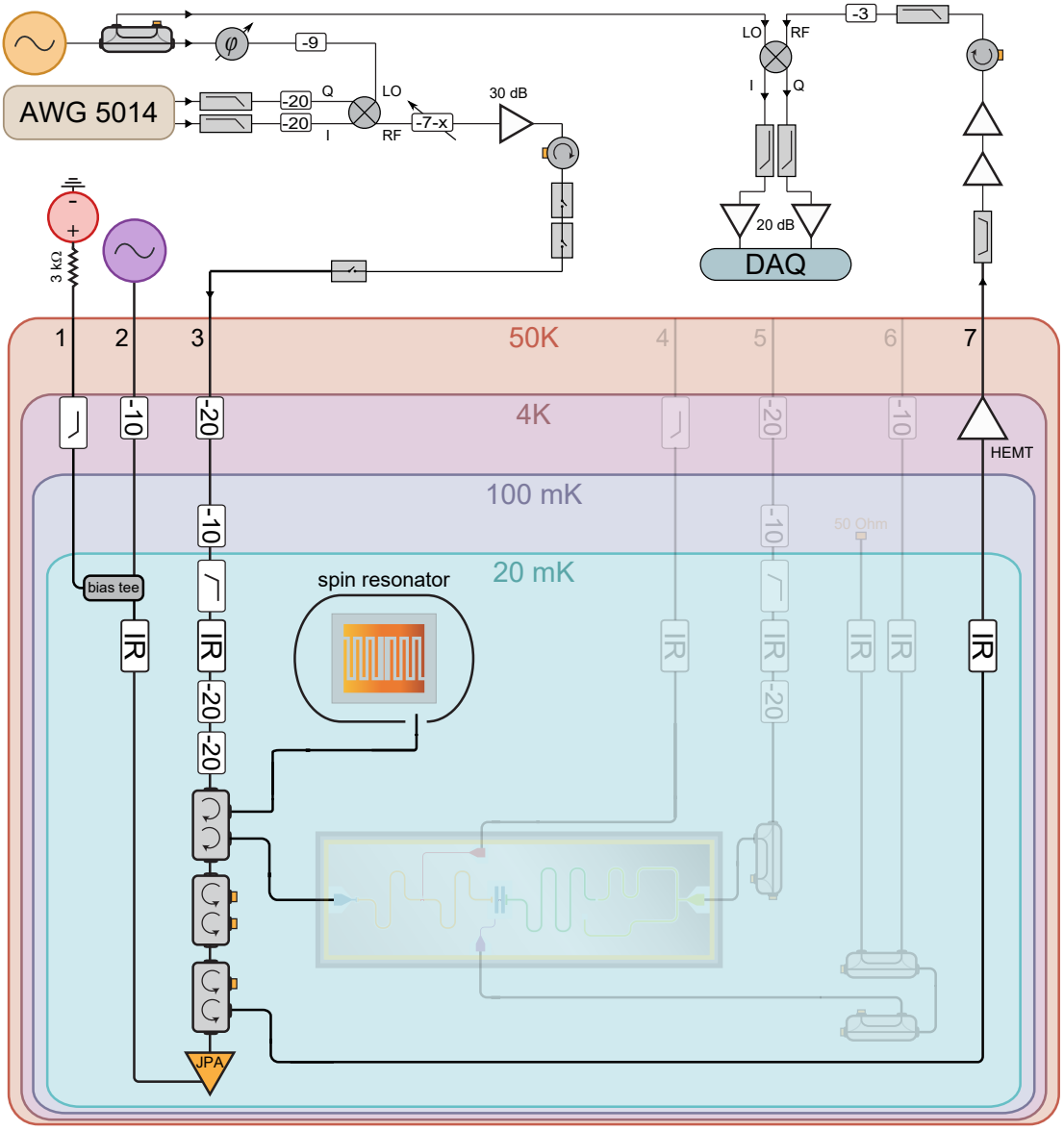

Figure 4.6: **Spin characterization setup.** Setup used to perform homodyne detection of spin-echo signal. Pulses used to drive the spins are generated via I/Q mixing of a microwave source (yellow), which is also used as reference local oscillator for homodyne demodulation. Pulses are sent to the fridge through line 3 and, after several attenuation stages, are routed to the spin resonator. Reflected signal is directed towards a JPA without distortion from the detuned SMPD (showed in transparency), additional amplification stage through a HEMT and room temperature amplifiers is operated before the signal is demodulated and digitized by an acquisition card (DAQ).

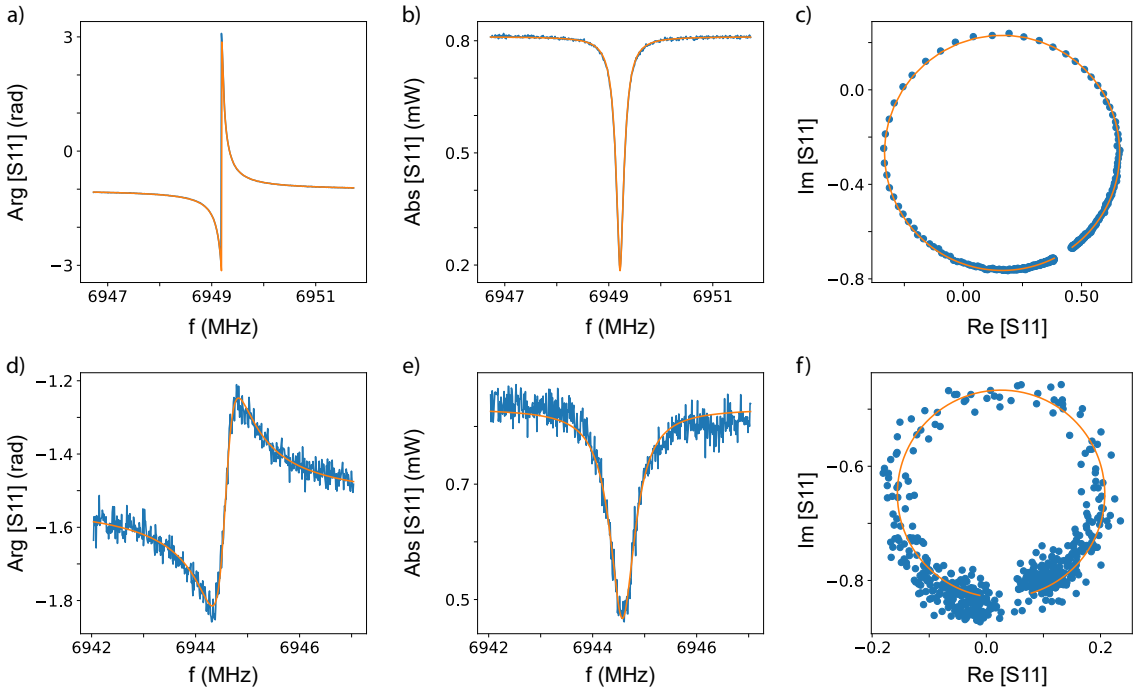

Figure 4.7: **Reflectometry of the spin resonator.** Measured S_{11} parameter phase, amplitude and complex resonance circle in absence of external magnetic field B_0 (a, b, c) and when $B_0 \simeq 16.7\,\mathrm{mT}$, the working point where the spin ensemble is in resonance with the resonator. A $4.3\,\mathrm{MHz}$ shift in frequency is observed when B_0 is ramped up, as well as an increase in internal losses due to degrading superconductivity.

Low-temperature setup

The fridge input line (3 in Fig. 4.6) is connected to the spin resonator input via a double circulator. The reflected signal is routed by the same circulator towards the single microwave photon detector input (in transparency), which is however detuned from the rest of the circuit and completely reflects the incoming signal, which is finally routed by two double circulators towards the input of the JPA and the detection chain.

The JPA output (reflected signal) is routed to a High-Electron-Mobility-Transistor (HEMT) amplifier from Low-Noise Factory anchored at the 4K stage of the cryostat, and then to output line. Infrared filters are inserted on all the lines leading to the sample to minimize out-of-equilibrium quasi-particle generation leading to microwave losses.

Resonator characterization

At first, the superconducting lumped-LC-resonator is characterized via reflectometry by using a Vector Network Analyzer (VNA) to measure the reflection coefficient S_{11} as a function of frequency ω, as showed in Fig. 4.7. Fitting these data with Eq. 2.44 yields the resonator frequency $\omega_0/2\pi = 6.949\,\mathrm{GHz}$, and the internal and external energy decay rates $\kappa_{\mathrm{int}} = 0.62 \times 10^6\,\mathrm{s}^{-1}$ and $\kappa_{\mathrm{ext}} = 0.99 \times 10^6\,\mathrm{s}^{-1}$ at zero applied field (Fig. 4.7a,b,c). Measurement of the external and internal energy decay rates κ_{ext}, κ_{int} as a function of VNA power leads to characteristic be-

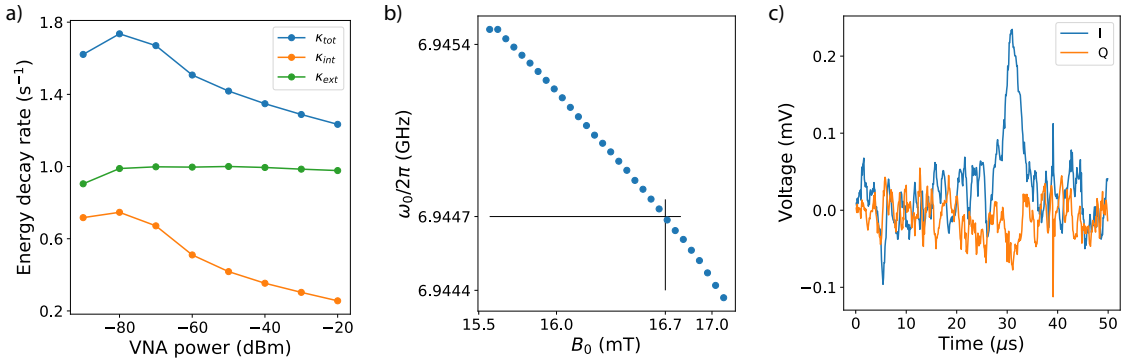

Figure 4.8: **Spin resonator characterization and echo trace.** (a) Spin resonator energy decay rate $\kappa = \kappa_{\text{ext}} + \kappa_{\text{int}}$ as a function of the probing VNA power. High powers saturate spurious two-level-system absorbers, leading to lower κ. (b) Dependence of resonator frequency ω_0 on B_0, black lines identify the working point at which $\omega_s(B_0) = \omega_0$. (c) I and Q quadratures of the field measured around time 2τ in an Hahn sequence, showing the appearance of the echo.

havior showing the saturation of internal losses κ_{int} related to two-level-systems at high powers (Fig. 4.8a).

In order to tune the bismuth donor spins in resonance with the resonator, we apply an external static magnetic field B_0. The field causes a small shift in resonator frequency (see Fig. 4.8b) and a deterioration of the internal quality factor, due to vortex penetration (see Section 2.3). Close to the working point $B_0 \simeq 16.7\,\text{mT}$ we measure $\omega_0/2\pi \simeq 6.9447\,\text{GHz}$, $\kappa_{\text{int}} = 3.3 \times 10^6\,\text{s}^{-1}$ and $\kappa_{\text{ext}} = 0.93 \times 10^6\,\text{s}^{-1}$ (Fig. 4.7d,e,f).

Spectroscopy

Measurable signal from the spins is retrieved through the Hahn echo sequence, exposed in section 3.3. After demodulation the signal is digitized by a fast acquisition card which returns a time-dependent voltage value $\langle X\rangle(t)$, $\langle Y\rangle(t)$ for the two signal quadratures. After rotation of the complex voltage on the $\langle X\rangle(t)$ quadrature (see Fig. 4.8c), we define the echo signal as the integral:

$$A_e = \int_{\Delta T} \langle X\rangle(t) dt, \tag{4.4}$$

where ΔT is an appropriate time window ($\sim 20\mu s$) centered on the echo.

Spectroscopy is performed by measuring $A_e(\mathbf{B_0})$ from 15 to 17 mT. A peak is observed around $B_0 \approx 16.7\,\text{mT}$, as seen in Fig. 4.9a.

One specific aspect is that, as explained in [43] and [42], this peak corresponds to spins located below the wire only. This is due to the strain imparted by the aluminum wire onto the substrate, which is compressive below the wire and tensile away from it, leading to 2 values for A as explained in Section 4.1 and therefore to a characteristic split-peak spectrum.

Rabi oscillations

We then use the spin-echo detection to calibrate the Rabi rotation angles. We apply a Hahn-echo-type sequence with amplitudes A and $2A$ respectively for the

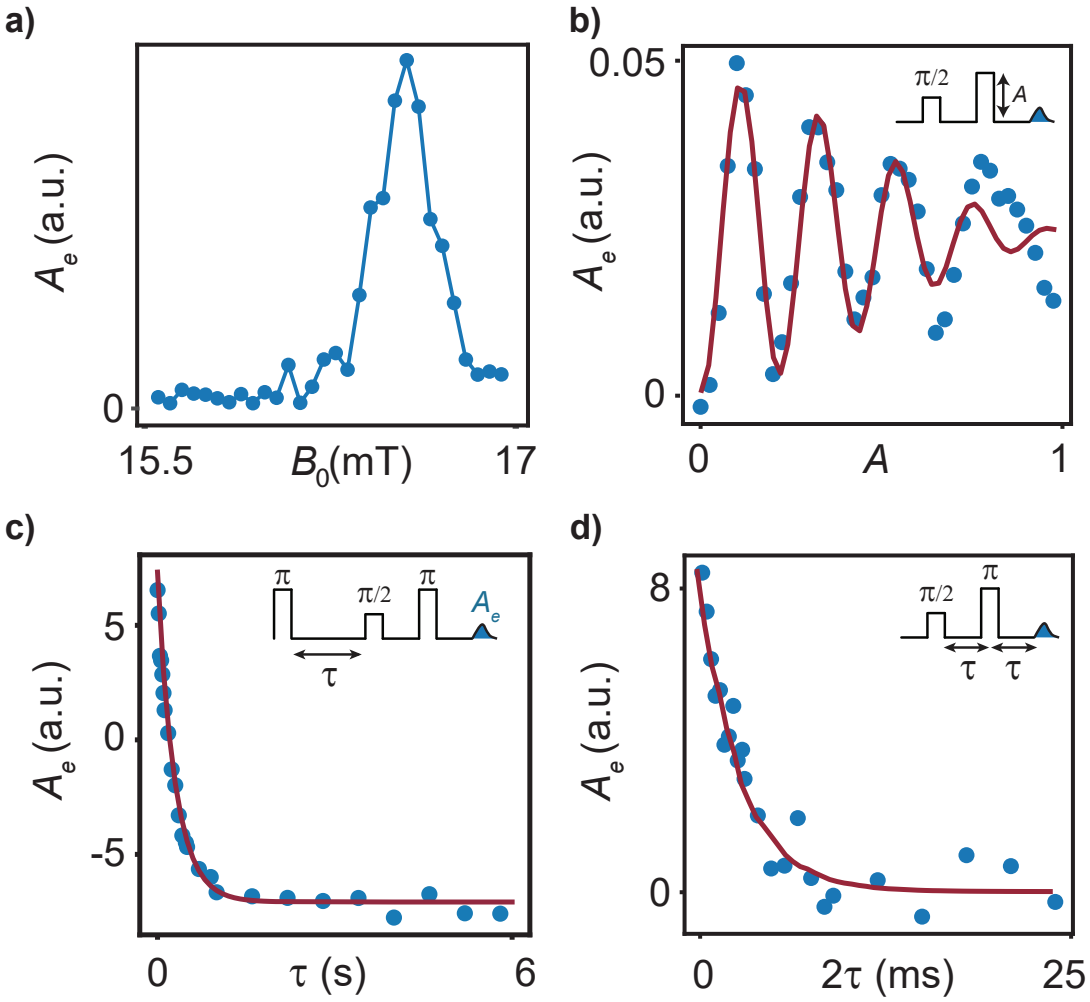

Figure 4.9: **ESR spectroscopy of the spin ensemble.** (a) Measured integrated echo (blue dots) as a function B_0. (b) Measured (blue dots) and simulated (solid line) integrated echo as a function of the amplitude A of the π pulse of the Hahn echo sequence revealing Rabi oscillations. (c) Measured (blue dots) and simulated (solid line) integrated echo as a function of the delay τ between the inversion π-pulse and the Hahn echo sequence. An exponential fit (not shown) yield a characteristic decay time $T_1 = 300 \pm 10\,\mathrm{ms}$. (d) Measured (blue dots) and simulated (solid line) integrated echo as a function of the delay τ between $\pi/2$ and π pulses of the Hahn echo sequence. An exponential fit (not showed) yields a characteristic decay time $T_2 = 2.7\,\mathrm{ms}$.

first pulse and the refocusing pulse. The maximum echo amplitude A_e is reached when the two pulses realize a $\pi/2$ and a π rotation respectively.

After pulse calibration, we measure Rabi oscillations of the spin ensemble. For that, we apply a Hahn-echo sequence in which we sweep the π pulse amplitude A. The resulting Rabi oscillations in A_e are shown in Fig. 4.9b.

The amplitude of these oscillations decays with the pulse amplitude. This decay is not due to decoherence, but to the spread of Rabi frequencies among the ensemble due to the spatial inhomogeneity of the B_1 field. We phenomenologically model this distribution by a Gaussian $\rho(g_0) = \mathrm{e}^{-(g_0-\bar{g_0})^2/2\sigma_{g_0}^2}/\mathcal{N}$, $\mathcal{N}$ being a normalization factor. We use the simulation program presented in section 3.4 to determine the standard deviation that reproduces the Rabi oscillations decay (the simulated curve is shown in Fig.4.9b), and find $\sigma_{g_0}/2\pi \approx 30\,\mathrm{Hz}$, and $\sigma_{g_0}/\bar{g_0} \sim 0.1$.

Note that this inhomogeneity in g_0 is much smaller than what could be inferred from Fig. 4.3f. The reason is that we detect only spins located below the wire, as explained earlier. This area is shown as a dashed rectangle in Fig. 4.3f); and indeed, in this rectangle, the coupling constant g_0 shows little variation.

Spin relaxation

The spin relaxation time T_1 is measured through an inversion recovery sequence: a π pulse followed after time τ by a Hahn-echo detection sequence. Fig. 4.9c shows A_e as a function of τ. An exponential fit yields a characteristic decay time $T_1 = 300\pm10\,\mathrm{ms}$. This relaxation time is directly linked to the Purcell rate through:

$$\Gamma_\mathrm{p}(\Delta = 0) = 4\frac{g_0^2}{\kappa} = \frac{1}{T_1}. \tag{4.5}$$

Using the measured resonator decay rate $\kappa = \kappa_\mathrm{int} + \kappa_\mathrm{ext}$, we infer an average spin-photon coupling constant $\bar{g_0}/2\pi \approx 300\,\mathrm{Hz}$, in agreement with the simulations shown in Fig.4.3f.

Coherence time

We then measure the spin coherence time by measuring A_e as a function of the delay 2τ between the $\pi/2$ pulse and the echo (see Fig. 4.9d). An approximately expponential decay is observed. A fit (shown in Fig. 4.9d) yields $T_2 = 2.7\,\mathrm{ms}$.

Complementary measurements described in [42] show that this decoherence is due to the dipolar coupling of the donor spins with dangling bond spins at the silicon/silicon oxide interface. Spectral diffusion should result in a Gaussian decay; but, because the echo signal results from the contribution of all spins in the detection volume, the distribution of coherence time (due to the varying donor depth) convoluted with the implantation profile conspires to give an effectively exponential decay.

Spin density estimation

Here we show how by means of a numerical model one can reproduce experimental data and estimate the number of spins addressed in an echo experiment.

We consider the realistic model introduced in section 3.4 in which the spin ensemble has inhomogeneous linewidth Γ_2^* much larger than the cavity linewidth:

$\Gamma_2^* \gg \kappa$. In this case we can approximate the spectral density of spins ρ_{spin} to be constant over the cavity linewidth, ρ_{spin} is the only parameter that sets the absolute amplitude of the echo signal, and can be estimated by reproducing experimental observation through simulation.

The experimental signal to be reproduced is the voltage trace issuing of a full Hahn-echo sequence, comprising the $\pi/2$, π and echo amplitudes. For this measurement, the same amplification is used on the echo and pulses in order to preserve the correct amplitude ratio $V_{\text{e}}^{(\text{I})}/V_{\pi/2}^{(\text{I})}$ with respect to the reference $\pi/2$ pulse. Figure 4.10 shows the experimental data (blue dots) obtained after averaging over ~ 200 repetitions. By means of the simulation tool we numerically reproduce the experiment, adjusting ρ_{spin} to obtain the observed ratio $\langle X_{\text{e}}\rangle/\langle X_{\pi/2}\rangle$ (Fig. 4.10 orange curve). With this method we infer a spin density $\rho_{\text{spin}} \approx 14.6\,\text{spins/kHz}$, which yields a total number of spins taking part in the Hahn echo $N \approx 1.46 \times 10^4$. This value is obtained by computing the number of spins excited in the simulation.

From the estimation of the spin density we can also estimate the cooperativity through the expression:

$$C = \rho_{\text{spin}} \frac{g_0^2}{\kappa} \tag{4.6}$$

which gives $C \simeq 5 \times 10^{-3}$, consistent with the low-cooperativity limit ($C \ll 1$) considered in the model of the spin ensemble.

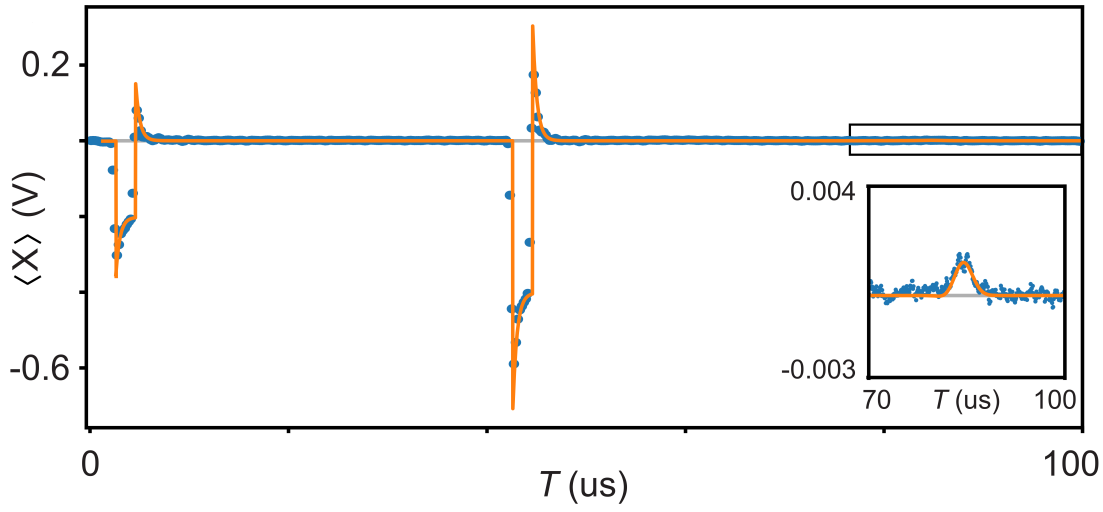

Figure 4.10: **Estimation of the spin spectral density.** (a) Measured (blue dots) and simulated (orange solid line) electromagnetic field amplitude at the output of the spin cavity as a function of the time T from the $\pi/2$ pulse of an echo sequence. The echo appears as a slight increase of the field amplitude at twice the separation between the $\pi/2$ and π pulse (inset). The spin spectral density ρ_{spin} is the only free parameter of the simulation, accordance with the experimental data is achieved for $\rho_{\text{spin}} = 14.6$ spins kHz^{-1}.

Chapter 5

Single microwave photon detector

A single photon detector is a device able to reveal the presence of a photon by triggering a measurable phenomenon. Efficient photon detectors in the optical domain rely on the photoelectric effect to convert incoming photons into an electrical signal. Current applications include bioluminescence detection, DNA sequencing, single-molecule spectroscopy, fluorescence measurement, quantum metrology and quantum information processing [44]. Photon detection becomes increasingly challenging at lower frequencies, since photons do not have enough energy to induce photo-ionization or trigger other usually exploited phenomena (e.g. Cooper pair breaking). For this reason, in the microwave domain single photon counters have remained elusive for a long time. Nevertheless, during the past decade, the problem of single microwave photon detection has been addressed in several experiments, leading to the development of devices based on circuit quantum electrodynamics to perform microwave photodetection.

In order to be able to detect spin fluorescence we need the single microwave photon detector (SMPD) to be operational. This implies five characteristics. High efficiency and low dark counts are required in order to have an acceptable SNR even at low number of spins. The detection efficiency must not depend on the shape of the wave-packet or on the precise knowledge of its arrival time. Frequency tunability is needed, to tune the detector in resonance with the spin resonator frequency ω_0. Finally, the detector must allow cyclic operation in order to gather signal on timescales of the order of the spin decay rate $T_{\mathrm{P}} \sim 1\,\mathrm{s}$.

In this chapter, we present our implementation of a single microwave photon detector based on a transmon qubit. In section 5.1 we give an overview of the existing solutions and present our approach to the problem (5.2), we then present the transmon qubit (5.2) which forms the basis of our device. In section 5.2 we give the Hamiltonian of the single microwave photon detector and derive a model to calculate its efficiency and bandwidth, and we introduce the relevant figures of merit in section 5.3. Section 5.4 is dedicate to the design, simulation and fabrication of the SMPD, in section 5.6 we present the measurement apparatus and characterize the detector.

5.1 State of the art: detecting microwave photons with superconducting circuits

The main challenge of detecting microwave photons is to identify measurable phenomena triggered by their presence, as they have energies 5 orders of magnitude lower than their optical counterparts. The leading strategy in the microwave domain consists of engineering individual quantum systems whose interaction with the incoming photon will leave a robust imprint on the quantum system of interest. From the point of view of quantum information processing, the task of photon detection can be seen as the reliable transfer of the quantum information carried by an incoming photon onto the state of a well-controlled two-level system (qubit). The rapid development of quantum devices based on superconducting circuits [45, 46] has enabled the emergence of novel instruments in the microwave domain comprising linear amplifiers operating close to the quantum limit [47, 48, 49], squeezers [50, 51], lossless frequency converters [52], or microwave isolators [53]. As the key missing element of this quantum optics toolbox, Single Microwave Photon Detectors (SMPD) have been an intense research topic in the past decade with numerous theoretical proposals [54, 55, 56] as well as various proof-of-principle demonstrations [57, 58, 59, 60, 61, 62, 63, 64, 65]. Among these, few different strategies are pursued. In the following we present a brief description of two single-microwave-photon-detectors designs.

An SMPD design based on a similar principle to the one used in this thesis has been introduced by Inomata et al. [61]. It relies on the deterministic switching of an artificial Λ-type three-level system. This system is implemented using the dressed states of a driven superconducting quantum circuit. Figure 5.1 shows the device (a) and its working principle (b). The Λ-system consists of a superconducting flux qubit of frequency ω_{q} dispersively coupled to a $\lambda/2$ resonator of frequency ω_{r}. The energy level of the system is pictured in Fig. 5.1(b), restricted to the resonator being in the ground $|0\rangle$ or first excited $|1\rangle$ state.

During the detection step, when a drive pulse of frequency ω_{d} and power P_{d} is applied to the qubit, the four levels hybridize to form dressed states $|\tilde{1}\rangle, |\tilde{2}\rangle, |\tilde{3}\rangle, |\tilde{4}\rangle$. Under a proper choice of P_{d}, the two radiative decay rates from the upper levels to the lowest-two levels become identical. This realizes an impedance-matched Λ-system comprising $|\tilde{1}\rangle$, $|\tilde{2}\rangle$ and $|\tilde{4}\rangle$ (or $|\tilde{1}\rangle$, $|\tilde{2}\rangle$ and $|\tilde{3}\rangle$).

An incident single microwave photon, synchronously applied with the drive pulse through the signal port and in resonance with the $|\tilde{1}\rangle \rightarrow |\tilde{4}\rangle$ transition, deterministically induces a Raman transition,$|\tilde{1}\rangle \rightarrow |\tilde{4}\rangle \rightarrow |\tilde{2}\rangle$, and is downconverted to a photon at the $|\tilde{4}\rangle \rightarrow |\tilde{2}\rangle$ transition frequency. This process is accompanied by an excitation of the qubit. Readout of the qubit state via a parametric phase-locked oscillator leads to the binary answer click/no-click of the detector.

Note that this detector does not require any temporal shaping of the input photons, nor precise time-dependent control of system parameters adapted to the temporal mode of the input photons. Moreover, rapid resetting can be achieved with a resonant drive inducing the $|\tilde{2}\rangle \rightarrow |\tilde{3}\rangle \rightarrow |\tilde{1}\rangle$ transition (see 5.1(c,e)).

As reported in Fig. 5.1(d), the authors measured a single-photon-detection efficiency of 0.66 ± 0.06 over a detection bandwidth of $16\,\mathrm{MHz}$. Each detection cycle lasts $760\,\mathrm{ns}$ and the dark-count probability is 0.014 ± 0.001, corresponding to a dark count rate of the order of $10^4\,\mathrm{counts/s}$.

A second type of microwave photon detector based on the Ramsey interferom-

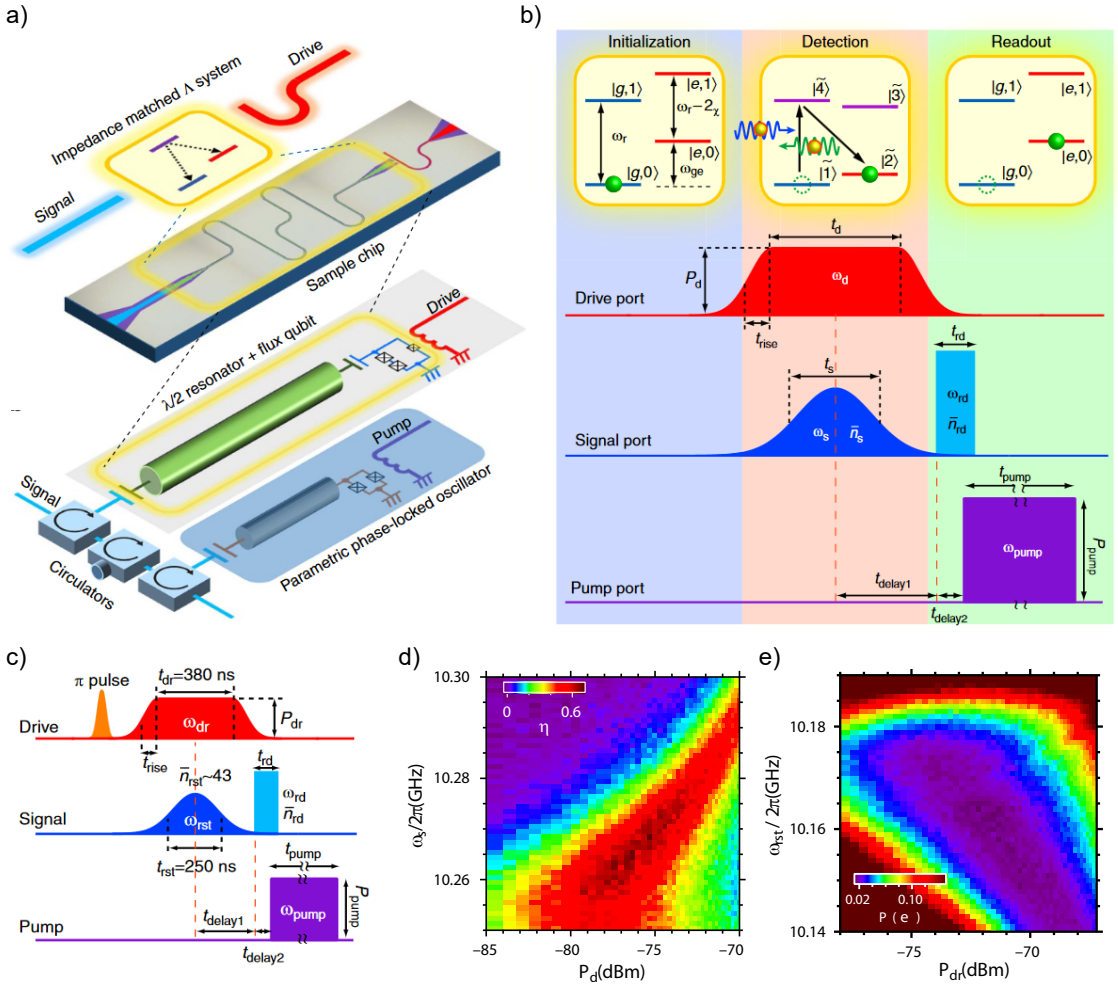

Figure 5.1: **SMPD using an artificial Λ-type three-level system.** (a) Schematic of the SMPD device from the work of Inomata et al. A flux qubit is dispersively coupled to a $\lambda/2$ resonator, a port coupled to the qubit allows to apply drive pulses. A parametric phase locked oscillator allows for fast qubit readout. (b) Detection principle. After the system is set to its ground state a drive pulse is applied during a time t_d, the four levels of the system hybridize and an impinging photon at frequency $|\tilde{1}\rangle \rightarrow |\tilde{4}\rangle$ induces a Raman transition $|\tilde{1}\rangle \rightarrow |\tilde{4}\rangle \rightarrow |\tilde{2}\rangle$ accompanied by the emission of a photon (green) and the excitation of the qubit. Readout of the qubit state leads to a click/no-click answer of the detector. (c) Pulse sequence for the reset of the detector. The inverse Raman process is activated by shining a tone at frequency corresponding to the $|\tilde{2}\rangle \rightarrow |\tilde{3}\rangle$ transition. (d) Measured detection efficiency as a function of drive frequency and power. (e) Qubit excited state probability $p(e)$ as a function of the reset frequency and power.

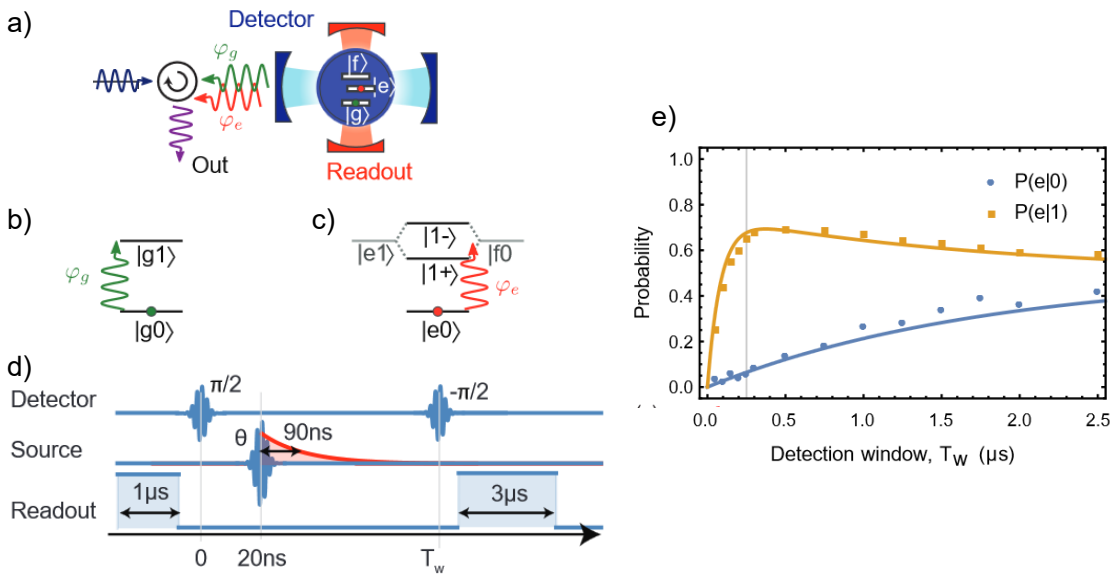

Figure 5.2: **SMPD using conditional phase gate.** (a) Illustration of the setup. A transmon qubit is coupled to a detector resonator and a readout resonator. The detector resonator is resonant with the first to second-excited transition of the qubit. (b) Energy diagram of the qubit-resonator system when the qubit is in the ground state. An impinging photon at the bare resonator frequency is reflected with a phase $\varphi_g = \pi$. (c) Energy diagram of the qubit-resonator system when the qubit is in the excited state. An impinging photon at the bare resonator frequency does not interact with the system and is reflected with a phase $\varphi_e = 0$. (d) The pulse scheme consisting of two $\pi/2$pulses on the qubit, separated by a duration Tw. A single photon source is used for detector calibration, the angle θ determining the weights of the superposition vacuum-single photon. A readout pulse is used to measure the state of the detection-qubit at the end of the protocol, as well as to preselect the single shot traces to discard thermal population. (e) Dark count probability $P(e|0)$ (blue), photon detection efficiency $P(e|1)$ (yellow), as a function of the detection window T_{w}.

etry of a transmon qubit has been developed by Besse at al. [64].

As depicted in figure 5.2(a), the detector consists of a transmon qubit coupled to two resonators. One detector resonator and a readout resonator, used to dispersively readout the qubit state. The first to second-excited state transition of the qubit $|e\rangle \rightarrow |f\rangle$ is tuned in resonance with the detector resonator.

The working principle of the detector is shown in Fig. 5.2. When the transmon is in the ground state (b), photons impinging on the detector at the bare resonator frequency acquire a phase $\varphi_g = \pi$ as they are reflected. By contrast, with the transmon in the first excited state (c), the cavity mode hybridizes with the resonant qubit mode $|e\rangle \leftrightarrow |f\rangle$, thus photons at the bare cavity frequency are not resonant and reflected without interacting. By consequence they acquire no phase $\varphi_e = 0$.

Note that the interaction between the photon and the qubit mediated by the resonator is symmetric, thus the interaction can also be interpreted as a phase-flip gate of the qubit induced by the reflection of the single photon. The detection is based on the realization of a phase gate on the detection-qubit controlled by

the presence of a photon.

The detection protocol is shown in figure 5.2(d). It consists in initializing the transmon in the state $(|g\rangle + |e\rangle)/\sqrt{2}$ by applying a $\pi/2$-pulse, then waiting a detection time T_{w} before applying a second $\pi/2$-pulse, effectively completing a Ramsey sequence on the qubit. At the end, the qubit state is readout via the second resonator.

The author demonstrated a detection efficiency $\eta_{\mathrm{d}} \simeq 0.7$ over a bandwith of $\sim 20\,\mathrm{MHz}$, equal to the detector resonator linewidth. Since this detector design is based on the Ramsey interferometry of a transmon qubit, dark counts are induced by the dephasing, leading to $10^4 - 10^5\,\mathrm{count/s}$.

Other demonstrations are briefly touched on here. In Ref.[58],[60] and [65], the photon mode must be known in advance for good performances, therefore these proposals are not well suited for randomly emitted photons. Several waveform independent architectures present high efficiencies ($\eta > 0.5$), but dark count rates are often not explicitly stated but can be inferred from measurements. In Ref.[59] and [62], the incoming photon triggers a bifurcation in a superconducting circuit, the Josephson Photo-Multiplier. This scheme is optimized for speed at the expense of the dark-count rate which is expected to be of the order of $10^6\,\mathrm{counts/s}$ for detection bandwidth larger than $20\,\mathrm{MHz}$. Ref.[63], similar to the device of *Besse at al.*, is based on the Ramsey interferometry of a transmon qubit, dark counts are therefore induced by the dephasing of the qubit leading to $10^4 - 10^5\,\mathrm{count/s}$ for detection bandwidth of $3 - 10\,\mathrm{MHz}$.

In the past two years, it has been proposed and demonstrated a novel photon detection architecture [57] with a dark count rate of $10^3\,\mathrm{counts/s}$ over a detection bandwidth of $2\,\mathrm{MHz}$. It relies on dissipation engineering [66] that consists of steering a quantum system into irreversible dynamics using the friction brought by open environments. The proposed microwave photon detector is a practical architecture being not only high efficiency and intrinsically robust against dark count but also the only one being continuously operated and frequency tunable. In the following we present its working principle and characteristics.

5.2 SMPD working principle and theory

The single microwave photon detector designed, fabricated and employed in this thesis is based on the process of four-wave mixing, sketched in Fig. 5.3. This novel design has been introduced and first realized by *Lescanne et al.* [57], and has the main advantage that dark counts are not affected by the properties of coherence of the qubit.

Four-wave mixing is a parametric non-linear process in which the interaction between excitations at two frequencies ω_{b} and ω_{p} (*buffer and pump*) produce excitations at two new frequencies ω_{q} and ω_{w} (*qubit and waste*), provided that the following energy conservation condition is satisfied: $\omega_{\mathrm{b}} + \omega_{\mathrm{p}} = \omega_{\mathrm{q}} + \omega_{\mathrm{w}}$. In our particular instance, the non-linearity required to mediate this interaction is provided by a superconducting qubit.

Consider a qubit of excitation frequency ω_{q}, coupled to two baths at frequencies ω_{b} and ω_{w}, and to a pump line at frequency ω_{p}. As illustrated in figure 5.3: the non-linearity of the qubit can be exploited to mix an incoming microwave photon at frequency ω_{b}, that we need to detect, with a classical *pump* tone at

radio-frequency ω_{p} (5.3b). The four-wave mixing process converts these two photons into the excitation of the qubit at frequency ω_{q} and an outgoing photon at frequency $\omega_{\mathrm{w}} = \omega_{\mathrm{b}} + \omega_{\mathrm{p}} - \omega_{\mathrm{q}}$ (5.3c). The qubit is then readout leading to a "click" if it is found in the excited state, revealing the capture of the photon.

However, the process just described is reversible: the qubit and the outgoing photon can still be converted back into two photons at frequencies ω_{b} and ω_{p}, leading to a detection error. The solution is to make the capture process irreversible, by engineering the dissipation of the output bath at frequency ω_{w}. In fact, fast relaxation to the environment allows to keep its average photon occupation number close to zero.

Finally, we remark that this detection scheme comes with an intrinsic way to reset the system to its initial state. By populating the waste bath with photons at frequency ω_{w}, the reverse conversion process, suppressed during normal operation, is stimulated. The possibly excited qubit is brought back to its ground state and a photon at frequency ω_{w} is converted into a buffer photon at frequency ω_{b} (Figure 5.3e).

In what follows, we will present the different elements taking part to the detection process. A superconducting transmon qubit, and two coplanar-waveguide resonator acting as photonic baths. We will introduce the four-wave mixing Hamiltonian and the adiabatic elimination of the waste bath, we give a simple model for the detector circuit and introduce the main figures of merit. Finally we will move to the experimental realization.

The transmon qubit

Building upon the non-linearity afforded by the Josephson junction, we can construct a variety of circuit elements capable of effectively encoding quantum bits of information as well as performing non-linear mixing of modes. We exploit these two aspects to build the single microwave photon counter: the four wave mixing interaction where two excitations are converted into two other excitations in distinct spatial modes and at distinct frequencies and the quantum bit which is used as a witness on which the incoming photon leaves its imprint. The transmon qubit enables us to combine both functions in a single element.

In transmon qubits, the transition between the first two energy levels is detuned from that of its first to second excited state by the anharmonicity, which is typically designed to be $200 - 300$ MHz. With this configuration, transitions between the two lowest levels of the transmon can be addressed with microwave pulses as short as a few nanoseconds. Physically, transmon qubits are constructed with two large superconducting capacitor C structures in parallel with a single Josephson junction with a Josephson energy E_{J}. The transmon Hamiltonian is simply given by;

$$\hat{H} = \frac{\hat{Q}^2}{2C} - E_{\mathrm{J}} \cos 2\pi\hat{\phi}/\phi_0 \tag{5.1}$$

In order to match with the literature notations, we introduce dimension-less quantum variables, the number of cooper-pair on the capacitor plate $\hat{N} = \hat{Q}/2e$ and the phase across the Josephson junction $\varphi = 2\pi\hat{\phi}/\phi_0$ with $\phi_0 = h/2e$ the quantum flux. The transmon Hamiltonian expresses as:

$$\hat{H} = 4E_{\mathrm{C}}\hat{N}^2 - E_{\mathrm{J}} \cos\hat{\varphi} \tag{5.2}$$

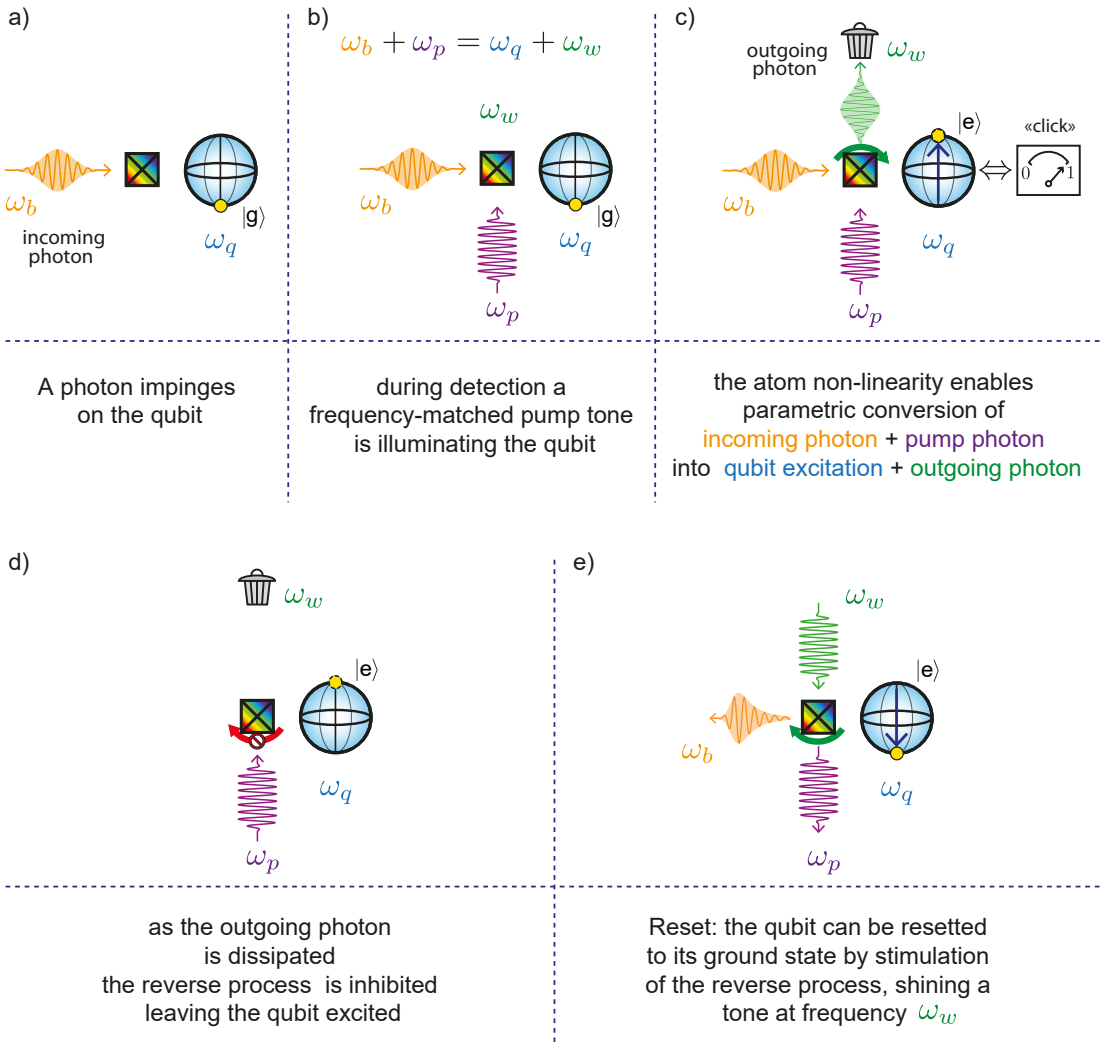

Figure 5.3: **Four waves mixing.** Schematic of irreversible photon capture using four waves mixing and engineered dissipation. (a) A photon at frequency ω_b impinges on a qubit of frequency ω_q. (b) The qubit is coupled to a bath at frequency ω_w, a pump tone is continuously shone on the qubit at frequency satisfying the matching condition $\omega_b + \omega_p = \omega_q + \omega_w$. (c) The qubit non-linearity enables the conversion of the two incoming excitations into an excitation of the qubit and an outgoing photon at frequency ω_w. (d) Engineered dissipation of the bath at frequency ω_w allows fast dissipation of the generated photon and ensures the irreversibility of the conversion process. The incoming excitation is irreversibly mapped on the qubit state. (e) Qubit reset protocol: the inverse mixing process, resetting the qubit to the ground state and generating a photon at frequency ω_b is activated by shining a tone at frequency ω_w with the pump on.

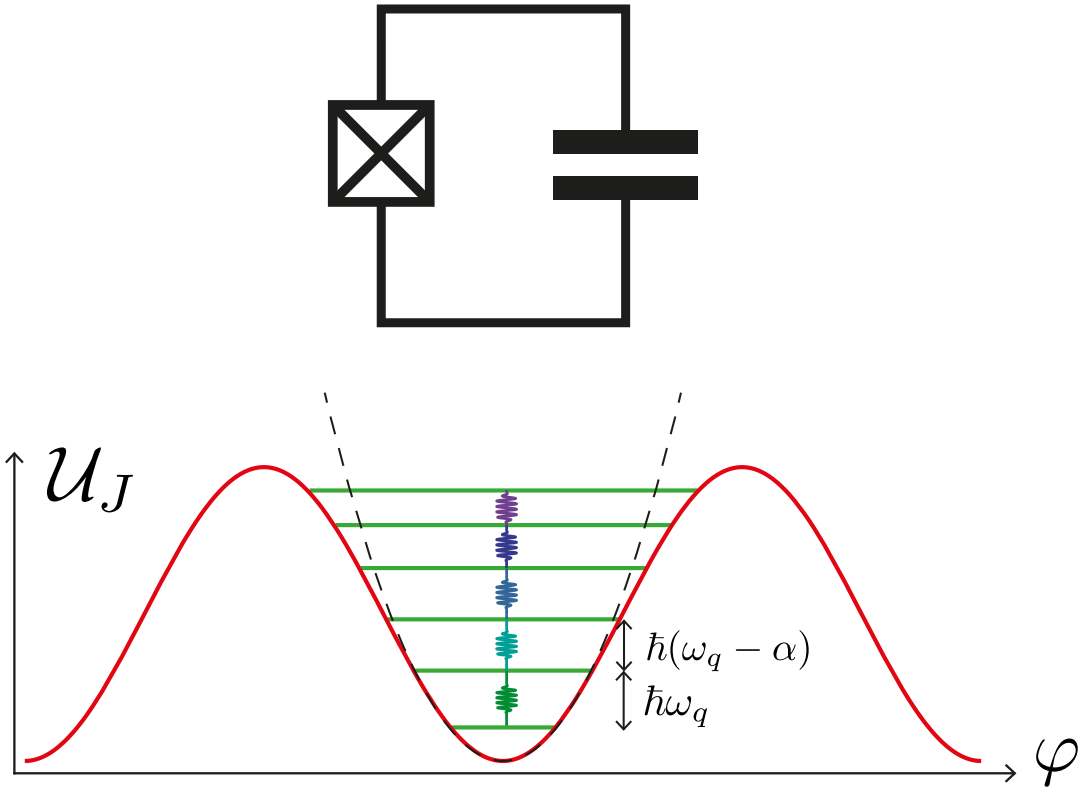

Figure 5.4: **Transmon qubit.** (Top) Circuit representation of a superconducting qubit. The Josephson junction (crossed box) plays the role of a non-linear inductor, lifting the degeneracy of harmonic oscillator transitions. (Bottom) Cosine potential of the transmon qubit (red line), dependent on the superconducting phase φ. The resulting quantized energy ladder present an anharmonicity α. The harmonic oscillator parabolic potential is shown for comparison (dashed line).

with the charging energy defined as $E_C = e^2/2C$.

The transmon qubit is characterised by a weak anharmonicity, its wavefunctions are only weakly perturbed compared to the harmonic oscillator. Therefore, it is convenient to directly express its Hamiltonian in the Fock state basis using the annihilation and creation operator of the harmonic oscillator $\hat{q}$ and $\hat{q}^\dagger$ where $[\hat{q}, \hat{q}^\dagger] = 1$. The cooper-pair number and the phase across the junction are then given by $\hat{N} = N_{\mathrm{ZPF}}(\hat{q} - \hat{q^\dagger})/i$ and $\hat{\varphi} = \varphi_{\mathrm{ZPF}}(\hat{q} + \hat{q^\dagger})$ with $N_{\mathrm{ZPF}} = (E_J/32E_C)^{1/4}$ and $\varphi_{\mathrm{ZPF}} = (2E_C/E_J)^{1/4}$. In the Fock state basis, the transmon Hamiltonian is given by:

$$\hat{H} = -4E_C N_{\mathrm{ZPF}}^2(\hat{q} - \hat{q}^\dagger)^2 - E_J \cos\left(\varphi_{\mathrm{ZPF}}(\hat{q} + \hat{q}^\dagger)\right) \tag{5.3}$$

The weak transmon anharmonicity means that transmon wave function only explores the bottom of the cosine potential in its ground and first excited states. It can be translated into the fact that the zero-point-fluctuations of the phase variable remain small $\varphi_{\mathrm{ZPF}} = (2E_C/E_J)^{1/4} \ll 1$. As a consequence, this regime is therefore achieved in the limit where the charging energy remains small compared to the Josephson energy $E_C \ll E_J$, the Josephson junction must be in parallel to a large capacitor. In practice, the transmon regime is reached for $E_J/E_C >$

40, for lower ratios, the transmon frequency becomes sensitive to charge offsets. In this transmon limit, the Hamiltonian is well approximated by a fourth order expansion of the cosine potential leading to the following Hamiltonian

$$\hat{H} = \underbrace{\sqrt{\frac{E_J E_C}{2}}(\hat{q} - \hat{q}^\dagger)^2 + \sqrt{\frac{E_J E_C}{2}}(\hat{q} + \hat{q}^\dagger)^2}_{\text{harmonic oscillator}} \underbrace{- \frac{E_C}{24}(\hat{q} + \hat{q}^\dagger)^4}_{\text{non-linearity}} + O(E_C\sqrt{\frac{E_C}{E_J}}) \tag{5.4}$$

By simplifying the expression, we obtain the transmon Hamiltonian under the form of an harmonic oscillator combined with a strong four-wave mixing term. This equation will be of great interest for the construction of the single microwave photon detector.

$$\boxed{\hat{H} = \sqrt{8E_J E_C}\hat{q}^\dagger\hat{q} - \frac{E_C}{12}(\hat{q} + \hat{q}^\dagger)^4} \tag{5.5}$$

By expanding the non-linear term, we collect all combinations of $\hat{q}$ and $\hat{q}^\dagger$. However, the only relevant terms are the energy conserving ones. The terms that do not conserve energy lead to fast rotating contributions which average out on timescales relevant for the system dynamics, such approximation is known as the rotating wave approximation (RWA).

$$\hat{H} = (\sqrt{8E_J E_C} - E_C)\hat{q}^\dagger\hat{q} - \frac{E_C}{2}\hat{q}^{\dagger 2}\hat{q}^2 \tag{5.6}$$

Remarkably, the following Hamiltonian is diagonal in the Fock state basis. The qubit frequency corresponds to the transition from the ground state $|g\rangle$ to the first excited state $|e\rangle$. It is given by

$$\omega_q = (\sqrt{8E_J E_C} - E_C)/\hbar. \tag{5.7}$$

Importantly, the transition frequency between the first excited state $|e\rangle$ and second excited state $|f\rangle$ is given by $\omega_q^{ef} = (\sqrt{8E_J E_C} - \mathbf{2}E_C)/\hbar$. As expected, the frequencies strongly differ from each other. The transmon anharmonicity, defined as the mismatch between these two frequencies $\alpha = |\omega_q^{ef} - \omega_q| = E_C/\hbar$, is simply given by the charging energy. A typical anharmonicitiy of $200 - 300$ MHz is much larger than the typical transmon linewidth (< 10 kHz), therefore the circuit's lowest transition behaves as a legitimate qubit.

Circuit electrodynamics

Having introduced two key components of circuit QED systems, superconducting resonators and transmons, we now look into how they can be integrated to form a useful quantum device. In particular, we will show how such resonators are essential for the readout of the transmon qubit, the calibration of the photon flux as well as the construction of the SMPD. Let's first study the coupling of a transmon to a single oscillator.

Transmon qubit dispersively coupled to a resonator

Physically, when a transmon is placed in proximity to a resonator, the charges of one element can influence those of the other through a coupling capacitor. Importantly, this is treated rigorously in appendix B.4 as it allows to extract circuit

Hamiltonians from the finite element electromagnetic simulation. We summarise this coupling by a parameter of the Hamiltonian, g, which can be computed exactly for a given model of the circuit. The capacitive coupling translate as a simple linear coupling between modes in the rotating wave approximation. The system Hamiltonian is given by:

$$\hat{H} = \underbrace{\hbar\omega_\mathrm{b}\hat{b}^\dagger\hat{b}}_{\text{oscillator}} + \underbrace{\hbar(\omega_\mathrm{q}+\alpha)\hat{q}^\dagger\hat{q} - \frac{\alpha}{12}(\hat{q}+\hat{q}^\dagger)^4}_{\text{transmon}} + \underbrace{\hbar g(\hat{b}^\dagger\hat{q}+\hat{b}\hat{q}^\dagger)}_{\text{capacitive coupling}} \tag{5.8}$$

The first step to treat this Hamiltonian consists in finding the dressed mode associated the linear coupled system. In a second step, the dressed mode will be injected into the transmon four-wave mixing term.

Let us focus on the linear part of the Hamitonian given by:

$$\hat{H}_\mathrm{lin} = \hbar\omega_\mathrm{b}\hat{b}^\dagger\hat{b} + \hbar\omega_\mathrm{q}\hat{q}^\dagger\hat{q} + \hbar g(\hat{b}^\dagger\hat{q}+\hat{b}\hat{q}^\dagger) \tag{5.9}$$

Due to the linear coupling, the two modes hybridise leading to two uncoupled dressed modes. This hybridisation corresponds to a mode rotation with an angle $\theta = \frac{1}{2}\arctan 2g/\Delta$ where $\Delta = \omega_\mathrm{b} - \omega_\mathrm{q}$ is the frequency detuning between the modes. We place ourselves in the dispersive limit where the coupling is much larger than the detuning, $g \ll \Delta$, for which the modes are only weakly hybridised. The dressed modes are given by:

$$\tilde{\hat{b}} = \cos(\theta)\hat{b} + \sin(\theta)\hat{q} \approx \hat{b} + \frac{g}{\Delta}\hat{q} \tag{5.10}$$

$$\tilde{\hat{q}} = \cos(\theta)\hat{q} - \sin(\theta)\hat{b} \approx \hat{q} - \frac{g}{\Delta}\hat{b} \tag{5.11}$$

In the dressed basis, the linear Hamiltonian is simply given by:

$$\hat{H}_\mathrm{lin} = \hbar\tilde{\omega_\mathrm{b}}\tilde{\hat{b}}^\dagger\tilde{\hat{b}} + \hbar\tilde{\omega_\mathrm{q}}\tilde{\hat{q}}^\dagger\tilde{\hat{q}} \tag{5.12}$$

where $\tilde{\omega_\mathrm{q}} = \omega_\mathrm{q} - \frac{g^2}{2\Delta}$ and $\tilde{\omega_\mathrm{b}} = \omega_\mathrm{b} + \frac{g^2}{2\Delta}$

The second step consists of rewriting the full Hamiltonian in the dressed basis.

$$\boxed{\hat{H}/\hbar = \tilde{\omega_\mathrm{b}}\tilde{\hat{b}}^\dagger\tilde{\hat{b}} + (\tilde{\omega_\mathrm{q}}+\alpha)\tilde{\hat{q}}^\dagger\tilde{\hat{q}} - \frac{\alpha}{12}(\tilde{\hat{q}}+\tilde{\hat{q}}^\dagger + \frac{g}{\Delta}(\tilde{\hat{b}}+\tilde{\hat{b}}^\dagger))^4} \tag{5.13}$$

Remarkably, the non-linearity is mixing the dressed modes in a non-trivial way. The direct expansion of the non-linear term directly leads to the dispersive Hamiltonian of circuit quantum electrodynamics after the rotating wave approximation in which the non-energy-conserving terms are dropped. For simplicity, we will give up the tilde notation associated to dressed modes. The dispersive Hamiltonian reads:

$$\boxed{\hat{H}/\hbar = \omega_\mathrm{b}\hat{b}^\dagger\hat{b} + \omega_\mathrm{q}\hat{q}^\dagger\hat{q} - \frac{\alpha}{2}\hat{q}^{\dagger 2}\hat{q}^2 - \frac{K}{2}\hat{b}^{\dagger 2}\hat{b}^2 - \chi\hat{b}^\dagger\hat{b}\hat{q}^\dagger\hat{q}} \tag{5.14}$$

with

$$\chi = 2\alpha\frac{g^2}{\Delta^2} \tag{5.15}$$

$$K = \alpha\frac{g^4}{\Delta^4} \tag{5.16}$$

K and χ are referred to as the self-Kerr of the resonator and cross-Kerr between the transmon and the resonator. For typical parameters such as $\alpha = 2\pi \times 200$ MHz, $g = 2\pi \times 100$ MHz and $\Delta = 2\pi \times 1$ GHz, on the one hand the self-Kerr is of the order of $K \sim 2\pi \times 10$ kHz while the oscillator linewidth is typically $\kappa = 2\pi \times 1$ MHz, therefore self-Kerr is usually neglected in the circuit dynamics. On the other hand, cross-Kerr is typically of the order of $\chi \sim 2\pi \times 1$ MHz, therefore it plays a crucial role in the oscillator-qubit dynamics.

The cross-Kerr term, also known as dispersive shift, can be understood as a frequency shift of a given mode conditioned on the state of another one. It is of great interest in circuit quantum electrodynamics as it allows for the quantum non-demolition readout of the qubit state by probing the oscillator resonance frequency as well as the absolute calibration of a photon flux by probing the dephasing of the qubit while the resonator is illuminated.

Quantum non-demolition qubit readout

The dispersive Hamiltonian shown in Eq.5.14 can be recasted by factorizing the cross-Kerr term into the harmonic oscillator energy. Neglecting the self-Kerr contribution, we get:

$$\hat{H}/\hbar = (\omega_\mathrm{b} - \chi \hat{q}^\dagger \hat{q}) \hat{b}^\dagger \hat{b} + \omega_\mathrm{q} \hat{q}^\dagger \hat{q} - \frac{\alpha}{2} \hat{q}^{\dagger 2} \hat{q}^2 \tag{5.17}$$

This Hamiltonian implies that the frequency of the oscillator mode $\hat{b}$ depends on the state of the qubit mode $\hat{q}$: when the qubit is its ground state $|g\rangle$, the oscillator frequency is $\omega_\mathrm{b}^\mathrm{g} = \omega_\mathrm{b}$ while when the qubit is in its excited state $\omega_\mathrm{b}^\mathrm{e} = \omega_\mathrm{b} - \chi$. A measure of the complex reflection coefficient with a probe tone at $\omega_\mathrm{b}^\mathrm{g}$ or $\omega_\mathrm{b}^\mathrm{e}$, allows for the discrimination of the resonator frequency and thus the readout of the state of the qubit.

Photon-induced qubit dephasing

Another implication of the dispersive qubit-resonator Hamiltonian Eq.5.17, is that the qubit frequency also depends on the absolute photon occupation of the harmonic oscillator as the Hamiltonian can be rewritten as:

$$\hat{H}/\hbar = \omega_\mathrm{b} \hat{b}^\dagger \hat{b} + (\omega_\mathrm{q} - \chi \hat{b}^\dagger \hat{b}) \hat{q}^\dagger \hat{q} - \frac{\alpha}{2} \hat{q}^{\dagger 2} \hat{q}^2 \tag{5.18}$$

When the resonator is continuously illuminated, it is populated by $\bar{n}$ photons on average. We expect the qubit transition frequency to be shifted by $-\hbar\chi\bar{n}/2$ on average. However, the photon population is strongly fluctuating due to the photon shot noise, then it leads to a fluctuation of the qubit frequency and the dephasing of the qubit at a rate of the order of $\kappa\bar{n}$ where κ is the linewidth of the resonator.

A quantitative calculation [67] of this phenomenon can be performed in the general case of arbitrary resonator linewidth κ_b and cross-Kerr χ. When a tone is applied with an amplitude ϵ and a detuning δ with respect to the cavity resonance frequency, it generates a coherent state $|\alpha_g\rangle$ and $|\alpha_e\rangle$ that depends on the state of

the qubit ground or excited. Their complex amplitude is given by:

$$\alpha_g = \frac{\epsilon}{\kappa_\mathrm{b}/2 + i(\delta + \chi/2)} \tag{5.19}$$

$$\alpha_e = \frac{\epsilon}{\kappa_\mathrm{b}/2 + i(\delta - \chi/2)} \tag{5.20}$$

It corresponds to a photon occupancy of $\bar{n}_g = |\alpha_g|^2$ or $\bar{n}_e = |\alpha_e|^2$ depending on the state of the qubit. The presence of intra-cavity photon induces both a frequency shift of the qubit Δ_q and dephasing of the qubit at a rate Γ_q. They are actually the real and imaginary part of a quantity that depends on the overlap between the two coherent states:

$$\boxed{\Delta_s + i\Gamma_s = -\chi\alpha_g\bar{\alpha_e} = \frac{-4\chi|\epsilon|^2}{(\kappa_\mathrm{b} + 2i\delta)^2 + \chi^2}} \tag{5.21}$$

Qualitatively, when the coherent states associated to ground and excited overlap, the qubit gets only detuned and not dephased while when the coherent states are far away from each other and thus the qubit measurement become effective, the qubit dephasing dominates over its detuning.

This effect can be turned into a powerful calibration method for the determination of the absolute microwave power applied on the resonator. Indeed by precisely measuring the qubit frequency and dephasing rate in a Ramsey sequence while illuminating the resonator, the resonator photon occupancy $\bar{n}_{e/g}$ can be accurately determined. From this, one can compute the incident power applied on the resonator. When the incident tone is applied on resonance, the incident power is given by:

$$P_\mathrm{in} = \frac{1}{4}\frac{\kappa_\mathrm{b}^2}{\kappa_\mathrm{b} - \kappa_\mathrm{b}^\mathrm{loss}}\hbar\omega_\mathrm{b}\bar{n}_g = \hbar\omega_\mathrm{b}\frac{|\epsilon|^2}{\kappa_\mathrm{b} - \kappa_\mathrm{b}^\mathrm{loss}} \tag{5.22}$$

with $\kappa_\mathrm{b}^\mathrm{loss}$ the internal loss rate of the resonator.

To conclude, this calibration method is a key part of the experiment as it has been employed to calibrate the absolute attenuation associated with the input line of the cryostat and therefore the absolute efficiency of the photon detector.

The SMPD Hamiltonian

In this section, we will use the quantization method introduced above to derive the SMPD Hamiltonian.

In the case of the SMPD circuit shown in Fig.5.5, the transmon qubit is capacitively coupled to two distinct harmonic modes: the buffer mode $\hat{b}$ at a frequency ω_b with a coupling constant g_b, the waste mode $\hat{w}$ at a frequency ω_w with a coupling constant g_w. The qubit hybridises with both modes leading to a dressed qubit mode given by:

$$\hat{q} \leftarrow \hat{q} + \frac{g_\mathrm{b}}{\Delta_\mathrm{b}}\hat{b} + \frac{g_\mathrm{w}}{\Delta_\mathrm{w}}\hat{w} \tag{5.23}$$

An extra ingredient is required for the SMPD, the four-wave-mixing process is activated by a strong off-resonant pump tone. Being off-resonance, it is well described by a complex amplitude $\xi_t = \xi_0 e^{-i\omega_p t}$ oscillating at the pump frequency ω_p that displaces the qubit mode. Therefore the qubit mode dressed by the coupled resonators and displaced by the pump tone reads

$$\hat{q} \leftarrow \hat{q} + \frac{g_\mathrm{b}}{\Delta_\mathrm{b}}\hat{b} + \frac{g_\mathrm{w}}{\Delta_\mathrm{w}}\hat{w} + \xi_t. \tag{5.24}$$

The overall dressed Hamiltonian is therefore given by:

$$\hat{H}/\hbar = \omega_{\rm b}\hat{b}^\dagger\hat{b}+\omega_{\rm w}\hat{w}^\dagger\hat{w}+(\omega_{\rm q}+\alpha)\hat{q}^\dagger\hat{q}-\frac{\alpha}{12}(\hat{q}+\hat{q}^\dagger+\frac{g_{\rm b}}{\Delta_{\rm b}}(\hat{b}+\hat{b}^\dagger)+\frac{g_{\rm w}}{\Delta_{\rm w}}(\hat{w}+\hat{w}^\dagger)+\xi_t+\xi_t^*)^4 \quad (5.25)$$

We can then expand the four-wave mixing term. We keep the energy conserving processes according to the rotating wave approximation and neglect the self-Kerr contributions.

$$\hat{H}/\hbar = \quad \omega_{\rm b}\hat{b}^\dagger\hat{b} + \omega_{\rm w}\hat{w}^\dagger\hat{w} + \omega_{\rm q}\hat{q}^\dagger\hat{q} - \frac{\alpha}{2}\hat{q}^{\dagger 2}\hat{q}^2 \quad (5.26)$$

$$-\chi_{\rm b}\hat{b}^\dagger\hat{b}\hat{q}^\dagger\hat{q} - \chi_{\rm w}\hat{w}^\dagger\hat{w}\hat{q}^\dagger\hat{q} - 2\alpha|\xi(t)|^2\hat{q}^\dagger\hat{q} \quad (5.27)$$

$$-\sqrt{\chi_{\rm b}\chi_{\rm w}}(\xi_t\hat{b}\hat{q}^\dagger\hat{w}^\dagger + \xi_t^*\hat{b}^\dagger\hat{q}\hat{w}) \quad (5.28)$$

Owing to the presence of the oscillating pump, a non-trivial term emerges from the four-wave mixing and survives from the rotating wave approximation when the pump frequency is chosen to be:

$$\omega_p = \omega_{\rm q} + \omega_{\rm w} - \omega_{\rm b} - \chi_{\rm w} \quad (5.29)$$

This Hamiltonian is describing the SMPD photon capture process.

$$\boxed{\hat{H}_{\rm SMPD}/\hbar = -\sqrt{\chi_{\rm b}\chi_{\rm w}}(\underbrace{\xi_t\hat{b}\hat{q}^\dagger\hat{w}^\dagger}_{\text{photon absorption}} + \underbrace{\xi_t^*\hat{b}^\dagger\hat{q}\hat{w}}_{\text{inhibited photon emission}})} \quad (5.30)$$

As described earlier, this Hamiltonian makes the absorption of an incoming photon in the buffer mode $\hat{b}$ by the qubit *irreversible* by linking this process to the creation to an extra photon into an highly damped waste mode $\hat{w}$. As the photon in the waste mode $\hat{w}$ is quickly damped out, the qubit cannot emit its excitation back into the buffer mode $\hat{b}$ using the reciprocal process. The strength of the interaction is given by $\sqrt{\chi_{\rm b}\chi_{\rm w}}|\xi_0|$. It depends on the pump amplitude but also on the cross-Kerr terms of the mode $\hat{b}$ and $\hat{w}$ with the qubit, leading to clear guideline for the circuit design.

The SMPD irreversibility from dissipation engineering

In this section, we will study the SMPD dynamics under the light of bath engineering in order to make explicit the irreversible character of the photon capture.

To describe the dynamics of the system in the presence of a strongly damped waste mode $\hat{w}$, it is convenient to use the master equation which describe the evolution of the system density matrix $\hat{\rho}$ under the SMPD Hamiltonian dynamics and the energy relaxation of the waste mode $\hat{w}$ into a cold bath.

The energy relaxation of mode $\hat{w}$ at a rate $\kappa_{\rm w}$ is described by the following Linblad operator associated with the jump operator $\sqrt{\kappa_{\rm w}}\hat{w}$:

$$\mathcal{D}[\sqrt{\kappa_{\rm w}}\hat{w}]\hat{\rho} = \kappa_{\rm w}\left(\hat{w}\hat{\rho}\hat{w}^\dagger - \frac{1}{2}\hat{w}^\dagger\hat{w}\hat{\rho} - \frac{1}{2}\hat{\rho}\hat{w}^\dagger\hat{w}\right). \quad (5.31)$$

In the interaction picture, the master equation is given by:

$$\partial_t\hat{\rho} = \underbrace{\frac{1}{i\hbar}[\hat{H}_{\rm SMPD},\hat{\rho}]}_{\text{Hamiltonian dynamics}} + \underbrace{\mathcal{D}[\sqrt{\kappa_{\rm w}}\hat{w}]\hat{\rho}}_{\text{irreversible dynamics}} \quad (5.32)$$

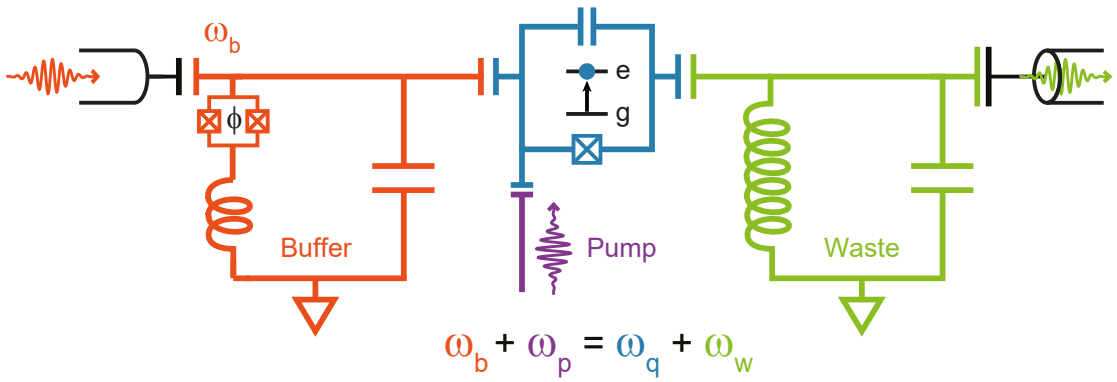

Figure 5.5: **SMPD circuit illustration.** Circuit representation of the SMPD. The buffer resonator (orange) is tuned at the frequency of photons to be detected by changing the magnetic flux Φ threading a SQUID (red). When a photon enters the buffer resonator it interacts with a transmon qubit coupled capacitively (blue), if a pump tone (purple) is shone on the qubit at the frequency-matching condition $\omega_\mathrm{p} = \omega_\mathrm{q} + \omega_\mathrm{w} - \omega_\mathrm{b}$ then the qubit is left excited and a photon at frequency ω_w is created in the waste resonator (green). Engineered dissipation of the waste allows for fast decay of the photon into the transmission line, inhibiting the reverse mixing process.

A very powerful approximation tool is the adiabatic elimination. In the limit where the dissipation rate κ_w is large compared to the Hamiltonian dynamics governed by $\sqrt{\chi_\mathrm{b}\chi_\mathrm{w}}|\xi_0|$, one can consider that the waste mode $\hat{w}$ is always close to its ground state, therefore it does not contribute to the system dynamics anymore and can be eliminated. This procedure can be carefully performed as described in appendix B.4.

One can then derive an effective master equation for the reduced density matrix where the waste mode has been traced out such that:

$$\hat{\rho}_\mathrm{bq} = \mathrm{Tr}_\mathrm{w}[\hat{\rho}] \tag{5.33}$$

The adiabatic elimination leads to remarkably simple effective master equation:

$$\boxed{\partial_t \hat{\rho}_\mathrm{bq} = \mathcal{D}\left[\Gamma_\mathrm{SMPD}\hat{b}\hat{q}^\dagger\right]\hat{\rho}_\mathrm{bq}} \tag{5.34}$$

with

$$\Gamma_\mathrm{SMPD} = 4\frac{\chi_\mathrm{b}\chi_\mathrm{w}}{\kappa_\mathrm{w}}|\xi_0|^2 \tag{5.35}$$

The Hamiltonian dynamics completely vanished and has been replaced by a fully irreversible evolution described by the jump operators $\Gamma_\mathrm{SMPD}\hat{b}\hat{q}^\dagger$. As opposed to usual jump operator such as energy relaxation ($\hat{b}$) or dephasing ($\hat{b}^\dagger\hat{b}$) , this one describes a strongly correlated dynamics between two distinct modes. When a photon in the input mode $\hat{b}$ is annihilated, it irreversibly triggers an excitation of the qubit state.

We now add the coupling of the buffer mode $\hat{b}$ to the incoming lines at a rate κ_b bringing a photon flux $|\epsilon_\mathrm{b}|^2$ described with a drive term of strength ϵ_b:

$$\partial_t \hat{\rho}_\mathrm{bq} = \mathcal{D}\left[\Gamma_\mathrm{SMPD}\hat{b}\hat{q}^\dagger\right]\hat{\rho}_\mathrm{bq} + \mathcal{D}\left[\sqrt{\kappa_\mathrm{b}}\hat{b}\right]\hat{\rho}_\mathrm{bq} - i[\epsilon_\mathrm{b}(\hat{b}+\hat{b}^\dagger), \hat{\rho}_\mathrm{bq}] \tag{5.36}$$

At early time, the qubit irreversibly absorbs the incoming photons flux $|\epsilon_\mathrm{b}|^2$ at a rate $\partial_t p_e$, the efficiency is then defined by the ratio:

$$\boxed{\eta = \frac{\partial_t p_e}{|\epsilon_\mathrm{b}|^2} = \frac{4\mathcal{C}}{(1+\mathcal{C})^2}} \tag{5.37}$$

where the cooperativity of the photon capture is defined as

$$\boxed{\mathcal{C} = \frac{\Gamma_\mathrm{SMPD}}{\kappa_\mathrm{b}} = 4|\xi_0|^2 \frac{\chi_\mathrm{b}\chi_\mathrm{w}}{\kappa_\mathrm{b}\kappa_\mathrm{w}}}. \tag{5.38}$$

Unit efficiency is reached for $\mathcal{C} = 1$. The pump strength $|\xi_0|$ being defined as the phase across the Josephson junction induced by the pump, it must remain much smaller than π. This finite pump strength establishes a design criterion on the cross-Kerr coefficient and the dissipation rate to reach unit efficiency:

$$\frac{\kappa_\mathrm{b}\kappa_\mathrm{w}}{\chi_\mathrm{b}\chi_\mathrm{w}} \ll 4\pi^2 \approx 40 \tag{5.39}$$

In practice, for the design of the SMPD in this thesis, we used the following criterion $\boxed{\chi_\mathrm{b}\chi_\mathrm{w} > \kappa_\mathrm{b}\kappa_\mathrm{w}}$. This criterion is used to carefully adjust the capacitive coupling, the frequency detuning and the capacitive coupling to the lines. This criterion also sets an upper bound on the bandwidth of the detector as it is approximately set by the linewidth of the input mode leading to $\mathrm{BW}_\mathrm{SMPD} \sim \kappa_\mathrm{b} < \chi_\mathrm{b}\chi_\mathrm{w}/\kappa_\mathrm{w}$

SMPD efficiency from a coupled cavity model

The dissipation engineering formalism requires that the bath dissipation rate κ_w is much larger than the SMPD Hamiltonian dynamics for the adiabatic elimination procedure to perform well. We found out that for the purpose of photon detection, a simpler model allows to evade this constraint and to compute the SMPD efficiency with more general settings.

For the purpose of photon detection, the system dynamics is only relevant as long as the qubit remains in its ground state. Indeed, once the qubit is excited, the photon detector is saturated as the SMPD Hamiltonian is effectively switched off. The following photons will be simply reflected off the cavity.

When the qubit is in its ground state and the incoming field contains much less than a photon on average, then the effective system dynamics is identical to the one of two resonantly coupled cavities with the qubit simply tracking the position of the photon. It will be in its ground state if the photon is in the buffer mode $\hat{b}$ and in its excited state if the photon is in the waste mode $\hat{w}$. In other words, the coupling dynamics between the states $|1_\mathrm{b}, g_\mathrm{q}, 0_\mathrm{w}\rangle \leftrightarrow |0_\mathrm{b}, e_\mathrm{q}, 1_\mathrm{w}\rangle$ will be identical to the linear dynamics between $|1_\mathrm{b}, 0_\mathrm{w}\rangle \leftrightarrow |0_\mathrm{b}, 1_\mathrm{w}\rangle$.

For a resonantly coupled cavity, if a single photon is fully transmitted from the transmission line on the buffer side into the transmission line of the waste side, it implies that it will also the case for the SMPD and, as the qubit keeps track of the photon flux from one side to the other, it will be excited with unit probability.

We can then compute the detection efficiency as transmission probability of a photon across two linearly coupled cavities with an effective coupling $|\xi_0|\sqrt{\chi_\mathrm{b}\chi_\mathrm{w}}$.

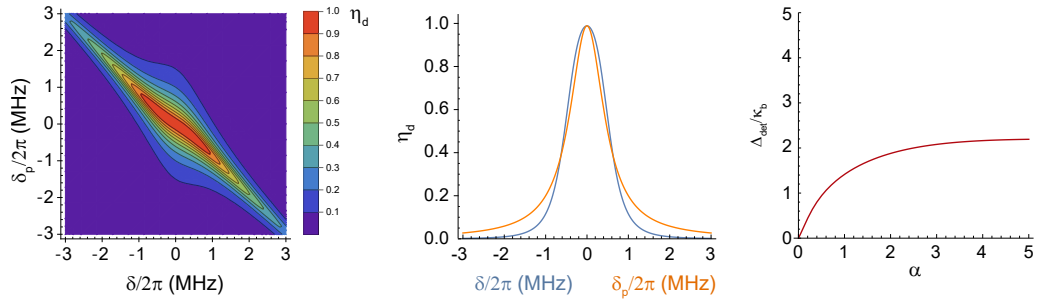

Figure 5.6: **SMPD S21 for different pump detunings.** (a) SMPD transmission parameter $|S_{21}|^2$ as a function of δ and δ_p, as obtained from the coupled-cavities model for realistic experimental parameters. (b) Cuts at $\delta_\mathrm{p} = 0$ (blue curve) and $\delta = 0$ (orange curve). (c) Detection bandwith as a function of κ_b and κ_w at optimal transmission $\kappa_\mathrm{nl} = \kappa_\mathrm{b}$.

Using simple linear scattering theory as detailed in appendix B.4, we obtain the detector efficiency as a function of the incoming photon detuning δ:

$$\eta(\delta) = \frac{4\mathcal{C}}{\left|1 + \mathcal{C} - 4\frac{\delta(\delta+\delta_p)}{\kappa_\mathrm{b}\kappa_\mathrm{w}} + 2i\frac{\delta}{\kappa_\mathrm{b}} + 2i\frac{(\delta+\delta_p)}{\kappa_\mathrm{w}}\right|^2}. \tag{5.40}$$

where $\mathcal{C} = 4|\xi_0|^2\frac{\chi_\mathrm{b}\chi_\mathrm{w}}{\kappa_\mathrm{b}\kappa_\mathrm{w}}$ is the cooperativity, δ is the detuning of the incoming photon with the $\hat{b}$ mode and δ_p the frequency detuning of the pump compared to its optimal frequency, it translates to a detuning between the two coupled cavities in the linear model.

We recover the expression found in Eq.5.37 when the photon is on resonance with mode $\hat{b}$ and the pump is optimal tuned:

$$\eta(\delta = 0) = \frac{4\mathcal{C}}{(1+\mathcal{C})^2} \tag{5.41}$$

Remarkably, this efficiency formula extends well beyond the strong damping approximation assumed in the adiabatic elimination treatment.

An extra quantity can be extracted from Eq.5.40, as it describes the efficency behavior as function of the photon detuning, we can compute the bandwidth of the detector for unit cooperativity defined as the full-width-half-maximum:

$$\boxed{\Delta_\mathrm{SMPD} = \sqrt{2}\sqrt{\sqrt{\kappa_\mathrm{b}^2\kappa_\mathrm{w}^2 + \left(\frac{\kappa_\mathrm{b}-\kappa_\mathrm{w}}{2}\right)^4} - \left(\frac{\kappa_\mathrm{b}-\kappa_\mathrm{w}}{2}\right)^2}} \tag{5.42}$$

Let's evaluate the SMPD bandwidth for a few cases. For $\kappa_\mathrm{b} \approx \kappa_\mathrm{w}$, one gets $\Delta_\mathrm{SMPD} \approx \sqrt{2\kappa_\mathrm{b}\kappa_\mathrm{w}}$. For $\kappa_\mathrm{b} \ll \kappa_\mathrm{w}$, $\Delta_\mathrm{SMPD} \approx 2\kappa_\mathrm{b}$ and reciprocally for $\kappa_\mathrm{b} \gg \kappa_\mathrm{w}$, $\Delta_\mathrm{SMPD} \approx 2\kappa_\mathrm{w}$.

To conclude, the SMPD design and working principle is well described by effective models. Realistic parameters enables to reach unit efficiency in the capture process for detection bandwidth in the MHz range. We will now study the practical limitation of the device due to cyclic operation, non-zero qubit occupancy and decoherence processes.

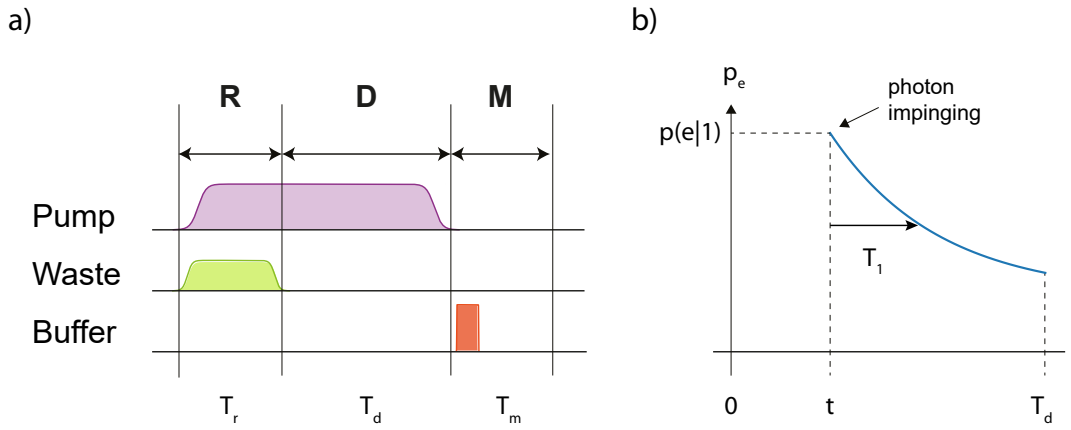

Figure 5.7: **SMPD detection cycle.** (a) The detection cycle of the SMPD constituted by reset (R), detection (D) and qubit measurement (M) steps, respectively of duration T_r, T_d and T_m. Each pulse is applied on a specific element of the SMPD, indicated on the left. (b) A photon impinging on the SMPD at time $0 < t < T_\mathrm{d}$ is captured with probability $p(e|1)$. After the capture, the probability of the qubit still being excited decreases exponentially with characteristic time $T_{1,\mathrm{q}}$.

5.3 SMPD operation

In this section, we will describe how we operate the device in practice and what are the main sources of inefficiencies.

SMPD detection cycle

We now describe more precisely the details of SMPD operation. SMPD operation consists in repeated cycles, of total duration T_c, which can be separated in 3 steps: qubit reset (R), detection (D), and qubit readout (M), as shown in fig. 5.7(a).

Reset (R): the qubit is set to its ground state by turning on the pump at frequency ω_p (violet pulse) while applying to the waste resonator a weak resonant coherent tone at frequency ω_w (green pulse) for a duration T_r.

Detection (D): the microwave at ω_w is switched off, while the pump is kept on for a time T_d. Photon detection occurs via the 4-Wave-Mixing process described earlier.

Measurement (M): the qubit state is readout by probing the dispersive shift of the buffer resonator with a pulse of duration T_m (orange pulse).

The fact that part of the cycle time is not used for detection leads to a finite duty cycle $\eta_\mathrm{duty} = T_\mathrm{d}/T_\mathrm{c}$, which impacts the total detector efficiency. Finally, note that the detector evidently saturates for signals providing more than 1 photon every T_d approximately.

SMPD figures of merits

Here we introduce the figures of merit of the SMPD: efficiency and dark count rate, detailing how they are impacted by experimental parameters and imper-

fections. In particular, we show that long qubit $T_{1,\mathrm{q}}$ is beneficial for detector performances, while qubit $T_{2,\mathrm{q}}$ has no impact on them.

Efficiency

Efficiency is the average probability $P(\mathrm{click}|1)$ of measuring a "click" when a photon is impinging on the detector. Consider a photon impinging on the buffer mode at random time t, within the detection window of length T_{d}. For an ideal qubit, the detection efficiency would be given by formula Eq.5.41. However, the qubit is imperfect and it can relax after being excited due to a finite relaxation time $T_{1,\mathrm{q}}$. The probability of the qubit still being excited at the end of the detection window is $\exp\{-(T_{\mathrm{d}}-t)/T_{1,\mathrm{q}}\}$. A second source of imperfection is the qubit readout fidelity, namely the probability of measuring a click if the qubit is excited $p(click|e)$. By averaging the photon arrival time t on the detection window, we find that the average probability $P(\mathrm{click}|1)$ of measuring a "click" is:

$$\eta_{\mathrm{d}} = p(\mathrm{click}|e)\eta_{4\mathrm{wm}}\frac{1}{T_{\mathrm{d}}}\int_0^{T_{\mathrm{d}}} e^{-(T_{\mathrm{d}}-t)/T_{1,\mathrm{q}}}dt = \tag{5.43}$$

$$= p(\mathrm{click}|e)\eta_{4\mathrm{wm}}\frac{T_{1,\mathrm{q}}}{T_{\mathrm{d}}}\left(1-e^{-T_{\mathrm{d}}/T_{1,\mathrm{q}}}\right). \tag{5.44}$$

$$\eta_d \xrightarrow{T_{\mathrm{d}}\ll T_{1,\mathrm{q}}} p(\mathrm{click}|e)\eta_{4\mathrm{wm}}\left(1-\frac{T_{\mathrm{d}}}{T_{1,\mathrm{q}}}\right) \tag{5.45}$$

Dark count rate

The dark count rate is the rate of false positives measured by the detector. The relevance of this figure of merit comes from the fact that it affects the maximum SNR reachable with a photon detector, as highlighted in section 2.6. The probability of a false positive during a detection step starting at $t = 0$, after a reset of the qubit, can have two origins. First, due to readout infidelity $p(\mathrm{click}|g)$ a qubit measurement can lead to a click even if the qubit is in its ground state, this happens with probability $p(\mathrm{click}|g)p(g|0)$. Second, non-zero temperature of the qubit can lead to thermal excitations with probability p_{th} at equilibrium. After the reset this thermal probability is $p_{\mathrm{th}}(1-e^{-t/T_{1,\mathrm{q}}})$. Thus we expect an average dark count rate:

$$\nu_{\mathrm{dc}} = p(\mathrm{click}|g)p(g|0) + P(\mathrm{click}|e)p_{\mathrm{th}}(1-e^{-T_{\mathrm{d}}/T_{1,\mathrm{q}}}) \tag{5.46}$$

In practice, the probability $p(click|g)$ is extremely small thanks to the high fidelity qubit detection. Indeed, readout outcomes of the ground and excited states follow two distinct Gaussian distributions that are separated by at least 5σ in practice. This overlap is therefore vanishingly small.

$$\nu_{\mathrm{dc}} \approx P(\mathrm{click}|e)p_{\mathrm{th}}(1-e^{-T_{\mathrm{d}}/T_{1,\mathrm{q}}})) \xrightarrow{T_{\mathrm{d}}\ll T_{1,\mathrm{q}}} P(\mathrm{click}|e)p_{\mathrm{th}}\frac{T_{\mathrm{d}}}{T_{1,\mathrm{q}}} \tag{5.47}$$

As seen from the above formulas both efficiency and dark counts benefit from longer $T_{1,\mathrm{q}}$. Conversely, $T_{2,\mathrm{q}}$ does not influence the SMPD figures of merit. Note that this is only true in the limit where the dephasing rate is much smaller than

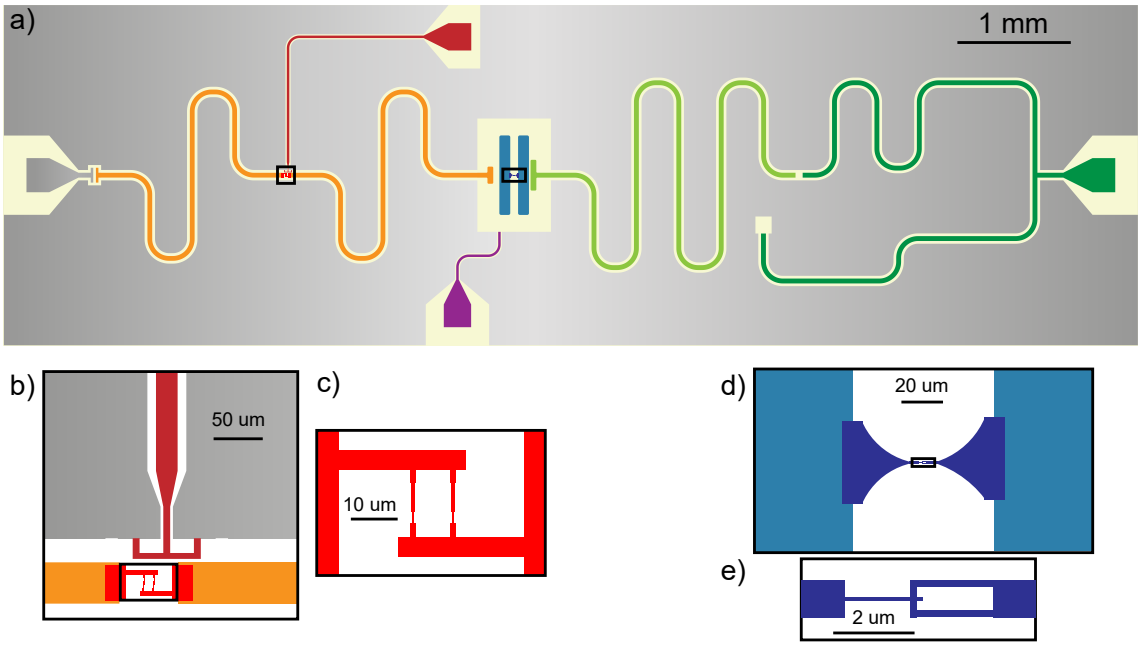

Figure 5.8: **SMPD chip design.** (a) Design of the mask employed to fabricate the SMPD chip. Coplanar waveguide $\lambda/2$ resonators are used as buffer (orange) and waste (light green), a Purcell filter (dark green) is employed to increase the coupling between the waste and the output line without affecting the qubit lifetime. (b,c) Zoom on the SQUID embedded at the current antinode of the buffer resonator, an on-chip fluxline (red) is used to generate magnetic flux through the SQUID loop and tune the buffer frequency. (d,e) Zoom of the qubit Josephson junction, bottle-opener design is used to increase reproducibility in fabrication and decrease mask failure.

the strength of the parametric process $\xi_0\sqrt{\chi_a\chi_b} \sim \sqrt{\kappa_\mathrm{b}\kappa_\mathrm{w}} \sim (100ns)^{-1}$. Indeed, in case of strong dephasing, the photon capture process could be strongly inhibited by the Zeno effect which freezes the qubit into one of its pointer states $|g\rangle$ and $|e\rangle$. In practice, the dephasing is negligible in the SMPD dynamics.

5.4 SMPD chip

Here, we present the design and fabrication of the SMPD chip.

Design

We first discuss the design choices that were made, based on the SMPD working principle presented in the previous section.

- **Buffer resonator** As explained in Chapter 4, the frequency of the photons emitted by the spins is fixed by the spin resonator frequency design at a value ω_0. In order to detect them, it is therefore necessary to tune the buffer resonator frequency ω_b (which is the SMPD input) in resonance with ω_0. As explained in Chapter 2, this can be achieved by inserting a SQUID in a resonator; here we use a CPW geometry and target a maximum frequency of 7.35 GHz, close to the Bismuth donor spin frequency, and a tuning range of $\approx$ 200 MHz. Finally, the buffer resonator coupling to the input line is

critical as it plays a role in the SMPD bandwidth as seen in Eq.5.42. Here, we target a bandwidth of $2\,\mathrm{MHz}$ with a target $\kappa_\mathrm{b}/2\pi \simeq 1\,\mathrm{MHz}$ and $\kappa_\mathrm{w} = 3\kappa_\mathrm{b}$.

- **Waste resonator:** Because of the waste resonator role in the SMPD process, photons should be rapidly damped into the measurement line, implying a large damping rate κ_w, targeted to be $\kappa_\mathrm{w}/2\pi \sim 3\,\mathrm{MHz}$. The waste resonator frequency can be chosen freely; here we choose to have it slightly higher than ω_b, with $\omega_\mathrm{w}/2\pi \sim 8\,\mathrm{GHz}$.

- **Transmon qubit:** As can be seen from Section 5.1, the exact value of the qubit frequency ω_q has no strong impact on the SMPD operation. It is therefore interesting to design its frequency to be far detuned from the buffer and waste resonator frequency; in that way we can minimize transmon qubit relaxation by spontaneous emission of a photon through these resonators. We choose to target a frequency $\omega_\mathrm{q} \simeq 5\,\mathrm{GHz}$. The pump frequency satisfying the four-wave mixing condition should therefore be around $6\,\mathrm{GHz}$. Based on Eq.5.41, an optimal SMPD operating condition can be achieved for arbitrary qubit-resonator couplings by adjusting the pump tone amplitude. In practice however, excessively high pump powers should be avoided as they may cause heating; this implies that the qubit dispersive coupling to both the buffer and the waste resonator should be sufficiently high. Another aspect is that qubit readout requires $\chi_\mathrm{b}, \chi_\mathrm{w} \geq \kappa_\mathrm{b}, \kappa_\mathrm{w}$. Overall, we target $\chi_\mathrm{b} \sim \chi_\mathrm{w} \sim 2\pi \times 5\,\mathrm{MHz}$.

Based on these considerations, the chip design is shown in Fig. 5.8. The buffer resonator is shown on the left (orange), with an electrode (in red) used to pass a dc current through an antenna to change the magnetic flux in the SQUID Φ and therefore tune $\omega_\mathrm{b}(\Phi)$. The transmon is in the middle of the chip (in blue). One electrode (in purple) is capacitively coupled to the transmon, and connected to a waveguide; it is used to drive the qubit both resonantly and at the pump frequency for the SMPD operation. The buffer resonator (in light green) is on the right side of the picture. It is coupled to the measurement line through a stub (in dark green), whose goal is to present a $50\,\Omega$ impedance at frequency ω_w, and a much higher impedance at ω_q. In this way, the waste resonator field can be damped at a large rate κ_w, without affecting the qubit relaxation rate. This arrangement is known as a "Purcell filter" and is frequently used in circuit QED chip design [68].

Simulation

We now explain how the chip design shown in Fig. 5.8 is simulated in order to predict the values of the relevant physical parameters. A commercial software such as the finite-element eigensolver ANSYS HFSS is well-suited to simulate the linear resonator parameters (frequency and damping rate). Here, we also need parameters governed by the Josephson junction non-linearity (the dispersive couplings); they are obtained through the Energy Participation Ratio (EPR) method, described in [69].

Linear simulation

The chip simulation starts by determining the frequency and damping rates of the lowest-frequency modes, using the HFSS frequency eigensolver. In doing so

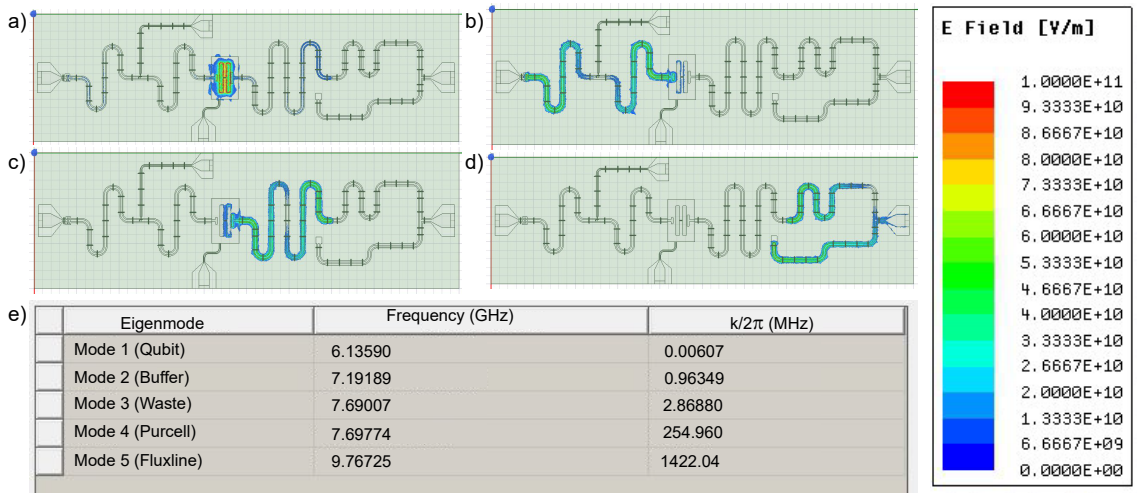

e)

Eigenmode	Frequency (GHz)	k/2π (MHz)
Mode 1 (Qubit)	6.13590	0.00607
Mode 2 (Buffer)	7.19189	0.96349
Mode 3 (Waste)	7.69007	2.86880
Mode 4 (Purcell)	7.69774	254.960
Mode 5 (Fluxline)	9.76725	1422.04

Figure 5.9: **SMPD simulations.** Finite element electromagnetic simulation using ANSYS HFSS. The frequencies and energy decay rates for the first five eigenmodes of the circuit are reported in table (e). The electric field amplitude obtained injecting 1J of energy is plotted for the first four modes: (a) qubit, (b) buffer, (c) waste, (d) Purcell. The fifth resonance correspond to a mode of the SQUID fluxline.

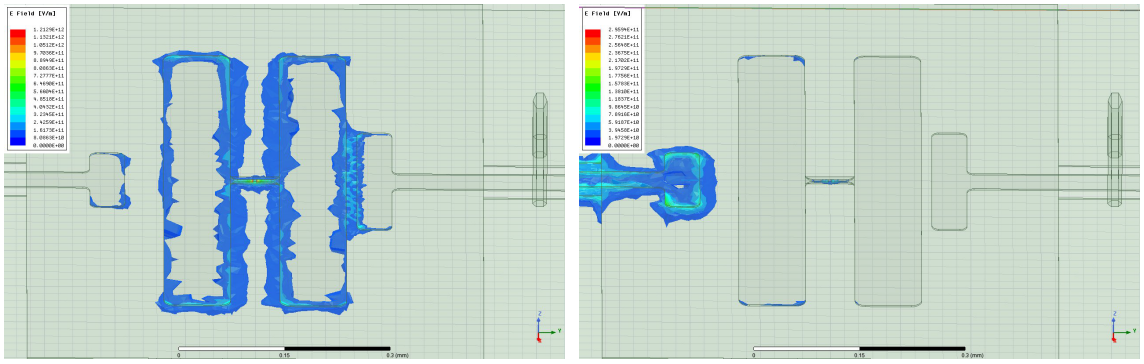

Figure 5.10: **EPR method.**

we replace the SQUID and transmon Josephson junction by the linear part of the Josephson inductance. The results for the 5 lowest-frequency modes are shown in Fig.5.9, together with a graphical representation of the electric-field distribution associated with each mode. The first 4 modes can be straightforwardly associated to the circuits involved in the SMPD design: respectively, the qubit, the buffer resonator, the waste resonator, and the Purcell filter. Their frequency and damping rates follow approximately the design considerations presented earlier. Note that the waste resonator damping rate is 3 times larger than the buffer resonator. The predicted qubit energy decay rate $\kappa_q/2\pi = 6\,\mathrm{kHz}$ corresponds to a relaxation time $T_{1,q} = \kappa_q^{-1} = 25\mu s$, long enough to ensure low dark count rates according to Eq.5.47 for typical detection times $T_d \sim 5\,\mu s$ and qubit thermal occupation $p(e|0) \sim 0.01$.

Qubit	
$\omega_q/2\pi$	6.136 GHz
$\chi_q/2\pi$	$\sim$ 200 MHz
$\chi_b/2\pi$	3 MHz
$\chi_w/2\pi$	8 MHz
$T_{1,q}$	25 µs
Buffer mode	
$\omega_b/2\pi$	7.19 GHz
$\kappa_b/2\pi$	0.96 MHz
Waste mode	
$\omega_w/2\pi$	7.69 GHz
$\kappa_w/2\pi$	2.86 MHz

Table 5.1: Table of the simulated parameters.

Simulating non-linear terms with the EPR method

The dispersive couplings are then simulated using the Energy Participation Ratio method, which we briefly describe now. This method applies when several microwave modes are non-resonantly coupled to a Josephson junction, as is the case in our design. The energy participation ratio of mode i into the junction p_i is defined as the ratio between the electromagnetic energy stored into the junction when mode i is excited. This quantity is directly accessible from the linear simulations performed in HFSS. In Fig.5.10a, the electric field profile of the qubit mode is shown (mode 1 in the Table of Fig.5.9); the fraction of the field located at the junction yields the participation ratio p of the linear qubit mode into the junction. This can then be used to estimate the qubit anharmonicity χ_q using formulas derived in Ref. [69] and Annex. In Fig.5.10b, the electric field profile when the buffer mode is excited is shown. Although it is dominantly located around the buffer resonator electrode as expected, field lines are also visible at the junction location; they yield the participation ratio of the buffer mode in the junction, which in turn yields quantitative predictions for the dispersive coupling χ_b.

The EPR method can be conveniently implemented by using the Python library *pyEPR* provided and maintained by Z. Minev, Z. Leghtas and P.Reinhold.

The simulation results for the chip design depicted in Fig. 5.8 are shown in Table 5.1. In addition to the frequencies and damping rates already discussed, we now access the dispersive coupling terms. The qubit term χ_q is much larger than the others, since the participation ratio of the qubit mode is evidently also larger. This term describes the qubit anharmonicity. A value of 200 MHz is typical for a transmon qubit. Dispersive couplings χ_b in the $3-5$ MHz are obtained, as requested in the design section.

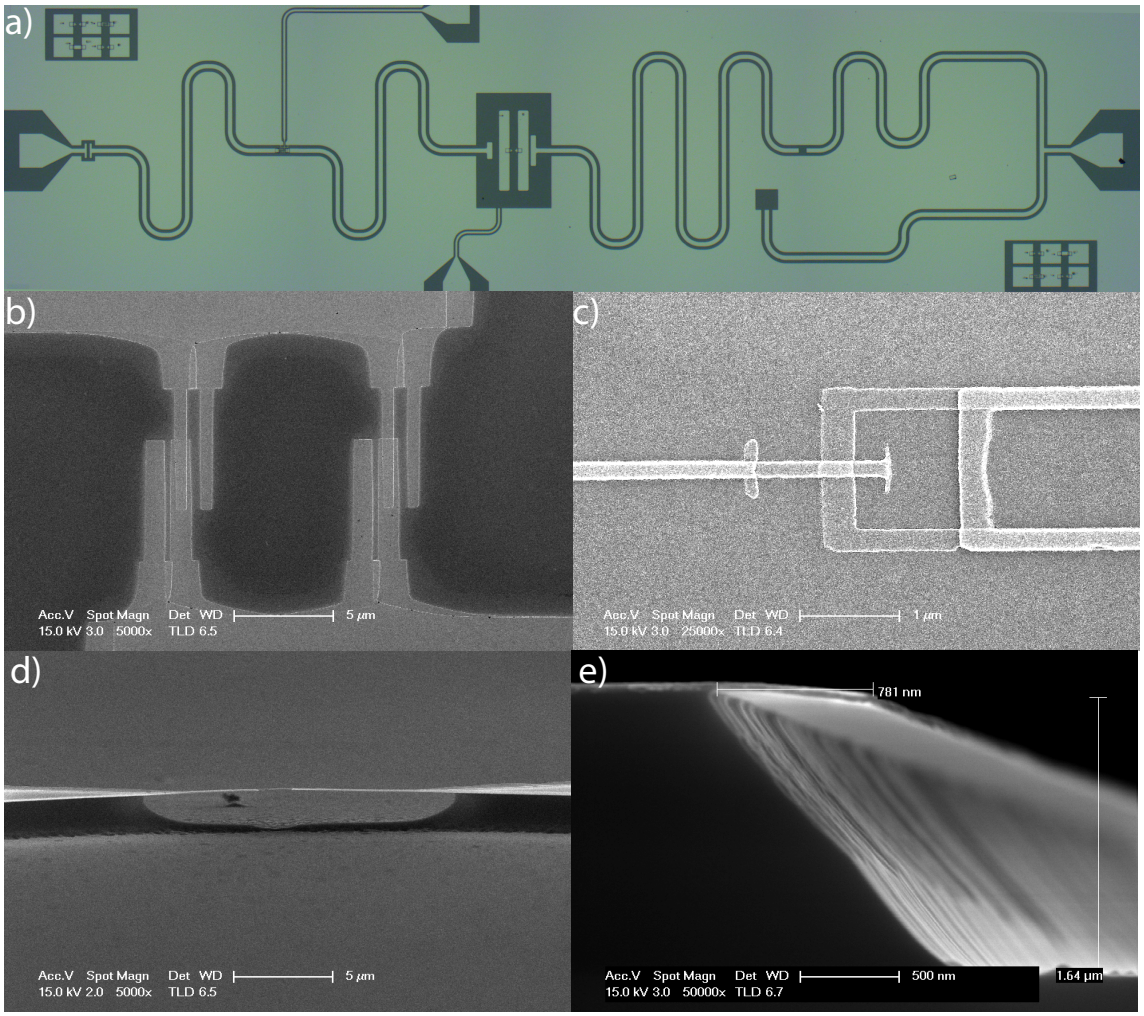

Figure 5.11: **SMPD chip.** (a) Optical microscope image of the SMPD chip, patterned in aluminium (light green) on top of silicon chip (dark green). (b) Scanning-electron-microscope (SEM) image of the SQUID loop embedded in the buffer resonator. (c) SEM image of the Josephson junction of the transmon qubit. (d,e) Trenching of the silicon with SF_6 is adopted in order to reduce microwave losses. As a results the Josephson junction is suspended (d) as well as the outer sides of CPW lines (e).

Fabrication

The SMPD circuit is fabricated using wet etching of a $60\,\mathrm{nm}$ aluminium layer evaporated on a high-resistivity intrinsic silicon substrate. Before metal deposition, the substrate is pre-cleaned with a SC1 process. The wafer is first immersed for $10\,\mathrm{min}$ at $80\,°\mathrm{C}$ in a bath of 5 parts H_2O to 1 part H_2O_2 $(30\,\%)$ to 1 part NH_4OH $(29\,\%)$, then is immersed for $2\,\mathrm{min}$ in HF $(5\,\%)$ solution to remove the surface oxide. The substrate is then loaded in an electron-beam evaporator within $10\,\mathrm{minutes}$, after which a $60\,\mathrm{nm}$ aluminium layer is deposited. Patterning of the circuit is achieved by electron beam lithography of a UV3 resist mask, followed by wet etching of the aluminium using a TMAH-based developer (Microposit CD26). The Josephson junctions (see Fig.5.11(b-c)) are evaporated using the Dolan bridge technique and recontacted to the main circuit through aluminium bandage patches [70]. Finally, circuit gaps are isotropically trenched ($\sim 2\,\mu$m, see Fig.5.11(d-e)) with a

SF6-based reactive ion etch, which has shown to decrease the internal losses of superconducting resonators [16, 71]. The resulting $10\,\mathrm{mm}$ by $3\,\mathrm{mm}$ chip, shown in Fig. 5.11(a), is glued and wired to a Printed-Circuit-Board, placed in a copper box, magnetically shielded, and attached to the cold stage of the dilution refrigerator. The full detailed recipe can be found in Fig. B.1.

5.5 Setup

The measurement setup used to characterize the SMPD is shown in Fig. 5.12. It consist of a room-temperature (top) and a low-temperature (bottom) part. Components that are present but which do not enter into play during this characterization are shown in transparency, notably the spin resonator which lays 15 MHz away from the characterization point, well outside the bandwidth of the SMPD and of the characterization pulses. This very same setup will also be used for the spin-detection experiment illustrated in the next chapter, with the difference that all the elements will be tuned into resonance.

Room temperature setup

The room-temperature setup includes four microwave sources and two four-channel arbitrary waveform generators (AWG 5014 from Tektronix). Microwave pulses needed to operate the detector are generated by mixing the output of a source with two AWG channels driving the I and Q ports of an I/Q mixer at intermediate frequencies indicated in fig. 5.12. SMPD operation and characterization requires:

- a dc flux-bias of the SQUID in the buffer resonator, in order to tune ω_b. This bias is provided by a dc current source (Yokogawa 7651) connected to an on-chip antenna close to the SQUID (input line 4 in fig. 5.12).
- Microwave pulses at the pump frequency ω_p to satisfy the four-wave mixing condition $\omega_\mathrm{p} = \omega_\mathrm{q} + (\omega_\mathrm{w} - \chi_\mathrm{w}) - \omega_\mathrm{b}$. Pump pulses are generated through I/Q mixing of a source Keysight, shown in purple in Fig. 5.12). The signal is amplified and then passed through a $70\,\mathrm{MHz}$ band-pass filter to prevent spurious side-band resonances to generate unwanted mixing at other frequencies, pump pulses reach the cryostat through line 6.
- Microwave pulses to readout the qubit state via the qubit-state-dependent dispersive shift of the buffer resonator. Such pulses, at frequency $\omega_\mathrm{b} - \chi_\mathrm{qb}$ (the buffer frequency when qubit in the excited state), are generated from the mixing of the output of a Keysight microwave generator (yellow) and conveyed to the fridge via line 3.
- Microwave pulses at the waste frequency ω_w to reset the qubit, generated via a Vaunix Labbrick, shown in green in Fig. 5.12 and routed to the fridge via line 5.
- Microwave pulses at the qubit frequency ω_q in order to calibrate qubit readout and characterize the qubit properties ($T_{1,\mathrm{q}}$, $T_{2,\mathrm{q}}$). A single sideband mixer is used to generate qubit pulses by mixing of the signal from a Vaunix Labbrick, shown in blue in Fig. 5.12.
- JPA control: qubit readout pulses are amplified by a flux-pumped JPA in degenerate mode, JPA frequency is adjusted via dc flux biasing of a SQUID

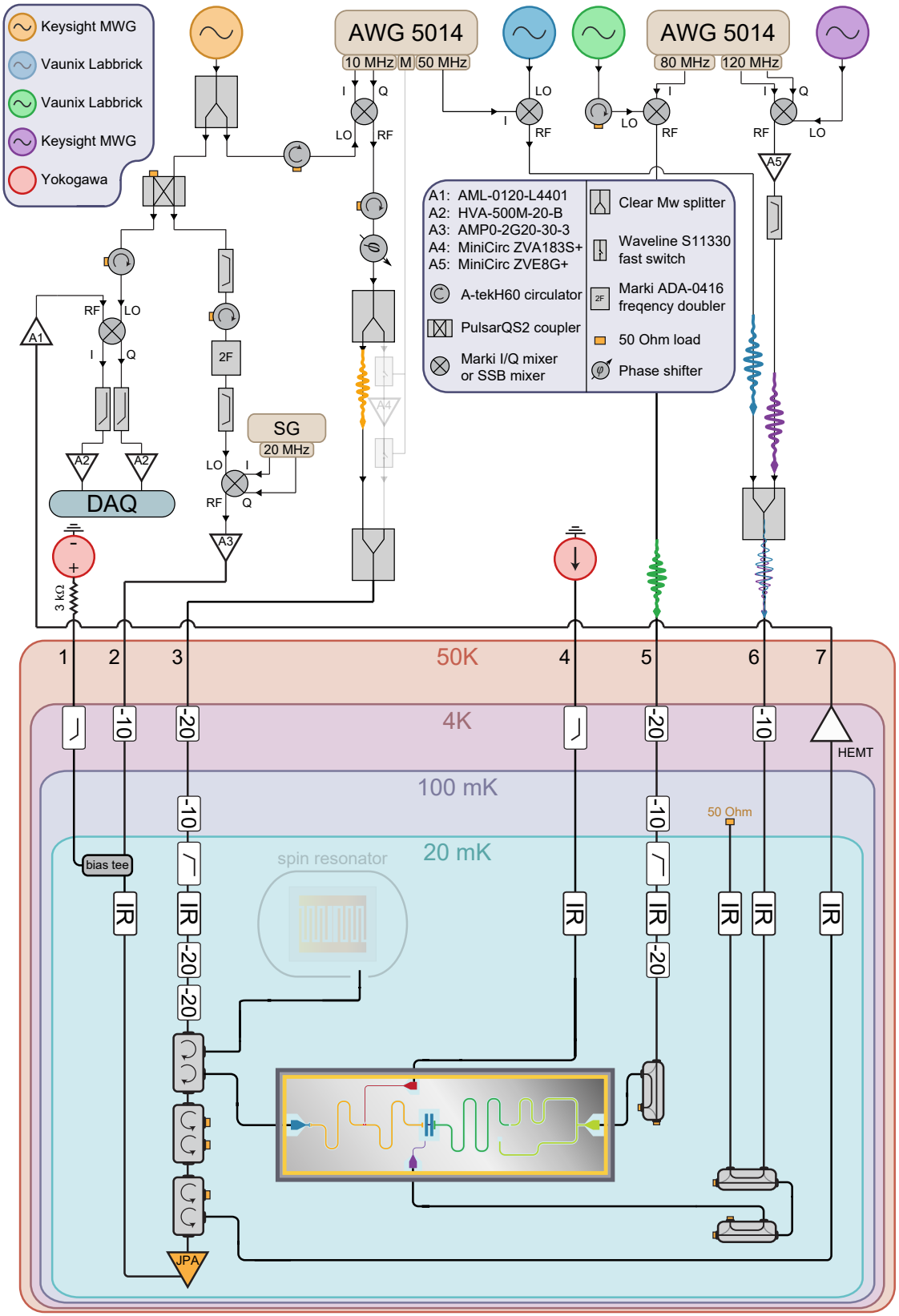

Figure 5.12: **Setup.** The setup used for the characterization of the SMPD. At this stage the spin resonator (transparent) is detuned and does not affect microwave signals sent to the SMPD chip.

array by means of an adjacent on-chip antenna. This antenna is fed by a constant voltage source biasing a resistor at room-temperature (line 1 in Fig. 5.12). The JPA also requires flux-pumping to achieve gain. This pump tone is generated by frequency-doubling of the source used to generate the readout pulses (line 2 in Fig. 5.12), followed by mixing with a double intermediate frequency produced by a signal generator ('SG' in Fig. 5.12). The relative phase between signal and pump is adjusted with a phase shifter for maximum gain on the signal-bearing quadrature.

The SMPD output (line 7) consists of the qubit readout pulses, whose phase encodes the qubit state as explained in Section 5.2. The pulses are further amplified at room-temperature, mixed with the local oscillator (yellow source in the schematics), and finally digitized, yielding the quadratures $I(t)$ and $Q(t)$. They oscillate at the intermediate frequency $\omega_{\mathrm{IF}} = 10\,\mathrm{MHz}$. Numerical demodulation yields the average quadrature of the qubit readout pulse, $I = \int I(t)dt$ and $Q = \int Q(t)dt$.

Low temperature setup

As explained later (in section 5.6), qubit readout is performed via the SMPD buffer resonator. Readout pulses are sent through line 3, which is heavily attenuated at low-temperatures in order to minimize spurious qubit excitations and therefore dark counts (see Fig. 5.12). At 20 mK, the pulse is reflected on the spin resonator, routed by the same circulator towards the SMPD input (buffer resonator), and the signal reflected on the SMPD is finally routed towards the input of the JPA and the detection chain. Two double circulators isolate the SMPD from the JPA, to minimize noise reaching the SMPD. The JPA output (reflected signal) is routed to a High-Electron-Mobility-Transistor (HEMT) amplifier from Low-Noise Factory anchored at the 4K stage of the cryostat, and then to output line 7. Infrared (IR) filters are inserted on all the lines leading to the SMPD to minimize out-of-equilibrium quasi-particle generation leading to dark counts.

Line 4 is used to pass current to tune the magnetic flux Φ through the SQUID loop. It is filtered at $4\,\mathrm{K}$ by a low-pass filter with cutoff frequency $450\,\mathrm{MHz}$, and at $20\,\mathrm{mK}$ by an IR filter.

Line 5 is used to send pulses to the waste resonator, to reset the SMPD state. Similar to line 3, high attenuation levels at low temepratures are needed to minimize the thermal photon population at ω_{b} and therefore the dark counts. At $20\,\mathrm{mK}$, this attenuation reaches $40\,\mathrm{dB}$, with $20\,\mathrm{dB}$ implemented by a physical attenuator and $20\,\mathrm{dB}$ by a directional coupler.

Line 6 conveys to the SMPD the pump tone. In order to minimize heating of the low-temperature stage by the strong pump , the necessary attenuation of the line at $20\,\mathrm{mK}$ is achieved with a $20\,\mathrm{dB}$ directional coupler that routes most of the pump power towards the $100\,\mathrm{mK}$ stage where it gets dissipated. A further $20\,\mathrm{dB}$ attenuation is provided by a second directional coupler.

5.6 Characterization

In this section we characterize the various SMPD sub-circuits.

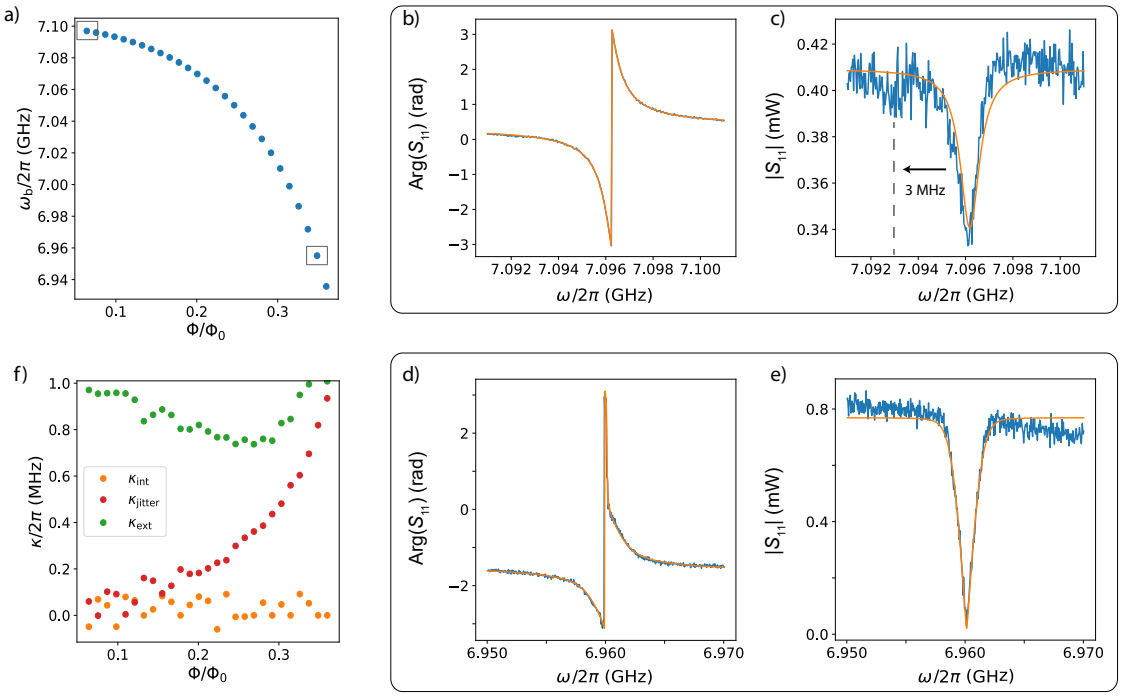

Figure 5.13: **Buffer characterization.** (a) Buffer frequency $\omega_b(\Phi)$ as a function of the magnetic flux threading the squid loop. A tunability range $\sim 200\,\mathrm{MHz}$ is achieved. Boxes indicates the zero-bias point and the working point, at which the detector is characterized. (b) Phase and (c) amplitude of the buffer reflection coefficient S_{11} at the zero bias point. A small feature visible at $3\,\mathrm{MHz}$ from the resonance frequency is due to the dispersive shift of ω_b because of the dispersive coupling with the qubit. Orange lines represent fits using resonator input-output theory. The extracted frequency and energy decay rates are reported in table 5.2. (d) Phase and (e) amplitude of the buffer reflection coefficient S_{11} at the characterization point $\omega_b = 6.96\,\mathrm{GHz}$, close to the working point $\omega_b = 6.94\,\mathrm{GHz}$. Orange lines represent fits using resonator input-output theory and taking into account frequency jittering due to noise on the flux bias. The extracted frequency and energy decay rates are reported in table 5.2. (f) Energy decay rates of the buffer resonator as a function of the magnetic flux bias Φ threading the SQUID. The values are obtained from a fit of the S_{11} parameter, by taking into account the jittering of the buffer frequency.

Buffer resonator

The buffer resonator is first characterized by a measurement of its reflection coefficient $S_{11}(\omega)$ with a VNA. The resonance at $\Phi = 0$ is shown in Fig.5.13(b-c). A fit using the formula of Ch.2 yields $\omega_b(0)/2\pi = 7.096\,\mathrm{GHz}$, $\kappa_{b,ext}/2\pi = 0.95\,\mathrm{MHz}$, and $\kappa_{b,int}/2\pi = 0.09\,\mathrm{MHz}$. These values are in agreement with the design parameters.

In the $|S_{11}|(\omega)$ data, we observe, in addition of the main Lorentzian dip indicative of the buffer resonator response, another smaller dip at lower frequency. As we will see later, this is due to the coupling to the qubit. The main peak is the buffer resonator response when the qubit is in its ground state (with the highest probability), whereas the other peak is the resonator response when the qubit is in its excited state (which occurs with much lower probability, explaining the lower amplitude of this second peak). From the frequency separation between

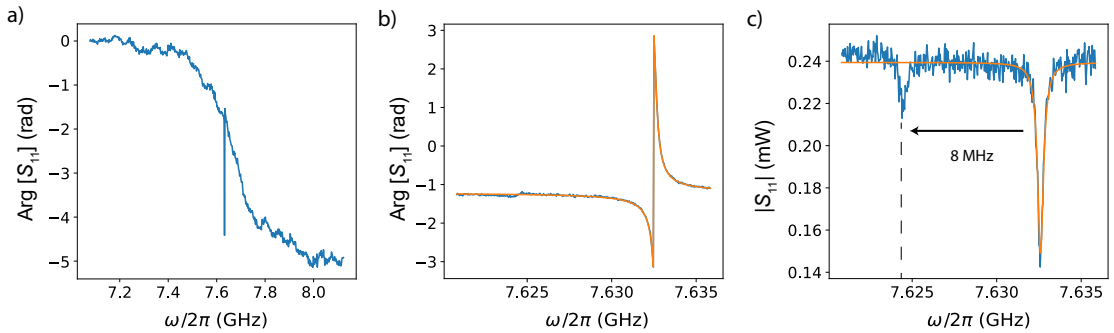

Figure 5.14: **Purcell and waste characterization.** (a) Phase of the S_{11} reflection coefficient measured in correspondence of the Purcell filter. The waste resonator appears as a much narrower resonance aligned with the filter. (b) Phase and (c) amplitude of the waste resonator reflection coefficient S_{11}. The feature visible $8\,\mathrm{MHz}$ aside from the resonance frequency is due to the dispersive shift of ω_w due to the dispersive coupling with the qubit. Orange lines represent fits using resonator input-output theory. The extracted frequency and energy decay rates are reported in table 5.2.

these two peaks, we directly get $\chi_\mathrm{b}/2\pi \simeq 3\,\mathrm{MHz}$, again in agreement with the design value.

The buffer resonator frequency is then measured as a function of the applied magnetic flux Φ. Figure 5.13(a) shows the resulting $\omega_\mathrm{b}(\Phi)$, with Φ expressed in units of the flux quantum Φ_0. As expected, the buffer resonator frequency is tunable over a range $\sim 200\,\mathrm{MHz}$. At finite values of Φ, we observe that the resonance shape deviates from a Lorentzian, as expected in presence of a Gaussian-distributed flux-noise. We therefore fit the curves with the model presented in Ch.2, with the variance of the frequency jitter $\kappa_\mathrm{b,jitter}$ as an additional fitting parameter. The results are shown in Fig. 5.13(f). While the coupling and internal resonator losses remain constant with Φ, $\kappa_\mathrm{b,jitter}$ increases with Φ, roughly following the slope $d\omega_\mathrm{b}/d\Phi$. This confirms the presence of flux-noise in the SQUID loop. The typical noise variance extracted from this analysis $\kappa_\mathrm{b,jitter}/(d\omega/d\Phi) = 5.5\times10^{-5}\,\Phi_0$ is much larger than the typical value of flux-noise in superconducting circuits, which is on the order of $1-5\times10^{-6}\Phi_0$. A posteriori, we understand that this was due to the use of a noisy current source and to insufficient filtering in this particular experiment. The buffer resonator response close to the spin resonator frequency (20 MHz residual detuning) is shown in Fig.5.13(d-e).

Waste resonator

The waste resonator reflection coefficient is shown in Fig.5.14. A large frequency range (see Fig.5.14(a)) shows the 2π phase shift due to the Purcell filter, centred on $7.6\,\mathrm{GHz}$, and of width $\sim 200\,\mathrm{MHz}$ consistent with the design value (see Fig. 5.8). Around $7.6\,\mathrm{GHz}$, a much narrower resonance is the waste resonator response. It is shown more closely in Figs.5.14(b-c). As in the buffer case, we see, in addition to the main resonator peak, another smaller peak, at a distance $\chi_\mathrm{w}/2\pi \sim 8\,\mathrm{MHz}$, which we again attribute to the qubit excited state. Fitting the main peak with the formula derived in 2 yields $\omega_\mathrm{w}/2\pi = 7.633\,\mathrm{GHz}$, $\kappa_\mathrm{w,ext}/2\pi = 0.38\,\mathrm{MHz}$, and $\kappa_\mathrm{w,int}/2\pi = 0.09\,\mathrm{MHz}$. Whereas the frequency is in agreement with the design

Qubit	
$\omega_{\mathrm{q}}/2\pi$	6.135 GHz
$\alpha/2\pi$	$\sim$ 200 MHz
$\chi_{\mathrm{b}}/2\pi$	3.1 MHz
$\chi_{\mathrm{w}}/2\pi$	8.2 MHz
$T_{1,\mathrm{q}}$	$\sim 9\,\mu$s
$T_{2,\mathrm{q}}$	$\sim 10\,\mu$s
p_{thermal}	~ 0.012

Buffer mode	unbiased	biased
$\omega_{\mathrm{b}}/2\pi$	7.09 GHz	6.96 GHz
$\kappa_{\mathrm{b,ext}}/2\pi$	0.95 MHz	0.99 MHz
$\kappa_{\mathrm{b,int}}/2\pi$	0.09 MHz	0.08 MHz
$\kappa_{\mathrm{b,jitter}}/2\pi$	0.00 MHz	0.74 MHz

Waste mode	
$\omega_{\mathrm{w}}/2\pi$	7.62 GHz
$\kappa_{\mathrm{w,ext}}/2\pi$	0.38 MHz
$\kappa_{\mathrm{w,int}}/2\pi$	0.09 MHz

Table 5.2: Table of the experimental parameters.

value, the coupling rate is one order of magnitude lower. This is due to a mistake in the design of the coupling capacitance between the waste resonator and the Purcell filter. As explained in section 5.2, efficient photon detection is nevertheless still possible, by tuning properly the pump amplitude to reach the impedance matching condition.

Transmon qubit

Detecting the qubit requires to use the qubit state readout technique presented in Section 5.2. In principle, this can be achieved using its dispersive coupling either to the buffer or to the waste resonator. The waste resonator would be a logical choice for several reasons. First, the waste resonator frequency is fixed, which is convenient for readout. Second, qubit readout pulses may heat the attenuators, especially when the SMPD is operated in the cyclic mode. This heating is less harmful if it happens on the waste line than on the buffer input line. However, because of the low value of κ_{w} as explained earlier, qubit readout via the waste resonator would be too slow, and in this thesis manuscript we have instead performed qubit readout through the buffer resonator.

The first step of qubit characterization consists in measuring its spectrum. This is achieved using the dispersive coupling to the buffer resonator. As seen in Fig.5.15(a), a low-amplitude microwave signal at frequency ω_{b} is continuously sent to the device, and the reflection coefficient measured with a VNA. A second microwave tone of varying frequency ω is sent at the same time on the qubit pump line. When $\omega = \omega_{\mathrm{q}}$, the qubit gets excited, leading to a change in S_{11}, as seen in Fig.5.15(b). We obtain $\omega_{\mathrm{q}}/2\pi = 6.145\,$GHz, close to the design value. Two peaks

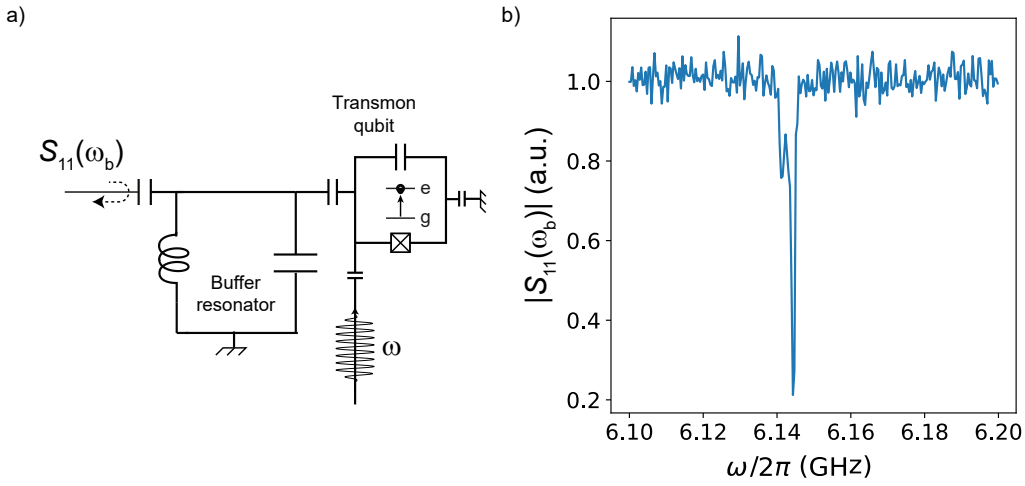

Figure 5.15: **Two-tone spectroscopy.** (a) Principle of two-tone spectroscopy of the transmon qubit through the buffer resonator. The reflection coefficient $S_{11}(\omega_\mathrm{b})$ of the buffer resonator is probed while a microwave tone at frequency ω is shone on the qubit. When $\omega = \omega_\mathrm{q}$ the qubit is partially excited and S_{11} changes due to the dispersive shift of the buffer frequency. (b) Absolute value of the buffer reflection coefficient as a function of ω.

are visible in Fig. 5.15b, because the qubit frequency depends on the photon number in the buffer resonator (see Section 5.2), which fluctuates between 0 and 1, due to the continuous probing by the tone at ω_b. The qubit frequency slightly changed upon thermal cycles of the cryostat; in the final measurements reported in this thesis, $\omega_\mathrm{q}/2\pi = 6.135\,\mathrm{GHz}$.

Once identified ω_q, qubit single-shot readout is performed by sending a weak ($\bar{n} \approx 0.3$) $1.2\,\mu$s-pulse at frequency $\omega_\mathrm{b} - \chi_\mathrm{b}$ on the buffer line. If the qubit is in $|g\rangle$, the pulse is reflected without phase shift, since the buffer resonator frequency is then ω_b. If the qubit is in $|e\rangle$, the pulse is reflected with a π phase shift since it is then at resonance with the buffer resonator. This is visible in Fig.5.16(a-b), which shows the distribution of (I, Q) values obtained by repeating a qubit readout pulse 5×10^3 times, in a situation where the qubit is with comparable probability in $|g\rangle$ or in $|e\rangle$. We see that the distribution is centred on 2 values, corresponding to the 2 qubit states. A histogram of I is also shown in Fig.5.16(c-d). We define the qubit state threshold at $I_\mathrm{th} = 2.5\,\mathrm{mV}$; when $I < I_\mathrm{th}$ the qubit is declared in $|g\rangle$; and in $|e\rangle$ if $I > I_\mathrm{th}$. By repeating the readout pulse many times, the qubit excited state probability p_e is then obtained.

Even without applying a pulse, a finite excited state probability $p(click|0) = 0.012$ is measured (see fig. 5.16(c)), much larger than the value expected at thermal equilibrium at $20\,\mathrm{mK}$. This well-known phenomenon in circuit Quantum Electrodynamics has been attributed to high-frequency radiation close to the frequency of the aluminum gap ($80\,\mathrm{GHz}$), whose absorption in the thin-film that constitutes the qubit leads to quasi-particle generation and recombination, and finally to spurious qubit excitations. As explained in Ch.2, they are one of the main limitations of the SMPD, as they will cause dark counts. The qubit readout fidelity is $p(click|1) = 0.62$, limited by qubit relaxation during readout and to the threshold, chosen to minimize the ratio $p(click|0)/p(click|1)$.

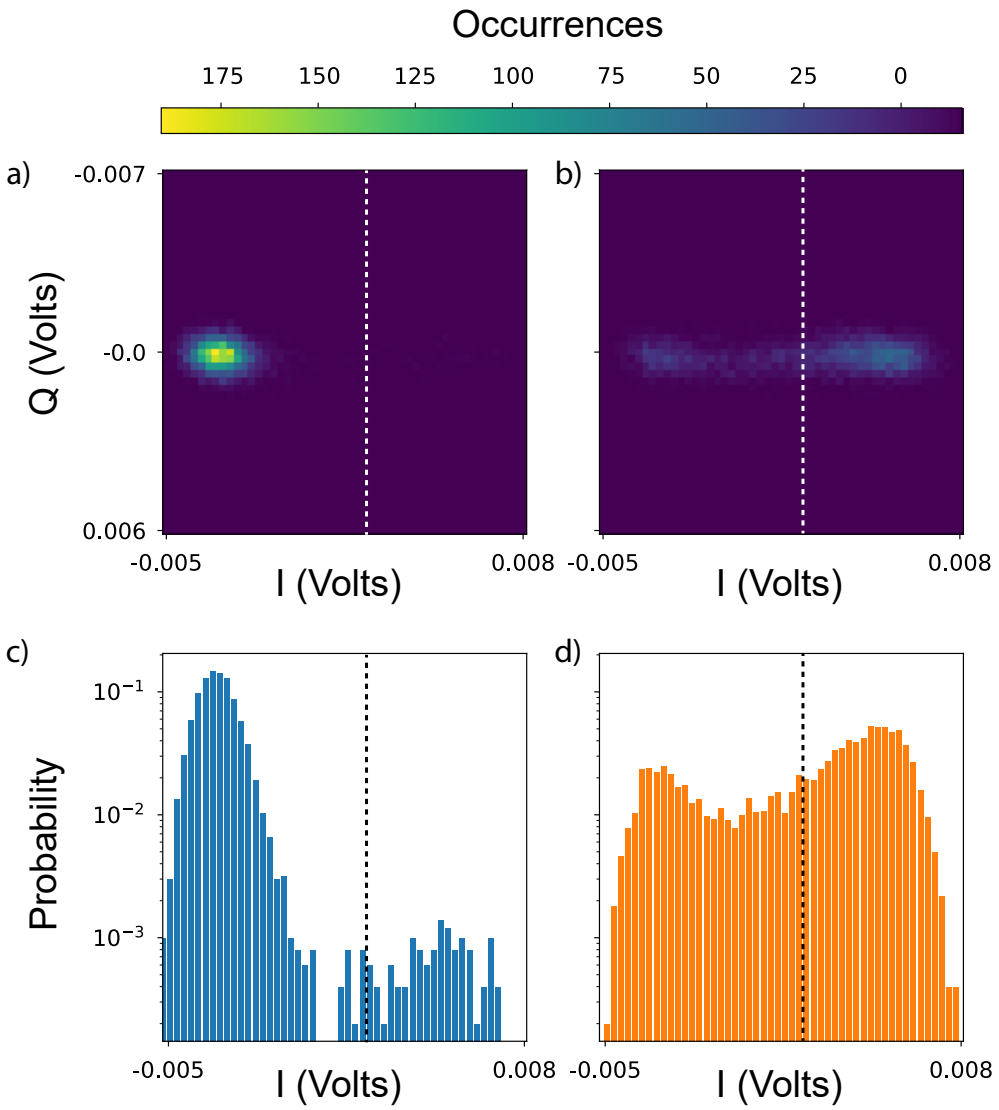

Figure 5.16: **Qubit readout.** (a) Histogram showing the occurrences for the average (I, Q) of a pulse used to dispersively readout the qubit through the buffer resonator. Here no pulse is applied to the qubit prior to the measurement. The region of the I, Q plane where most of the measurements fall is identified with the qubit being in its ground state. (b) Qubit readout histogram recorded after applying a π-pulse on the qubit. The distribution is now centred on 2 values, corresponding to the 2 qubit states. The presence of finite probability of finding the qubit in the ground state even after a π-pulse is due to qubit relaxation during the measurement. White dotted line indicates the threshold used to discriminate between ground and excited states. (c,d) Projection on the I axis of the above histograms, normalized and plotted in logaritmic scale.

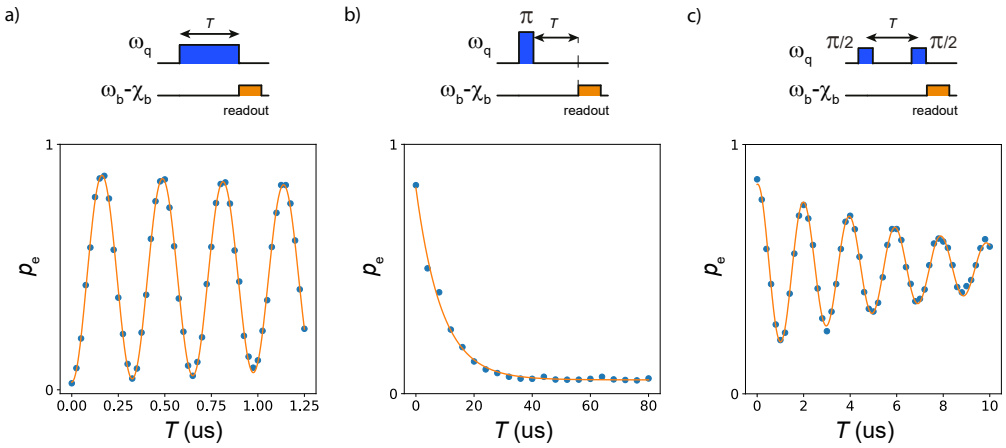

Figure 5.17: **Qubit characterization.** (a) Qubit Rabi sequence (top). A pulse of duration T and frequency ω_q is shone on the qubit then its state is readout. (bottom) Rabi oscillations are measured in the excited state probability p_e as a function of T (blue dots). A fit (orange line) allows to extract the pulse duration corresponding to a π-pulse. (b) Qubit T_1 sequence (top). The qubit is excited with a π-pulse and then readout after a time T. (bottom) Qubit excited state probability $p_e(T)$ (blue dots), exponential fit (orange line) leads to a qubit relaxation time $T_{1,q} = 9\,\mu s$. (c) Qubit Ramsey sequence (top). Two $\pi/2$ pulses are applied to the qubit, separated by a free evolution time T, then the state is readout. (bottom) Measured (blue dots) and fitted (orange line) $p_e(T)$. Decay of Ramsey fringes allows to extract a qubit decoherence time $T^*_{2,q} = 10\,\mu s$

Qubit coherence times

We now move to the characterization of the qubit. First, we calibrate the duration and amplitude to realize a π-pulse on the qubit. This is done via a measurement of Rabi oscillations: a resonant tone of amplitude A and varying duration T is applied to the qubit, followed by a readout pulse. Repetition of the experiment allows to extract p_e for each pulse duration, shown in figure 5.17b, revealing Rabi oscillations. The duration corresponding to a π-pulse is the shortest for which maximum p_e is achieved (~ 120 ns).

A qubit property of primary importance for the SMPD operation is the relaxation time $T_{1,q}$. It is measured by applying a π-pulse and measuring p_e after a waiting time T. The resulting $p_e(T)$ is shown in figure 5.17; an exponential fit yields $T_{1,q} \simeq 9\,\mu s$.

Another qubit property is its coherence time $T^*_{2,q}$, which is an interesting figure of merit although it has no impact on the SMPD performance. It is measured via a Ramsey sequence: a detuned (~ 1 MHz) $\pi/2$-pulse is applied to the qubit, which is then left evolving freely during a time T, after which a second $\pi/2$-pulse is applied followed by qubit state readout. As shown in Fig. 5.17c, p_e oscillates at the detuning frequency for varying T. An exponential fit of the oscillations envelope yields $T^*_{2,q} \sim 10\,\mu s$.

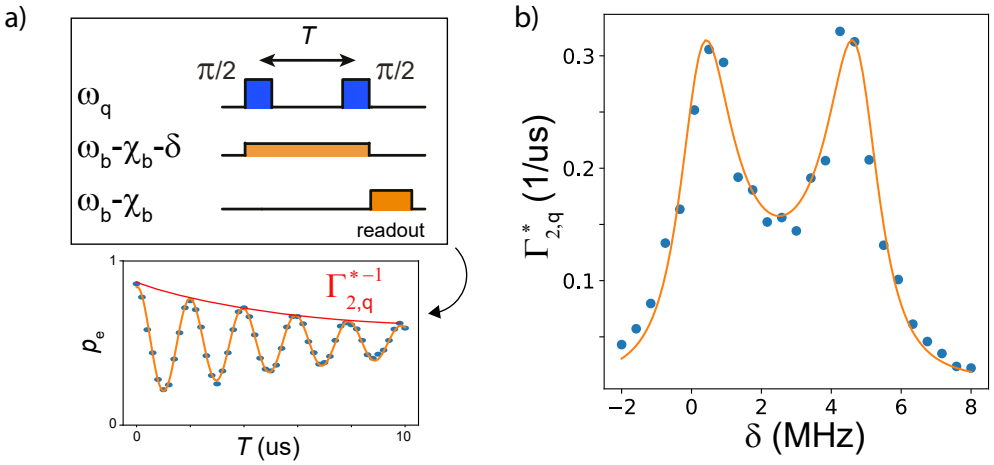

Figure 5.18: **Photon number calibration.** (a) Pulse sequence used for photon number calibration (top). A Ramsey sequence composed of two $\pi/2$ pulses separated by a time T is played while the buffer resonator is populated with a weak coherent state of frequency $\omega_\mathrm{b} - \chi_\mathrm{b} - \delta$. (bottom) Varying T allows to extract frequency and decay rate $\Gamma^*_{2,\mathrm{q}}$ of Ramsey fringes. (b) Ramsey fringes decay rate $\Gamma^*_{2,\mathrm{q}}$ (blue dots) as a function of δ. Analytical fit (orange line) allows to extract the average number of photons populating the buffer resonator at resonance.

Photon number calibration

For estimating the detection efficiency of the SMPD, it is essential to determine quantitatively the photon flux impinging on the buffer resonator. This requires in-situ calibration, since the line attenuation is not known precisely enough for this purpose. This calibration is performed using the photon-number-induced qubit decoherence, as explained in Section 5.2.

The calibration protocol is depicted in Fig. 5.18. Ramsey fringes are measured, while a constant-amplitude pulse at frequency $\omega_\mathrm{b} - \chi_\mathrm{b} + \delta$ is sent to the buffer resonator. For each value of δ, the dephasing rate $T^{*-1}_{2,\mathrm{q}}$ is fitted as explained earlier. The resulting $T^{*-1}_{2,\mathrm{q}}$ curve is shown in Fig. 5.18. We observe two peaks, corresponding to the qubit-dependent buffer resonator frequencies ω_b and $\omega_b - \chi_b$. A fit using Eq.5.21 yields the average photon number at resonance with the buffer frequency for the pulse amplitude used, $\bar{n}$, and therefore a quantitative calibration of the photon flux.

Calibrating the number of photons in presence of flux noise

As mentioned earlier, the buffer resonator experiences significant flux noise that needs to be taken into account carefully in the photon calibration. To do so, we convolve response of the expected photon-induced dephasing and detuning with a Gaussian distributed frequency noise.

$$\langle \Delta_s \rangle + i\langle \Gamma_s \rangle = \frac{1}{\sigma\sqrt{2\pi}} \int_{-\infty}^{+\infty} d\delta' e^{-\frac{\delta'^2}{2\sigma^2}} \frac{-4\chi|\epsilon|^2}{(\kappa_\mathrm{b} + 2i(\delta - \delta'))^2 + \chi^2}, \tag{5.48}$$

where ϵ is the drive rate, χ the dispersive shift and κ_b, the dissipation rate in the absence of jittering. The magnitude of this noise σ and κ_b are independently calibrated using the fit of the reflection coefficient of the resonator at various

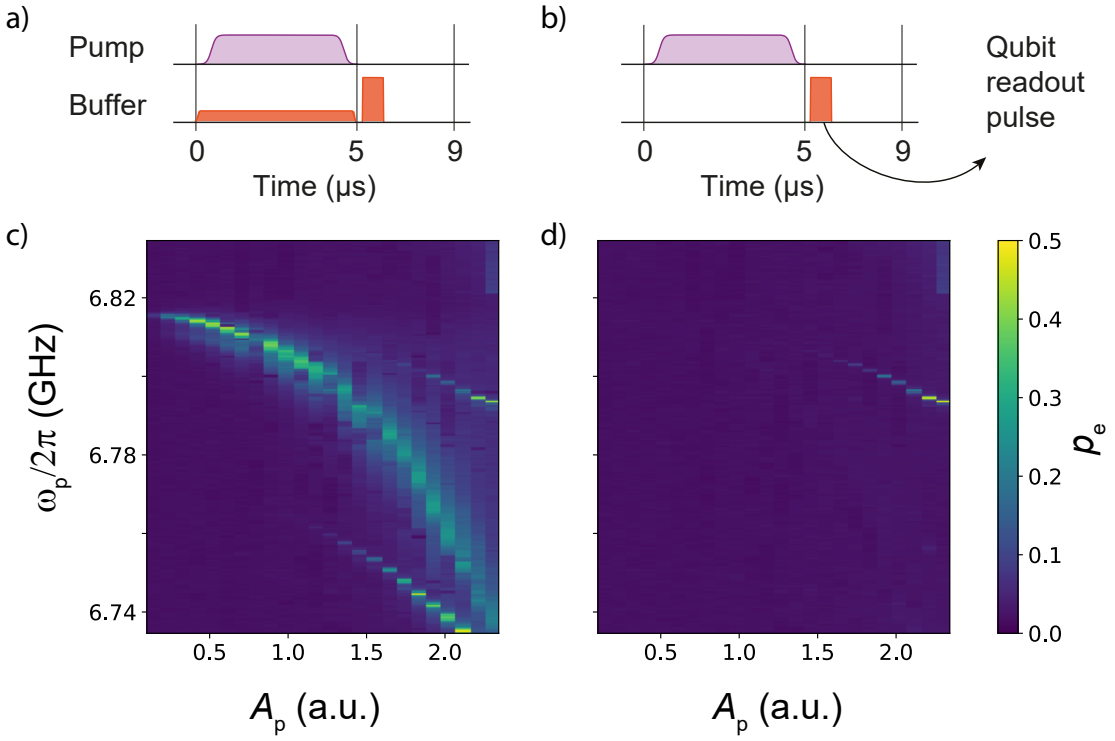

Figure 5.19: **Four-Wave Mixing process** (a,b) Pulse sequences used for the calibration of the pump frequency ω_p and amplitude A_p to activate the four-wave mixing process. A pump tone is shone on the qubit while a weak coherent tone is shone (a) or not (b) on the SMPD. Finally the qubit state is read out. (c) Probability of measuring the qubit in $|e\rangle$ as a function of ω_p and A_p. When the four wave mixing condition is matched $\omega_\mathrm{p} = \omega_\mathrm{q}(A_\mathrm{p}) + \omega_\mathrm{w} - \chi_\mathrm{w} - \omega_\mathrm{b}$, then p_e increases. Spurious processes involving other mixing terms are also recorded. (d) Same measurement repeated with no signal at the input of the SMPD. Spurious processes not involving the buffer tone are not suppressed.

flux bias point as described in section 5.6. The fit of photon-induced dephasing is shown in Fig.5.18. Once the drive rate is determined, the absolute input power is then given by:

$$P_\mathrm{in} = \frac{|\epsilon|^2}{\kappa_\mathrm{b} - \kappa_\mathrm{b}^\mathrm{loss}} \hbar\omega_\mathrm{b} \tag{5.49}$$

with κ_b^loss the internal loss rate of the resonator in the absence of jitering infered from the reflection coefficient fit.

4-wave mixing

After the individual characterization of each element composing the SMPD chip, we move to the calibration of the four-wave mixing process enabling photon detection.

In order to adjust the pump frequency to satisfy the 4-wave mixing condition, we use the pulse sequence described in Fig. 5.19a. A weak signal is sent to the buffer resonator at frequency ω_b, while the pump frequency ω_p and amplitude A_p are varied. The qubit excited state probability p_e is measured as an indicator of the occurrence of the wave-mixing process. The result is shown in Fig. 5.19c.

For each pump amplitude A_p we observe a peak in p_e appearing at a frequency $\omega_\mathrm{p} = \omega_\mathrm{p}^0(A_\mathrm{p})$ depending on A_p. This frequency is close to the expected four-wave mixing condition $\omega_\mathrm{p} = \omega_\mathrm{q} + \omega_\mathrm{w} - \chi_\mathrm{w} - \omega_\mathrm{b}$, and depends on A_p in a quadratic way. This dependence is expected based on the photon-pump-induced qubit Stark shift (cf. Eq. B.114). At higher powers, two additional peaks are seen to appear, also dependent on A_p.

To confirm that the main peak is due to the four-wave mixing process, we repeat the same measurement in the absence of the weak tone on the buffer resonator (see Fig. 5.19b). The main peak as well as the low frequency one are no longer visible, indicating that their origin is a parametric mixing process involving buffer photons. We attribute the main peak, associated to higher transition amplitude, to the desired four-waves mixing process. We attribute the secondary peak to another unidentified mixing process. The high-frequency satellite peak is always present, indicating that it does not depend on the buffer photon population. In the following, we disregard these extra spurious non-linear processes, by tuning the pump parameters in such a way that the four-wave mixing peak is well-separated from them. For our experiment the chosen working point is $\omega_\mathrm{p}/2\pi = 6.81$ GHz and $A_\mathrm{p} = 0.8$.

Reset calibration

The remaining part of the SMPD detection cycle is the reset, whose calibration we discuss now. The pulse sequence used is shown in Fig. 5.20a. A microwave pulse of duration T_r is sent toto the waste resonator input at its resonance frequency ω_w (thus populating the resonator with photons), together with a pump tone at the same frequency ω_p used for the detection part, and calibrated pump amplitude amplitude $A_\mathrm{p} = 0.8$; these pulses are followed by qubit readout. Figure 5.20b shows p_e as a function of the reset tone amplitude A_r for a fixed reset length $T_\mathrm{r} = 2\,\mu$s. We observe that p_e is minimised for $A_\mathrm{r} = 0.9$. For this chosen amplitude, figure 5.20d shows p_e when applying a reset pulse of duration T_r after a π-pulse. Reset of duration $T_\mathrm{r} \sim 2.5\,\mu$s enables to reduce the averaged qubit population by a factor 10. There is a trade-off between the reset duration and the residual excited state population. Longer reset pulses reduce the residual excited state population leading in principle to lower dark counts but they also decrease the duty cycle and thus the overall efficiency. With $2.5\ \mu$s pulses, the qubit is initialized with an residual population around 1.5×10^{-3}, starting from a thermal population around 1.5×10^{-2}. The qubit will then rethermalize at a rate $p_\mathrm{th}/T_1 \sim 10^{-3}\ \mu\mathrm{s}^{-1}$, the residual population is therefore doubled after only $1\ \mu$s, longer reset pulses would then be ineffective at improving the dark-count rate. In practice, we measure a residual population around 3×10^{-3} however this population is overestimated due to the finite duration of the readout and the unloading time of the pulses.

Note that after a photon detection, the qubit is in its excited state. A single reset pulse is unable to reset the qubit perfectly, however after only a few sequences the remaining qubit population vanishes exponentially quickly. As a consequence, we observe weak correlation between successive detection events.

Figures of merit

We now move to the measurement of the SMPD figures of merit: efficiency, bandwidth and dark counts.

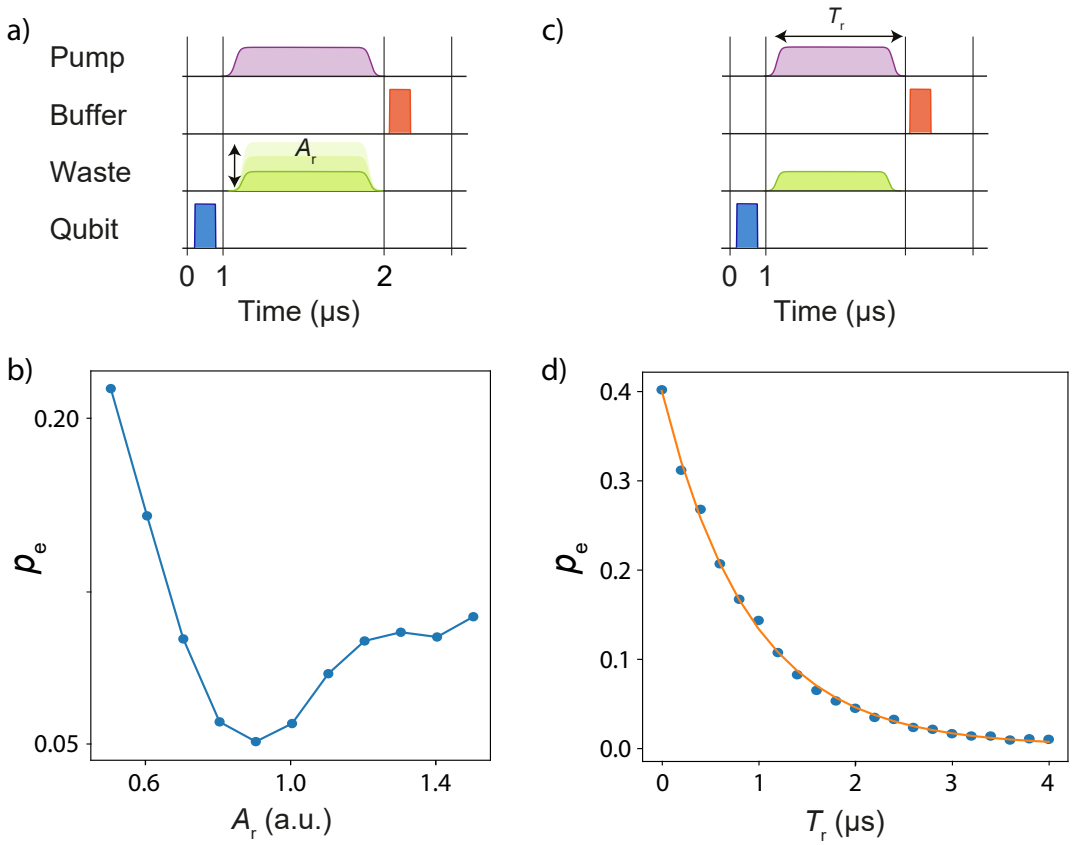

Figure 5.20: **SMPD reset calibration.** (a) Pulse sequence used to calibrate the reset tone amplitude A_r. The qubit is excited by a π-pulse, then the pump is turned on and a tone at frequency ω_w and amplitude A_r is shone on the waste resonator. Then qubit is readout. (b) Qubit excited state probability $p_\mathrm{e}(A_\mathrm{r})$ as a function of the reset amplitude. Maximum reset efficiency is reached for $A_\mathrm{r} = 0.9$. (c) Pulse sequence used to calibrate the reset duration T_r. (d) Qubit excited state probability $p_\mathrm{e}(T_\mathrm{r})$ as a function of the reset duration, at the calibrated amplitude.

Efficiency

We now measure the detection efficiency η_d. The protocol is described in Fig. 5.21. A microwave pulse is sent at the buffer resonator frequency, populating it with a coherent state of amplitude ϵ, calibrated via the procedure described in Section 5.6, together with a pump pulse of duration $T_\mathrm{d} = 5\,\mu\mathrm{s}$. The qubit excited state probability is then given by

$$p_\mathrm{e} = \eta_d \epsilon^2, \tag{5.50}$$

From the measured $p_\mathrm{e}(\epsilon^2)$ (see Figure 5.21b), we extract $\eta_\mathrm{d} = 0.53 \pm 0.1$. As explained in Section 5.3, the detection efficiency for a single photon state is expected to depend on T_d via Eq.5.45. The measurement of $\eta_d(T_\mathrm{d})$ is shown in Fig. 5.21c (blue dots). Fit using Eq.5.45 (orange line) is in good agreement with the data, and allows to extract a four-wave mixing efficiency $\eta_\mathrm{4wm} \simeq 1$, the limiting factor in the efficiency being $T_\mathrm{1,q}$ qubit relaxation. This confirms that other spurious processes, identified at calibration (see Fig.5.19), do not affect the working of the SMPD.

Note that the maximum efficiency $\eta_\mathrm{d}^\mathrm{max} = 0.68 \pm 0.1$ is reached for $T_\mathrm{d} \sim 1\,\mu$s. However, we choose to operate at $T_\mathrm{d} = 5\,\mu$s to increase the duty cycle of the

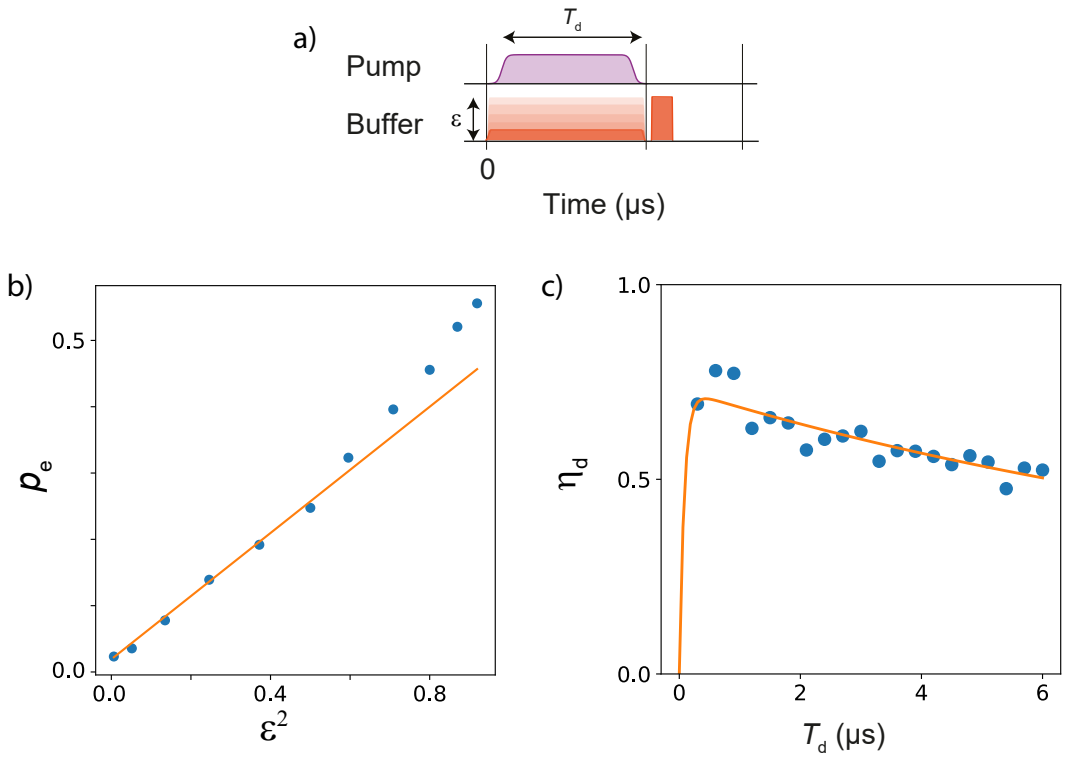

Figure 5.21: **Photodetection efficiency measurement.** (a) Pulse sequence used for the measurement of the detection efficiency η_d. With the pump on a weak coherent state of amplitude ϵ is shone on the SMPD for a time T_d. Then the qubit state is readout. (b) Qubit excited state probability $P_e(\epsilon^2)$ as a function of the coherent state power for fixed $T_d = 5\,\mu s$. A linear fit allows to extract the slope η_d. (c) Measured (blue dots) and fitted (orange line) efficiency η_d as a function of the detection duration T_d.

detector. At this working point one obtains $\eta_d = 0.53 \pm 0.1$, limited by qubit lifetime and the excited state readout fidelity.

Detection bandwidth

To characterize the detection bandwidth Δ_{det}, we measure the detection efficiency η_d as a function of the frequency ω of a weak coherent tone with average photon number $|\epsilon|^2 < 1$. The data are shown in figure 5.22c, yielding a FWHM detection bandwidth $\Delta_{det}/2\pi = 2.1$ MHz. This value deviates from $\Delta_{det}/2\pi = 0.85$ MHz, predicted by the coupled-cavities model presented in section 5.2. However, by considering the jittering of the buffer resonator frequency caused by flux-noise, via gaussian convolution, we reach good agreement as shown in Fig.5.22c.

We note that, since $\Delta_{det} > \kappa$, the SMPD bandwidth is larger than the spin resonator bandwidth. Therefore, there should be no filtering of the photons emitted by the spins by fluorescence.

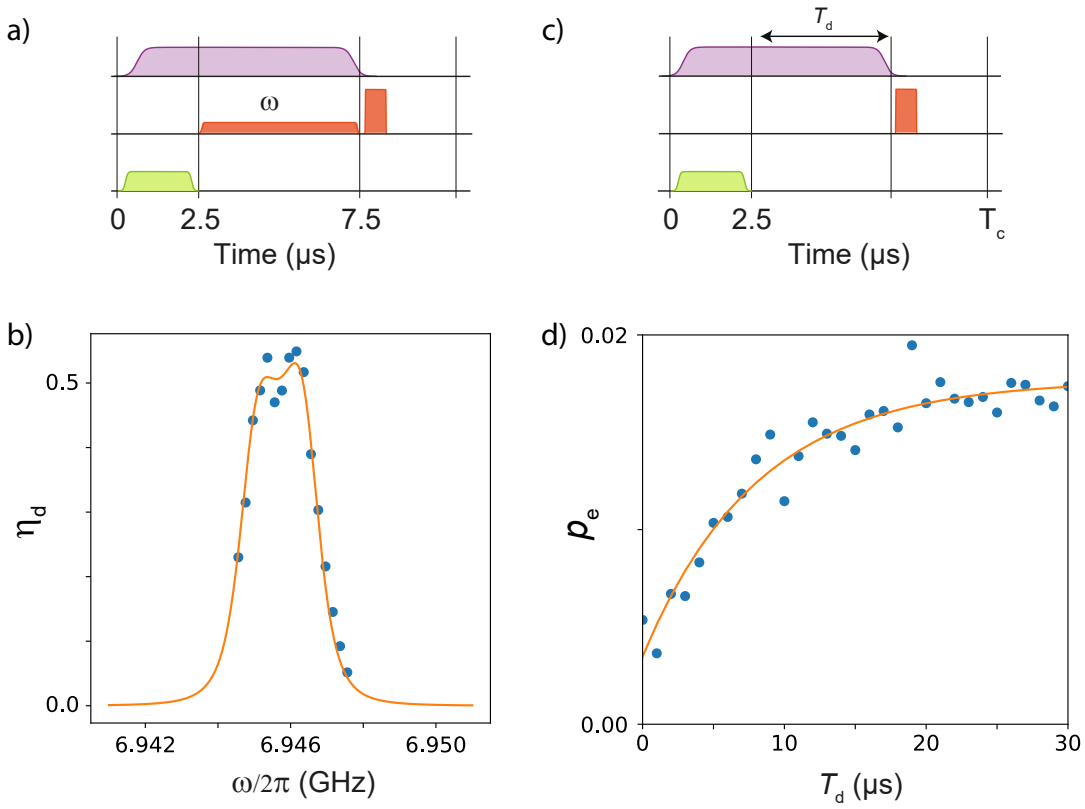

Figure 5.22: **SMPD FOM.** (a) Pulse sequence used to measure $\eta_{\rm d}(\omega)$. After the reset the pump is activated for $T_{\rm d} = 5\,\mu$s while a weak tone at frequency ω is shone on the SMPD. (b) Measured (blue dots) and computed (orange curve) $\eta_{\rm d}(\omega)$. (c) Pulse sequence used to measure the dark count rate $\nu_{\rm dc}(T_{\rm d})$. After the reset the pump is activated for a duration $T_{\rm d}$ before qubit readout. (d) Measured (blue dots) and fitted (orange line) $p_{\rm e}(T_{\rm d})$. The measured dark count rate is obtained as $\nu_{\rm dc} = p_{\rm e}/T_{\rm c}$.

Dark counts

The measured rate is related to the probability of qubit excitation during a detection cycle:

$$\nu_{\rm dc} = \frac{p_{\rm e}}{T_{\rm c}}. \tag{5.51}$$

We measure $\nu_{\rm dc}$ by measuring $p_{\rm e}$ in absence of signal as function of the detection window duration $T_{\rm d}$, after a reset step (see Fig.5.22b). The reset step initializes the qubit at $p_{\rm e} \approx 0.35\times10^{-2}$, below its thermal excitation probability of 1.2×10^{-2}. After the reset, $p_{\rm e}$ increases with increasing detection time $T_{\rm d}$, attaining a maximum value $p_{\rm e}^{\rm eq} = 1.77\times10^{-2}$ in a characteristic time $T_{1,\rm q} = 9\ \mu$s (see Fig.5.22d). In our experiments we will use $T_{\rm d} = 5\,\mu$s on a total cycle time $T_{\rm c} = 11.7\,\mu$s, which gives $\nu_{\rm dc} = 0.85\,$counts/ms.

Note that the attained qubit equilibrium population $p_{\rm e}^{\rm eq} = 1.77\times10^{-2}$ measured in the detection process is higher than the qubit thermal population $\sim 1.2\times10^{-2}$, measured in absence of the pump tone. The excess $\delta p_{\rm e} \sim 0.6\times10^{-2}$ is due to the presence of the pump activating the four-wave mixing that can affect $p_{\rm e}$ in two ways. A first contribution can come from the pump heating the qubit. This effect can be isolated by shining a pump tone detuned from the four-wave mixing match-

ing condition, in doing so we measure a negligible rise of the excited population, smaller than 10^{-3}, compared to the population in absence of pumping. The second effect contributing to δp_{e} is attributed to the finite temperature of the buffer line, populated with thermal photons that triggers the detector over its full bandwidth Δ_{det} and leads to dark counts that are integrated over the qubit lifetime T_1. The expected rise of qubit population is thus given by $\delta p_{\mathrm{e}} = \eta_{\mathrm{d}} \Delta_{\mathrm{det}} T_1 p_{\mathrm{th,buffer}}/(2\pi)$. Substitution of the measured δp_{e} gives a thermal occupancy of the buffer line of $p_{\mathrm{th,buffer}} \sim 1 \times 10^{-3}$ that corresponds to a residual temperature for the microwave line of ~ 45 mK.

Operating the photon counter

To operate the photon counter we repeat cyclically the detection sequence shown in figure 5.23(a). The sequence is composed by a reset part of duration $T_{\mathrm{r}} = 2.5\,\mu$s, a detection part of of duration $T_{\mathrm{d}} = 5\,\mu$s and a qubit measurement plus dead time part, $T_{\mathrm{m}} \approx 4.2\,\mu$s, for a total cycle length of $T_{\mathrm{c}} = 11.7\,\mu$s. The detection duty cycle is $\eta_{\mathrm{duty}} = 0.43$. One measurement trace, of few seconds duration, consists of $\sim 10^6$ detection cycles.

When no signal is sent to the detector we measure clicks corresponding to dark counts, as shown in the top part of Fig.5.23(b). By acquiring several measurement traces, we observe that the dark count rate ν_{dc} increases over time, reaching a steady state value $\nu_{\mathrm{dc}} = 1.53\,\mathrm{ms}^{-1}$ (see Fig.5.23(c), note that on the plot the starting point is at 1.25, higher than expected due to temperature rise caused by previous sequences). This increase is attributed to the heating of the cold stage of the refrigerator, due to the continuous power delivered by detection sequences. Moreover, relevant measurements in the next chapter will be performed after reaching thermal equilibrium $\nu_{\mathrm{dc}} = 1.53\,\mathrm{ms}^{-1}$.

When we apply a weak coherent state to the input of the detector we observe an increased number of counts (see Fig.5.23(b), bottom). The SMPD can detect one photon per detection cycle, and a significant probability of having more than one photon in the detection window leads to saturation. This can be assessed in the calibration procedure, the number of detected photons starts becoming non linear as the power of the coherent tone is increased, as shown in Fig. 6.4d. The non-linearity starts becoming relevant for a photon flux of about $0.2\,\mathrm{photons}/\mu\mathrm{s}$, corresponding to one photon per detection window $T_{\mathrm{d}} = 5\,\mu$s. Note that the relation between the photon flux and the observed count rate is in agreement with the efficiency $\eta_{\mathrm{d}}\eta_{\mathrm{duty}} = 0.23$.

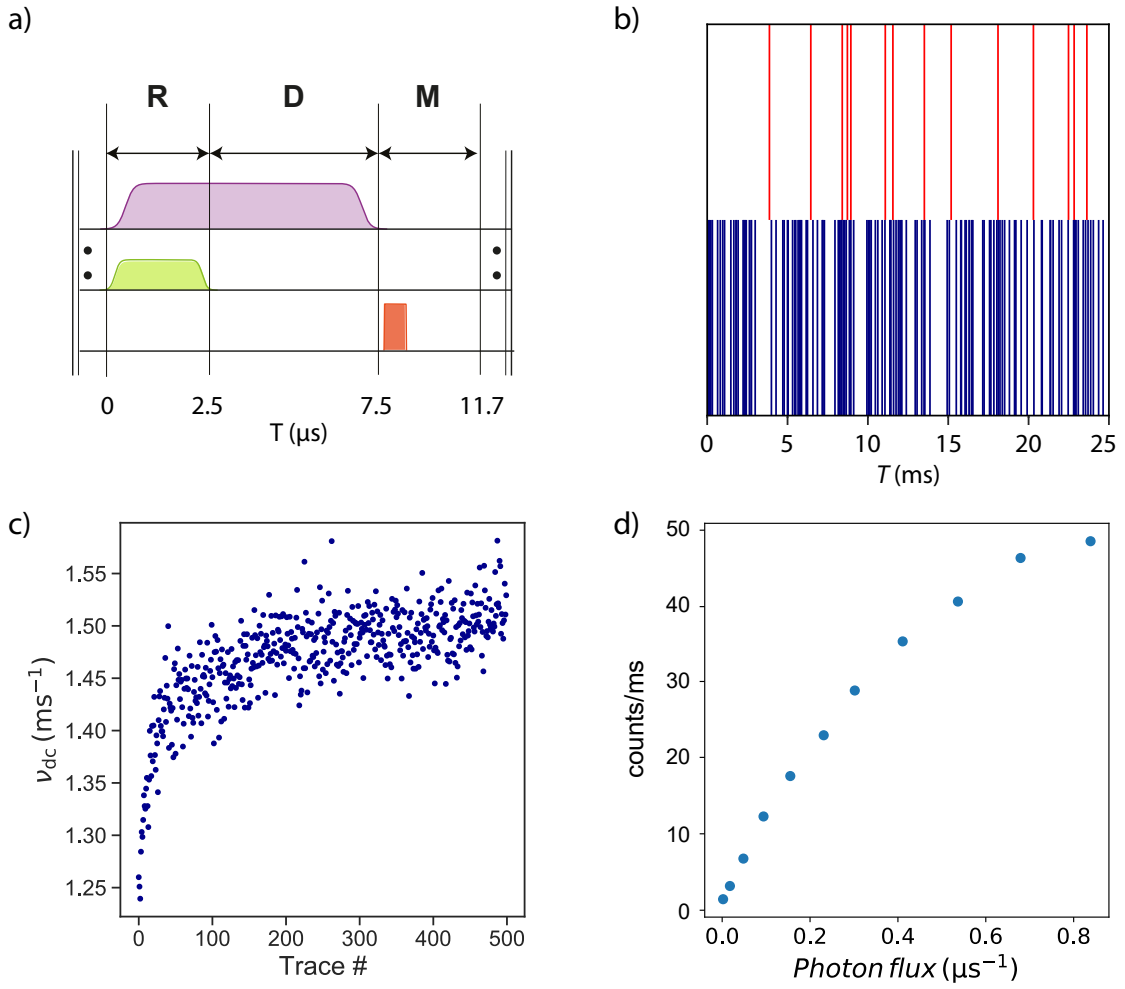

Figure 5.23: **SMPD cyclic operation.** (a) Detection cycle employed in the continuous operation of the SMPD. (b) Photo-detection trace. Each vertical bar corresponds to a click of the detector when shining no tone (red bars) or a weak coherent tone (blue bars). In this plot, each trace consists of $\sim 2 \times 10^3$ SMPD cycles. (c) Dark count rate ν_{dc} measured over one trace of $\sim 2\,s$ for subsequent measurement traces. ν_{dc} increases due to the heating induced by the fast repetition of detection cycles, and saturates at $1.53\,\mathrm{counts/s}$. (d) Detection count rate measured as a function of the impinging photon flux. The SMPD starts saturating when the flux is greater than one photon per SMPD detection window $\sim 0.2\,\mu\mathrm{s}^{-1}$.

Chapter 6

Detecting spins with a microwave photon counter

We now turn to the central results of this manuscript : the detection of the small ensemble of bismuth donor spins in silicon characterized in Chapter 4, by the SMPD device described in Chapter 5.

We start with a brief state-of-the-art of the detection of spontaneous emission by a spin ensemble, which was demonstrated in pioneering experiments on nuclear spins in the 1980s, using quadrature detection.

We then move to our experiments. We detect the stream of incoherent photons emitted spontaneously by the bismuth donor spins after excitation by a π pulse, using the SMPD. We also use the SMPD for spin-echo detection. We characterize the sensitivity achieved in both methods, and find that fluorescence detection yields a larger signal-to-noise ratio than spin-echo detection. We finally show that SMPD detection enables all the standard ESR spectroscopy characterization (spectroscopy, coherent nutation, coherence time measurements).

6.1 State-of-the-art

Inductive detection of spin fluorescence

The first detection of spontaneous emission by an ensemble of spins was achieved by E. Hahn and J. Clarke at Berkeley [5]. Another major result is the demonstration by R. Ernst that such "spin noise" can also be detected at room-temperature using liquid-state NMR [6]. Here, we briefly describe these two pioneering experiments.

The experiment by Hahn and Clarke [5] is sketched in Fig. 6.1a. A sample of $NaClO_3$ is inductively coupled to a LC resonator, cooled at $4\,$K. The output voltage is amplified by a SQUID amplifier and its power spectrum detected by a Spectrum Analyzer. The resonator frequency is chosen to be resonant with the Nuclear Quadrupolar Resonance of the ^{35}Cl nuclei, at $30\,$MHz. The key result is visible in Fig. 6.1b, which shows the power spectrum obtained after saturating the nuclear spins by a strong pulse. On top of the LC resonator power spectrum (broad Lorentzian), a narrower bump appears at the nuclear spin frequency. This additional noise is the spontaneous emission, at radiofrequency, of the nuclear spin ensemble, upon return to thermal equilibrium.

Compared to our experimental conditions, we can make several comments.

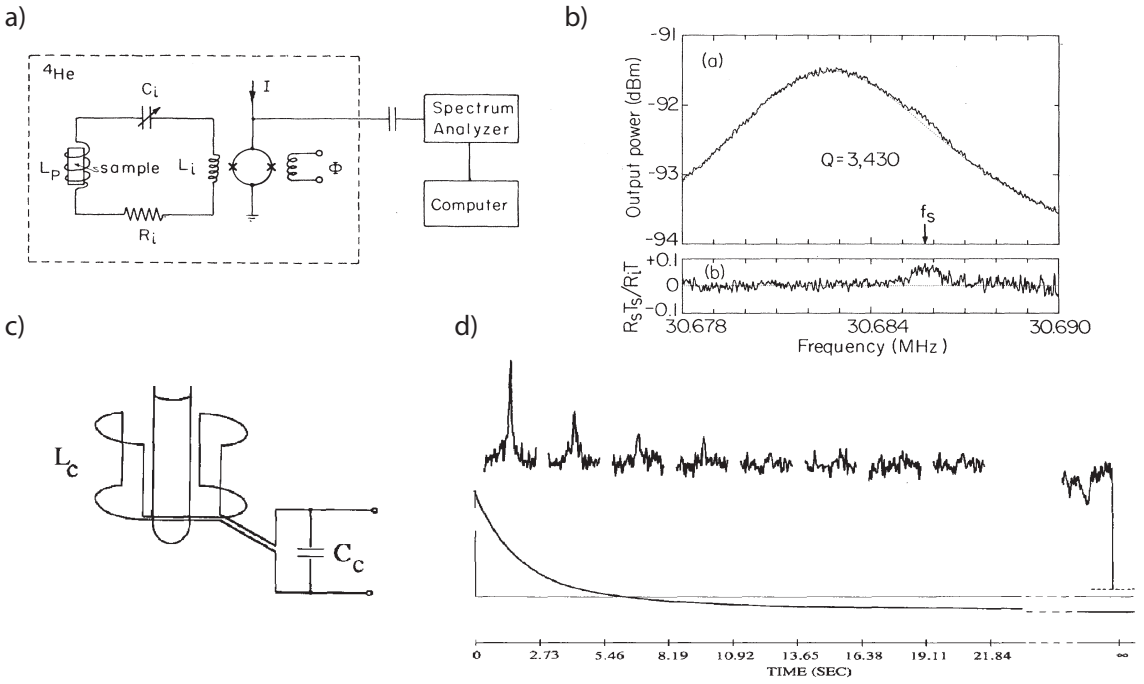

Figure 6.1: **Inductive detection of spin fluorescence.** (a) Illustration of the setup used by Hahn and Clarke [5] A sample of $NaClO_3$ is coupled inductively to an LC resonator and cooled to 4K. A SQUID is used to amplify the output signal. A spectrum analyzer is used to measure the power spectrum, showed in (b). The spontaneous emission of the spin ensemble appears as a slight increase in the Loretzian power sectrum of the resonator. (c) Setup used by McCoy and Ernst for the detection of the fluorescence of a benzene sample at room temperature. (d) The resulting time-resolved output noise power spectrum, after spin saturation, leading to a relaxation time $T_1 = 20\,\mathrm{s}$.

The nuclear spin relaxation time is estimated to be of the order of days, but the radiative relaxation rate is estimated to be $\Gamma_P \sim 10^{-16}\mathrm{s}^{-1}$. Therefore, nuclear spin relaxation is dominantly non-radiative, and a large quantity of nuclear spins ($\sim 10^{21}$) is needed to detect the spontaneously emitted photons. Still, the emitted noise represents $\sim 5\%$ of the total Johnson-Nyquist noise in the detection bandwidth πT_2.

The detection of nuclear spin spontaneous emission at cryogenic temperatures using a SQUID amplifier triggered another pioneering experiment, by McCoy et al [6]. Its purpose is to demonstrate that spontaneous emission can even be detected at room-temperature, using liquid-state NMR spectroscopy and a commercial spectrometer. The experiment is sketched in Fig. 6.1c. A sample of benzene was used, and the proton resonance was detected at 300 MHz at room-temperature. The spin relaxation time is $T_1 = 20\,\mathrm{s}$, here also dominantly non-radiative. Figure 6.1d shows the time-resolved measurement of the output noise power spectrum, after saturating the spins at $t = 0$. At short times, a peak is observed at the proton resonance frequency, indicating emission of spin noise, as expected. Upon return to thermal equilibrium, the bump progressively disappears and is replaced by a dip at thermal equilibrium.

This detection of spontaneous emission at room-temperature is made possible by the narrow linewidth enabled by liquid-state NMR, and the high resonance fre-

quency. It makes it possible to overcome the Johnson-Nyquist and amplifier noise at 300K. Interestingly, we note that the damping in Fig. 6.1d is non-exponential, due to collective effects (called radiation damping in magnetic resonance) because of the large number of spins present in the experiment.

While spin fluorescence is detected in these two experiments, it is considered mostly as a phenomenon of fundamental nature. For instance, McCoy and Ernst explicitly say that "It is unlikely that nuclear spin noise will be of practical importance for analytical NMR. It can only be detected for extremely strong resonance lines and in these cases conveys no structural information that could not be obtained in easier ways." [6]. And indeed, both experiments are performed with quadrature detection, where no gain in sensitivity can be expected compared to pulse detection as explained in Ch.2. In this thesis, our purpose is to revisit spin noise detection, using a SMPD instead of quadrature detection. In the regime where spins are fully polarized and relax radiatively, we will show that fluorescence detection can be more sensitive than pulsed magnetic resonance detection thanks to the SMPD.

Qubit-detected magnetic resonance

Also relevant to this work are experiments where spins are detected using superconducting qubits.

In [72], the ESR spectrum of an ensemble of NV centers in diamond was detected using a transmon qubit. The two systems were interfaced by a frequency tunable resonator. The diamond was directly glued on the superconducting device. The NV spins were first excited by a microwave pulse, and their FID was collected by the resonator. The resonator was then tuned in a few nanoseconds at resonance with a transmon qubit (also on the chip). The two systems then were left in interaction for a time chosen such that the resonator field was entirely transferred into the transmon qubit, whose state was then read-out. Therefore, this experiment demonstrated the detection of the FID emitted by a spin ensemble at the single photon level by the transmon qubit. However, spin fluorescence was not detected.

Another set of experiments uses direct magnetic coupling between a spin ensemble and a magnetically-sensitive superconducting circuit, either a flux-qubit [73, 74], a SQUID embedded in a non-linear resonator, or a superconducting resonator. Here, the spins are not resonant with the superconducting circuit, but their magnetization gives rise to a measurable signal when they are excited, which enables cw spectroscopy. The method was applied to NV centers in diamond and to rare-earth-ions-doped crystals. High spin detection sensitivity were predicted, but not experimentally demonstrated so far. Long spin relaxation times may be a problem at low temperatures, in absence of the Purcell effect.

6.2 Detecting spin fluorescence with a microwave photon counter

We now come to the detection of microwave spin fluorescence using a single photon counter. A complete schematic of the experiment is showed in figure 6.2. The experiment combines the spin resonator device presented in Ch.4, and the SMPD characterized in Ch.5. The two devices are connected via microwave lines and a circulator. The latter makes it possible to drive the spins, and re-directs

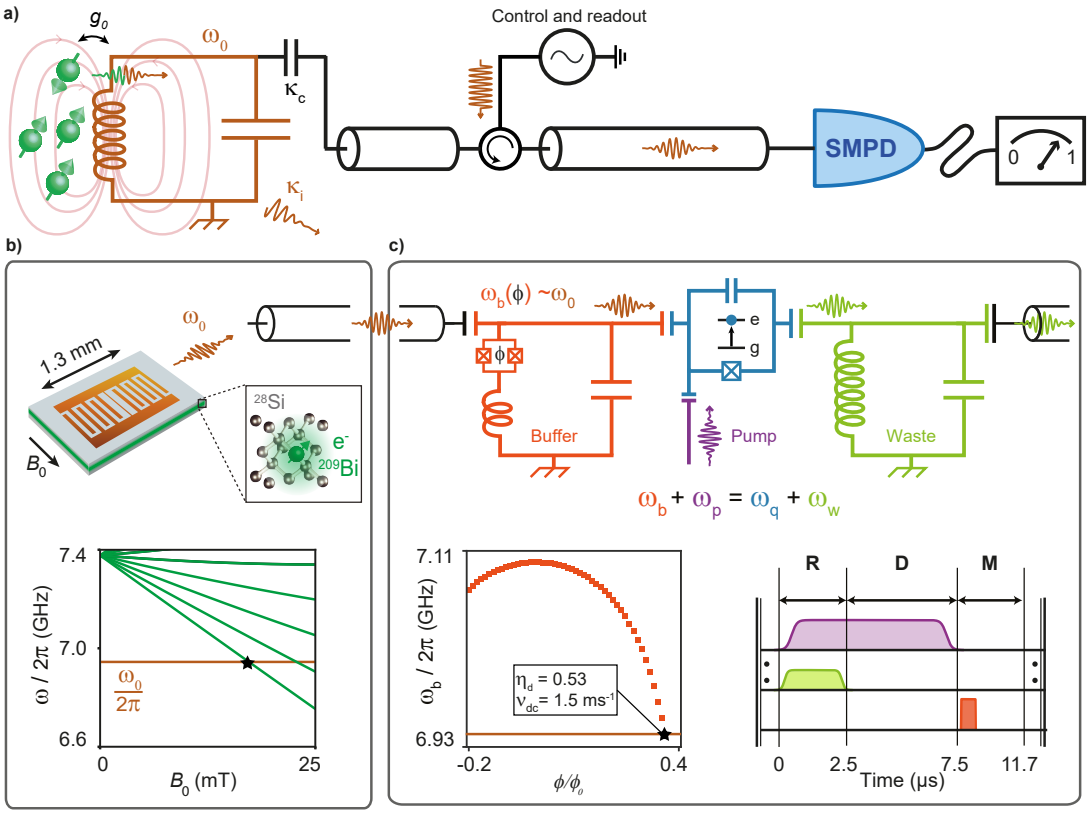

Figure 6.2: **Principle of spin detection with an SMPD.** (a) Schematics of the experiment. The spin device is connected to the SMPD through a microwave line. A circulator allows to drive the spins with microwave pulses and to route the photons emitted by the spins while relaxing radiatively towards the detector. (b) Spin device schematics. A magnetic field $B_0 \sim 17\,\mathrm{mT}$ is applied parallel to the substrate to tune the lowest bismuth donor frequency in resonance with the resonator frequency $\omega_0/2\pi \simeq 6.946\,\mathrm{GHz}$. (c) SMPD device and operation schematics. The buffer resonator frequency is tuned in resonance with the spin resonator $\omega_\mathrm{b}(\Phi) = \omega_0$ applying magnetic flux Φ to the buffer SQUID loop. Incoming photons at the buffer are converted into excitation of the transmon qubit and into a photon in the waste resonator. The SMPD is operated continuously by repeating a Reset-Detection-Measurement cycle of duration $11.7\,\mu\mathrm{s}$. The SMPD efficiency η_d and dark count rate ν_dc at the working point are indicated in the inset.

the reflected pulses as well as spin signal (echo, fluorescence, ...) towards the SMPD input.

Setup

Room-temperature and low-temperature setups are identical to those discussed in Ch4 and Ch5, and showed in figure 6.3. The SMPD is now tuned into resonance with the spin cavity $\omega_\mathrm{b} = \omega_0$. Moreover, experimental sequences now include both pulses driving the spins and pulses needed for the SMPD cyclic operation.

Pulses needed to drive the spins are generated with the same source and I/Q channels as for the qubit readout pulses (Keysight MWG, shown in yellow in Fig. 6.3). Note that, since qubit readout is performed at $\omega_\mathrm{b} - \chi_\mathrm{qb}$ while spins

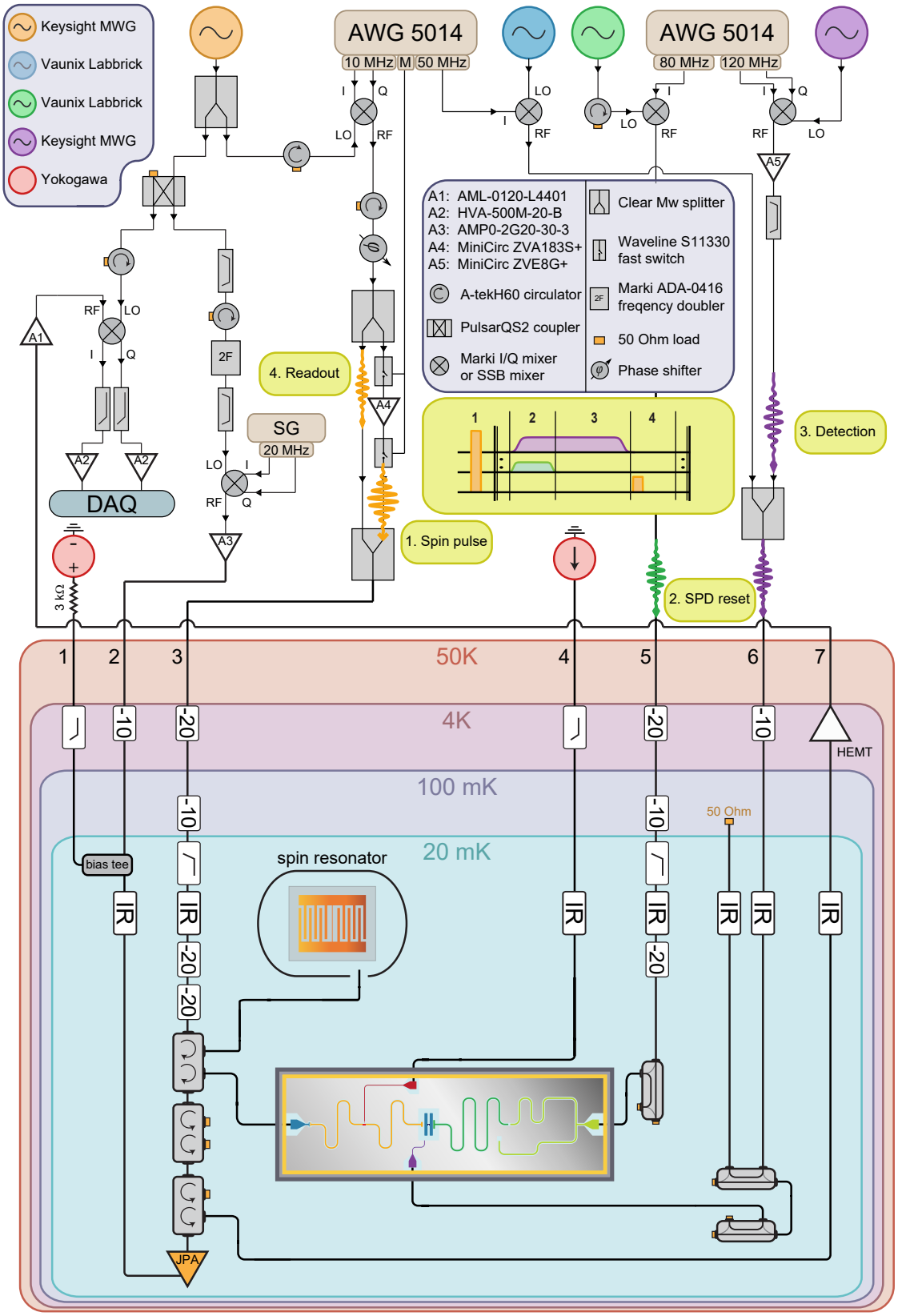

Figure 6.3: **Setup.**

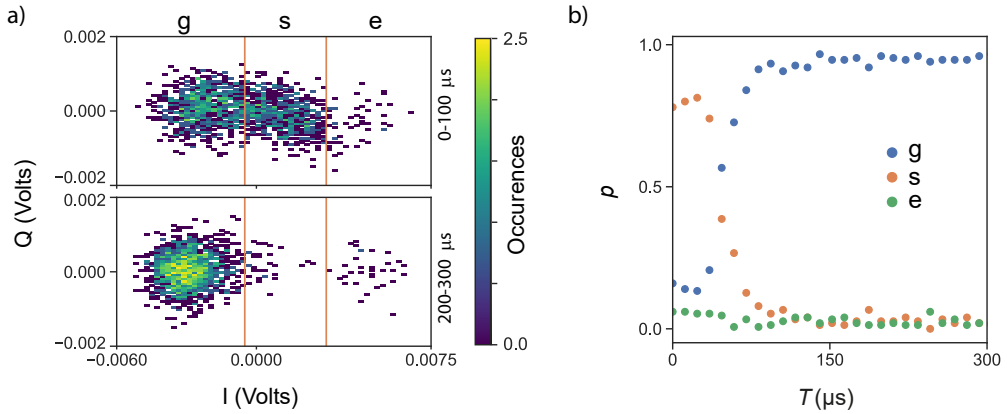

Figure 6.4: **Qubit dead time.** (a) Readout histogram of the state of the qubit after a π-pulse on the spin ensemble. In the first $100\,\mu s$ (top) a consistent fraction of readout outcomes lay in a region of the I, Q plane that is markedly neither ground (g) or excited (e) state, and that we name scrambled state (s). For comparison, after$200\,\mu s$ (bottom) we retrieve the standard qubit readout histogram. (b) Probability of a qubit readout laying in the g, e or s region of the I, Q plane, as a function of the time T after a spin π-pulse. Normal readout is retrieved after $\sim 150\,\mu s$.

are driven at $\omega_0 = \omega_b$, different mixing frequencies are applied for the two pulses. Both types of pulses are sent via the same line (line 3 in Fig. 6.3), but because spin driving pulses require much larger powers than qubit readout pulses, the line is split, the spin pulse is amplified, and then recombined. Two microwave switches are used to isolate the amplification branch outside the spin pulse window, in order to limit the injection of amplifier noise in the line.

The low-temperature setup is identical to the one introduced in section 5.5.

SMPD dead-time

When a control pulse is applied to the spins (for instance, a π pulse), it is reflected on the spin resonator input, and reaches the SMPD buffer input. Moreover, the pulse frequency is resonant with the buffer resonator, since $\omega_b = \omega_0$. A large field build-up in the buffer resonator is therefore unavoidable, which is likely to impact negatively the transmon qubit operation and thus also the SMPD.

In order to characterize the impact of a spin driving pulse on the qubit, we perform the following experiment, described in Fig. 6.4. We compare the outcome of qubit readout in normal conditions as described in Ch.5 (Fig. 6.4a bottom panel) to the outcome of qubit readout following a π pulse applied to the spins (Fig. 6.4a top panel). Whereas in usual conditions, qubit readout yields two well-separated clusters of points in the (I,Q) plane, after a π pulse this is no longer the case. Qubit readout yields a continuum of points, very different from normal transmon readout. Although we do not have a quantitative understanding of the signal visible in this case, we interpret it qualitatively as being caused by excitation of the transmon qubit into states of higher energy than e.

In order to characterize further this behavior, we define two thresholds in I. For the lowest values, the state is assigned to g, for the highest values, the state is assigned to e, and in the middle, it is called s (for *scrambled*). We follow the

time evolution of the qubit state following a π pulse, as a function of the delay T between the π pulse and qubit readout. The result is visible in Fig. 6.4b. We see that for $T > 100\mu$s, only state g is populated, indicating that the qubit is back to its equilibrium population, and that the SMPD can be used. In the following, we discard all the detection events within the first $200\,\mu$s after any spin pulse, so that the SMPD has an effective dead-time of 200μs.

Note that besides the impact that spin pulses have on the SMPD, one may also wonder if the repeated SMPD qubit readout pulses may cause spurious excitation of the spins, since they are sent on the same input line. This is prevented by the fact that, as seen in Ch5, qubit readout is performed at $\omega_{\rm b} - \chi_{\rm b}$ with $\chi_{\rm b}/2\pi \simeq 3\,$MHz, which is detuned from ω_0 by several times the buffer resonator bandwidth $\kappa/2\pi = 0.68\,$MHz.

SMPD detection cycle

The SMPD cycle parameters are close to those described in Ch.5. They are visible in Fig.6.2(c). The total cycle duration is $T_{\rm c} = 11.7\,\mu$s, with a reset step $T_{\rm r} = 2.5\,\mu$s (green + violet pulses), a detection step $T_{\rm d} = 5\,\mu$s (violet pulse) and a qubit readout step $T_{\rm m} \simeq 1.2\mu$s (orange pulse). In addition, a 3μs waiting time between detection and measurement and between two subsequent cycles, in order to ensure that the buffer resonator is empty from readout photons.

We recall that, as reported in section 5.6, the intrinsic detection efficiency measured at $\omega_{\rm b} \sim \omega_0$ for a detection window $T_{\rm d} \simeq 5\,\mu$s, is $\eta_{\rm d} = 0.53 \pm 0.1$, and the the dark count rate is $\nu_{\rm dc} = 0.85\,$clicks/ms at calibration, but it increases to $\nu_{\rm dc} = 1.53\,$clicks/ms during measurements since heating effects play an important role as described below. The detection duty cycle is $\eta_{\rm duty} = T_{\rm d}/T_{\rm c} = 0.43$.

Fluorescence detection

We now come to the implementation of spin fluorescence detection by the SMPD. The experimental sequence is described in Fig.6.5(a). A 1μs π pulse is applied to the spins, after which 2×10^5 SMPD detection cycles are repeated. Each cycle i, centred at time t_i, yields a binary outcome $c(t_i) \in \{0, 1\}$ corresponding to a "no-click" or "click" event. Figure 6.5(b) shows a typical measurement trace. It is visible that there are more clicks at short times than at long times, indicative of the spin emission.

Repeating the measurement 500 times and histogramming the number of counts, we extract the average count rate $\langle \dot{c}(t_d) \rangle$ as a function of the delay t_d after the inversion π pulse. Figure 6.5(c) shows this rate with and without π-pulse applied. Without pulse, a constant $\langle \dot{c}(t_d) \rangle = 1.53\,$counts/ms is recorded, which corresponds to the dark count rate ν_{dc} of the SMPD. When applying a spin π-pulse, $\langle \dot{c}(t_d) \rangle$ shows an excess of $0.85\,$counts/ms exponentially decaying towards the baseline, with a fitted characteristic time $309\,$ms. This time is close to the spin relaxation time $T_1 = 300\,$ms measured in chapter 4 by the inversion recovery sequence. We therefore attribute the excess of counts to photons spontaneously emitted by the spins upon relaxation, in agreement with Eq. 3.38. Note that at short t_d, we observe an extra excess rate of $0.3\,$counts/ms decaying with a $20\,$ms time constant (inset of figure 6.5(c)); we will come back to this phenomenon in subsection 6.2, and disregard it for the time being.

To analyze the photo-counting statistics of the fluorescence signal, we integrate

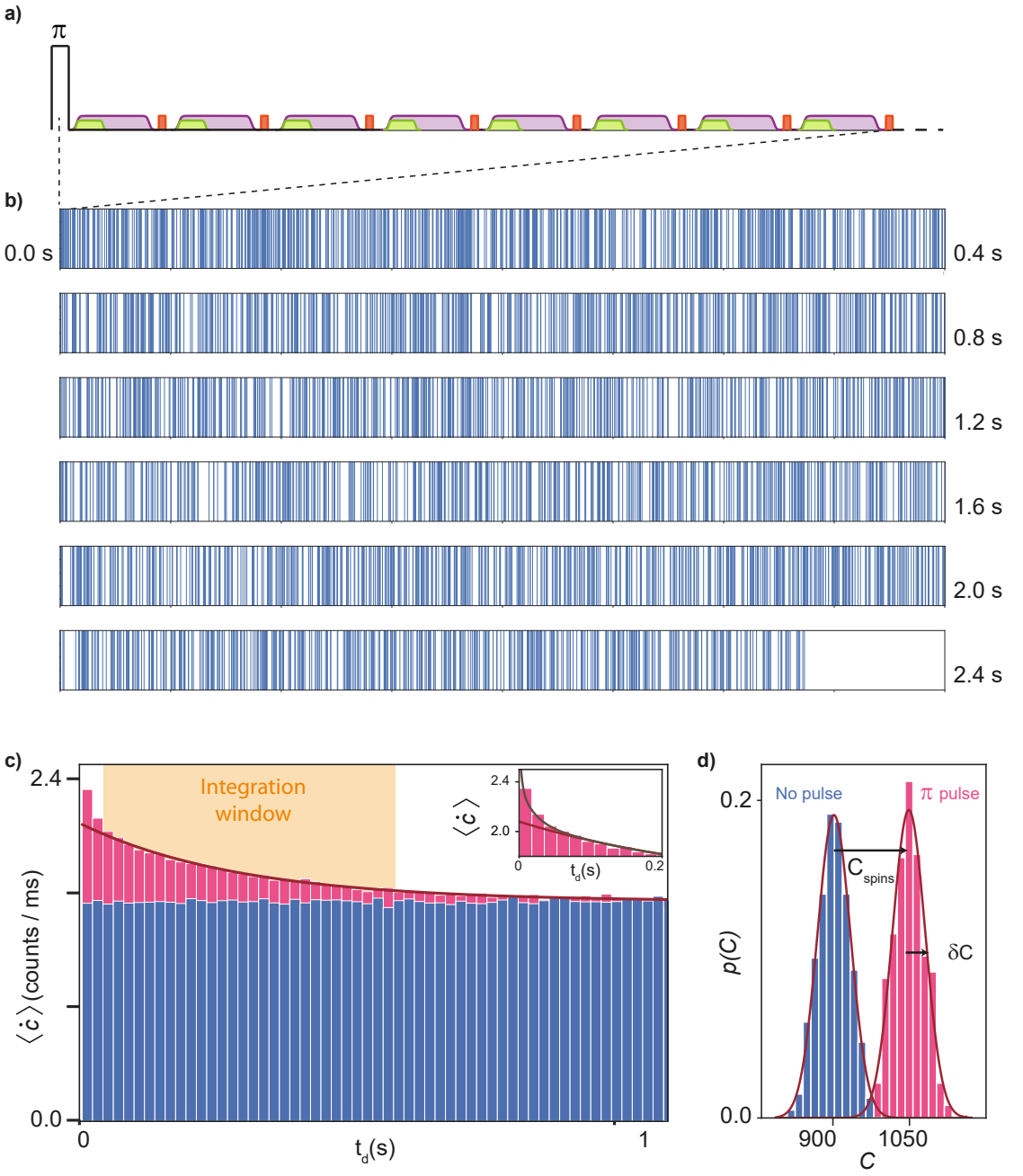

Figure 6.5: **Spin fluorescence detection.** (a) Schematic of the pulse sequence applied in the experiment of fluorescence detection. A π-pulse is applied to the spin ensemble, followed by the continuous repetition of the SMPD detection cycle. (b) A full SMPD detection trace after excitation of the spins with a π-pulse. Vertical blue lines indicate clicks of the detector, more clicks are observed at short times with respect to long ones. (c) Average count rate $\langle \dot{c} \rangle (t_d)$ measured in 19 ms time bins in the case where a π pulse is (magenta) or is not (blue) applied to the spins. An exponential fit for $t_d > 46.8\,\mathrm{ms}$ (solid line) leads to the characteristic time $T_1 = 309\,\mathrm{ms}$. The observed excess rate at short times $t_d < 50\,\mathrm{ms}$ (inset) has been investigated and attributed to fast-relaxing two-levels-systems. (d) Measured probability distribution of the number of counts C integrated from $46.8\,\mathrm{ms}$ to $585\,\mathrm{ms}$, obtained for 500 repetitions of the experiment when a π pulse is either applied (magenta) or not (blue) to the spins. Solid lines represent Poissonian fits.

the number of counts $C = \sum_i c(t_i)$ over a window of duration $t_w = 540\,\mathrm{ms}$. We choose this window as indicated in Fig. 6.5c from $45\,\mathrm{ms}$ to $585\,\mathrm{ms}$ in such a way as to avoid the extra counts at short times, and nevertheless integrate the dominant contribution from the spins. The resulting probability histogram $p(C)$ is shown in Fig. 6.5(d). With and without π pulse, an average of $\langle C(\pi)\rangle = 1050$ and $\langle C(0)\rangle = 900$ counts are detected, the difference defining the spin signal $C_{\mathrm{spin}} = 150$ photons. The typical deviation from this average value is given by the standard deviation of $p(C)$. The latter is measured to be $\delta C = 30$, as expected for a Poissonian distribution of the dark counts, since we do find $\delta C \simeq \sqrt{\nu_{\mathrm{dc}} t_{\mathrm{w}}}$.

One aspect of the trace shown in Fig. 6.5(b) is worth noting. While in our experiment only one click out of 4 (in the beginning of the trace) can be attributed to a photon emitted by a spin, it is likely that future experiments will reach the opposite regime, where most clicks originate from the spins. Then, in this regime, each click of the detector will reveal the quantum jump of an individual electron spin from its excited to its ground state. This phenomenon has never been observed in inductive detection so far, and this is an indication that fluorescence detection by a SMPD may have practical interest for magnetic resonance spectroscopy.

To stress the crucial role of the SMPD in this measurement, we compare the SNR using the SMPD to the one that may be expected from an ideal quadrature detection, which is given by $\frac{C_{\mathrm{spin}}}{2\sqrt{M/8}}$ according to Eq. 2.104 (measuring only one quadrature effectively divides the photon number by a factor 2). For a detection bandwidth $\sim 1\,\mathrm{MHz}$ and a detection time $500\,\mathrm{ms}$, the number of measured modes is $M = 5 \cdot 10^5$. Therefore, an ideal quadrature detection may only reach a SNR of 0.25 at best, whereas even with an imperfect SMPD device we already reach a SNR $C_{\mathrm{spin}}/\delta C = 4.6$.

Estimation of the overall efficiency

In order to estimate the overall detection efficiency, we estimate how many spins are excited by the π pulse. We rely on the spin density measurement described in Ch.4 (note that a second method shall be presented later in this chapter, for consistency), and we run simulations for the π pulse parameters used in the experiment. We find that $N = 1.4 \cdot 10^4$ spins are excited. Therefore, the overall detection efficiency is $C_{\mathrm{spin}}/N = 10^{-2}$.

This overall efficiency is the product of several factors, $\eta = \eta_{\mathrm{d}}\eta_{\mathrm{c}}\eta_{\mathrm{duty}}\eta_{\mathrm{int}}$, all of which have been determined independently as explained earlier apart from the collection efficiency η_{c}. From the measured value of η, we thus deduce $\eta_{\mathrm{c}} = 0.07 \pm 0.015$. This value is lower than the expected collection efficiency caused by the spin resonator internal losses, $\kappa_{\mathrm{ext}}/\kappa = 0.22$, revealing the presence of additional losses, at the level of $\eta_{\mathrm{c}}\kappa/\kappa_{\mathrm{ext}} = 0.3$. Part (if not all) of these losses are attributed to microwave losses in-between the spin resonator and the SMPD (cables, circulator).

The fact that we can account in a nearly quantitative way for the magnitude of the detected fluorescence signal is a direct proof that the relaxation of bismuth donor spins occurs dominantly by spontaneous emission. Indeed, in previous demonstrations of the Purcell effect [2], the evidence was only indirect, through the dependence of the spin relaxation time on the spin-resonator detuning or coupling constant, but without actually measuring the photons emitted.

TLS fluorescence

We now focus on the excess counts observed at short t_d (see Fig.6.5(c)) and decaying within a characteristic time of order $20\,\mathrm{ms}$. In order to investigate their origin, we repeat the experiment of the previous section (measurement of the SMPD count rate following a π pulse), and scan the magnetic field B_0 around the spin resonance. Figure 6.6a shows the count rate $\langle \dot{c}(t_d) \rangle$ as a function of B_0. On the color plot, it is visible that the bismuth donor spin signal vanishes when B_0 is far from the spin resonance. In contrast, the rapid decay in the first $\sim 10\,\mathrm{ms}$ remains constant for all B_0. Therefore, the excess count rate at short time does not originate from the bismuth donor spins.

Further insight is obtained by performing the following complementary measurement (see 6.6(b) and (c)). The count rate $\langle \dot{c}(t_d) \rangle$ following a π pulse is first measured at $B_0 = 0\,\mathrm{G}$ (Fig.6.6(b)). It is then re-measured in the exact same conditions, but with the buffer resonator frequency tuned away from ω_0 (Fig.6.6c) by 5 MHz. The excess count rate at short time is visible in Fig.6.6(b), but not in Fig.6.6(c). We thus conclude that this excess count originates from the spin resonator at ω_0.

Based on the previous results, we attribute the rapidly-decaying excess count to the fluorescence of TLS coupled to the spin resonator, and excited by the π pulse. Indeed, TLS are obviously coupled to the microwave field in the resonator, since they contribute to the resonator internal losses (see Section 4.3), and are therefore unavoidably excited by the π pulse. Exactly as for bismuth donor spins, their relaxation towards thermal equilibrium occurs for one part non-radiatively, and for another part radiatively, even though the ratio of the rates between the two relaxation channels is unknown. This represents the first observation of TLS fluorescence, which again confirms the sensitivity and the interest of SMPD detection even beyond magnetic resonance spectroscopy.

6.3 Hahn echo detection by photon counting

We now demonstrate that the SMPD can also be used for spin-echo detection, analogous to the detection of photon echoes with an optical photon counter [75].

The experiment is described in Fig. 6.7. Because the echo duration $T_\mathrm{E} \simeq 2\,\mu\mathrm{s}$ is shorter than T_c the detection cycle, at most one photon can be detected at the echo time 2τ. We thus center the detection step D of the SMPD at 2τ. We also chose $\tau = 350\,\mu\mathrm{s}$, larger than the detector dead time. Also, to avoid detector saturation, we purposely chose pulse parameters for the echo to contain much less than 1 photon: while the first pulse duration is $2\mu\mathrm{s}$, corresponding to a $\pi/2$ pulse at the chosen power, the refocusing pulse duration is $3\mu\mathrm{s}$, corresponding to a $3\pi/4$ rotation.

Several photon-counting traces are shown in Fig. 6.7(b). Note the much shorter time scale ($1\,\mathrm{ms}$) than in Fig. 6.5. The impact of the two control pulses is clearly visible, up to $100\mu\mathrm{s}$ after their application at times $t = 0$ and $t = \tau$. At 2τ, one click is observed more frequently than at other times, revealing the echo emission. Averaging several echo sequences yields $\langle c(t_i) \rangle$ (see Fig. 6.7(c)), with the echo visible at 2τ.

Figure 6.7(d) shows the click probability histogram at the echo time and out of the echo time. The average number of detected photons during the spin-echo $c_\mathrm{echo} = \langle c(2\tau) \rangle - \langle c(t_i > 2\tau) \rangle = 0.3$ is, as expected from Section 3.3, much lower than

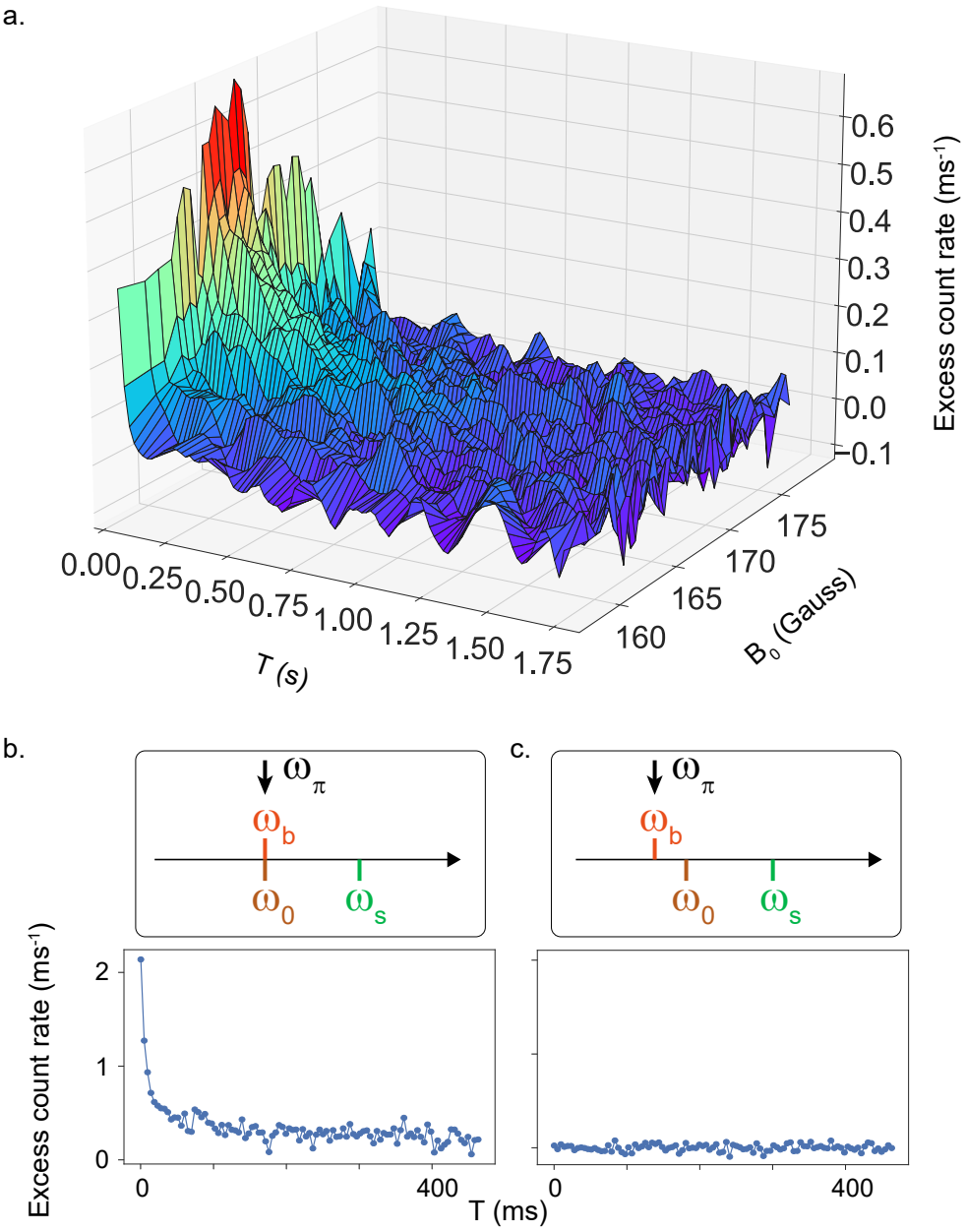

Figure 6.6: **Two-level-system photon emission.** (a) SMPD count rate above dark count level as a function of B_0 after a π-pulse applied to the spin resonator. When B_0 is such that the spins are in tune with the resonator the fluorescence signal appears, decaying within a characteristic time $T_{\mathrm{P}} \approx 300\,\mathrm{ms}$. When spins are detuned their fluorescence disappears but a fast-relaxing photon signal persists at short times. (b) Photon counting trace with the spin ensemble frequency ω_{s} detuned from the resonator ω_0. After a π-pulse at $\omega_\pi = \omega_0 = \omega_{\mathrm{b}}$, a fluorescence signal relaxing on a $\sim 20\,\mathrm{ms}$ timescale is recorded. (c) Photon counting trace with both the spins and the resonator detuned from the SMPD. A pulse is applied at the detector frequency $\omega_p i = \omega_{\mathrm{b}}$ and no signal is recorded. This rules out the SMPD as the origin of the short-time fluorescence.

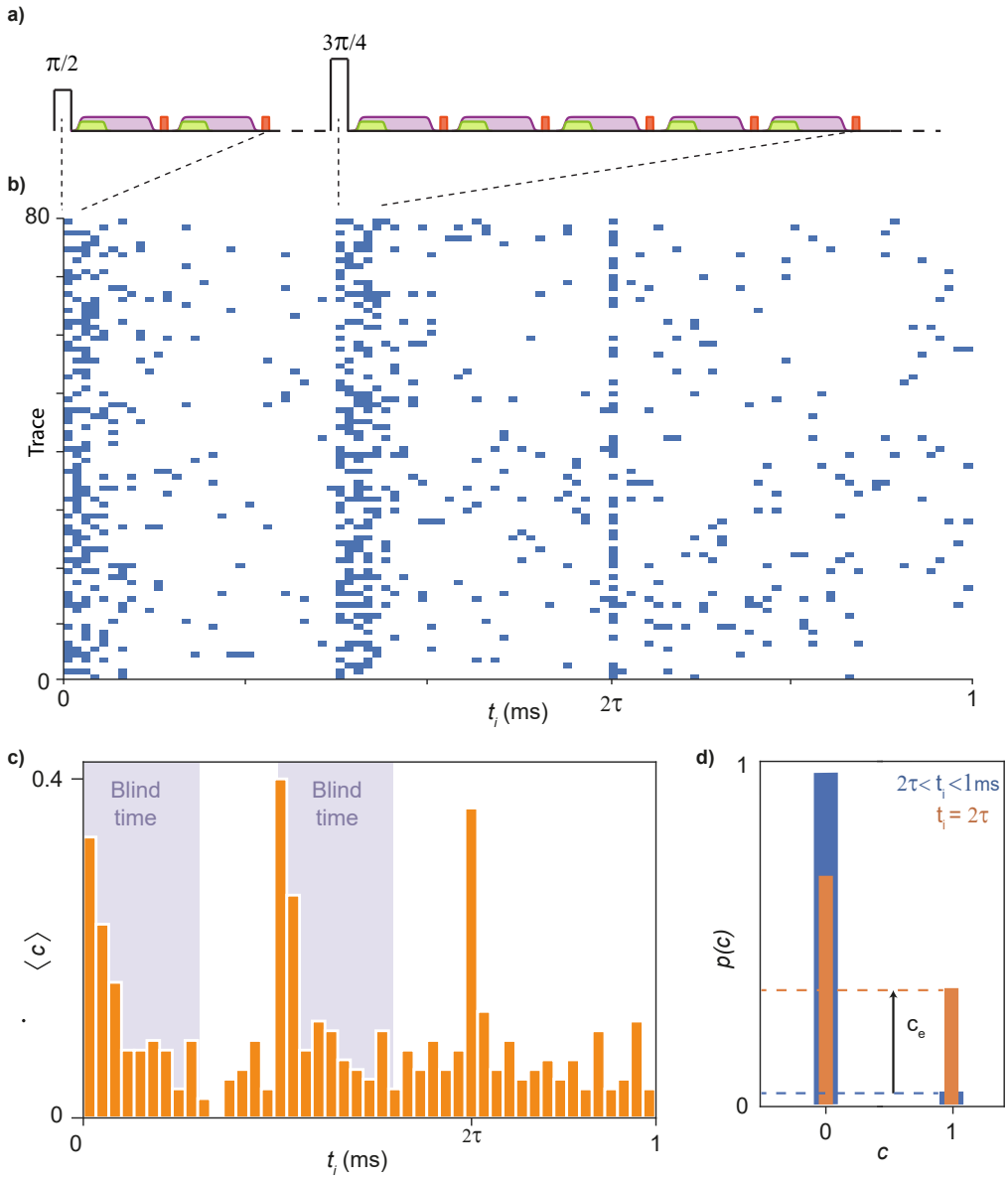

Figure 6.7: **SMPD Hahn-echo detection.** (a) Pulse sequence used in the experiment for Hahn-echo detection using the SMPD. A Hahn echo sequence is played on the spin ensemble, while the SMPD is operated cyclically. (b) Photo-counting traces recorded during 80 repetitions of the echo sequence, blue squares represent clicks of the detector. Increased click probability is recorded in correspondance of the pulses and at echo time 2τ. (c) Average number of counts $\langle c \rangle$ in 23 µs bins, as a function of the time t from the beginning of the echo sequence, averaged over 83 sequences. Blue-shadowed areas represent the 200 µs blind time of the detector after each strong spin pulse. The increased count probability at $t_i = 2\tau$ is the spin-echo. (d) Average probability $p(c)$ of having one or no count in the time bin centred at echo time $t_i = 2\tau$ (orange) or in one of the subsequent bins $2\tau < t_i < 1$ ms (blue). The difference between click probabilities (dashed lines) lead to a signal c_e of 0.3 photons re-emitted coherently.

the number of photons C_{spin} detected by fluorescence in Fig. 6.5. The standard deviation $\delta c_{\text{echo}} = 0.46$ during the echo (Fig. 6.7) yields a signal-to-noise ratio $c_{\text{echo}}/\delta c_{\text{echo}} = 0.65$.

6.4 Spin detection sensitivity comparison

We now have all the elements to compare the sensitivities reached in various detection modalities.

We first note that our experiment reaches a SNR of 4.6 in SMPD fluorescence detection, and 0.65 in SMPD echo detection (both measurements being performed with the same repetition time $\sim 2T_1$ and thus with the same initial spin polarization). Even though we did not explicitly measure the SNR of quadrature echo detection, we can estimate it to be at most 1.7 using Eqs. 3.53 and 3.54, which state that quadrature-detected echo should have a SNR larger than SMPD-detected echo by a factor $2\sqrt{\eta_{\text{d}}}$. Therefore, we conclude that our experiment reaches the regime in which fluorescence detection is more sensitive than echo detection.

It is also relevant to discuss the absolute spin detection sensitivity achieved. As already discussed, we detect $1.4 \cdot 10^4$ spins in fluorescence with a single-shot SNR of 4.6. Therefore, the single-shot spin detection sensitivity is 2600 spins, or equivalently $2600\,\text{spins}/\sqrt{Hz}$ since the repetition time is $1\,\text{s}$. This number is comparable to the spin detection sensitivity achieved in the first quantum-limited ESR spectroscopy experiments [3, 31]; however, a higher sensitivity was reached in more recent experiments [76, 77]. This is due to the different spin resonator geometry adopted, with a much smaller mode volume than the one chosen in our experiment, resulting in larger values of Γ_P and therefore a higher SNR (see Eqs.3.53, 3.54).

6.5 Spin ensemble characterization by photon detection

We finally demonstrate that SMPD detection can be used for usual spin characterization measurements.

Spin spectroscopy is performed by varying the magnetic field B_0 around the resonance value and using the two presented detection methods, namely SMPD detection of fluorescence and Hahn echo. These measurements are reported in figure 6.8, together with the result of quadrature echo-detection, showing that all three methods give consistent spectra.

Second, we measure Rabi oscillations through the fluorescence signal. In figure 6.9a, the spin signal C_{spin} is plotted as a function of the driving pulse duration τ, for three different pulse amplitudes A. Oscillations are observed, with a Rabi frequency Ω_{Rabi} linearly dependent on A (Fig. 6.9c), reflecting the Rabi oscillations of $\langle S_z \rangle$ since $C_{\text{spin}} = \eta[N + 2\langle S_z \rangle]/2$.

Rabi nutations can also be measured through photon detection of the Hahn echo, by varying the duration τ of the refocusing pulse. The SMPD signal $\langle c(2\tau) \rangle$ shows the expected oscillations (fig. 6.9b).

The oscillation contrast in figs. 6.9a and b diminishes with pulse duration τ due to the spread of Rabi frequencies in the ensemble. Moreover, the Rabi contrast in the fluorescence signal is seen to decay faster than in the echo. Using

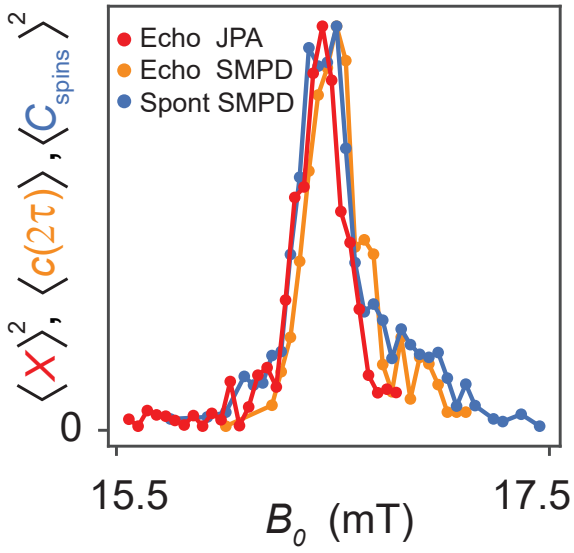

Figure 6.8: **Spectroscopy.** Spectrum of the bismuth donor spins obtained by sweeping B_0 around the resonance and detecting the spin signal with the following three methods: quadrature echo detection (red curve), echo detection by photon counting (orange curve) and fluorescence by photon counting (blue curve).

the coupling constant spread $\sigma_{g0}/2\pi = 30\,\text{Hz}$ deduced from the quadrature-echo-detected Rabi oscillations in Chapter 4, the simulations reproduce quantitatively the measurements, as seen in Fig. 6.9, both for the fluorescence and the echo. Therefore, we conclude that the spread in g_0 has a stronger impact on fluorescence than on the echo [77].

This can be qualitatively understood by the different relative contribution of spin packets to the overall signal. In fluorescence, the contribution of a packet is directly given by the value of $\langle S_z \rangle$ at the end of the pulse. In spin echoes, the transfer function is more non-linear, and effectively filters out contributions from spins that do not undergo a $\pi/2$ pulse [4].

Finally, spin coherence time is measured by microwave photon echo detection. In fig. 6.10, $\langle c(2\tau) \rangle$ is plotted as a function of τ. An exponential fit to the data yields $T_2 = 2.7\,\text{ms}$, in agreement with the value measured using homodyne detection and reported in section 4.3.

6.6 Quantitative comparison between the echo emission and direct fluorescence signals

In the simplified, analytical model of Section 3.3, quantitative predictions are made for the fluorescence and echo signals detected by a SMPD. Their ratio is entirely determined by the device parameters, and in particular the number of spins excited by the pulses, which was determined by spin-echo quadrature measurements in Chapter 4. It is therefore possible to perform a "consistency check", and verify that our data are compatible with the measured signal ratio. An interesting aspect is that by taking the ratio of SMPD signals $C_{\text{spin}}/c_{\text{echo}}$, the overall

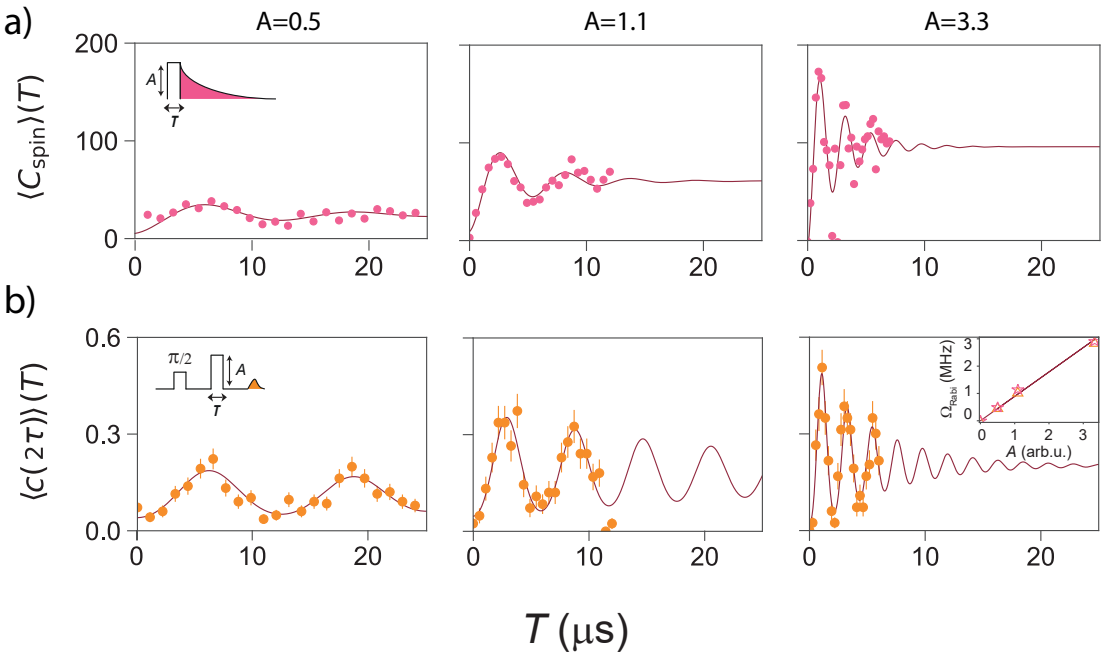

Figure 6.9: **Spin ensemble Rabi oscillations.** (a) Measured (magenta dots) and simulated (solid line) average spin fluorescence signal $\langle C_{\text{spin}} \rangle$ as a function of the duration T of a microwave pulse exciting the spins, for three different pulse amplitudes A. (b) Measured (orange dots) and simulated (solid line) average number of clicks $\langle c(2\tau) \rangle$ detected at echo time, as a function of the duration T of the second pulse of the Hahn echo sequence, for three different pulse amplitudes A. (inset) Extracted Rabi frequency Ω_{Rabi} as a function of the pulse amplitude A for fluorescence (magenta stars) and echo (orange triangles) measurement with the SMPD.

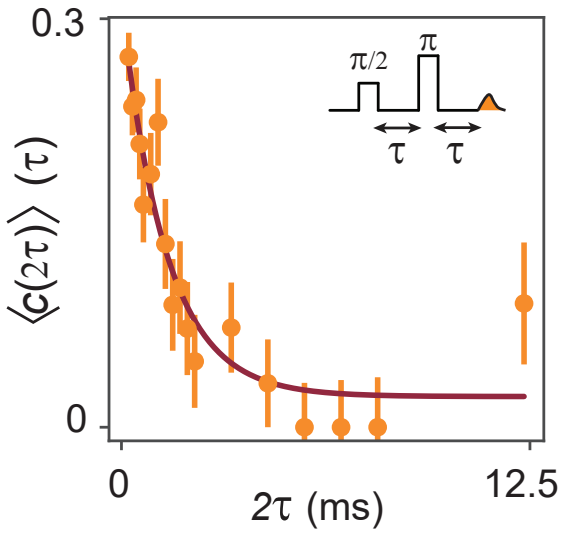

Figure 6.10: **Spin ensemble coherence time.** Measured (orange dots) average number of photons detected at echo time $\langle c(2\tau) \rangle$ as a function of the time delay τ between the pulses of the Hahn echo sequence. An exponential fit (solid line) yields a coherence time $T_2 = 2.7\,\text{ms}$.

efficiency cancels out. In the following, we compute the spin density that yields the measured $C_{\mathrm{spin}}/c_{\mathrm{echo}}$.

In order to make this reasoning quantitative, we again resort to simulations of both the echo sequence and the π pulse. From each simulation, we extract the number of spins involved by computing the change in the total magnetization $\langle S_z \rangle$. The ratio $\langle S_z^{\mathrm{spin}} \rangle / \langle S_z^{\mathrm{echo}} \rangle$ should be equal to the experimentally determined $C_{\mathrm{spin}}/(\eta_{\mathrm{duty}} c_{\mathrm{echo}})$, where the η_{duty} correction is due to the fact that echo detection is gated and therefore is insensitive to the detector duty cycle. We use the spin spectral density ρ_{spin} as the only adjustable parameter to reach the agreement between simulation and experiment. For the experimental value of C_{spin} we use the data shown in Fig. 6.5. For c_{e} we use different pulse parameters than that of Fig. 6.7 (same parameters for the $\pi/2$ pulse, but lower amplitude and $5.5\,\mu\mathrm{s}$ duration for the π pulse), to get a lower value of c_{e} and minimize the risk of SMPD saturation. The experimental ratio is then $C_{\mathrm{spin}}/(\eta_{\mathrm{duty}} c_{\mathrm{echo}}) = 3 \times 10^3$, reproduced by simulations for $\rho_{\mathrm{spin}} = 12\,\mathrm{spins\,kHz^{-1}}$. This yields $N = 1.2 \times 10^4$, which confirms that both estimates of N are consistent.

Chapter 7

Conclusion and perspectives

7.1 Measuring spin fluorescence with a single microwave photon detector

The main result of this thesis is a proof-of-principle demonstration of spin fluorescence measurement using a single microwave photon detector (SMPD). This result represents the first use of an SMPD for quantum sensing, and introduces a novel methodology for ESR spectroscopy.

For the demonstration we made use of the spins of bismuth donors in silicon coupled to a superconducting resonator in the Purcell regime, cooled at 10mK. We implemented an operational SMPD and connected it to the output port of the spin resonator. Upon excitation, spins relax to the ground state emitting a fluorescence signal which is detected by the SMPD. The main advantage of this technique with respect to echo detection resides in the fact that the SNR can reach much higher values. This is due to the fact that the noise is entirely governed by detector imperfections (non-zero dark counts, and finite detection efficiency). In contrast, quadrature detection is fundamentally limited by vacuum noise.

7.2 Future direction: single-spin detection with an improved detector

As discussed in this thesis, detection of spin fluorescence reveals its potential with respect to echo detection at low number of spins. Spectroscopy of small ($\sim 1-10$) spin ensembles is interesting in the case of volume-limited samples or even single molecules. Here, access to non-ensemble-averaged spectroscopic information is out of the sensitivity of standard ESR techniques.

The ability to reach single spin detection would also enable hybrid quantum information protocols based on heralded entanglement between a spin and a superconducting circuit. This requires high-fidelity single-shot readout of a single spin, achievable in principle for sufficiently high detection efficiency and low dark counts.

Improving the detection efficiency Future experiments will easily improve the detection efficiency compared to the results in this thesis. Simply fabricating the resonator out of niobium instead of aluminum would suppress the vortex-induced internal losses, and increase η_c by a factor 4. A qubit with longer $T_{1,q}$

would also increase the efficiency. An overall efficiency $\eta = 0.2$ should be reachable in the near future.

Decreasing the Purcell time. A decrease in T_p leads to a faster spin radiative relaxation. This allows to reduce the total measurement time, thus diminishing the number of dark counts occurring. The Purcell time T_P is inversely proportional to the spin-resonator coupling g_0 and proportional to the resonator κ. Increased g_0 is obtained with optimized resonator designs as for example bow-tie resonators used in ref. [4]. Purcell spin relaxation times of $\sim 1\,\mathrm{ms}$ have already been demonstrated.

Decreasing the dark count rate. Diminishing the dark count rate reduces the number of false positives detected within the window over which the spin relaxes radiatively. Lower dark counts can be achieved in two ways. First, improving the thermalization of microwave lines. Second, increasing the qubit $T_{1,\mathrm{q}}$ through improved fabrication processes. State-of-the-art transmon qubits show that it should be possible to reach $T_{1,\mathrm{q}} \sim 0.1 - 0.3\,\mathrm{ms}$ [78]. This would lead to an order of magnitude reduction of the dark count rate.

Using the SNR estimates derived in this thesis shows that with these improved figures of merit, single-spin detection should be achievable. An interesting aspect is that the method applies equally well to spins with short coherence times such as that encountered in real-world spin systems, making practical single-spin ESR spectroscopy a possible future perspective.

Part III

Appendices

Appendix A

Beam splitter model for collection efficiency

Beam splitter with ancillary vacuum state

We model the limited collection efficiency η_{c} with a beam splitter. For simplicity we consider a pure input state $|\varphi\rangle_{\mathrm{a}}$, which we write in the basis of Fock states as:

$$|\varphi\rangle_{\mathrm{a}} = \sum_{n=0}^{\infty} \varphi_n |n\rangle_{\mathrm{a}} = \sum_{n=0}^{\infty} \varphi_n \frac{\left(\hat{a}^{\dagger}\right)^n}{\sqrt{n!}} |0\rangle_{\mathrm{a}} . \tag{A.1}$$

We now apply the beam-splitter transformation to the state $|\varphi\rangle_{\mathrm{a}}$. We first consider the case in which on the complementary beam-splitter arm we inject the vacuum $|0\rangle_{\mathrm{b}}$:

$$|\varphi_{\mathrm{out}}\rangle\rangle = B^{\dagger} |\varphi\rangle_{\mathrm{a}} |0\rangle_{\mathrm{b}} = \sum_{n=0}^{\infty} \frac{\varphi_n}{\sqrt{n!}} B^{\dagger} \left(\hat{a}^{\dagger}\right)^n B |0\rangle_{\mathrm{a}} |0\rangle_{\mathrm{b}} \tag{A.2}$$

where we used $B |0\rangle_{\mathrm{a}} |0\rangle_{\mathrm{b}} = |0\rangle_{\mathrm{a}} |0\rangle_{\mathrm{b}}$, i.e. the beam splitter transforms vacuum into vacuum. By recalling the beam-splitter evolution:

$$B^{\dagger} \hat{a} B = \hat{a}\sqrt{\eta_{\mathrm{c}}} + \hat{b}\sqrt{1-\eta_{\mathrm{c}}} \tag{A.3}$$

$$B^{\dagger} \hat{b} B = \hat{a}\sqrt{1-\eta_{\mathrm{c}}} - \hat{b}\sqrt{\eta_{\mathrm{c}}} \tag{A.4}$$

at the output one has:

$$|\varphi_{\mathrm{out}}\rangle\rangle = \sum_{n=0}^{\infty} \varphi_n \sum_{k=0}^{n} \sqrt{\binom{n}{k}} \eta_{\mathrm{c}}^{\frac{k}{2}} (1-\eta_{\mathrm{c}})^{\frac{n-k}{2}} |k\rangle_{\mathrm{a}} |n-k\rangle_{\mathrm{b}} . \tag{A.5}$$

Now a measurement of the projector $|0\rangle\langle 0|_{\mathrm{a}} \otimes \mathbb{1}_{\mathrm{b}}$ operated by the photon counter leads to the probability of having no counts:

$$p_0 = \mathrm{Tr}\left[|0\rangle\langle 0|_{\mathrm{a}} \otimes \mathbb{1}_{\mathrm{b}} \, |\varphi_{\mathrm{out}}\rangle\rangle\langle\langle\varphi_{\mathrm{out}}| \right] \tag{A.6}$$

leading:

$$p_0 = \sum_{n=0}^{\infty} |\varphi_n|^2 (1-\eta_{\mathrm{c}})^n \tag{A.7}$$

Beam splitter with non-vacuum mixed ancillary state

With the purpose of modeling dark counts, we consider the case in which the ancillary state is a thermal mixed state with low occupation number, namely:

$$\hat{\rho}_{\mathrm{b}} = (1-p_{\mathrm{th}}) |0\rangle_{\mathrm{b}} \langle 0| + p_{\mathrm{th}} |1\rangle_{\mathrm{b}} \langle 1| \tag{A.8}$$

where p_{th} is some small probability denoting the probability of thermal occupation. The density matrix of the input state on a is:

$$\hat{\rho}_{\mathrm{a}} = \sum_{m,n=0}^{\infty} \varphi_n \varphi_m^* \left|n\right\rangle_{\mathrm{a}} \left\langle m\right| \tag{A.9}$$

The total input density matrix reads:

$$\hat{\rho}_{\mathrm{in}} = \hat{\rho}_{\mathrm{a}} \otimes \hat{\rho}_{\mathrm{b}} = (1-p_{\mathrm{th}}) \left|\varphi_{\mathrm{in}}^0\right\rangle\!\rangle \langle\!\langle \varphi_{\mathrm{in}}^0\right| + p_{\mathrm{th}} \left|\varphi_{\mathrm{in}}^1\right\rangle\!\rangle \langle\!\langle \varphi_{\mathrm{in}}^1\right| \tag{A.10}$$

with:

$$\left|\varphi_{\mathrm{in}}^j\right\rangle\!\rangle = \sum_{n=0}^{\infty} \frac{\varphi_n}{\sqrt{n!}} \left(\hat{a}^\dagger\right)^n \left(\hat{b}\right)^j \left|0\right\rangle_{\mathrm{a}} \left|0\right\rangle_{\mathrm{b}}. \tag{A.11}$$

We now apply the beam splitter evolution to $\hat{\rho}_{\mathrm{in}}$:

$$\hat{\rho}_{\mathrm{out}} = B^\dagger \hat{\rho}_{\mathrm{in}} B = (1-p_{\mathrm{th}}) \left|\varphi_{\mathrm{out}}^0\right\rangle\!\rangle \langle\!\langle \varphi_{\mathrm{out}}^0\right| + p_{\mathrm{th}} \left|\varphi_{\mathrm{out}}^1\right\rangle\!\rangle \langle\!\langle \varphi_{\mathrm{out}}^1\right| \tag{A.12}$$

where $\left|\varphi_{\mathrm{out}}^j\right\rangle\!\rangle = B^\dagger \left|\varphi_{\mathrm{in}}^j\right\rangle\!\rangle$. Note that $\left|\varphi_{\mathrm{out}}^0\right\rangle\!\rangle$ is that of equation A.5, while for $\left|\varphi_{\mathrm{out}}^1\right\rangle\!\rangle$ one has:

$$\left|\varphi_{\mathrm{out}}^1\right\rangle\!\rangle = \sum_{n=0}^{\infty} \frac{\varphi_n}{\sqrt{n!}} \sum_{k=0}^{n} \binom{n}{k} \eta_{\mathrm{c}}^{\frac{k}{2}} (1-\eta_{\mathrm{c}})^{\frac{n-k}{2}} \left(a^\dagger\right)^k \left(b^\dagger\right)^{n-k} \left(\hat{a}^\dagger \sqrt{1-\eta_{\mathrm{c}}} - \hat{b}^\dagger \sqrt{\eta_{\mathrm{c}}}\right) \left|0\right\rangle_{\mathrm{a}} \left|0\right\rangle_{\mathrm{b}} = \tag{A.13}$$

$$= \sum_{n=0}^{\infty} \varphi_n \sum_{k=0}^{n} \sqrt{\binom{n}{k}} \eta_{\mathrm{c}}^{\frac{k}{2}} (1-\eta_{\mathrm{c}})^{\frac{n-k}{2}} \left[\frac{k}{\sqrt{\eta_{\mathrm{c}}}} \left|n-k\right\rangle_{\mathrm{b}} - \sqrt{\eta_{\mathrm{c}}} \sqrt{n-k+1} \left|n-k+1\right\rangle_{\mathrm{b}}\right] \left|k\right\rangle_{\mathrm{a}} \tag{A.14}$$

Finally, we measure the projector $\left|0\right\rangle_{\mathrm{a}} \left\langle 0\right| \otimes \mathbb{1}_{\mathrm{b}}$ onto $\hat{\rho}_{\mathrm{out}}$:

$$p_0 = \mathrm{Tr}\left[\hat{\rho}_{\mathrm{out}} \left|0\right\rangle_{\mathrm{a}} \left\langle 0\right| \otimes \mathbb{1}_{\mathrm{b}}\right] = \mathrm{Tr}_{\mathrm{b}}\left[(1-p_{\mathrm{th}}) \left|\langle\!\langle \varphi_{\mathrm{out}}^0\right| \left|0\right\rangle_{\mathrm{a}}\right|^2 + p_{\mathrm{th}} \left|\langle\!\langle \varphi_{\mathrm{out}}^1\right| \left|0\right\rangle_{\mathrm{a}}\right|^2\right] \tag{A.15}$$

leading to:

$$p_0 = (1-p_{\mathrm{th}}) \sum_{n=0}^{\infty} \left|\varphi_n\right|^2 (1-\eta_{\mathrm{c}})^n + p_{\mathrm{th}} \eta_{\mathrm{c}} \sum_{n=0}^{\infty} \left|\varphi_n\right|^2 (1-\eta_{\mathrm{c}})^n (n+1) \tag{A.16}$$

Appendix B

Elements of superconducting circuits modeling

B.1 Field quantization in few words

In order to proceed to the field quantization one has to identify decoupled pairs of conjugate canonical variables that satisfy Hamilton's equations of motion. Since in classical electrodynamics the dynamics of the electromagnetic field is described by Maxwell's equations, which constitute a system of coupled differential equations, one has to reformulate them, identifying such pairs of decoupled conjugate variables. This derivation consists of five steps:

- write the Maxwell equations for the field in vacuum, in the Coulomb gauge, for which one can take the scalar potential to be zero.
- Express the fields and the vector potential in the Fourier space.
- Introduce a set of normal variables α that decouples the Maxwell equations in the Fourier space. This corresponds to a decomposition on the basis of traveling polarized monochromatic plane waves, each with defined wavevector and polarization.
- Write the Hamiltonian in the canonical form, with conjugate variables Q and P corresponding to the real and imaginary part of the normal variables α.
- Proceed to quantization using Dirac's method.

As a result, the quantized version of the Hamiltonian for a monochromatic mode reads:

$$\hat{H} = \hbar\omega\left(\hat{a}^\dagger\hat{a} + \frac{1}{2}\right) \tag{B.1}$$

where the annihilation operator $\hat{a}$ is the quantized counterpart of the normal mode variable α, and satisfies the commutation relation $[\hat{a}, \hat{a}^\dagger] = 1$. The conjugate canonical position and momentum variables $\hat{Q}$ and $\hat{P}$ are:

$$\hat{Q} = \sqrt{\frac{\hbar}{2\omega}}\left(\hat{a} + \hat{a}^\dagger\right) \tag{B.2}$$

$$\hat{P} = i\sqrt{\frac{\hbar\omega}{2}}\left(\hat{a} - \hat{a}^\dagger\right) \tag{B.3}$$

Their variance is bounded by the Heisemberg uncertainty relation:

$$\langle \Delta \hat{Q}^2 \rangle \langle \Delta \hat{P}^2 \rangle \geq \hbar^2/4 \tag{B.4}$$

In the following, we will not make use of operators $\hat{Q}$ and $\hat{P}$ but rather of their dimensionless counterparts $\hat{X}$ and $\hat{Y}$, usually known as *quadratures* in the theory of microwave signals, defined as

$$\hat{X} = \sqrt{\frac{\omega}{2\hbar}}\hat{Q} \tag{B.5}$$

$$\hat{Y} = \sqrt{\frac{1}{2\hbar\omega}}\hat{P} \tag{B.6}$$

satisfying $[\hat{X}, \hat{Y}] = i/2$ and $\langle \Delta \hat{X}^2 \rangle \langle \Delta \hat{Y}^2 \rangle \geq 1/16$.
The electric and magnetic field associated to the monochromatic mode are expressed as:

$$\hat{\mathbf{E}} = E_{\text{zpf}} \left(\hat{a} - \hat{a}^\dagger \right) \tag{B.7}$$

$$\hat{\mathbf{B}} = B_{\text{zpf}} \left(\hat{a} + \hat{a}^\dagger \right) \tag{B.8}$$

where the field zero-point fluctuations are $E_{\text{zpf}} = \sqrt{\hbar/2\omega\epsilon V}$ and $B_{\text{zpf}} = \sqrt{\hbar\omega/2c\epsilon V}$, with V the mode volume, ϵ the permittivity of the medium and c the speed of light.

B.2 LC oscillator quantization

Here we derive and quantize the Hamiltonian of a simple LC resonator, which comes into play both in the chip containing the spin ensemble and as a component of the single microwave photon detector. This treatment will allow us to calculate the voltage and current zero-point fluctuations, which determine the coupling of spins to the resonator, we will also introduce the quantities and the notation that will facilitate further derivations in the following sections.

Consider an LC resonator, in order to proceed to the quantization we derive its Hamiltonian in terms of canonical position and momentum, and proceed then with Dirac quantization rules. We begin deriving the Lagrangian of the circuit, using the magnetic flux Φ threaded by the inductance L as generalized position coordinate:

$$\Phi(t) = \int_{-\infty}^{t} L \frac{dI(t')}{dt'}\, dt' = LI(t) \tag{B.9}$$

where I is the current flowing through the inductance. The potential energy of the circuit, stored in the inductor, is calculated as:

$$\mathcal{U}_{\text{L}}(t) = \int_{-\infty}^{t} VI\, dt' = \int_{-\infty}^{t} L \frac{dI}{dt'} I\, dt' = \frac{1}{2} LI^2(t) = \frac{1}{2L}\Phi^2(t) \tag{B.10}$$

where we used the fact that the voltage drop V across the inductor corresponds to the rate of change of threaded flux $V = LdI/dt$. Analogously the kinetic energy of the circuit, stored in the capacitor, is:

$$\mathcal{T}_{\text{C}}(t) = \int_{-\infty}^{t} VI\, dt' = \int_{-\infty}^{t} VC \frac{dV}{dt'}\, dt' = \frac{1}{2} CV(t)^2 = \frac{1}{2} C\dot{\Phi}^2(t) \tag{B.11}$$

where we made use of the relation $I = CdV/dt$, holding for a capacitance C. The Lagrangian of the system reads:

$$\mathcal{L} = \mathcal{T}_{\mathrm{C}}(t) - \mathcal{U}_{\mathrm{L}}(t) = \frac{1}{2}C\dot{\Phi}^2(t) - \frac{1}{2L}\Phi^2(t). \tag{B.12}$$

The momentum conjugate to the canonical coordinate Φ is naturally defined as:

$$Q = \frac{\partial \mathcal{L}}{\partial \dot{\Phi}} = C\dot{\Phi} = CV \tag{B.13}$$

so that the Hamiltonian is obtained straightly through the Legendre transformation

$$\mathcal{H} = Q\dot{\Phi} - \mathcal{L} = \frac{Q^2}{2C} + \frac{\Phi^2}{2L}. \tag{B.14}$$

At this point one can proceed with the standard Dirac's quantization rules and promote the canonical position Φ and momentum Q to quantum operators satisfying the canonical commutation relation $[\hat{\Phi}, \hat{Q}] = i\hbar$:

$$\hat{H} = \frac{\hat{Q}^2}{2C} + \frac{\hat{\Phi}^2}{2L}. \tag{B.15}$$

At this point it is natural to introduce the annihilation and creation operators $\hat{a}$ and $\hat{a}^\dagger$:

$$\hat{a} = \frac{1}{\sqrt{2\hbar Z_0}}\left(\hat{\Phi} + iZ_0\hat{Q}\right) \tag{B.16}$$

$$\hat{a}^\dagger = \frac{1}{\sqrt{2\hbar Z_0}}\left(\hat{\Phi} - iZ_0\hat{Q}\right) \tag{B.17}$$

where $\omega_0 = 1/\sqrt{LC}$ is the resonator frequency and $Z_0 = \sqrt{L/C}$ its impedance. In terms of annihilation and creation operators the Hamiltonian rewrites

$$\hat{H} = \hbar\omega_0\left(\hat{a}^\dagger\hat{a} + \frac{1}{2}\right). \tag{B.18}$$

One can now express the current $\hat{I}$ in the inductor and the voltage $\hat{V}$ across capacitor plates as:

$$\hat{I} = \frac{\hat{\Phi}}{L} = \sqrt{\frac{\hbar\omega_0^2}{2Z_0}}\left(\hat{a}^\dagger + \hat{a}\right) = I_{\mathrm{ZPF}}\left(\hat{a}^\dagger + \hat{a}\right) \tag{B.19}$$

$$\hat{V} = \frac{\hat{\Phi}}{L} = i\sqrt{\frac{\hbar Z_0\omega_0^2}{2}}\left(\hat{a}^\dagger - \hat{a}\right) = iV_{\mathrm{ZPF}}\left(\hat{a}^\dagger - \hat{a}\right). \tag{B.20}$$

where the current and voltage zero-point fluctuations I_{ZPF} and V_{ZPF} inherit their name from being the fluctuations of these two quantities in the vacuum state $|0\rangle$:

$$I_{\mathrm{ZPF}} = \sqrt{\delta\hat{I}^2} = \sqrt{\langle 0|\,\hat{I}^2\,|0\rangle - \langle 0|\,\hat{I}\,|0\rangle^2} = \sqrt{\frac{\hbar\omega_0^2}{2Z_0}} \tag{B.21}$$

$$V_{\mathrm{ZPF}} = \sqrt{\delta\hat{V}^2} = \sqrt{\langle 0|\,\hat{V}^2\,|0\rangle - \langle 0|\,\hat{V}\,|0\rangle^2} = \sqrt{\frac{\hbar Z_0\omega_0^2}{2}}. \tag{B.22}$$

These fluctuations are responsible for fluctuations of electric and magnetic field in the space surrounding the LC resonator and thus come into play in determining the coupling of the resonator to nearby electric and magnetic dipoles.

B.3 SQUID

Symmetric SQUID Inductance

Let's consider a superconducting loop containing two identical Josephson junctions in parallel, the current flowing from left to right can be written as the sum of the currents in the two branches:

$$I = I_1 + I_2 = I_\mathrm{c} \sin\varphi_1 + I_\mathrm{c} \sin\varphi_2 = 2I_\mathrm{c} \cos\left(\frac{\varphi_1 - \varphi_2}{2}\right) \sin\left(\frac{\varphi_1 + \varphi_2}{2}\right). \tag{B.23}$$

The superconducting phase difference $\varphi_1 - \varphi_2$ is constrained by the total phase difference around the loop:

$$\oint_C \nabla\theta \cdot d\mathbf{l} = 2\pi n = (\theta_\mathrm{b} - \theta_\mathrm{a}) + (\theta_\mathrm{c} - \theta_\mathrm{b}) + (\theta_\mathrm{d} - \theta_\mathrm{c}) + (\theta_\mathrm{a} - \theta_\mathrm{d}) \tag{B.24}$$

we now use the two following equations, the first one relates the vector potential $\mathbf{A}$, the gauge invariant phase gradient $\nabla\theta$ and the supercurrent density $\mathbf{J}$, the second one is the expression of the gauge invariant phase across the junction barrier:

$$\nabla\theta = \frac{2\pi}{\Phi_0}(\Lambda\mathbf{J} + \mathbf{A}) \tag{B.25}$$

$$\varphi_1 = \theta_\mathrm{b} - \theta_\mathrm{a} - \frac{2\pi}{\Phi_0}\int_a^b \mathbf{A} \cdot d\mathbf{l} \tag{B.26}$$

where Φ_0 is the already introduced flux quantum and Λ is known as London coefficient and depends on the electron mass and charge and the density of the condensate. We obtain:

$$2\pi n = \varphi_1 + \frac{2\pi}{\Phi_0}\int_a^b \mathbf{A}\cdot d\mathbf{l} + \frac{2\pi}{\Phi_0}\int_b^c (\Lambda\mathbf{J} + \mathbf{A}) - \varphi_2 + \frac{2\pi}{\Phi_0}\int_c^d \mathbf{A}\cdot d\mathbf{l} + \frac{2\pi}{\Phi_0}\int_d^a (\Lambda\mathbf{J} + \mathbf{A}) \tag{B.27}$$

which leads to

$$\varphi_1 - \varphi_2 = -\frac{2\pi}{\Phi_0}\left[\oint_C \mathbf{A}\cdot d\mathbf{l} + \int_b^c \Lambda\mathbf{J} + \int_d^a \Lambda\mathbf{J}\right] + 2\pi n. \tag{B.28}$$

The integration of $\mathbf{A}$ on the closed loop gives the total enclosed flux Φ_ext. The integration of the supercurrent density can be taken deep inside the superconducting material where, past the London penetration depth, $\mathbf{J}$ vanishes. Thus

$$\varphi_1 - \varphi_2 = -2\pi\frac{\Phi_\mathrm{ext}}{\Phi_0} + 2\pi n \tag{B.29}$$

which back in eq. B.23 gives:

$$I = 2I_\mathrm{c} \cos\left(\pi\frac{\Phi_\mathrm{ext}}{\Phi_0}\right) \sin\left(\frac{\varphi_1 + \varphi_2}{2}\right) \tag{B.30}$$

which is analogous to the first Josephson relation 2.45 with $\varphi = \varphi_1 + \varphi_2$ and a tunable critical current $I_\mathrm{c}(\Phi_\mathrm{ext}) = 2I_\mathrm{c}\cos(\pi\Phi_\mathrm{ext}/\Phi_0)$. This reflects also on the Josephson inductance eq. 2.47 which becomes tunable with the external flux. By embedding a SQUID into an LC resonator one can now make it tunable. Changing the magnetic flux Φ_ext threading the SQUID loop causes a change in the inductance of the resonator which leads to a frequency shift.

Note that for sake of simplicity in the above treatment we considered identical junctions, asymmetrical SQUIDs with $I_{\mathrm{c}1} \neq I_{\mathrm{c}2}$ have smoother tunability curves.

Asymmetric SQUID Inductance

Let's consider a SQUID device, we use as generalized coordinate the fluxes associated to each of the two branches $\Phi_i = \phi_0\varphi_i$, each junction contributes to the total Hamiltonian with:

$$\hat{H} = \mathcal{T}(Q_1, Q_2) - E_{\mathrm{J}1}\cos\varphi_1 - E_{\mathrm{J}2}\cos\varphi_2 \tag{B.31}$$

Since $\hat{\varphi}_1$ and $\hat{\varphi}_2$ are not independent variables but are linked by eq. B.29 one can rephrase the problem by using the new variables $\hat{\delta} = \hat{\varphi}_1 - \hat{\varphi}_2$ and $\hat{\varphi} = (\hat{\varphi}_1 + \hat{\varphi}_2)/2$:

$$\hat{H} == \mathcal{T}(Q_1, Q_2) - E_{\mathrm{J}1}\cos\left(\varphi + \frac{\delta}{2}\right) - E_{\mathrm{J}2}\cos\left(\varphi - \frac{\delta}{2}\right). \tag{B.32}$$

Since we consider a SQUID without current bias, we can set to zero the current flowing through the device, $\hat{I} = 0$, which fixes $\hat{\varphi}$ in terms of $\hat{\delta}$:

$$0 = \hat{I} = \frac{\partial\hat{Q}}{\partial t} = \frac{\partial\hat{H}}{\partial\hat{\varphi}} \tag{B.33}$$

giving:

$$\tan\hat{\varphi} = \frac{E_{\mathrm{J}1} - E_{\mathrm{J}2}}{E_{\mathrm{J}1} + E_{\mathrm{J}2}}\tan\frac{\hat{\delta}}{2} = \Delta\tan\frac{\hat{\delta}}{2}. \tag{B.34}$$

The SQUID inductance is now obtained as

$$L = \left(\frac{\partial^2\hat{H}}{\partial\hat{\varphi}^2}\right)^{-1} = \frac{1}{(E_{\mathrm{J}1} + E_{\mathrm{J}2})\cos\pi\frac{\Phi_{\mathrm{ext}}}{\Phi_0}}\sqrt{\frac{1 + \Delta^2\tan^2\pi\frac{\Phi_{\mathrm{ext}}}{\Phi_0}}{(1 - \Delta^2\tan^2\pi\frac{\Phi_{\mathrm{ext}}}{\Phi_0})^2}} \tag{B.35}$$

which satisfies:

$$\frac{1}{E_{\mathrm{J}1} + E_{\mathrm{J}2}} \leq L \leq \frac{1}{|E_{\mathrm{J}1} - E_{\mathrm{J}2}|} \tag{B.36}$$

or defininig the junction inductance $L_{\mathrm{i}} = E_{\mathrm{Ji}}^{-1}$:

$$\frac{L_1L_2}{L_1 + L_2} \leq L \leq \frac{L_1L_2}{|L_2 - L_1|} \tag{B.37}$$

which defines the boundaries for the tunability of the SQUID inductance $L_{\min} \leq L \leq L_{\max}$.

B.4 Resonator coupled to a transmon qubit: EPR method

In this section we analyze the dynamic of a coupled cavity-qubit system using the EPR method.

Lagrangian

Let's consider a system composed by an LC oscillator – of inductance L_R, capacitance C_R and magnetic flux Φ_R – coupled via a capacitance C_c to a Transmon qubit of Josephson energy E_J, capacitance C_J and magnetic flux Φ_J. We proceed by writing the Lagrangian using the magnetic flux Φ as generalized position

coordinate :

$$\mathcal{L} = \mathcal{T} - \mathcal{U} \tag{B.38}$$

$$\mathcal{T} = \frac{1}{2}C_R\dot{\Phi}_R^2 + \frac{1}{2}C_J\dot{\Phi}_J^2 + \frac{1}{2}C_c(\dot{\Phi}_J - \dot{\Phi}_R)^2 \tag{B.39}$$

$$\mathcal{U} = \left[\frac{1}{2L}\Phi_R^2 + \frac{1}{2}\frac{E_J}{\phi_0^2}\Phi_J^2\right]_{lin} + \left[-E_J\cos\frac{\Phi}{\phi_0} - \frac{1}{2}\frac{E_J}{\phi_0^2}\Phi_J^2\right]_{nl} \tag{B.40}$$

where we separated the linear and non-linear contributions to the potential energy.

In the following we proceed by diagonalizing the linear part of the Lagrangian, co-diagonalizing the inductance and capacitance matrices, and finally we will expand the non-linear part in term of the obtained eigenvectors. We introduce the following matrix notation:

$$\mathbf{\Phi} = \begin{pmatrix}\Phi_J \\ \Phi_R\end{pmatrix} \tag{B.41}$$

$$C = \begin{pmatrix}C_J + C_c & -Cc \\ -Cc & C_R + C_c\end{pmatrix} \tag{B.42}$$

$$L^{-1} = \begin{pmatrix}E_J\phi_0^{-2} & 0 \\ 0 & L^{-1}\end{pmatrix} = \begin{pmatrix}L_J^{-1} & 0 \\ 0 & L_R^{-1}\end{pmatrix} \tag{B.43}$$

so that:

$$\mathcal{L}_{lin} = \frac{1}{2}\dot{\mathbf{\Phi}}^T C\dot{\mathbf{\Phi}} - \frac{1}{2}\mathbf{\Phi}^T L^{-1}\mathbf{\Phi} \tag{B.44}$$

We now follow Ref.[12] for the simultaneous diagonalization of the capacitance and inverse-inductance matrices.

Diagonalizing the inverse-inductance matrix

We look for the real orthogonal matrix $O_L^T O_L = \mathbb{1}$ that diagonalizes the inverse inductance matrix:

$$O_L^T L^{-1} O_L = \Lambda_L^{-1}\mathbb{1}_L^{-1} \tag{B.45}$$

since in our case the matrix is already diagonal we have:

$$O_L = \mathbb{1} \quad \text{and} \quad \Lambda_L^{-1} = \begin{pmatrix}L_J^{-1} & 0 \\ 0 & L_R^{-1}\end{pmatrix} \tag{B.46}$$

one can define the rescaled flux as:

$$\breve{\mathbf{\Phi}} = \Lambda_L^{-\frac{1}{2}} O_L^T \mathbf{\Phi} = \begin{pmatrix}L_J^{-\frac{1}{2}}\Phi_J \\ L_R^{-\frac{1}{2}}\Phi_R\end{pmatrix} \tag{B.47}$$

and the rescaled capacitance matrix as:

$$\breve{C} = \Lambda_L^{\frac{1}{2}} C \Lambda_L^{\frac{1}{2}} = \begin{pmatrix}(C_J + C_c)L_J & -C_c\sqrt{L_R L_J} \\ -C_c\sqrt{L_R L_J} & (C_R + C_c)L_R\end{pmatrix} \tag{B.48}$$

so that the Lagrangian reads:

$$\mathcal{L}_{lin} = \frac{1}{2}\dot{\mathbf{\Phi}}^T (O_L\Lambda_L^{-\frac{1}{2}}\Lambda_L^{\frac{1}{2}}O_L^T)\; C\; (O_L\Lambda_L^{-\frac{1}{2}}\Lambda_L^{\frac{1}{2}}O_L^T)\dot{\mathbf{\Phi}} - \frac{1}{2}\mathbf{\Phi}^T(O_L O_L^T)\; L^{-1}\; (O_L O_L^T)\mathbf{\Phi} \tag{B.49}$$

$$= \frac{1}{2}\dot{\breve{\mathbf{\Phi}}}^T \breve{C}\dot{\breve{\mathbf{\Phi}}} - \frac{1}{2}\breve{\mathbf{\Phi}}^T \mathbb{1}_L^{-1}\breve{\mathbf{\Phi}}$$

Diagonalizing the capacitance matrix

We now look for the real orthogonal matrix $O_{\breve{C}}^T O_{\breve{C}} = \mathbb{1}$ that diagonalizes the capacitance matrix:

$$O_{\breve{C}}^T \breve{C} O_{\breve{C}} = \Lambda_{\breve{C}} \mathbb{1}_C \tag{B.50}$$

which turns out to be:

$$O_{\breve{C}}^T = \begin{pmatrix} \frac{\Delta+\sqrt{\Delta^2+C^2}}{\sqrt{\left(\Delta+\sqrt{\Delta^2+C^2}\right)^2+C^2}} & \frac{-C}{\sqrt{\left(\Delta+\sqrt{\Delta^2+C^2}\right)^2+C^2}} \\ \frac{-\Delta+\sqrt{\Delta^2+C^2}}{\sqrt{\left(\Delta-\sqrt{\Delta^2+C^2}\right)^2+C^2}} & \frac{C}{\sqrt{\left(\Delta-\sqrt{\Delta^2+C^2}\right)^2+C^2}} \end{pmatrix} \tag{B.51}$$

with:

$$\Delta = C_J L_J - C_R L_R + C_c(L_J - L_R) = C_J L_J \left(1 + \frac{C_c}{C_J}\right) - C_R L_R \left(1 + \frac{C_c}{C_R}\right) \tag{B.52}$$

$$C = 2C_c\sqrt{L_J L_R} \tag{B.53}$$

It's easy to show that $O_{\breve{C}}$ and $O_{\breve{C}}^T$ can be expressed as rotations by introducing the rotation angle $\theta = \arctan x$ with $x = C/\Delta$, and noting that $\sqrt{1+x^2} = \cos^{-1}\theta$ and $x = \tan\theta$. Making use of the following trigonometric identities:

$$\sin\theta = 2\sin\frac{\theta}{2}\cos\frac{\theta}{2}$$
$$\cos\theta = 1 - 2\sin^2\frac{\theta}{2} = 2\cos^2\frac{\theta}{2} - 1$$

one finds that:

$$O_{\breve{C}}^T = \begin{pmatrix} \frac{\sqrt{1+x^2}+1}{\sqrt{\left(1+\sqrt{1+x^2}\right)^2+x^2}} & \frac{-x}{\sqrt{\left(1+\sqrt{1+x^2}\right)^2+x^2}} \\ \frac{\sqrt{1+x^2}-1}{\sqrt{\left(1-\sqrt{1+x^2}\right)^2+x^2}} & \frac{x}{\sqrt{\left(1-\sqrt{1+x^2}\right)^2+x^2}} \end{pmatrix} = \begin{pmatrix} \cos\frac{\theta}{2} & -\sin\frac{\theta}{2} \\ \sin\frac{\theta}{2} & \cos\frac{\theta}{2} \end{pmatrix}. \tag{B.54}$$

The eigenvalue matrix $\Lambda_{\breve{C}}$ is:

$$\Lambda_{\breve{C}} = \frac{1}{2}\begin{pmatrix} \sigma + \sqrt{\Delta^2 + C^2} & 0 \\ 0 & \sigma - \sqrt{\Delta^2 + C^2} \end{pmatrix} \tag{B.55}$$

with:

$$\sigma = C_J L_J \left(1 + \frac{C_c}{C_J}\right) + C_R L_R \left(1 + \frac{C_c}{C_R}\right). \tag{B.56}$$

One can now define the eigenmode flux variable as:

$$\mathbf{\Phi}_m := O_{\breve{C}}^T \breve{\mathbf{\Phi}} \tag{B.57}$$

which has the explicit form:

$$\mathbf{\Phi}_m = \begin{pmatrix} \Phi_1 \\ \Phi_2 \end{pmatrix} := \begin{pmatrix} \cos\frac{\theta}{2} & -\sin\frac{\theta}{2} \\ \sin\frac{\theta}{2} & \cos\frac{\theta}{2} \end{pmatrix} \begin{pmatrix} \breve{\Phi}_J \\ \breve{\Phi}_R \end{pmatrix} = \begin{pmatrix} \cos\frac{\theta}{2} & -\sin\frac{\theta}{2} \\ \sin\frac{\theta}{2} & \cos\frac{\theta}{2} \end{pmatrix} \begin{pmatrix} L_J^{-\frac{1}{2}} & 0 \\ 0 & L_R^{-\frac{1}{2}} \end{pmatrix} \begin{pmatrix} \Phi_J \\ \Phi_R \end{pmatrix}. \tag{B.58}$$

In terms of $\mathbf{\Phi}_m$ the Lagrangian is now diagonal:

$$\mathcal{L}_{lin} = \frac{1}{2}\dot{\mathbf{\Phi}}_m^T \Lambda_{\breve{C}} \mathbb{1}_C \dot{\mathbf{\Phi}}_m - \frac{1}{2}\mathbf{\Phi}_m^T \mathbb{1}_L^{-1} \mathbf{\Phi}_m. \tag{B.59}$$

The inverse relation that expresses Φ in terms of Φ_m gives the so-called eigenvector matrix E:

$$\begin{pmatrix}\Phi_J\\ \Phi_R\end{pmatrix} = \begin{pmatrix}\sqrt{L_J}\cos\frac{\theta}{2} & \sqrt{L_J}\sin\frac{\theta}{2}\\ -\sqrt{L_R}\sin\frac{\theta}{2} & \sqrt{L_R}\cos\frac{\theta}{2}\end{pmatrix}\mathbf{\Phi}_m = E\ \mathbf{\Phi}_m. \tag{B.60}$$

Finally the eigenfrequencies matrix of the linearized system is defined from the Euler-Lagrange equation of motion and given by:

$$\Omega = \Lambda_{\breve{C}}^{-\frac{1}{2}} = \begin{pmatrix}\sqrt{\frac{2}{\sigma+\sqrt{\Delta^2+C^2}}} & 0\\ 0 & \sqrt{\frac{2}{\sigma-\sqrt{\Delta^2+C^2}}}\end{pmatrix} = \begin{pmatrix}\omega_1 & 0\\ 0 & \omega_2\end{pmatrix} \tag{B.61}$$

Diagonalized Hamiltonian

We now move to the Hamiltonian formalism by introducing the canonical momentum associated to $\mathbf{\Phi}_m$:

$$\boldsymbol{Q}_m := \frac{\partial\mathcal{L}}{\partial\dot{\mathbf{\Phi}}_m} = \Lambda_{\breve{C}}\mathbb{1}_C\dot{\mathbf{\Phi}}_m, \tag{B.62}$$

the Hamiltonian is obtained from a Legendre transformation on $\mathcal{L}_{full}$:

$$\mathcal{H}_{full} = \dot{\mathbf{\Phi}}_m^T\boldsymbol{Q}_m - \mathcal{L}_{full} \tag{B.63}$$

which can again be separated into linear and non-linear part as:

$$\mathcal{H}_{full}(\mathbf{\Phi}_m, \boldsymbol{Q}_m) = \mathcal{H}_{lin}(\mathbf{\Phi}_m, \boldsymbol{Q}_m) + \mathcal{H}_{nl}(\mathbf{\Phi}_m, \boldsymbol{Q}_m) \tag{B.64}$$

which explicitly read:

$$\mathcal{H}_{lin}(\mathbf{\Phi}_m, \boldsymbol{Q}_m) = \frac{1}{2}\boldsymbol{Q}_m^T\ \Omega^2\mathbb{1}_L\ \boldsymbol{Q}_m + \frac{1}{2}\mathbf{\Phi}_m^T\ \mathbb{1}_L^{-1}\ \mathbf{\Phi}_m \tag{B.65}$$

$$\mathcal{H}_{nl}(\mathbf{\Phi}_m, \boldsymbol{Q}_m) := -\mathcal{L}_{nl}(\mathbf{\Phi}_m). \tag{B.66}$$

As for the Lagrangian, the linear part of the Hamiltonian is diagonal on the basis of the eigenmode fluxes $\mathbf{\Phi}_m$, while the non-linear part can be expanded on this basis up to any order to obtain the desired approximation.

Quantizing the Josephson circuit

We now quantize $\mathcal{H}_{full}$ using Dirac's canonical approach. Before proceeding we introduce the complex action-angles variables α_m which are the classical analog of the bosonic amplitude operators. The vector of action-angle variables is defined by the following non-canonical transformation:

$$\boldsymbol{\alpha}(t) := \frac{1}{\sqrt{2\hbar\Omega}}\left(\mathbf{\Phi}_m(t)1_H^{-\frac{1}{2}} + i\Omega\boldsymbol{Q}_m(t)1_H^{\frac{1}{2}}\right) \tag{B.67}$$

1_H being unity with dimensions of inductance, and the normalization being chosen so that the Poisson bracket of the action-angles is $\{\alpha_m, \alpha_{m'}^*\}_P = 1/i\hbar\delta_{mm'}$. The Hamiltonian remains diagonal in terms of the action-angle variables:

$$\mathcal{H}_{lin} = \frac{\hbar}{2}\left(\boldsymbol{\alpha}^T\Omega\boldsymbol{\alpha}^* + \boldsymbol{\alpha}^{*T}\Omega\boldsymbol{\alpha}\right). \tag{B.68}$$

The procedure consists now in quantizing the action-angle variables to obtain the annihilation and creation operators, and expressing the normal-mode magnetic flux and charge in terms of these operators:

$$\hat{\mathbf{\Phi}}_m = \mathbf{\Phi}_m^{zpf}\left(\hat{a} + \hat{a}^\dagger\right) \tag{B.69}$$

$$\hat{\boldsymbol{Q}}_m = i\boldsymbol{Q}_m^{zpf}\left(\hat{a}^\dagger - \hat{a}\right) \tag{B.70}$$

where:

$$\mathbf{\Phi}_m^{zpf} := \sqrt{\frac{\hbar}{2}}\Omega^{1/2} I_{H^{1/2}} \tag{B.71}$$

$$\boldsymbol{Q}_m^{zpf} := \sqrt{\frac{\hbar}{2}}\Omega^{-1/2} I_{H^{-1/2}} \tag{B.72}$$

are the zero-point fluctuations of flux and charge operators. More explicitly in our case we can write:

$$\mathbf{\Phi}_m^{zpf} := \sqrt{\frac{\hbar}{2}}\left(\frac{2}{\sigma+\sqrt{\Delta^2+C^2}}\right)^{\frac{1}{4}} \tag{B.73}$$

$$\boldsymbol{Q}_m^{zpf} := \sqrt{\frac{\hbar}{2}}\left(\frac{\sigma+\sqrt{\Delta^2+C^2}}{2}\right)^{\frac{1}{4}} \tag{B.74}$$

One can also extract the physically relevant zero-point fluctuations of the flux variables $\hat{\Phi}_J$ and $\hat{\Phi}_R$ using the eigenvector matrix E:

$$\begin{pmatrix}\Phi_J^{zpf}\\ \Phi_R^{zpf}\end{pmatrix} = E\ \begin{pmatrix}\Phi_1^{zpf}\\ \Phi_2^{zpf}\end{pmatrix} = E\ \mathbf{\Phi}_m^{zpf} \tag{B.75}$$

To express the non-linear part of the Hamiltonian we use the fact that the flux associated to the Josephson junction can be expressed as:

$$\hat{\Phi}_J = E_{11}\hat{\Phi}_1 + E_{12}\hat{\Phi}_2 = E_{11}\Phi_1^{zpf}(\hat{a}_1 + \hat{a}_1^\dagger) + E_{12}\Phi_2^{zpf}(\hat{a}_2 + \hat{a}_2^\dagger) \tag{B.76}$$

$$\hat{\varphi}_J = \frac{\hat{\Phi}_J}{\phi_0^2} = E_{11}\varphi_1^{zpf}(\hat{a}_1 + \hat{a}_1^\dagger) + E_{12}\varphi_2^{zpf}(\hat{a}_2 + \hat{a}_2^\dagger) \tag{B.77}$$

and one can rewrite:

$$\begin{aligned}(E_{11}\varphi_1^{zpf})^2 &= \frac{\hbar}{2\phi_0^2}\left(\frac{2}{\sigma+\sqrt{\Delta^2+C^2}}\right)^{\frac{1}{2}} L_J\cos^2\frac{\theta}{2} := p_{1J}\frac{\hbar\omega_1}{2E_J}\\ (E_{12}\varphi_2^{zpf})^2 &= \frac{\hbar}{2\phi_0^2}\left(\frac{2}{\sigma-\sqrt{\Delta^2+C^2}}\right)^{\frac{1}{2}} L_J\sin^2\frac{\theta}{2} := p_{2J}\frac{\hbar\omega_2}{2E_J}\end{aligned} \tag{B.78}$$

with p_{1J} and p_{2J} are called *energy-participation ratios* of eigenmodes 1 and 2 to the Josephson dipole and determine how much the Josephson non-linearity participates in each mode. By using the explicit expressions $\omega_1 = \sqrt{\frac{2}{\sigma+\sqrt{\Delta^2+C^2}}}$ and $\omega_2 = \sqrt{\frac{2}{\sigma-\sqrt{\Delta^2+C^2}}}$, using $L_J = \phi_0^2/E_J$

$$p_{1J} = \cos^2\frac{\theta}{2}, \qquad p_{2J} = \sin^2\frac{\theta}{2}, \tag{B.79}$$

where we recall that:

$$\theta = \arctan\left(\frac{C}{\Delta}\right) \tag{B.80}$$

$$C = 2C_c\sqrt{L_J L_R} \tag{B.81}$$

$$\Delta = C_J L_J\left(1+\frac{C_c}{C_J}\right) - C_R L_R\left(1+\frac{C_c}{C_R}\right) \tag{B.82}$$

Full Hamiltonian

We can now express the full Hamiltonian using the amplitude operators:

$$\hat{H}_{full} = \hbar\omega_1\hat{a}_1^\dagger\hat{a}_1 + \hbar\omega_2\hat{a}_2^\dagger\hat{a}_2 - E_J\sum_{n=2}^{\infty}\frac{(-1)^n}{(2n)!}\hat{\varphi}_J^{2n} \tag{B.83}$$

with:

$$\hat{\varphi}_J = \sqrt{\frac{\hbar}{2E_J}}\left[\sqrt{p_1\omega_1}(\hat{a}_1+\hat{a}_1^\dagger) + \sqrt{p_2\omega_2}(\hat{a}_2+\hat{a}_2^\dagger)\right] \tag{B.84}$$

$$p_1 = \cos^2\frac{\theta}{2} \tag{B.85}$$

$$p_2 = \sin^2\frac{\theta}{2} \tag{B.86}$$

$$\omega_1 = \sqrt{\frac{2}{\sigma+\sqrt{\Delta^2+C^2}}} \tag{B.87}$$

$$\omega_2 = \sqrt{\frac{2}{\sigma-\sqrt{\Delta^2+C^2}}} \tag{B.88}$$

$$C = 2C_c\sqrt{L_J L_R} \tag{B.89}$$

$$\Delta = C_J L_J\left(1+\frac{C_c}{C_J}\right) - C_R L_R\left(1+\frac{C_c}{C_R}\right) \tag{B.90}$$

$$\sigma = C_J L_J\left(1+\frac{C_c}{C_J}\right) + C_R L_R\left(1+\frac{C_c}{C_R}\right) \tag{B.91}$$

Note that in the case of uncoupled resonator and qubit ($C_c = 0$) we retrieve the expected behavior:

$$C \to 0 \quad (x \to 0,\ \theta = \arctan x \to 0) \tag{B.92}$$

$$\Delta \to C_J L_J - C_R L_R \tag{B.93}$$

$$\sigma \to C_J L_J + C_R L_R \tag{B.94}$$

$$O_{\check{C}}^T \to \begin{pmatrix} 1 & 0 \\ 0 & 1 \end{pmatrix} \tag{B.95}$$

$$\Omega \to \begin{pmatrix} \omega_J & 0 \\ 0 & \omega_R \end{pmatrix} \tag{B.96}$$

$$p_1 \to 1 \tag{B.97}$$

$$p_2 \to 0 \tag{B.98}$$

4^{th} order approximation and dispersive qubit readout

The resonator coupled to the transmon qubit can be used for reading out the state of the qubit with minimum perturbation. This technique is called *dispersive readout* and is based on the shift of the coupled resonator frequency based on the qubit state. One can simply derive this dispersive shift by chopping the non-linear term at the 4-th order:

$$\hat{H}_{full} = \hbar\omega_1 \hat{a}_1^\dagger \hat{a}_1 + \hbar\omega_2 \hat{a}_2^\dagger \hat{a}_2 - \frac{E_J}{24}\left(\frac{\hbar}{2E_J}\right)^2 \left[\sqrt{p_1\omega_1}(\hat{a}_1 + \hat{a}_1^\dagger) + \sqrt{p_2\omega_2}(\hat{a}_2 + \hat{a}_2^\dagger)\right]^4 \tag{B.99}$$

applying the rotating wave approximation with $|\omega_1 - \omega_2| \gg 0$, neglecting constant energy terms, the last term reads:

$$\begin{aligned} &\hat{a}_1^\dagger \hat{a}_1 \left(12 p_1\omega_1 p_2\omega_2 + 6(p_1\omega_1)^2\right) + 6(p_1\omega_1)^2(\hat{a}_1^\dagger\hat{a}_1)^2 + \\ &+\hat{a}_2^\dagger \hat{a}_2 \left(12 p_1\omega_1 p_2\omega_2 + 6(p_2\omega_2)^2\right) + 6(p_2\omega_2)^2(\hat{a}_2^\dagger\hat{a}_2)^2 + \\ &+24 p_1\omega_1 p_2\omega_2 \hat{a}_1^\dagger\hat{a}_1\hat{a}_2^\dagger\hat{a}_2 \end{aligned} \tag{B.100}$$

which, plugged back into the Hamiltonian, leads to:

$$\begin{aligned} \hat{H}_{full} =& \hbar\omega_1 \left[1 - p_1\left(p_2\frac{\hbar\omega_2}{8E_J} + p_1\frac{\hbar\omega_1}{16E_J} + p_1\frac{\hbar\omega_1}{8E_J}\hat{a}_1^\dagger\hat{a}_1\right)\right]\hat{a}_1^\dagger\hat{a}_1 \\ &+\hbar\omega_2 \left[1 - p_2\left(p_1\frac{\hbar\omega_1}{8E_J} + p_2\frac{\hbar\omega_2}{16E_J} + p_2\frac{\hbar\omega_2}{8E_J}\hat{a}_2^\dagger\hat{a}_2\right)\right]\hat{a}_2^\dagger\hat{a}_2 \\ &-\frac{\hbar\omega_1\hbar\omega_2}{4E_J} p_1 p_2\ (\hat{a}_1^\dagger\hat{a}_1)\ (\hat{a}_2^\dagger\hat{a}_2). \end{aligned} \tag{B.101}$$

In the weak coupling regime ($C_c \ll 1$), $\hat{a}_1$ and $\hat{a}_2$ almost coincide with the annihilation operators respectively of the resonator mode and qubit mode. Thus, the last term represents a shift of the frequency of each of these modes, based on the population of the other one, in other words the frequency of the resonator depends on the state of the qubit and the frequency of the qubit depends on the number of photons in the resonator. This dispersive shift effect is obtained when $|\omega_1 - \omega_2| \gg 0$ and is exploited to readout the state of the qubit by measuring the frequency of the coupled resonator.

SMPD Hamiltonian

As already anticipated in section 5.2, the SMPD system consists of three electromagnetic modes, the buffer, qubit and waste, coupled through a Josephson junction. A strong radio-frequency drive, the pump, is applied to the qubit mode to activate the four-waves mixing process. Following Ref. [57], and grounded on the EPR method, we can write the Hamiltonian of the system as:

$$\hat{H} = \sum_{m=b,w,q} \hbar\omega_m \hat{m}^\dagger\hat{m} - E_J\left[\cos(\hat{\varphi}) + \frac{\hat{\varphi}^2}{2}\right] + 2\epsilon_p \cos(\omega_p t)\left(\hat{q} + \hat{q}^\dagger\right) \tag{B.102}$$

where E_J is the Josephson energy and ϵ_p and ω_p are the angular frequency and amplitude of the pump. The index m refers to the buffer, waste and qubit modes of respective angular frequency ω_m and annihilator operator $\hat{m}$, and where:

$$\hat{\varphi} = \sum_{m=b,w,q} \varphi_m\left(\hat{m} + \hat{m}^\dagger\right), \tag{B.103}$$

so that the phase across the junction can be decomposed as the sum of the phases of each mode, as derived in the EPR analysis (cfr. Eq. B.84).

We now proceed as in section 3.2 and move to the frame displaced by the mean field pump amplitude $\xi_p e^{-i\omega_p t}$, with $\xi_p \approx -\epsilon_p/(\omega_q - \omega_p)$, provided that the pump is adiabatically switched on and off with respect to the detuning $\omega_q - \omega_p$ ($\sim -500\,\text{MHz}$ in our experiment). Moreover, we place ourselves in the interaction picture with respect to the Hamiltonian $\sum_m (\omega_m - \delta_m)\hat{m}^\dagger\hat{m}$ where δ_m are arbitrary detunings used to cancel the ac-Stark shifts due to the Kerr effect. The transformed Hamiltonian is:

$$\hat{H} = \sum_{m=b,w,q} \hbar\delta_m \hat{m}^\dagger\hat{m} - E_J \left[\cos\left(\hat{\varphi}'\right) + \frac{\hat{\varphi}'^2}{2}\right] \tag{B.104}$$

where:

$$\hat{\varphi}' = \sum_{m=b,w,q} \varphi_m \left(\hat{m}e^{-i(\omega_m-\delta_m)t} + \hat{m}^\dagger e^{i(\omega_m-\delta_m)t}\right) + \varphi_q \left(\xi_p e^{-i\omega_p t} + \xi_p^* e^{i\omega_p t}\right). \tag{B.105}$$

At this point we take the energy conservation condition of the four-waves mixing process:

$$\omega_p = (\omega_q - \delta_q) + (\omega_w - \delta_w) - (\omega_b - \delta_b), \tag{B.106}$$

we then expand the cosine terms up to fourth order (similarly to Eq. B.99) and keep the non-rotating terms:

$$\hat{H} \approx \hat{H}_{Stark} + \hat{H}_{Kerr} + \hat{H}_{4WM} \tag{B.107}$$

where:

$$\hat{H}_{Stark} = \sum_{m=b,w} \hbar\left(\delta_m - \chi_{qm}\left|\xi_p\right|^2\right)\hat{m}^\dagger\hat{m} + \hbar\left(\delta_q - 2\chi_{qq}\left|\xi_p\right|^2\right)\hat{q}^\dagger\hat{q}, \tag{B.108}$$

$$\hat{H}_{Kerr} = \sum_{m=b,w,q} -\frac{\hbar\chi_{mm}}{2}\hat{m}^{\dagger 2}\hat{m}^2 - \hbar\chi_{qb}\hat{b}^\dagger\hat{b}\hat{q}^\dagger\hat{q} - \hbar\chi_{qw}\hat{w}^\dagger\hat{w}\hat{q}^\dagger\hat{q} - \hbar\chi_{qb}\hat{q}^\dagger\hat{q}\hat{b}^\dagger\hat{b}, \tag{B.109}$$

$$\hat{H}_{4WM} = \hbar g_3 \hat{b}\hat{w}^\dagger\hat{q}^\dagger + \hbar g_3^* \hat{b}^\dagger\hat{w}\hat{q} \tag{B.110}$$

with:

$$\hbar\chi_{mm} = \frac{E_J}{2}\phi_m^4 \tag{B.111}$$

$$\hbar\chi_{mn} = E_J\phi_m^2\phi_n^2 \tag{B.112}$$

$$\hbar g_3 = -E_J\xi_p\phi_q^2\phi_b\phi_w = -\xi_p\sqrt{\chi_{qb}\chi_{qw}}. \tag{B.113}$$

We neglected the terms $\hat{m}^\dagger\hat{m}$ arising from the normal ordering of the fourth-order term since their effect is just to shift the bare frequencies ω_m by a constant amount.

We can now apply the two-level system approximation to the transmon qubit: since its anharmonicity χ_{qq} ($\sim 200\,\text{MHz}$) is much larger than all the dissipation and excitation rates ($\sim 1\,\text{MHz}$), in the following, we project the qubit mode onto its two lowest energy levels $|g\rangle$ and $|e\rangle$. We thus replace the bosonic operator $\hat{q}$ by the two-level lowering operator $\hat{\sigma} = |g\rangle\langle e|$. Moreover, we choose the mode reference frames such that $\delta_q = 2\chi_{qq}\left|\xi_p\right|^2$, $\delta_b = \chi_{qb}\left|\xi_p\right|^2$, and $\delta_w = \chi_{qw}\left|\xi_p\right|^2 + \Delta$, where we have introduced an arbitrary detuning Δ which can be chosen to cancel the cross-Kerr effect between the qubit and the waste χ_{qw}. This leads to $\hat{H}_{Stark} = \hbar\Delta\hat{w}^\dagger\hat{w}$. The

pump frequency thus needs to be adapted for each value of ξ_p in order to always verify Eq. B.106:

$$\omega_p = \omega_q + \omega_w - \omega_b - \Delta - |\xi_p|^2 (2\chi_{qq} + \chi_{qw} - \chi_{qb}) . \tag{B.114}$$

The final Hamiltonian reads:

$$\hat{H} = \hbar\Delta\hat{w}^\dagger\hat{w} + g_3\hat{b}\hat{w}^\dagger\hat{\sigma}^\dagger + g_3^*\hat{b}^\dagger\hat{w}\hat{\sigma} - \sum_{m=b,w}\frac{\chi_{mm}}{2}\hat{m}^{\dagger 2}\hat{m}^2 - \chi_{qb}\hat{b}^\dagger\hat{b}\hat{\sigma}^\dagger\hat{\sigma} - \chi_{qw}\hat{w}^\dagger\hat{w}\hat{\sigma}^\dagger\hat{\sigma} - \chi_{bw}\hat{b}^\dagger\hat{b}\hat{w}^\dagger\hat{w} \tag{B.115}$$

Engineering irreversible interaction: adiabatic elimination of the waste mode

The just-derived Hamiltonian generates a reversible four-waves mixing unitary evolution: once an incoming photon in the buffer mode is converted to an excitation of the qubit plus a photon in the waste mode, the reverse process can happen with equal probability, causing the loss of the information about the absorbed photon stored in the qubit.

In order to suppress the reversibility one can engineer the dissipation of the waste mode such that the converted photon is quickly and irremediably lost in the environment. For this to happen, the energy decay rate of the waste mode κ_w has to be larger than the coupling g_3 of the waste mode to the buffer through the four-wave mixing process. If this is verified one can proceed in an analogous way as done in section 3.2 and use the adiabatic approximation to trace out the state of the system on the waste degrees of freedom, obtaining an effective evolution for the remaining subsystem. Since the system is now embedded in an environment we move to the Lindblad formalism for the evolution of the density matrix, and account for the dephasing of the qubit (at rate κ_ϕ) and dissipation of the qubit, buffer and waste (κ_q, κ_b and κ_w) through Lindblad operators, the master equation reads:

$$\dot{\hat{\rho}} = \frac{1}{i\hbar}[\hat{H}, \hat{\rho}] + \mathcal{D}_{\hat{\Gamma}_w}(\hat{\rho}) + \mathcal{D}_{\hat{\Gamma}_b}(\hat{\rho}) + \mathcal{D}_{\hat{\Gamma}_\sigma}(\hat{\rho}) + \mathcal{D}_{\hat{\gamma}_z}(\hat{\rho}) \tag{B.116}$$

with:

$$\hat{\Gamma}_m = \sqrt{\kappa_m}\hat{m} \tag{B.117}$$

$$\hat{\gamma}_z = \sqrt{\frac{\kappa_\phi}{2}}\hat{\sigma}^+\hat{\sigma}. \tag{B.118}$$

To perform the adiabatic approximation, we place ourselves in the regime where $|g_3|, \chi_{qb}, \chi_{bw}, \chi_{bb}, \kappa_b, \kappa_q, \kappa_\phi \sim \delta\kappa_w$, and δ is a small parameter $\delta \ll 1$. In our experiment, $\chi_{qw} = \kappa_w \sim 1$, and we assume $\Delta/\kappa_w \sim 1$. In this regime, the waste mode can be adiabatically eliminated, leading to an effective dynamics for the buffer and qubit modes alone. We search for a solution of the full buffer-qubit-waste dynamics of the form:

$$\begin{aligned}\hat{\rho} =& \hat{\rho}_{00} \otimes |0\rangle\langle 0| + \delta\left(\hat{\rho}_{10} \otimes |1\rangle\langle 0| + \hat{\rho}_{01} \otimes |0\rangle\langle 1|\right) + \\ &+ \delta^2\left(\hat{\rho}_{11} \otimes |1\rangle\langle 1| + \hat{\rho}_{02} \otimes |0\rangle\langle 2| + \hat{\rho}_{20} \otimes |2\rangle\langle 0|\right) + O(\delta^3)\end{aligned} \tag{B.119}$$

where $\hat{\rho}_{mn} = \langle m|\hat{\rho}|n\rangle$ is the reduced density matrix acting on the buffer Hilbert space with $|m\rangle$, $|n\rangle$ being the Fock states basis of the waste mode. Whereas $|n\rangle\langle m|$ acts on the waste Hilbert space. The goal here is to derive the dynamics

of $\hat{\rho}_{qb} = \mathrm{Tr}_w(\hat{\rho}) = \hat{\rho}_{00} + \delta^2\hat{\rho}_{11}$ up to second order in δ, where Tr_w denotes the partial trace over the waste degrees of freedom. The low occupancy of the waste mode justifies this expansion. We are interested in the dynamics of the reduced density operator for the qubit-buffer modes $\hat{\rho}_{qb}$, which is obtained by taking the partial trace over the waste mode. We rewrite the Hamiltonian of Eq. B.115 in the following form:

$$\hat{H} = \hbar g_3 \hat{b}\hat{\sigma}^\dagger\hat{w}^\dagger + \hbar g_3^* \hat{b}^\dagger\hat{\sigma}\hat{w} + \left(\Delta - \hbar\chi_{qw}\hat{\sigma}^\dagger\hat{\sigma} - \hbar\chi_{bw}\hat{b}^\dagger\hat{b}\right)\hat{w}^\dagger\hat{w} + \hat{H}_{qb} \tag{B.120}$$

with:

$$\hat{H}_{qb} = -\frac{\hbar\chi_{bb}}{2}\hat{b}^{\dagger 2}\hat{b}^2 - \hbar\chi_{qb}\hat{b}^\dagger\hat{b}\hat{\sigma}^\dagger\hat{\sigma}. \tag{B.121}$$

We define the Lindbladian acting on the qubit-buffer subspace as:

$$\mathcal{L}_{qb}\left(\hat{\rho}_{qb}\right) = \frac{1}{i\hbar}\left[\hat{H}_{qb}, \hat{\rho}_{qb}\right] + \mathcal{D}_{\hat{\Gamma}_b}(\hat{\rho}) + \mathcal{D}_{\hat{\Gamma}_\sigma}(\hat{\rho}) + \mathcal{D}_{\hat{\gamma}_z}(\hat{\rho}). \tag{B.122}$$

By projecting Eq. B.116 on $\langle 0|\cdot|0\rangle$, $\langle 0|\cdot|1\rangle$ and $\langle 1|\cdot|0\rangle$, respectively, we get:

$$\frac{\dot{\hat{\rho}}_{00}}{\kappa_w} = \delta^2\left(i\rho_{01}\hat{A} - i\hat{A}^\dagger\rho_{10} + \rho_{11}\right) + \frac{1}{\kappa_w}\mathcal{L}_{qb}(\rho_{00}) + O(\delta^3) \tag{B.123}$$

$$\frac{\dot{\hat{\rho}}_{01}}{\kappa_w} = i\rho_{00}\hat{A}^\dagger - \rho_{01}\left(\frac{1}{2} - i\hat{\Delta}\right) + O(\delta) \tag{B.124}$$

$$\frac{\dot{\hat{\rho}}_{11}}{\kappa_w} = i\rho_{10}\hat{A}^\dagger - i\hat{A}\rho_{01} - i[\hat{\Delta}, \rho_{11}] - \rho_{11} + O(\delta) \tag{B.125}$$

where

$$\hat{A} = \frac{g_3}{\kappa_w\delta}\hat{b}\hat{\sigma}^\dagger \tag{B.126}$$

$$\hat{\Delta} = \frac{\Delta - \chi_{qw}\hat{\sigma}^\dagger\hat{\sigma}}{\kappa_w} \tag{B.127}$$

Note that $||\hat{A}||$ and $||\hat{\Delta}||$ are of order δ^0. Considering Eq. (B.124), we see that the derivative of ρ_{01} is composed of a term proportional to ρ_{00} that can be viewed as an external drive, and a term proportional to ρ_{01}, that includes a damping term. Since the variation of ρ_{00} is slow ($d\rho_{00}/\kappa_w dt$ of order δ^2, see Eq. (B.123)) in comparison to the damping term (of order 1), we can make the adiabatic approximation: we consider that ρ_{01} is continuously in its steady state. The same reasoning applies to ρ_{11}, we thus set to 0 the left hand sides of Eqs. B.124 and B.125. Moreover, by noting that $\hat{\Delta}\hat{A} = (\Delta - \chi_{qw})\hat{A}/\kappa_w$, we can solve for $\rho_{01}, \rho_{10}, \rho_{11}$ as a function of ρ_{00}. We find

$$\rho_{01} = \frac{1}{1 + 4|\frac{\Delta - \chi_{qw}}{\kappa_w}|^2}\left(2i - 4\frac{(\Delta - \chi_{qw})}{\kappa_w}\right)\rho_{00}\hat{A}^\dagger \tag{B.128}$$

$$\rho_{11} = \frac{1}{1 + 4|\frac{\Delta - \chi_{qw}}{\kappa_w}|^2}4\hat{A}\rho_{00}\hat{A}^\dagger\ . \tag{B.129}$$

We denote

$$\kappa_{\mathrm{nl}} = \frac{4|g_3|^2/\kappa_w}{1 + 4|\frac{\Delta - \chi_{qw}}{\kappa_w}|^2}\ , \tag{B.130}$$

$$\Delta_{nl} = \frac{4|g_3|^2/\kappa_w}{1 + 4|\frac{\Delta - \chi_{qw}}{\kappa_w}|^2}\frac{\chi_{qw} - \Delta}{\kappa_w}\ . \tag{B.131}$$

Inserting the solutions (B.128), (B.129) into Eq. (B.123) we find

$$\frac{d}{dt}\rho_{00} = -i\Delta_{nl}[\hat{b}^\dagger\hat{b}\hat{\sigma}\sigma^\dagger, \rho_{00}] + \mathcal{D}_{\hat{\Gamma}_{\rm nl}}\rho_{00} + \mathcal{L}_{qb}(\rho_{00}) + O(\delta^3)\ . \tag{B.132}$$

with:

$$\hat{\Gamma}_{\rm nl} = \sqrt{\kappa_{\rm nl}}\hat{b}\hat{\sigma}^\dagger \tag{B.133}$$

The term proportional to $\kappa_{\rm nl}$ is the non-linear damping term at the heart of the Single Microwave Photon Detector. It is maximized for $\Delta = \chi_{qw}$. In this configuration, the pump angular frequency $\omega_p = \omega_q + \omega_w - \omega_b - \chi_{qw}$ is such that $\hbar\omega_p$ exactly matches the energy difference between the initial state $\hat{b}^\dagger|0\rangle$ and final state $\hat{\sigma}^\dagger\hat{w}^\dagger|0\rangle$, and $\kappa_{\rm nl} = 4|g_3|^2/\kappa_w$. The term proportional to Δ_{nl} is a "generalized frequency pull" that corresponds to a tunable cross-Kerr effect between the qubit and buffer modes. Note that the ρ_{qb} follows the same dynamics as Eq. (B.132).

Coupled cavities model

The systematic approach leading to the adiabatic approximation result catches the full dynamics of the buffer-qubit-waste interaction, but it requires the adiabatic elimination condition to be satisfied for all dynamical degrees of freedom. Since as revealed later on, due to fabrication issues, we have $\kappa_{\rm b} > \kappa_{\rm w}$, the assumption made for adiabatic approximation does not hold anymore. In that case, instead of deriving the full master equation in the adiabatic approximation, one can use a different approach to evaluate the scattering parameter S_{21} of the detector, which is linked to bandwidth and efficiency.

Starting from the Hamiltonian Eq. B.120 one can calculate the evolution of the buffer and waste annihilation operators $\hat{b}$ and $\hat{w}$ using the Lindblad master equation (5.32):

$$\dot{\hat{b}} = -i\delta_{\rm b}\hat{b} + ig_3^*\hat{w}\hat{\sigma} - \frac{\kappa_{\rm b}}{2}\hat{b} + \sqrt{\kappa_{\rm in}}\hat{b}_{\rm in} \tag{B.134}$$

$$\dot{\hat{w}} = -i\delta_{\rm w}\hat{w} + ig_3\hat{b}\hat{\sigma}^\dagger - \frac{\kappa_{\rm w}}{2}\hat{w}, \tag{B.135}$$

where we reintroduced the $\delta_{\rm i}$ as the frequency detunings when moving to interaction picture (see Eq. B.104), we neglected the terms $\chi_{\rm mn}$ which are smaller than g_3, and we introduced a source term on the buffer side, describing the input field impinging on the detector. We now make the realistic assumption that the initial state is separable in the field-qubit subspaces $\hat{\rho} = \hat{\rho}^{(bw)} \otimes \hat{\rho}^{(q)}$, and evaluate the mean values of the operators tracing explicitly on the qubit subspace:

$$\langle\dot{\hat{b}}\rangle = -i\delta_{\rm b}\langle\hat{b}\rangle - i\mathcal{G}\langle\hat{w}\rangle - \frac{\kappa_{\rm b}}{2}\langle\hat{b}\rangle + \sqrt{\kappa_{\rm in}}\langle\hat{b}_{\rm in}\rangle \tag{B.136}$$

$$\langle\dot{\hat{w}}\rangle = -i\delta_{\rm w}\langle\hat{w}\rangle - i\mathcal{G}^*\langle\hat{b}\rangle - \frac{\kappa_{\rm w}}{2}\langle\hat{w}\rangle \tag{B.137}$$

where

$$\mathcal{G} = -\rho_{\rm eg}^{(q)}g_3 = \rho_{\rm eg}^{(q)}\xi_p\sqrt{\chi_{\rm qb}\chi_{\rm qw}}. \tag{B.138}$$

Note that $\mathcal{G}$ depends on time, as $\rho_{\rm eg}^{(q)}$ is itself time-dependent. This term describes a coupling between the buffer and waste modes, which is mediated by the four-wave mixing process, and whose 'direction' depends on the state of the qubit. One can verify that:

$$\dot{\rho}_{\rm eg}^{(q)} = -\dot{\rho}_{\rm ge}^{(q)} \propto i(\rho_{\rm gg} - \rho_{\rm ee}), \tag{B.139}$$

such that if the coupling increases in one direction, it decreases in the other direction. We can now solve the system of coupled equations for the average value of the buffer and waste intra-cavity fields $\beta = \langle \hat{b} \rangle$ and $\upsilon = \langle \hat{w} \rangle$:

$$\dot{\beta} = -i\delta_{\mathrm{b}}\beta - i\mathcal{G}\upsilon - \frac{\kappa_{\mathrm{b}}}{2}\beta + \sqrt{\kappa_{\mathrm{b}}}\beta_{\mathrm{in}} \tag{B.140}$$

$$\dot{\upsilon} = -i\delta_{\mathrm{w}}\upsilon - i\mathcal{G}^{*}\beta - \frac{\kappa_{\mathrm{w}}}{2}\upsilon \tag{B.141}$$

The equations for the Fourier components of β and υ are:

$$-i\delta\tilde{\beta} = -i\delta_{\mathrm{b}}\tilde{\beta} - i\mathcal{G}\tilde{\upsilon} - \frac{\kappa_{\mathrm{b}}}{2}\tilde{\beta} + \sqrt{\kappa_{\mathrm{b}}}\tilde{\beta}_{\mathrm{in}} \tag{B.142}$$

$$-i\delta\tilde{\upsilon} = -i\delta_{\mathrm{w}}\tilde{\upsilon} - i\mathcal{G}^{*}\tilde{\beta} - \frac{\kappa_{\mathrm{w}}}{2}\tilde{\upsilon} \tag{B.143}$$

where δ is the frequency of the Fourier component in the rotating frame. Using the relation between the intra-resonator fields and the input and output flux $\sqrt{\kappa_{\mathrm{b}}}\tilde{\beta} = \tilde{\beta}_{\mathrm{in}} + \tilde{\beta}_{\mathrm{out}}$, we can extract the frequency-dependent transmission coefficient $|S_{21}(\,\delta)|^2 = |\upsilon_{\mathrm{out}}/\beta_{\mathrm{in}}|^2$:

$$|\mathrm{S}_{21}(\delta)|^2 = \left| \frac{2\xi_{\mathrm{p}}\sqrt{\kappa_{\mathrm{b}}\kappa_{\mathrm{w}}\chi_{\mathrm{b}}\chi_{\mathrm{w}}}}{-4(\delta_{\mathrm{b}} - \delta)(\delta_{\mathrm{w}} - \delta) + 2i(\delta_{\mathrm{b}} - \delta)\kappa_{\mathrm{w}} + 2i(\delta_{\mathrm{w}} - \delta)\kappa_{\mathrm{b}} + \kappa_{\mathrm{b}}\kappa_{\mathrm{w}} + \chi_{\mathrm{b}}\chi_{\mathrm{w}}\xi_{\mathrm{p}}^2} \right|^2 . \tag{B.144}$$

Note that the buffer and waste modes interact resonantly through the four-wave mixing process activated by the pump, this can be expressed by writing $\delta_{\mathrm{w}} = \delta_{\mathrm{b}} + \delta_{\mathrm{p}}$, with δ_{p} denoting the pump shift with respect to the frequency matching condition ($\delta_{\mathrm{p}} = 0$).

Figure 5.6 reports plots of $|\mathrm{S}_{21}(\delta)|^2$ with realistic experimental parameters for three pump detunings, showing that maximum transmission through the detector (i.e. optimal four-wave mixing coupling between buffer and waste) is reached at the resonant condition, as expected. The expression for $|\mathrm{S}_{21}(\delta)|^2$ is essential to determine the efficiency and bandwidth of the detector as a function of the incoming photon frequency δ and the pump detuning δ_{p}, once the other parameters are known and will be used as a comparison with experimental measurements.

B.5 SMPD efficiency vs detection window

Impact of qubit relaxation on the efficiency

Here we derive a formula for the detection efficiency η_{d} as a function of the duration of the detection window T_{d}, taking into account the qubit relaxation time T_1. Let's consider a detection window of duration T_{d} starting at $t = 0$, a state containing a single photon with probability p_1 enters the SMPD at time t and excites the qubit with probability $\eta_0 p_1$. The probability of finding the qubit excited at the end of the detection window, when the readout is performed is:

$$P_{\mathrm{e}}(t) = \eta_{\mathrm{d}} p_1 = \eta_0 p_1 e^{-(T_{\mathrm{d}} - t)/T_1}. \tag{B.145}$$

such that one can define the new efficiency $\eta_{\mathrm{d}} = \eta_0 e^{-(T_{\mathrm{d}} - t)/T_1}$ taking into account qubit relaxation. Now consider a coherent state of low amplitude $\alpha = \sqrt{p_1} < 1$, continuously impinging on the SMPD. The probability of finding the qubit excited at the end of a detection window gives the efficiency:

$$\eta_{\mathrm{d}} = \frac{1}{T_{\mathrm{d}}} \int_0^{T_{\mathrm{d}}} \eta_0 e^{-(T_{\mathrm{d}} - t)/T_1} dt = \eta_0 \frac{T_1}{T_{\mathrm{d}}} \left(1 - e^{-T_{\mathrm{d}}/T_1}\right) \tag{B.146}$$

which takes into account both the relaxation of the qubit and the contribution of the continuously impinging photons.

B.6 SMPD recipe

Wafer preparation

SC1

5 H2O + H2O2(30%) + NH4OH(29%)	10'@80°C
HF (5%)	2'

Aluminum evaporation

Al	60 nm (1nm/s)

Circuit

Cleaning

Acetone / Isopropanol / Ultrasounds

Spincoating

Dehydratation bake	5' @ 150°C (for adhesion)
Cooldown N2	30''
UV3 spincoating	60'' @ 6000 @ 4000
Postbake	1' @ 130°C
Black box storage	

E-beam lithography

Meander mode ON	
Zoom	1.005
Dose	7 µC/cm2
Dose scaling	1.2
Poligon overlap	0.5 µm
Voltage	10 kV
Aperture	30 µm
Writefield	400 µm

Development & etching

Bake	1' @ 145°C
Cooldown	1'
CD26	3' to 6' @ room T

Cleaning

Acetone	10'
Isopropanol	10'

Junctions

Spincoating

Dehydratation bake	1' @ 110°C
Cooldown N2	30''
MAA EL10	3'' @ 500 @ 500 60'' @ 2000 @ 1000 5'' @ 7500 @ 1000
Postbake	5' @ 172°C
Cooldown	1'
PMMA A3950K	3'' @ 500 @ 500 60'' @ 3200 @ 1000 5'' @ 7000 @ 1000
Postbake	15' @ 175°C

x2

E-beam lithography

Meander mode ON	
Zoom	1.000
Dose	250 µC/cm2
Dose scaling	1.1 + 0.2 (junctions) 0.2 (undercut)
Poligon overlap	0.5 µm
Voltage	25 kV
Aperture	10 µm
Writefield	100 µm

Development

MIBK develop	60'' @ room T
Stopper	IPA 30''

Plasma ashing

Pressure	0.2 mb
Power	75 W
Time	10''

Junction evaporation

Milling	3'' + 3'' (5mA)
Al	35 nm (1nm/s) @ +29.6°
Ox	5' @ 10 mbar
Al	65 nm (1nm/s) @ -29.6°
Lift off	10' Aceton @ 80°C
(Junction stabilization	1' @ 100°C)

Bandage

Spincoating

Dehydratation bake	1' @ 110°C
Cooldown N2	30''
PMMA A6	5'' @ 500 @ 1000 60'' @ 3000 @ 3000
Postbake	15' @ 170°C

E-beam lithography

Meander mode ON	
Zoom	1.000
Dose	250 µC/cm2
Dose scaling	1.3
Poligon overlap	0.5 µm
Voltage	25 kV
Aperture	10 µm
Writefield	200 µm

Development

MIBK develop	60'' @ room T
Stopper	IPA 30''

Plasma ashing

Pressure	0.2 mb
Power	75 W
Time	10''

Bandage patch evaporation

Milling	1' standard recipe (65mA)
Al	100 nm (0.2 nm/s)
Lift off	2' Aceton @ 80°C

Trenching

Reactive ion etching

SF6	
Flow	20 sccm
Pressure	0.1 mbar
Voltage	43 V (35W)
Time	120''

Figure B.1: **SMPD recipe.**

Appendix C

Spin coupled to a cavity: Hamiltonian transformations and adiabatic elimination

C.1 Transforming the Hamiltonian

Displaced field description

In order to cancel the additional pump term appearing in Eq. 3.11 and simplify the description, we apply an unitary transformation to the Hamiltonian, shifting to the frame in which the cavity mode is displaced by some mean field amplitude $\alpha(t) = \alpha e^{-i\omega_d t}$:

$$D_\alpha = e^{\alpha(t)\hat{a}^\dagger - \alpha^*(t)\hat{a}}. \tag{C.1}$$

In order to preserve equations of motion 3.17, the Hamiltonian has to transform as $\hat{H} \to D_\alpha \hat{H} D_\alpha^\dagger + i\hbar \dot{D}_\alpha D_\alpha^\dagger$, and the Lindblad operators as $\hat{L}_i \to D_\alpha \hat{L}_i D_\alpha^\dagger$. One can thus choose α appropriately such that the term $i\hbar \dot{D}_\alpha D_\alpha^\dagger$ cancels out the pump term and the additional terms generated by the displacement operator. Under the displacement the transformed Hamiltonian is:

$$\begin{aligned} D_\alpha \hat{H} D_\alpha^\dagger =& \hbar\omega_0 \hat{a}^\dagger \hat{a} + \frac{\hbar}{2}\omega_s \hat{\sigma}_z + \hbar g_0 \left(\hat{a}\hat{\sigma}_+ + \hat{a}^\dagger \hat{\sigma}_-\right) - \hbar g_0 \left(\alpha(t)\hat{\sigma}_+ + \alpha^*(t)\hat{\sigma}_-\right) + \\ &+ i\hbar\sqrt{\kappa_{ext}} \left(\beta \hat{a}^\dagger e^{-i\omega_d t} + \beta^* \hat{a} e^{i\omega_d t}\right) + \hbar\omega_0 \left(-\alpha(t)\hat{a}^\dagger - \alpha^*(t)\hat{a}\right), \end{aligned} \tag{C.2}$$

where we omit all the constant terms which doesn't affect the dynamics. The last two terms are the ones we try to eliminate exploiting the additional $i\hbar \dot{D}_\alpha D_\alpha^\dagger$ term. The other term we want to eliminate from the dynamics is the one generated by D_α when acting on Lindblad operators $\hat{L}_{\text{phot}\pm}$, namely $\kappa(\alpha(t)\hat{a}^\dagger + \alpha^*(t)\hat{a})/2$.
An explicit expression of $i\hbar \dot{D}_\alpha D_\alpha^\dagger$ is given by:

$$i\hbar \dot{D}_\alpha D_\alpha^\dagger = i\hbar \left(\dot{\alpha}(t)\hat{a}^\dagger - \dot{\alpha}^*(t)\hat{a}\right) \tag{C.3}$$

so that we are looking for an $\alpha(t) = \alpha e^{-i\omega_d t}$ satisfying:

$$\begin{aligned} &\left(\dot{\alpha}(t)\hat{a}^\dagger - \dot{\alpha}^*(t)\hat{a}\right) - \sqrt{\kappa_{ext}} \left(\beta \hat{a}^\dagger e^{-i\omega_d t} + \beta^* \hat{a} e^{i\omega_d t}\right) \\ &+ i\omega_0 \left(\alpha(t)\hat{a}^\dagger + \alpha^*(t)\hat{a}\right) + \frac{\kappa}{2}(\alpha(t)\hat{a}^\dagger + \alpha^*(t)\hat{a}) = 0. \end{aligned} \tag{C.4}$$

Separating the terms in $\hat{a}$ and $\hat{a}^\dagger$, and performing the derivatives leads to the equation:

$$-i\omega_d\alpha + i\omega_0\alpha - \sqrt{\kappa_{ext}}\beta + \frac{\kappa}{2}\alpha = 0$$
$$\alpha = \frac{\sqrt{\kappa_{ext}}\beta}{\frac{\kappa}{2} + i(\omega_0 - \omega_d)} \tag{C.5}$$

which is exactly the mean intracavity field expected from input-output relations of a cavity under the drive β. The displaced Hamiltonian reads:

$$\hat{H} = \hbar\omega_0\hat{a}^\dagger\hat{a} + \frac{\hbar}{2}\omega_s\hat{\sigma}_z + \hbar g_0\left(\hat{a}\hat{\sigma}_+ + \hat{a}^\dagger\hat{\sigma}_-\right) - \hbar g_0\left(\alpha(t)\hat{\sigma}_+ + \alpha^*(t)\hat{\sigma}_-\right) \tag{C.6}$$

and the displaced density matrix to be used is $D_\alpha\hat{\rho}D_\alpha^\dagger$.

Hamiltonian in the spin rotating frame

We now perform a transformation and put us in the frame rotating at the spin frequency. This turns out to be useful for the subsequent adiabatic elimination of the fast evolving degrees of freedom. The transformation is described by the unitary:

$$R_{\omega_s} = e^{i\omega_s t(\hat{a}^\dagger\hat{a} + \hat{\sigma}_z/2)} \tag{C.7}$$

and leads to the transformed Hamiltonian $\hat{H} \to R_{\omega_s}\hat{H}R_{\omega_s}^\dagger + i\hbar\dot{R}_{\omega_s}R_{\omega_s}^\dagger$:

$$\hat{H} = \hbar\Delta\hat{a}^\dagger\hat{a} + \hbar g_0\left(\hat{a}\hat{\sigma}_+ + \hat{a}^\dagger\hat{\sigma}_-\right) - \hbar g_0\left(\tilde{\alpha}(t)\hat{\sigma}_+ + \tilde{\alpha}^*(t)\hat{\sigma}_-\right) \tag{C.8}$$

where $\Delta = \omega_0 - \omega_s$, $\tilde{\alpha}(t) = \alpha e^{-i(\omega_d - \omega_s)t}$.

C.2 Adiabatic elimination and the Purcell effect

Here we detail the adiabatic elimination adopted in section 3.2.

Adiabatic elimination is a method to describe the effective evolution of a subsystem evolving on a slow timescale with respect to other parts of the system. In our case, the evolution of the cavity degrees of freedom happens on a timescale $\sim 1/\kappa$ which is faster that the timescales of evolution of the spin system, and the timescale of interaction between the spin and the cavity: $\kappa \gg g_0 \gg \Gamma_{\text{phon}}, \gamma$. We follow the derivation of Ref. [79], and define the small parameter $\delta \sim g_0/\kappa \sim \sqrt{\Gamma_{\text{phon}}/\kappa}$.

Consider the density matrix $\hat{\rho}_{cs}$ in the displaced rotating frame, describing the state of the composite spin-cavity system. Its evolution is determined by the master equation:

$$\dot{\hat{\rho}}_{cs} = \frac{1}{i\hbar}[\hat{H}, \hat{\rho}_{cs}] + \sum_i \mathcal{D}_{\hat{L}_i}(\hat{\rho}_{cs}) \tag{C.9}$$

where the Hamiltonian is that of Eq. C.8 and the Lindblad super-operators $\mathcal{D}_{\hat{L}_i}$ describe the effect of the channels coupled to the system, and have explicit action on the density matrix given by:

$$\mathcal{D}_{\hat{L}_i}(\hat{\rho}) = \hat{L}_i\hat{\rho}\hat{L}_i^\dagger - \frac{1}{2}\left\{\hat{L}_i^\dagger\hat{L}_i, \hat{\rho}\right\} \tag{C.10}$$

Within our assumptions the $\hat{L}_i$ operators are:

$$\hat{L}_{\text{phot-}} = \sqrt{\kappa(1+n_{\text{th}})}\hat{a} \tag{C.11}$$

$$\hat{L}_{\text{phot+}} = \sqrt{\kappa n_{\text{th}}}\hat{a}^\dagger \tag{C.12}$$

$$\hat{L}_{\text{phon-}} = \sqrt{\Gamma_{\text{phon}}(1+n_{\text{ph}})}\hat{\sigma}_- \tag{C.13}$$

$$\hat{L}_{\text{phon+}} = \sqrt{\Gamma_{\text{phon}} n_{\text{ph}}}\hat{\sigma}_+ \tag{C.14}$$

$$\hat{L}_2 = \sqrt{\Gamma_2/2}\hat{\sigma}_{\text{z}}. \tag{C.15}$$

Since we are in the regime in which $\delta \ll 1$ we assume that the number of photons in the cavity is always smaller than one on the timescales g_0^{-1}, $\Gamma_{\text{phon}}^{-1}$, the density matrix can thus be expanded as:

$$\begin{aligned}\hat{\rho}_{cs} =& \hat{\rho}_{00}\left|0\right\rangle\left\langle 0\right| + \delta\left(\hat{\rho}_{01}\left|0\right\rangle\left\langle 1\right| + \hat{\rho}_{10}\left|1\right\rangle\left\langle 0\right|\right) + \\ &+ \delta^2\left(\hat{\rho}_{11}\left|1\right\rangle\left\langle 1\right| + \hat{\rho}_{02}\left|0\right\rangle\left\langle 2\right| + \hat{\rho}_{20}\left|2\right\rangle\left\langle 0\right|\right) + O(\delta^3)\end{aligned} \tag{C.16}$$

where $\hat{\rho}_{mn} = \left\langle m\right|\hat{\rho}_{\text{cs}}\left|n\right\rangle$ acts on the spin's Hilbert space. The goal is to derive the dynamics of the reduced density matrix $\dot{\hat{\rho}}_s = \text{Tr}_c[\dot{\hat{\rho}}_{cs}] = \dot{\hat{\rho}}_{00} + \delta^2\dot{\hat{\rho}}_{11} + O(\delta^3)$ up to second order in δ. Since $\dot{\hat{\rho}}_{00}$ is of order zero in δ, we keep the terms up to second order, while for $\dot{\hat{\rho}}_{11}$ we will keep the terms to the order zero. We consider the realistic regime in which the thermal photon population of the cavity is negligible, $n_{th} = 0$.

- We obtain $\dot{\hat{\rho}}_{00}$ by projecting Eq. C.9 on $\left\langle 0\right|$ and $\left|0\right\rangle$, using Eq. C.16:

$$\begin{aligned}\frac{\dot{\hat{\rho}}_{00}}{\kappa} &= \frac{1}{i\hbar\kappa}\left\langle 0\right|\left[\hat{H},\hat{\rho}_{cs}\right]\left|0\right\rangle + \delta^2\hat{\rho}_{11} + \frac{1}{\kappa}\sum_i \mathcal{D}_{\hat{L}_i}(\hat{\rho}_{00}) + O(\delta^3) = \\ &= \left[-i\frac{\delta g_0}{\kappa}\left(\hat{\sigma}_+\hat{\rho}_{10} - \hat{\rho}_{01}\hat{\sigma}_-\right) + i\frac{g_0}{\kappa}[\tilde{\alpha}(t)\hat{\sigma}_+ + \tilde{\alpha}^*(t)\hat{\sigma}_-, \hat{\rho}_{00}]\right] \\ &+ \delta^2\hat{\rho}_{11} + \frac{1}{\kappa}\sum_i \mathcal{D}_{\hat{L}_i}(\hat{\rho}_{00}) + O(\delta^3)\end{aligned} \tag{C.17}$$

  where the last sum runs only on Lindbladians associated to the spin decoherence and decay channels.

- Similarly we obtain $\dot{\hat{\rho}}_{11}$ through:

$$\frac{\dot{\hat{\rho}}_{11}}{\kappa} = -i\frac{g_0}{\kappa\delta}\left(\hat{\sigma}_-\hat{\rho}_{10} - \hat{\rho}_{01}\hat{\sigma}_+\right) - \hat{\rho}_{11} + O(\delta) \tag{C.18}$$

$$\frac{\dot{\hat{\rho}}_{10}}{\kappa} = -i\frac{g_0}{\kappa\delta}\hat{\sigma}_-\hat{\rho}_{00} - \hat{\rho}_{10}\left(\frac{1}{2} + i\frac{\Delta}{\kappa}\right) + O(\delta) \tag{C.19}$$

  The first term in the derivative of $\hat{\rho}_{10}$ represents a slow-varying drive (order δ) while the second one is a damping term of order 1. The adiabatic approximation consists in assuming that, because the damping is faster than the other terms, $\hat{\rho}_{10}$ is always in its steady-state. The same consideration

applies to $\hat{\rho}_{11}$ after substituting the steady state of $\hat{\rho}_{10}$ in the equation. We thus have:

$$\hat{\rho}_{10} = \frac{-ig_0}{\frac{\kappa}{2} + i\Delta}\frac{1}{\delta}\hat{\sigma}_-\hat{\rho}_{00} + O(\delta)$$

$$\hat{\rho}_{11} = \frac{1}{\kappa\delta^2}\frac{\kappa g_0^2}{\left(\frac{\kappa}{2}\right)^2 + \Delta^2}\hat{\sigma}_-\hat{\rho}_{00}\hat{\sigma}_+ + O(\delta) \tag{C.20}$$

Inserting the results of Eq. C.20 back into Eq. C.17 we find:

$$\dot{\hat{\rho}}_s = \dot{\hat{\rho}}_{00} + \delta^2\dot{\hat{\rho}}_{11} + O(\delta^3) = \frac{1}{i\hbar}[\hat{H}_s, \hat{\rho}_{00}] + \mathcal{D}_{\hat{P}}(\hat{\rho}_{00}) + \sum_i \mathcal{D}_{\hat{L}_i}(\hat{\rho}_{00}) + O(\delta^3) \tag{C.21}$$

$$\dot{\hat{\rho}}_{\rm s} \simeq \frac{1}{i\hbar}[\hat{H}_{\rm s}, \hat{\rho}_{\rm s}] + \mathcal{D}_{\hat{P}}(\hat{\rho}_{\rm s}) + \sum_i \mathcal{D}_{\hat{L}_i}(\hat{\rho}_{\rm s}), \tag{C.22}$$

where $\hat{H}_{\rm s} \simeq \langle 0|\,\hat{H}\,|0\rangle$ is the reduced Hamiltonian, and we used $\dot{\hat{\rho}}_{11} = 0$, and:

$$\hat{H}_s = -\hbar g_0\left(\tilde{\alpha}(t)\hat{\sigma}_+ + \tilde{\alpha}^*(t)\hat{\sigma}_-\right) \tag{C.23}$$

$$\hat{P} = \sqrt{\Gamma_p(\Delta)}\hat{\sigma}_- \tag{C.24}$$

$$\Gamma_p(\Delta) = \frac{\kappa g_0^2}{\left(\frac{\kappa}{2}\right)^2 + \Delta^2} \tag{C.25}$$

The new Lindbladian term $\mathcal{D}_{\hat{P}}$, is the result of the adiabatic elimination process, and describes the radiative relaxation of the spin system at rate $\Gamma_{\rm p}$. This enhanced relaxation phenomenon, known as Purcell effect, is responsible for the dominance of radiative relaxation over non-radiative phenomena, when $\Gamma_{\rm p} \gg \Gamma_{\rm phon}$. The above derivation shows that the presence of a lossy cavity with energy damping rate κ, coupled to the spin with coupling rate $g_0 \ll \kappa$, the so-called weak-coupling regime, remarkably leads to an enhancement of the spin relaxation rate.

Average field values in the adiabatic approximation

One can use the adiabatic approximation, which consists fundamentally in taking the expansion of $\hat{\rho}$ in terms of the intra-cavity field states $\{\delta^{m+n}\,|m\rangle\,\langle n|\}_{m+n\leq 2}$, to calculate mean values of the instantaneous field observables. For the number of intra-cavity photons one has:

$$\langle\hat{a}^\dagger\hat{a}\rangle = \mathbf{Tr}[\hat{a}^\dagger\hat{a}(\hat{\rho}_{00}\,|0\rangle\,\langle 0| + \delta\,(\hat{\rho}_{10}\,|1\rangle\,\langle 0| + \hat{\rho}_{01}\,|0\rangle\,\langle 1|) +$$

$$+\delta^2\,(\hat{\rho}_{11}\,|1\rangle\,\langle 1| + \hat{\rho}_{20}\,|2\rangle\,\langle 0| + \hat{\rho}_{02}\,|0\rangle\,\langle 2|))] + O(\delta^3) = Tr_{\rm s}[\delta^2\hat{\rho}_{11}] + O(\delta^3) \tag{C.26}$$

where $\hat{\rho}_{11}$ is obtained from the adiabatic approximation (see Eq. C.20). At order δ (i.e. neglecting terms of order $(\Gamma_{\rm p}/\kappa)^2$ in the observable mean value), one has:

$$\langle\hat{a}^\dagger\hat{a}\rangle = \frac{\Gamma_{\rm p}}{\kappa}\frac{\langle 1 + \hat{\sigma}_z\rangle}{2} + O(\delta^2) \tag{C.27}$$

This equation implies that the average number of photons generated by the spin in the resonator is related to the $M_z = \langle\hat{\sigma}_z\rangle$ component of the magnetization vector.

One can proceed similarly for the field amplitude to obtain $\langle \hat{a} \rangle = \mathrm{Tr}[\delta \hat{\rho}_{10}] + O(\delta^3)$, from which:

$$\langle \hat{a} \rangle = \frac{-ig_0}{\frac{\kappa}{2} + i\Delta} \frac{\langle \hat{\sigma}_x - i\hat{\sigma}_y \rangle}{2} + O(\delta^2), \tag{C.28}$$

where we used $\hat{\sigma}_- = (\hat{\sigma}_x - i\hat{\sigma}_y)/2$. This equation shows that the field amplitude produced by the spin in the cavity is related to the magnetization vector components $M_x = \langle \hat{\sigma}_x \rangle$ and $M_y = \langle \hat{\sigma}_y \rangle$.

C.3 Spin-induced electromagnetic noise

In adiabatic approximation one can compute the fluctuations of the electromagnetic field quadrature $\hat{X} = \frac{1}{2}(\hat{a}^\dagger + \hat{a})$ in an LC resonator coupled to an N-spin ensemble as follows:

$$\langle \Delta \hat{X}^2 \rangle = \frac{1}{2} \Big(\langle \Delta \hat{a}^{\dagger 2} \rangle + \langle \Delta \hat{a}^2 \rangle + 2 \langle \hat{a}^\dagger \hat{a} \rangle + 1 \Big) = \tag{C.29}$$

$$= \frac{1}{4} + \frac{\Gamma_p}{4\kappa} \langle N + \hat{S}_z \rangle - \frac{g_0^2}{4} \left(\frac{\langle \Delta \hat{S}_+^2 \rangle}{\left(\frac{\kappa}{2} - i\Delta\right)^2} + \frac{\langle \Delta \hat{S}_-^2 \rangle}{\left(\frac{\kappa}{2} + i\Delta\right)^2} \right) = \tag{C.30}$$

$$= \frac{1}{4} + \frac{\Gamma_p}{4\kappa} \langle N + \hat{S}_z \rangle - \frac{\Gamma_p}{4\kappa} \langle \Delta \hat{S}_+^2 + \Delta \hat{S}_-^2 \rangle \tag{C.31}$$

where the last equality holds at resonance ($\Delta = 0$), and where we used:

$$\langle \Delta \hat{a}^2 \rangle = \mathrm{Tr}[2\delta^2 \hat{\rho}_{20}] - \mathrm{Tr}[\delta \hat{\rho}_{10}]^2 = \frac{-g_0^2}{\left(\frac{\kappa}{2} - i\Delta\right)^2} \left(\frac{1}{2} \langle \hat{S}_+^2 \rangle - \langle \hat{S}_+ \rangle^2 \right) \tag{C.32}$$

$$\delta^2 \hat{\rho}_{20} = \frac{-g_0^2}{\left(\frac{\kappa}{2} - i\Delta\right)^2} \frac{1}{2} \hat{\rho}_{00} \hat{S}_+^2. \tag{C.33}$$

Since vacuum fluctuations on the quadrature equal $\langle \Delta \hat{X}^2 \rangle_0 = 1/4$, we see that the presence of spin polarization and transverse magnetization modifies the fluctuations of the electromagnetic field. One can now distinguish two limiting cases: the first is when the fluctuations are dominated by the longitudinal term $\langle N + \hat{S}_z \rangle$, the second is when they are dominated by the transverse magnetization terms $\langle \Delta \hat{S}_\pm^2 \rangle$.

Bibliography

[1] A. Schweiger and G. Jeschke, *Principles of pulse electron paramagnetic resonance*. Oxford University Press on Demand, 2001.

[2] A. Bienfait, J. Pla, Y. Kubo, X. Zhou, M. Stern, C. Lo, C. Weis, T. Schenkel, D. Vion, D. Esteve, *et al.*, "Controlling spin relaxation with a cavity," *Nature*, vol. 531, no. 7592, pp. 74–77, 2016.

[3] A. Bienfait, J. Pla, Y. Kubo, M. Stern, X. Zhou, C. Lo, C. Weis, T. Schenkel, M. Thewalt, D. Vion, *et al.*, "Reaching the quantum limit of sensitivity in electron spin resonance," *Nature nanotechnology*, vol. 11, no. 3, p. 253, 2016.

[4] V. Ranjan, S. Probst, B. Albanese, T. Schenkel, D. Vion, D. Esteve, J. Morton, and P. Bertet, "Electron spin resonance spectroscopy with femtoliter detection volume," *Applied Physics Letters*, vol. 116, no. 18, p. 184002, 2020.

[5] T. Sleator, E. L. Hahn, C. Hilbert, and J. Clarke, "Nuclear-spin noise," *Physical review letters*, vol. 55, no. 17, p. 1742, 1985.

[6] M. McCoy and R. Ernst, "Nuclear spin noise at room temperature," *Chemical physics letters*, vol. 159, no. 5-6, pp. 587–593, 1989.

[7] E. Albertinale, L. Balembois, E. Billaud, V. Ranjan, D. Flanigan, T. Schenkel, D. Estève, D. Vion, P. Bertet, and E. Flurin, "Detecting spins with a microwave photon counter," *arXiv preprint arXiv:2102.01415*, 2021.

[8] G. Grynberg, A. Aspect, and C. Fabre, *Introduction to quantum optics: from the semi-classical approach to quantized light*. Cambridge university press, 2010.

[9] C. Gerry, P. Knight, and P. L. Knight, *Introductory quantum optics*. Cambridge university press, 2005.

[10] D. M. Pozar, *Microwave engineering*. John Wiley & sons, 2011.

[11] A. A. Clerk, M. H. Devoret, S. M. Girvin, F. Marquardt, and R. J. Schoelkopf, "Introduction to quantum noise, measurement, and amplification," *Reviews of Modern Physics*, vol. 82, no. 2, p. 1155, 2010.

[12] S. M. Girvin, "Superconducting qubits and circuits: Artificial atoms coupled to microwave photons," *Lectures delivered at Ecole d'Eté Les Houches*, 2011.

[13] W. Woods, G. Calusine, A. Melville, A. Sevi, E. Golden, D. K. Kim, D. Rosenberg, J. L. Yoder, and W. D. Oliver, "Determining interface dielectric losses in superconducting coplanar-waveguide resonators," *Physical Review Applied*, vol. 12, no. 1, p. 014012, 2019.

[14] A. A. Abrikosov, "The magnetic properties of superconducting alloys," *Journal of Physics and Chemistry of Solids*, vol. 2, no. 3, pp. 199–208, 1957.

[15] C. Wang, Y. Y. Gao, I. M. Pop, U. Vool, C. Axline, T. Brecht, R. W. Heeres, L. Frunzio, M. H. Devoret, G. Catelani, *et al.*, "Measurement and control of quasiparticle dynamics in a superconducting qubit," *Nature communications*, vol. 5, no. 1, pp. 1–7, 2014.

[16] A. Bruno, G. De Lange, S. Asaad, K. Van Der Enden, N. Langford, and L. DiCarlo, "Reducing intrinsic loss in superconducting resonators by surface treatment and deep etching of silicon substrates," *Applied Physics Letters*, vol. 106, no. 18, p. 182601, 2015.

[17] K. Serniak, M. Hays, G. De Lange, S. Diamond, S. Shankar, L. Burkhart, L. Frunzio, M. Houzet, and M. Devoret, "Hot nonequilibrium quasiparticles in transmon qubits," *Physical review letters*, vol. 121, no. 15, p. 157701, 2018.

[18] A. A. Golubov, M. Y. Kupriyanov, and E. Il'Ichev, "The current-phase relation in josephson junctions," *Reviews of modern physics*, vol. 76, no. 2, p. 411, 2004.

[19] R. Jaklevic, J. Lambe, A. Silver, and J. Mercereau, "Quantum interference effects in josephson tunneling," *Physical Review Letters*, vol. 12, no. 7, p. 159, 1964.

[20] C. M. Caves, "Quantum limits on noise in linear amplifiers," *Physical Review D*, vol. 26, no. 8, p. 1817, 1982.

[21] F. D. O. Schackert, *A practical quantum-limited parametric amplifier based on the Josephson ring modulator*. Yale University, 2013.

[22] E. Flurin, *The Josephson mixer: a Swiss army knife for microwave quantum optics*. PhD thesis, Ecole normale supérieure-ENS PARIS, 2014.

[23] M. A. C. Beltran, *Development of a Josephson parametric amplifier for the preparation and detection of nonclassical states of microwave fields*. PhD thesis, Citeseer, 2010.

[24] C. Eichler, D. Bozyigit, C. Lang, M. Baur, L. Steffen, J. Fink, S. Filipp, and A. Wallraff, "Observation of two-mode squeezing in the microwave frequency domain," *Physical Review Letters*, vol. 107, no. 11, p. 113601, 2011.

[25] C. Wilson, T. Duty, M. Sandberg, F. Persson, V. Shumeiko, and P. Delsing, "Photon generation in an electromagnetic cavity with a time-dependent boundary," *Physical review letters*, vol. 105, no. 23, p. 233907, 2010.

[26] J. Mutus, T. White, E. Jeffrey, D. Sank, R. Barends, J. Bochmann, Y. Chen, Z. Chen, B. Chiaro, A. Dunsworth, *et al.*, "Design and characterization of a lumped element single-ended superconducting microwave parametric amplifier with on-chip flux bias line," *Applied Physics Letters*, vol. 103, no. 12, p. 122602, 2013.

[27] Z. Lin, K. Inomata, W. Oliver, K. Koshino, Y. Nakamura, J. Tsai, and T. Yamamoto, "Single-shot readout of a superconducting flux qubit with a flux-driven josephson parametric amplifier," *Applied Physics Letters*, vol. 103, no. 13, p. 132602, 2013.

[28] X. Zhou, V. Schmitt, P. Bertet, D. Vion, W. Wustmann, V. Shumeiko, and D. Estève, "High-gain weakly nonlinear flux-modulated josephson parametric amplifier using a squid array," *Physical Review B*, vol. 89, no. 21, p. 214517, 2014.

[29] B. Yurke, L. Corruccini, P. Kaminsky, L. Rupp, A. Smith, A. Silver, R. Simon, and E. Whittaker, "Observation of parametric amplification and deamplification in a josephson parametric amplifier," *Physical Review A*, vol. 39, no. 5, p. 2519, 1989.

[30] W. Wustmann and V. Shumeiko, "Parametric resonance in tunable superconducting cavities," *Physical Review B*, vol. 87, no. 18, p. 184501, 2013.

[31] C. Eichler and A. Wallraff, "Controlling the dynamic range of a josephson parametric amplifier," *EPJ Quantum Technology*, vol. 1, no. 1, pp. 1–19, 2014.

[32] L. D. Landau and E. M. Lifshitz, *Mechanics, Third Edition: Volume 1*. Butterworth-Heinemann, 1976.

[33] R. H. Dicke, "Coherence in spontaneous radiation processes," *Physical review*, vol. 93, no. 1, p. 99, 1954.

[34] J. A. Mlynek, A. A. Abdumalikov, C. Eichler, and A. Wallraff, "Observation of dicke superradiance for two artificial atoms in a cavity with high decay rate," *Nature communications*, vol. 5, no. 1, pp. 1–6, 2014.

[35] G. Feher, J. Gordon, E. Buehler, E. Gere, and C. Thurmond, "Spontaneous emission of radiation from an electron spin system," *Physical Review*, vol. 109, no. 1, p. 221, 1958.

[36] E. L. Hahn, "Spin echoes," *Physical review*, vol. 80, no. 4, p. 580, 1950.

[37] S. J. Balian, "Quantum-bath decoherence of hybrid electron-nuclear spin qubits," *arXiv preprint arXiv:1510.08944*, 2015.

[38] H. Mohammadi, T. Monteiro, and G. Morley, "Bismuth in silicon qubits: the role of hyperfine resonances," tech. rep., 2010.

[39] R. E. George, W. Witzel, H. Riemann, N. Abrosimov, N. Nötzel, M. L. Thewalt, and J. J. Morton, "Electron spin coherence and electron nuclear double resonance of bi donors in natural si," *Physical review letters*, vol. 105, no. 6, p. 067601, 2010.

[40] J. Mansir, P. Conti, Z. Zeng, J. J. Pla, P. Bertet, M. W. Swift, C. G. Van de Walle, M. L. Thewalt, B. Sklenard, Y.-M. Niquet, *et al.*, "Linear hyperfine tuning of donor spins in silicon using hydrostatic strain," *Physical review letters*, vol. 120, no. 16, p. 167701, 2018.

[41] G. Wolfowicz, S. Simmons, A. M. Tyryshkin, R. E. George, H. Riemann, N. V. Abrosimov, P. Becker, H.-J. Pohl, S. A. Lyon, M. L. Thewalt, *et al.*, "Decoherence mechanisms of 209 bi donor electron spins in isotopically pure 28 si," *Physical Review B*, vol. 86, no. 24, p. 245301, 2012.

[42] V. Ranjan, B. Albanese, E. Albertinale, E. Billaud, D. Flanigan, J. Pla, T. Schenkel, D. Vion, D. Esteve, E. Flurin, *et al.*, "Spatially-resolved decoherence of donor spins in silicon strained by a metallic electrode," *arXiv preprint arXiv:2101.04391*, 2021.

[43] J. Pla, A. Bienfait, G. Pica, J. Mansir, F. Mohiyaddin, Z. Zeng, Y.-M. Niquet, A. Morello, T. Schenkel, J. Morton, *et al.*, "Strain-induced spin-resonance shifts in silicon devices," *Physical Review Applied*, vol. 9, no. 4, p. 044014, 2018.

[44] M. D. Eisaman, J. Fan, A. Migdall, and S. V. Polyakov, "Invited review article: Single-photon sources and detectors," *Review of scientific instruments*, vol. 82, no. 7, p. 071101, 2011.

[45] A. Wallraff, D. I. Schuster, A. Blais, L. Frunzio, R.-S. Huang, J. Majer, S. Kumar, S. M. Girvin, and R. J. Schoelkopf, "Strong coupling of a single photon to a superconducting qubit using circuit quantum electrodynamics," *Nature*, vol. 431, no. 7005, pp. 162–167, 2004.

[46] F. Arute, K. Arya, R. Babbush, D. Bacon, J. C. Bardin, R. Barends, R. Biswas, S. Boixo, F. G. Brandao, D. A. Buell, *et al.*, "Quantum supremacy using a programmable superconducting processor," *Nature*, vol. 574, no. 7779, pp. 505–510, 2019.

[47] N. Bergeal, F. Schackert, M. Metcalfe, R. Vijay, V. Manucharyan, L. Frunzio, D. Prober, R. Schoelkopf, S. Girvin, and M. Devoret, "Phase-preserving amplification near the quantum limit with a josephson ring modulator," *Nature*, vol. 465, no. 7294, pp. 64–68, 2010.

[48] M. Castellanos-Beltran, K. Irwin, G. Hilton, L. Vale, and K. Lehnert, "Amplification and squeezing of quantum noise with a tunable josephson metamaterial," *Nature Physics*, vol. 4, no. 12, pp. 929–931, 2008.

[49] C. Macklin, K. O'brien, D. Hover, M. Schwartz, V. Bolkhovsky, X. Zhang, W. Oliver, and I. Siddiqi, "A near–quantum-limited josephson traveling-wave parametric amplifier," *Science*, vol. 350, no. 6258, pp. 307–310, 2015.

[50] F. Mallet, M. Castellanos-Beltran, H. Ku, S. Glancy, E. Knill, K. Irwin, G. Hilton, L. Vale, and K. Lehnert, "Quantum state tomography of an itinerant squeezed microwave field," *Physical Review Letters*, vol. 106, no. 22, p. 220502, 2011.

[51] E. Flurin, N. Roch, F. Mallet, M. H. Devoret, and B. Huard, "Generating entangled microwave radiation over two transmission lines," *Physical review letters*, vol. 109, no. 18, p. 183901, 2012.

[52] B. Abdo, K. Sliwa, F. Schackert, N. Bergeal, M. Hatridge, L. Frunzio, A. D. Stone, and M. Devoret, "Full coherent frequency conversion between two propagating microwave modes," *Physical review letters*, vol. 110, no. 17, p. 173902, 2013.

[53] A. Kamal, J. Clarke, and M. Devoret, "Noiseless non-reciprocity in a parametric active device," *Nature Physics*, vol. 7, no. 4, pp. 311–315, 2011.

[54] K. Koshino, K. Inomata, Z. Lin, Y. Nakamura, and T. Yamamoto, "Theory of microwave single-photon detection using an impedance-matched λ system," *Physical Review A*, vol. 91, no. 4, p. 043805, 2015.

[55] B. Royer, A. L. Grimsmo, A. Choquette-Poitevin, and A. Blais, "Itinerant microwave photon detector," *Physical review letters*, vol. 120, no. 20, p. 203602, 2018.

[56] A. L. Grimsmo, B. Royer, J. M. Kreikebaum, Y. Ye, K. O'Brien, I. Siddiqi, and A. Blais, "Quantum metamaterial for broadband detection of single microwave photons," *Physical Review Applied*, vol. 15, no. 3, p. 034074, 2021.

[57] R. Lescanne, S. Deléglise, E. Albertinale, U. Réglade, T. Capelle, E. Ivanov, T. Jacqmin, Z. Leghtas, and E. Flurin, "Irreversible qubit-photon coupling for the detection of itinerant microwave photons," *Physical Review X*, vol. 10, no. 2, p. 021038, 2020.

[58] S. Gleyzes, S. Kuhr, C. Guerlin, J. Bernu, S. Deleglise, U. B. Hoff, M. Brune, J.-M. Raimond, and S. Haroche, "Quantum jumps of light recording the birth and death of a photon in a cavity," *Nature*, vol. 446, no. 7133, pp. 297–300, 2007.

[59] Y.-F. Chen, D. Hover, S. Sendelbach, L. Maurer, S. Merkel, E. Pritchett, F. Wilhelm, and R. McDermott, "Microwave photon counter based on josephson junctions," *Physical review letters*, vol. 107, no. 21, p. 217401, 2011.

[60] A. Narla, S. Shankar, M. Hatridge, Z. Leghtas, K. M. Sliwa, E. Zalys-Geller, S. O. Mundhada, W. Pfaff, L. Frunzio, R. J. Schoelkopf, *et al.*, "Robust concurrent remote entanglement between two superconducting qubits," *Physical Review X*, vol. 6, no. 3, p. 031036, 2016.

[61] K. Inomata, Z. Lin, K. Koshino, W. D. Oliver, J.-S. Tsai, T. Yamamoto, and Y. Nakamura, "Single microwave-photon detector using an artificial λ-type three-level system," *Nature communications*, vol. 7, no. 1, pp. 1–7, 2016.

[62] A. Opremcak, I. Pechenezhskiy, C. Howington, B. Christensen, M. Beck, E. Leonard, J. Suttle, C. Wilen, K. Nesterov, G. Ribeill, *et al.*, "Measurement of a superconducting qubit with a microwave photon counter," *Science*, vol. 361, no. 6408, pp. 1239–1242, 2018.

[63] S. Kono, K. Koshino, Y. Tabuchi, A. Noguchi, and Y. Nakamura, "Quantum non-demolition detection of an itinerant microwave photon," *Nature Physics*, vol. 14, no. 6, pp. 546–549, 2018.

[64] J.-C. Besse, S. Gasparinetti, M. Collodo, T. Walter, P. Kurpiers, C. Eichler, and A. Wallraff, "Single-shot quantum non-demolition detection of itinerant microwave photons," in *APS March Meeting Abstracts*, vol. 2018, pp. A39–007, 2018.

[65] R. Dassonneville, R. Assouly, T. Peronnin, P. Rouchon, and B. Huard, "Number-resolved photocounter for propagating microwave mode," *Physical Review Applied*, vol. 14, no. 4, p. 044022, 2020.

[66] J. Poyatos, J. I. Cirac, and P. Zoller, "Quantum reservoir engineering with laser cooled trapped ions," *Physical review letters*, vol. 77, no. 23, p. 4728, 1996.

[67] J. Gambetta, A. Blais, D. I. Schuster, A. Wallraff, L. Frunzio, J. Majer, M. H. Devoret, S. M. Girvin, and R. J. Schoelkopf, "Qubit-photon interactions in a cavity: Measurement-induced dephasing and number splitting," *Physical Review A*, vol. 74, no. 4, p. 042318, 2006.

[68] E. A. Sete, J. M. Martinis, and A. N. Korotkov, "Quantum theory of a bandpass purcell filter for qubit readout," *Physical Review A*, vol. 92, no. 1, p. 012325, 2015.

[69] Z. K. Minev, Z. Leghtas, S. O. Mundhada, L. Christakis, I. M. Pop, and M. H. Devoret, "Energy-participation quantization of josephson circuits," *arXiv preprint arXiv:2010.00620*, 2020.

[70] A. Dunsworth, A. Megrant, C. Quintana, Z. Chen, R. Barends, B. Burkett, B. Foxen, Y. Chen, B. Chiaro, A. Fowler, *et al.*, "Characterization and reduction of capacitive loss induced by sub-micron josephson junction fabrication in superconducting qubits," *Applied Physics Letters*, vol. 111, no. 2, p. 022601, 2017.

[71] G. Calusine, A. Melville, W. Woods, R. Das, C. Stull, V. Bolkhovsky, D. Braje, D. Hover, D. K. Kim, X. Miloshi, *et al.*, "Analysis and mitigation of interface losses in trenched superconducting coplanar waveguide resonators," *Applied Physics Letters*, vol. 112, no. 6, p. 062601, 2018.

[72] Y. Kubo, I. Diniz, C. Grezes, T. Umeda, J. Isoya, H. Sumiya, T. Yamamoto, H. Abe, S. Onoda, T. Ohshima, *et al.*, "Electron spin resonance detected by a superconducting qubit," *Physical Review B*, vol. 86, no. 6, p. 064514, 2012.

[73] R. K. Zhukavin, K. Kovalevsky, V. Tsyplenkov, V. Shastin, S. Pavlov, H.-W. Hübers, H. Riemann, N. Abrosimov, and A. Ramdas, "Spin-orbit coupling effect on bismuth donor lasing in stressed silicon," *Applied Physics Letters*, vol. 99, no. 17, p. 171108, 2011.

[74] R. P. Budoyo, K. Kakuyanagi, H. Toida, Y. Matsuzaki, and S. Saito, "Electron spin resonance with up to 20 spin sensitivity measured using a superconducting flux qubit," *Applied Physics Letters*, vol. 116, no. 19, p. 194001, 2020.

[75] I. Abella, N. Kurnit, and S. Hartmann, "Photon echoes," *Physical review*, vol. 141, no. 1, p. 391, 1966.

[76] S. Probst, A. Bienfait, P. Campagne-Ibarcq, J. Pla, B. Albanese, J. Da Silva Barbosa, T. Schenkel, D. Vion, D. Esteve, K. Mølmer, *et al.*, "Inductive-detection electron-spin resonance spectroscopy with 65 spins/hz sensitivity," *Applied Physics Letters*, vol. 111, no. 20, p. 202604, 2017.

[77] V. Ranjan, S. Probst, B. Albanese, A. Doll, O. Jacquot, E. Flurin, R. Heeres, D. Vion, D. Esteve, J. Morton, *et al.*, "Pulsed electron spin resonance spectroscopy in the purcell regime," *Journal of Magnetic Resonance*, vol. 310, p. 106662, 2020.

[78] A. P. Place, L. V. Rodgers, P. Mundada, B. M. Smitham, M. Fitzpatrick, Z. Leng, A. Premkumar, J. Bryon, A. Vrajitoarea, S. Sussman, *et al.*, "New material platform for superconducting transmon qubits with coherence times exceeding 0.3 milliseconds," *Nature communications*, vol. 12, no. 1, pp. 1–6, 2021.

[79] Z. Leghtas, S. Touzard, I. M. Pop, A. Kou, B. Vlastakis, A. Petrenko, K. M. Sliwa, A. Narla, S. Shankar, M. J. Hatridge, *et al.*, "Confining the state of light to a quantum manifold by engineered two-photon loss," *Science*, vol. 347, no. 6224, pp. 853–857, 2015.

université PARIS-SACLAY

ÉCOLE DOCTORALE
Physique en Île-de-France (EDPIF)

Titre: Mesure de la fluorescence de spin avec un compteur de photons à micro-ondes

Mots clés: Fluorescence de spin, ESR, Transmon qubit, micro-ondes, compteur de photons

Résumé: La résonance magnétique est une branche de la science qui vise à détecter les spins via leur absorption et émission de rayonnement électromagnétique. On distingue deux domaines: la résonance magnétique nucléaire (RMN) qui vise à détecter les spins des noyaux, et la résonance de spin électronique (ESR) qui concerne la détection du spin des électrons non appariés. Dans cette thèse, nous introduisons une nouvelle méthode pour la spectroscopie ESR, consistant en la détection du signal de fluorescence micro-onde incohérent émis par un ensemble de spins relaxant vers leur état fondamental après avoir eté excités. Afin de démontrer cette méthode, nous utilisons les spins électroniques appartenant aux donneurs de bismuth dans le silicium. L'émission du signal de fluorescence est favorisée par l'effet Purcell, dû au couplage de l'ensemble de spins à un résonateur supraconducteur ayant un petit volume de mode et de faibles pertes. Nous connectons le port de sortie du système spin-résonateur à l'entrée d'un détecteur de photons micro-ondes accordable en fréquence (SMPD) récemment développé, basé sur le mélange à quatre ondes avec un qubit supraconducteur. Après une impulsion d'excitation, les spins relaxent vers leur état fondamental en émettant un flux de photons incohérents qui constitue le signal de fluorescence et qui est détecté par le SMPD. Nous montrons que le signal de fluorescence peut être utilisé pour effectuer la spectroscopie de l'ensemble et mesurer ses propriétés. Nous comparons cette technique à la détection par écho et discutons l'avantage en sensibilité pour un petit nombre de spins.

Title: Measuring spin fluorescence with a microwave photon counter

Keywords: Spin fluorescence, ESR, Transmon qubit, microwave, photon counter

Abstract: Magnetic resonance is a branch of science that aims to detect spins via their absorption and emission of electromagnetic radiation. Two areas can be distinguished: nuclear magnetic resonance (NMR) which aims at detecting the spins of nuclei, and electron spin resonance (ESR) that concerns the detection of the spin of unpaired electrons. In this thesis, we introduce a new method for ESR spectroscopy, consisting of the detection of the incoherent microwave fluorescence signal emitted by an ensemble spins relaxing to their ground state after an excitation pulse. In order to demonstrate this method, we use the electronic spins belonging to bismuth donors in silicon. Emission of the fluorescence signal is favored by the Purcell effect, due to the coupling of the spin ensemble to a superconducting resonator with small mode volume and low losses. We connect the output port of the spin-resonator system to the input of a newly-developed frequency-tunable single microwave photon detector (SMPD), based on four-wave mixing with a superconducting qubit. After an excitation pulse, the spins relax to their ground state emitting a stream of incoherent photons which constitutes the fluorescence signal and is detected with the SMPD. We show that the fluorescence signal can be used to perform spectroscopy of the ensemble and measure relevant properties. We compare this technique to standard echo detection and discuss its increased sensitivity for small numbers of spins.

Université Paris-Saclay
Espace Technologique / Immeuble Discovery
Route de l'Orme aux Merisiers RD 128 / 91190 Saint-Aubin, France